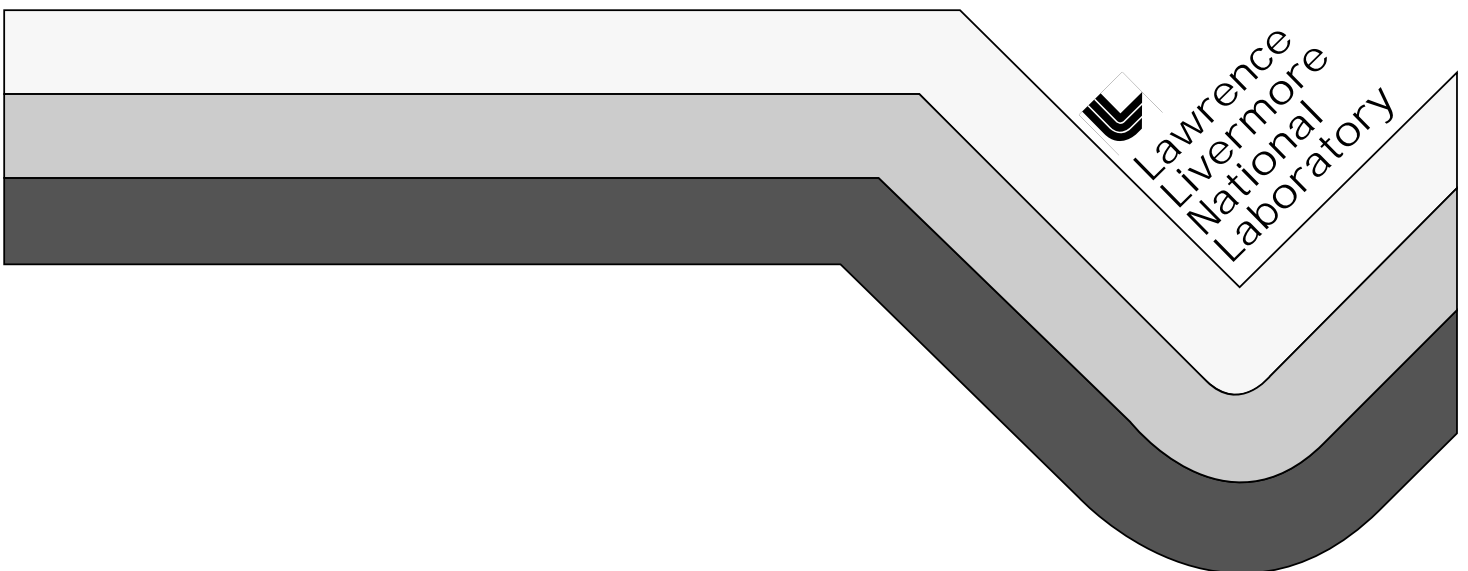


A Langevin Equation Model of Dispersion in the Convective Boundary Layer

John Sterling Nasstrom

**Ph.D. Dissertation
University of California, Davis**

August 1998



DISCLAIMER

This document was prepared as an account of work sponsored by an agency of the United States Government. Neither the United States Government nor the University of California nor any of their employees, makes any warranty, express or implied, or assumes any legal liability or responsibility for the accuracy, completeness, or usefulness of any information, apparatus, product, or process disclosed, or represents that its use would not infringe privately owned rights. Reference herein to any specific commercial product, process, or service by trade name, trademark, manufacturer, or otherwise, does not necessarily constitute or imply its endorsement, recommendation, or favoring by the United States Government or the University of California. The views and opinions of authors expressed herein do not necessarily state or reflect those of the United States Government or the University of California, and shall not be used for advertising or product endorsement purposes.

This report has been reproduced
directly from the best available copy.

Available to DOE and DOE contractors from the
Office of Scientific and Technical Information
P.O. Box 62, Oak Ridge, TN 37831
Prices available from (423) 576-8401

Available to the public from the
National Technical Information Service
U.S. Department of Commerce
5285 Port Royal Rd.,
Springfield, VA 22161

A Langevin Equation Model of Dispersion in the Convective Boundary Layer

John Sterling Nasstrom

Manuscript date: August 1998



A Langevin Equation Model of Dispersion
in the Convective Boundary Layer

By

JOHN STERLING NASSTROM
B.S. (University of California, Davis) 1980
M.S. (University of California, Davis) 1983

DISSERTATION

Submitted in partial satisfaction of the requirements for the degree of

DOCTOR OF PHILOSOPHY

in

Atmospheric Science

in the

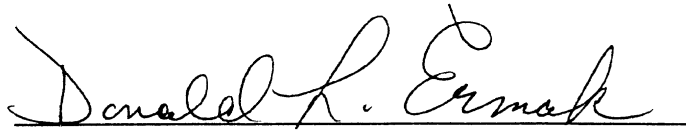
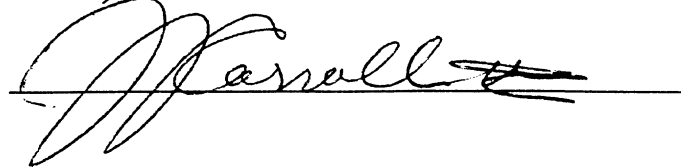
OFFICE OF GRADUATE STUDIES

of the

UNIVERSITY OF CALIFORNIA

DAVIS

Approved:

A handwritten signature in black ink, reading "Donald R. Esmak", written over a horizontal line.A handwritten signature in black ink, reading "Myron R. Kan", written over a horizontal line.A handwritten signature in black ink, reading "Marshall", written over a horizontal line.

Committee in Charge

1998

Contents

<i>Abstract</i>	v
<i>Acknowledgments</i>	vii
1. Introduction	1
2. Convective Boundary Layer	7
2.1 Turbulent structures in the CBL.....	7
2.2 Scaling relationships	10
2.3 Small-scale properties of turbulence	16
2.4 Dispersion phenomena.....	20
3. Langevin Equation Models	27
3.1 Lagrangian stochastic approach	28
3.2 Langevin equation	30
3.3 Kramers-Moyal expansion and Fokker-Planck equation	32
3.4 Langevin equation models for skewed turbulence	34
3.4.1 Previous studies	34
3.4.2 Assumptions	36
3.4.3 Nonlinear-Gaussian Langevin equation model	37
3.4.4 Linear-skewed Langevin equation model	42
3.4.5 Special case: Gaussian (unskewed) turbulence.....	46
3.4.6 Deterministic acceleration, $a(w)$, for the two Langevin equations.....	47
3.5 Assumptions and justification of Langevin equation approach.....	48

3.6 Numerical simulation of $w(t)$	51
3.6.1 Nonlinear-Gaussian Langevin equation model	52
3.6.2 Linear-Skewed Langevin equation model	52
3.7 Numerical simulation of $z(t)$	56
3.8 Reflection boundary conditions	57
4. Model Evaluation	65
4.1 Tests in unbounded turbulence	65
4.2 Well-mixed tests in bounded turbulence	78
4.3 CBL simulation	83
4.3.1 Two-dimensional conceptual model	84
4.3.2 Vertical velocity distribution	86
4.3.3 Lagrangian correlation time	88
4.3.4 Cross-wind-integrated concentration	90
4.3.5 Sensitivity tests	116
4.3.6 Discussion	117
5. Summary and Conclusions	123
<i>Appendices</i>	130
Appendix A: Bi-Gaussian velocity distribution	130
Appendix B: Linear-skewed model velocity moments, autocorrelation functions, position moments and joint velocity-position moments	133
Appendix C: Linear-skewed model random velocity increment distribution	139
Double-block distribution	139
Fluid velocity moments	143
Continuity of $w(t)$	144
Appendix D: CBL simulation sensitivity tests	149
<i>References</i>	177

Abstract

This dissertation presents the development and evaluation of a Lagrangian stochastic model of vertical dispersion of trace material in the convective boundary layer (CBL). This model is based on a Langevin equation of motion for a fluid particle, and assumes the fluid vertical velocity probability distribution is skewed and spatially homogeneous. This approach can account for the effect of large-scale, long-lived turbulent structures and skewed vertical velocity distributions found in the CBL. The form of the Langevin equation used has a linear (in velocity) deterministic acceleration and a skewed random acceleration. For the case of homogeneous fluid velocity statistics, this "linear-skewed" Langevin equation can be integrated explicitly, resulting in a relatively efficient numerical simulation method. It is shown that this approach is more efficient than an alternative using a "nonlinear-Gaussian" Langevin equation (with a nonlinear deterministic acceleration and a Gaussian random acceleration) assuming homogeneous turbulence, and much more efficient than alternative approaches using Langevin equation models assuming inhomogeneous turbulence. "Reflection" boundary conditions for selecting a new velocity for a particle that encounters a boundary at the top or bottom of the CBL were investigated. These include one method using the standard assumption that the magnitudes of the particle incident and reflected velocities are positively correlated, and two alternatives in which the magnitudes of these velocities are negatively correlated and uncorrelated. The constraint that spatial and velocity distributions of a well-mixed tracer must be the same as those of the fluid, was used to develop the Langevin equation models and the reflection boundary conditions. The two Langevin equation models and three reflection methods were successfully tested using cases for which exact, analytic statistical properties of particle velocity and position are known, including well-mixed spatial and velocity distributions. Simulations of laboratory experiments of CBL dispersion show that both homogeneous Langevin equation models can simulate the important aspects of dispersion in the CBL. The negatively-correlated-speed reflection boundary condition simulates the observed dispersion of material in the CBL significantly better than either of the other two reflection methods.

Acknowledgments

I am very grateful to Dr. Donald Ermak for the valuable guidance and support he has given me throughout this research. I am also grateful to Prof. John Carroll for the guidance and helpful suggestions he has given me, and to the other members of my committee, Professors Kyaw Tha Paw U, Roger Shaw, and Wolfgang Kollman, for their helpful comments and thoughtful examination of this work.

I would like to express my gratitude to Dr. Thomas Sullivan, Dr. James Ellis, Dr. Marvin Dickerson, Dr. Paul Gudiksen, and many other colleagues at Lawrence Livermore National Laboratory, for their support and encouragement. I thank Howard Rodean for his thorough review of previous work on Lagrangian stochastic modeling of turbulent dispersion, which was useful during my introduction to this subject. Support for this work was received from the Atmospheric Release Advisory Capability program of the U.S. Department of Energy in the Atmospheric Science Division of the University of California, Lawrence Livermore National Laboratory under contract number W-7405-Eng-48.

Discussions with Dr. Brian Sawford, Division of Atmospheric Research, CSIRO, Australia, were very helpful during this research. I also thank Dr. Erik Näslund for helpful dialogue, and for support for a guest researcher visit at the National Defense Research Establishment, Umeå, Sweden, during which some of this work was done.

Understanding, patience, and support from my wife, Sharon, and daughters, Samantha and Blaire, made this work possible.

1

Introduction

This dissertation presents the development and evaluation of a Langevin equation model for numerically simulating vertical dispersion of material in the convective atmospheric boundary layer. Dispersion models are important tools for assessing the health and environmental impacts of air pollutants. Convective boundary layers are prevalent during daytime, fair weather conditions over land, and are characterized by large turbulent structures with size comparable to the depth of the boundary layer (typically, 200-2000 m). The turbulent properties of the convective boundary layer, or CBL, cause the vertical dispersion of material to be dramatically different from that in other types of boundary layers (e.g., stable, nighttime boundary layers or near-neutral boundary layers during cloudy, strong-wind conditions). The Langevin equation for the motion of a fluid particle provides a means to simulate the possible trajectories of particles in complex turbulent flows, such as those found in the CBL, and to calculate the dispersion of trace material.

Dispersion of material in the CBL is dominated by large-scale, coherent turbulent structures or eddies. Strong updrafts or thermals cover approximately 40% of the horizontal area in the CBL, while compensating weaker downdrafts cover 60% of the area. This results in a positively skewed vertical velocity distribution. Because of the skewed vertical velocity, pollutant emitted into the CBL from an elevated, continuous source, has a higher probability of being emitted into a downdraft. Due to the large-scale coherent nature of the circulations, neutrally buoyant material emitted into a downdraft is typically carried directly to the surface. The result is that the height of the maximum

time-average concentration decreases with downwind distance. In contrast, material from a near-surface source either enters an updraft immediately or travels horizontally near the surface until it becomes incorporated in an updraft. After a short time, this results in a dramatic increase in the height of the maximum concentration with downwind distance. This behavior is not found in neutral or stable boundary layer turbulence which is characterized by smaller turbulent structures and unskewed vertical velocity distributions. For an elevated source, significant underprediction of ground-level pollutant concentrations can occur if the unique properties of CBL turbulence are not taken into account in dispersion models. CBL turbulence properties and dispersion phenomena will be reviewed in Chapter 2.

Lagrangian stochastic models based on the Langevin equation provide a means to determine the possible trajectories of fluid particles in a turbulent flow. The Langevin equation of motion for a particle equates the net acceleration on a particle to the sum of a deterministic acceleration and a random acceleration. Integration of the Langevin equation in time provides a means of calculating the time evolution of the velocity of a particle, and spatial trajectories. Using Monte Carlo simulations, ensemble-mean air concentration can be estimated from many independent realizations of possible trajectories of particles released at a source.

The Langevin equation modeling approach has been used successfully to simulate tracer dispersion in complex turbulent flows which have large-scale structures, and inhomogeneous and non-Gaussian turbulent properties (Wilson and Sawford, 1996). Because a Langevin equation model simulates the correlation in time of a particle's velocity, it can be used to model dispersion at travel times less than (and greater than) the Lagrangian velocity correlation time (typically 1 to 15 min in the CBL). This makes the

Langevin equation a viable model for simulating dispersion at any time typically of interest.

The Lagrangian stochastic approach using the Langevin equation has some significant advantages, compared to other approaches. Lagrangian stochastic methods require only information on the statistical properties of the velocity field. In contrast, Eulerian approaches based on the Reynolds-averaged conservation of species equation require information on the joint moments of velocity and concentration. Closure assumptions that are needed to determine these joint moments depend on the concentration distribution, and are not universally valid (Deardorff, 1978).

Unlike Langevin equation models, Eulerian or Lagrangian models based on the diffusion equation (which use an eddy diffusivity to parameterize the diffusive properties of turbulence) are only applicable for times much greater than Lagrangian correlation time, τ , of the fluid velocity (e.g., Sawford, 1985). At these times, material from a point source will already be diluted throughout the depth of the CBL. Therefore, the advection-diffusion equation is not a valid approach to simulating dispersion of material in the CBL, except for the initial diffusion of sources very near the surface where τ becomes small.

Numerical methods based on the Lagrangian approach have advantages because they are meshless. In contrast, Eulerian methods can suffer from numerical diffusion, may not conserve mass, and may produce negative concentrations (Seinfeld, 1988). Lagrangian methods can resolve point sources without additional computational cost or an approximate sub-grid parameterization, unlike Eulerian methods or hybrid Eulerian-Lagrangian, particle-in-cell methods (e.g., Lange, 1978). Unlike particle-in-cell methods, the accuracy of an individual particle trajectory calculation using a Lagrangian stochastic model is not dependent on grid resolution or the number of trajectories computed. In

addition, first-order chemical reactions or radioactive decay can be handled simply in a Lagrangian frame using functions of material age.

Simplified statistical models of vertical dispersion in the CBL (e.g., Weil, 1988) have been fairly successful in simulating dispersion from elevated sources in the CBL by using the skewness of vertical velocity at the source height and assuming a uniform horizontal mean wind velocity, and an infinite Lagrangian time scale. A Langevin equation approach, however, is not limited to these simplifying assumptions, and can be applied to other turbulent flows.

Langevin equation models that attempt to resolve the inhomogeneous properties of the vertical velocity fluctuations near the top and bottom of the CBL have been fairly successful (e.g., Luhar and Britter, 1989; Weil, 1989), but have a practical limitation that small numerical integration time steps are required for accurate solutions. It has been recognized that simplified Langevin equation models that assume skewed but homogeneous velocity statistics can capture the important aspects of dispersion from sources in the CBL (Hurley and Physick, 1993), and can use significantly longer time steps.

The use of longer numerical integration time steps makes dispersion models more efficient, and more useful for practical applications. For example, dispersion model predictions of air concentration patterns following accidental releases of hazardous material need to be made in a timely manner. Efficiency is also important for applications requiring a long numerical integration period (e.g., continental-scale dispersion from a Chernobyl-type accident).

The work presented in this dissertation further investigates the ability of homogeneous, skewed Langevin equation models to simulate CBL vertical dispersion. Previous Langevin equation models will be reviewed in Chapter 3. The development of a Langevin equation model for homogeneous, skewed turbulence will be presented in Chapter 3. This model is based on a "linear-skewed" Langevin equation, which assumes that the deterministic acceleration is a linear function of velocity and the random acceleration is non-Gaussian and skewed. As discussed by Thomson (1984, 1987), Sawford (1986) and Sawford & Guest (1987), there is a fundamental difficulty in applying this form of the Langevin equation: all the cumulants of the random term are non-zero and when higher order cumulants are important it is difficult to generate such a random variable. For inhomogeneous turbulence, it appears this difficulty has not been overcome. However, for the simplified case of homogeneous skewed turbulence, it will be shown that a linear-skewed Langevin equation model can be successfully developed. A model, used by previous investigators, based on a "nonlinear-Gaussian" form of the Langevin equation (which has a non-linear deterministic acceleration and a Gaussian random acceleration) will also be presented in Chapter 3 for comparison purposes.

Reflection boundary conditions consistent with the assumption of homogeneous, skewed turbulence are presented in Chapter 3. In a homogeneous Langevin equation model, interactions with boundaries must be handled by "reflection", the selection of a new velocity given the incident velocity. A sound basis for reflection boundary conditions in skewed turbulence was described by Thomson and Montgomery (1994), and was used in this work. In addition to a method using the standard assumption that the magnitude of the incident and reflected velocities are positively correlated, two alternatives were developed and tested.

Chapter 4 presents the results of tests, comparisons and evaluations of the two Langevin equation models and the three reflection boundary conditions using (a) simulations of cases for which analytic statistical properties of particle position and velocity are known, including well-mixed spatial and velocity distributions and (b) results of Willis and Deardorff's (1976b, 1978, 1981) laboratory experiments of CBL dispersion. A summary and the conclusions resulting from this work are presented in Chapter 5.

2

Convective Boundary Layer

Convective boundary layer (CBL) turbulence properties and dispersion phenomena will be reviewed in this chapter. Much of the foundation for the current understanding of CBL turbulence was laid by Deardorff (1970a, 1970b, 1972, 1974a, 1974b), who studied the CBL using 3-D numerical large-eddy simulations (LES). Much of our current understanding of tracer dispersion in the CBL comes from Willis and Deardorff's (1976a, 1976b, 1978 & 1981) water tank experiments, and from Lamb's (1978a, 1978b, 1982) numerical experiments using a Lagrangian dispersion model and Deardorff's LES data. In Section 2.1, turbulent structures in the CBL are reviewed. In Section 2.2, relevant turbulence scaling relationships are presented and discussed. The "universal" small-scale properties of turbulent motions are reviewed in Section 2.3. In Section 2.4, observed CBL dispersion phenomena are reviewed.

2.1 Turbulent structures in the CBL

The properties of turbulence in the CBL are dominated by large, long-lived turbulent structures that are driven by buoyancy forces associated with heating and/or evaporation from the surface. Fig. 2.1 shows a schematic diagram of the CBL. The dominant large scale turbulent structures have a depth comparable to the boundary layer depth, h , which is equal to the average height of the capping temperature inversion, z_i (typical values range from 200 m to 2 km). These structures have relatively strong vertical velocities (on the order of 1 m s^{-1}) and long time scales (1 to 15 min for air to circulate through the

depth of the boundary layer). As a result, material released into the CBL is mixed relatively quickly throughout the depth of the boundary layer. For example, the time required for this is one to two orders of magnitude less than in neutral boundary layers (Deardorff, 1972).

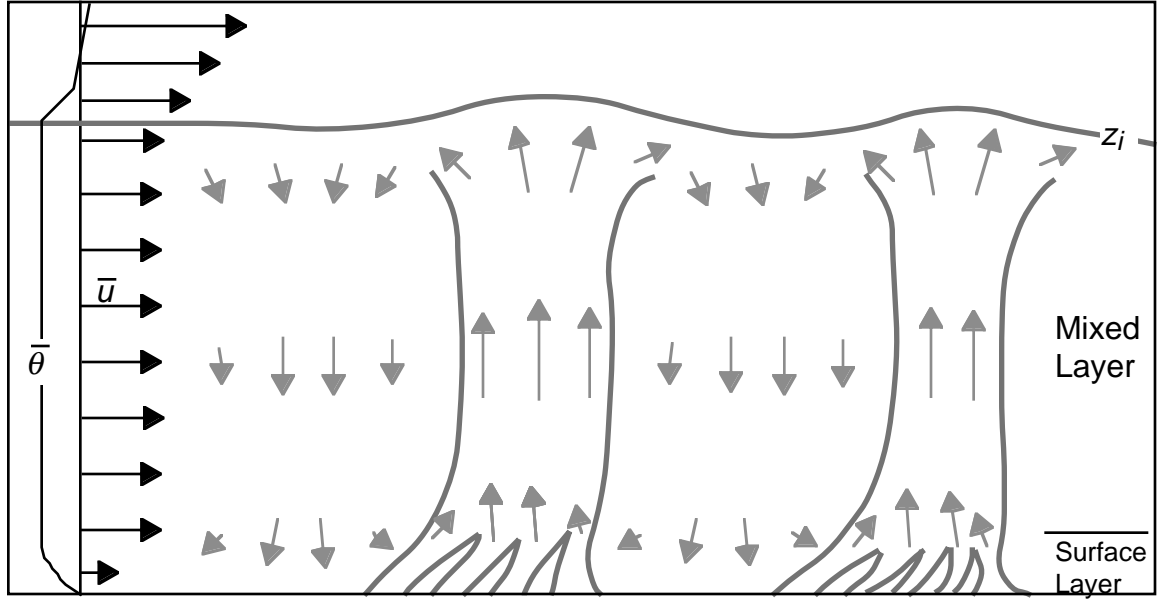


Fig. 2.1. Schematic diagram of the convective boundary layer showing the mean potential temperature profile, $\bar{\theta}(z)$; the mean wind profile, $\bar{u}(z)$ (darker vectors); deviations from mean wind (lighter vectors), boundaries of plumes and thermals; and height of temperature inversion, z_i (after Wyngaard, 1985; Williams and Hacker, 1993; Briggs, 1988).

The time- or area-averaged structure of the CBL can be divided into four layers: surface layer ($z < |L|$), free convection layer ($|L| < z < 0.1h$), mixed layer ($0.1h < z < 0.8h$), and interfacial or entrainment layer ($0.8h < z < 1.2h$) (Holtslag and Nieuwstadt, 1986). $|L|$ is the absolute value of the Obukhov length, and is the height above which buoyant production of turbulent kinetic energy dominates, in contrast to shear production closer to the surface. The surface layer is characterized by an unstable, superadiabatic temperature profile, upward turbulent heat flux, and nearly logarithmic wind profile. The mixed layer is characterized by well mixed, relatively uniform profiles of potential temperature and

wind velocity, and by upward heat flux that decreases approximately linearly with height. The entrainment layer is characterized by a stable temperature profile, downward heat flux that decreases to near zero at the top, and mean quantities that vary smoothly with height between the mixed layer value and the free atmosphere value above. The entrainment layer represents the area- or time-average thickness of a layer that is produced by updrafts impinging on a strongly stable temperature inversion, causing the height of the inversion, z_i , to vary considerably.

Observational studies in the laboratory (Willis and Deardorff, 1979) and atmosphere (e.g., Williams and Hacker, 1993), as well as LES numerical modeling studies (e.g., Schmidt and Schumann, 1989) have led to a general understanding of the turbulent structures in the CBL, and the associated circulation patterns. Warm rising air in the surface layer is organized into coherent structures called “plumes” with horizontal dimensions on the order 100 m. Surface-layer plumes extend continuously through the depth of the surface layer, and typically tilt downwind with height due to wind shear. The plumes merge and become organized as they rise in the surface and free convection layers to form the much larger updraft regions or “thermals” in the mixed layer. Thermals have average horizontal spacing of approximately h , and diameters as large as $0.45h$ (Young, 1988). Mixed-layer thermals are relatively vertical due to the more uniform wind in that layer, and extend continuously through the depth of the CBL.

Between updraft regions in the mixed layer are wider downdraft regions, covering approximately 60% of the horizontal area in the middle of the CBL. The cores of these downdrafts penetrate all the way through the free convection layer and surface layer. These downdrafts suppress upward motion and force the surface flow radially outward from their centers. Some thermals may be relatively closely spaced, with relatively weaker downdrafts occurring between them. Convergence lines form near the surface

between adjacent downdraft regions. Warm surface layer plumes are organized along these lines, with air moving vertically and horizontally toward mixed layer thermals that tend to occur above the intersections of these lines. The corresponding horizontal pattern is often described as "spokes" leading to "hubs" below the mixed layer thermals. The convergence lines can form irregular, interconnected polygon-shaped rings around the downdraft regions.

Updrafts are driven by buoyancy forces, and gain momentum as they rise in the mixed layer. When air in updrafts impinges on the stable inversion layer it can penetrate into the overlying, warmer (higher potential temperature), free-atmosphere air before becoming negatively buoyant and sinking back down into the mixed layer. The depth of the CBL increases (relative to an increase or decrease due to any larger-scale mean vertical velocity) through entrainment of free atmosphere air from above the inversion. In the entrainment process, curtains of free atmosphere air move downward around the thermals overshooting into the free atmosphere, and are incorporated into the mixed layer. At any instant the stable inversion layer may be only meters thick with relatively sharp discontinuities in temperature, moisture and wind velocity between the boundary layer air and the free atmosphere air above. However, the height of this layer can vary over hundreds of meters, between approximately $0.8h$ and $1.2h$, on average. The boundary layer depth, h , then represents a height where, on average, approximately 50% of the air has free atmosphere characteristics and 50% has CBL characteristics (Stull, 1988).

2.2 Scaling relationships

The important scaling parameters for average turbulent properties vary between layers in the atmospheric boundary layer, or ABL. The turbulence scaling regions along with the

important scaling parameters for each region of the unstable ABL were summarized by Holtslag and Nieuwstadt (1986), and are shown in Fig. 2.2.

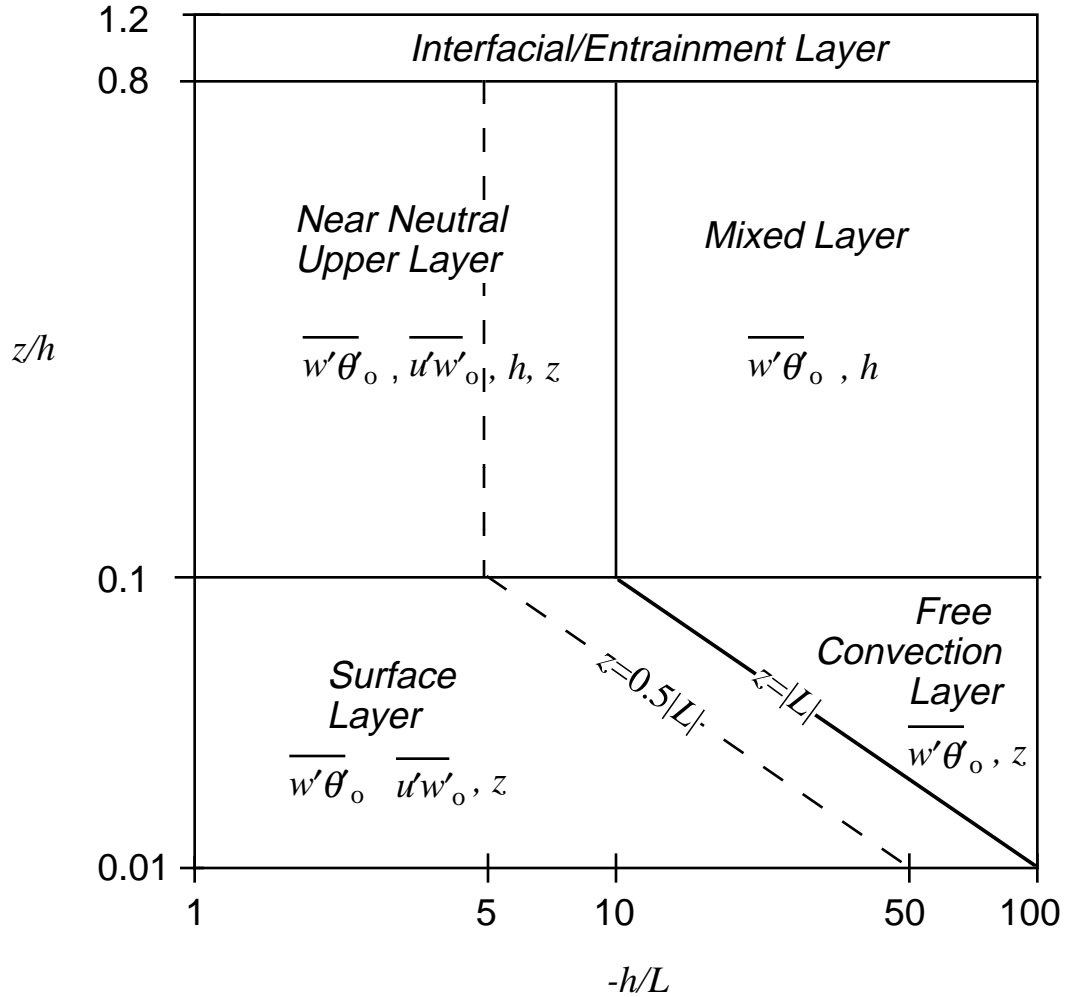


Fig. 2.2. Unstable boundary layer turbulence scaling regions and the corresponding basic turbulence scaling parameters (after Holtslag and Nieuwstadt, 1986).

The surface layer is the layer above the relatively thin viscous and roughness sublayers adjacent to the surface, and below approximately $0.1h$ or $|L|$ (whichever is lower). The important scaling parameters in the surface layer are the turbulent kinematic momentum flux or Reynolds stress at the surface, $\overline{u'w'_0}$; the surface kinematic turbulent heat flux, $\overline{w'\theta'_0}$; the height above the surface, z ; and the buoyancy parameter, $g/\bar{\theta}$, where θ is the

potential temperature*, $\bar{\theta}$ is the mean value, $\theta' = \theta - \bar{\theta}$ is the departure from the mean, and g is the gravitational acceleration. These basic parameters have been used in Monin-Obukhov similarity theory (e.g., Monin and Yaglom, 1971) to determine the important length and velocity scales for the statistical properties of meteorological variables in the surface layer. In addition to the height above ground, z , a second important length scale is the Obukhov length, L , (Obukhov, 1946) defined as

$$L = \frac{-|\overline{u'w'}_0|^{\frac{3}{2}}}{k \frac{g}{\bar{\theta}} \overline{w'\theta'}_0}, \quad (2.1.1)$$

where k is von Karman's constant. Shear production of turbulent kinetic energy dominates for $z < |L|$. Buoyant production dominates for $z > |L|$. The important velocity scale is the friction velocity, defined by $u_* = |\overline{u'w'}_0|^{\frac{1}{2}}$. Monin-Obukhov similarity theory has been used successfully to determine universal relationships for many turbulent quantities in the surface layer, such as means, variances and covariances of temperature, wind velocity and water vapor in steady-state horizontally-homogeneous conditions (Garratt, 1992).

When $-h/L > 10$, approximately, the boundary layer is in a "convective" state, and a free convection layer ($|L| < z < 0.1h$) exists. In this layer the buoyant production of turbulent kinetic energy dominates and u_* is no longer the important velocity scale. The height above ground, z , is the appropriate length scale. The appropriate velocity scale in this layer has been found to be the local free convection velocity scale defined by

$$w_f = \left[\frac{g}{\bar{\theta}} \overline{w'\theta'}_0 z \right]^{1/3}. \quad (2.1.2)$$

* Virtual potential temperature must be used if the air is not dry.

Wyngaard *et al.* (1971) found vertical velocity fluctuations scale with w_f in the free convection layer, with

$$\sigma_w = 1.34w_f, \quad (2.1.3)$$

where $\sigma_w = \left(\overline{w'^2}\right)^{1/2}$ is the standard deviation of the vertical velocity.

Panofsky *et al.* (1977) recommended the following expression which interpolates between the neutral limit predicted by Monin-Obukhov similarity theory ($\sigma_w = 1.3u_*$) and the free convection layer relationship:

$$\sigma_w = 1.3u_* \left[1 + 3 \left(\frac{-z}{L} \right) \right]^{1/3} \quad (2.1.4)$$

(note that the u_* and L are not relevant scales for the free convection layer, but the fact that $w_f \propto u_* (-z/L)^{1/3}$ has been used in determining this expression).

In the mixed layer of the CBL ($0.1h < z < 0.8h$, $-h/L > 10$), Deardorff (1970a, 1970b, 1972, 1974a, 1974b) showed that the important turbulence scaling parameters are h , $\overline{w'\theta'_0}$, and $\frac{g}{\theta}$. This is because the buoyant production of turbulence dominates over shear production, and the height of the capping inversion limits the size of eddies, becoming the important length scale. The velocity scale formed from these parameters is

$$w_* = \left[\frac{g}{\theta} \overline{w'\theta'_0} h \right]^{1/3}. \quad (2.1.5)$$

Deardorff showed that many turbulent properties of the CBL scale with h and w_* .

Deardorff (1970b, 1972) proposed that the relevant parameter for determining the state of the unstable boundary is h/L . He found that mixed layer scaling of vertical velocity and temperature fluctuations is valid for values of $-h/L$ as low as 4.5 (this is indicated

approximately by the vertical dashed line in Fig. 2.2). Mixed layer scaling of horizontal velocity fluctuations becomes valid for values $-h/L$ between 4.5 and 45. The range of validity of mixed layer scaling has typically been assumed to be approximately $-h/L > 10$, as indicated in Fig. 2.2. Using Eqs. (2.1.1) and (2.1.5) and $k = 0.4$, this corresponds to approximately $w_* > 3u_*$. Deardorff and Willis (1974) estimated that this corresponds to a typical range of validity in the CBL of $U < 6w_*$ or $U < 12 \text{ m s}^{-1}$ using typical values of $u_* / U = 0.05$ and $w_* = 2 \text{ m s}^{-1}$.

Mixed layer scaling has been used successfully to obtain universal profiles of vertical velocity statistics. For example, Fig. 2.3a shows measurements of scaled vertical velocity standard deviation, σ_w , as a function of scaled height from various experiments summarized by Wyngaard (1988). Fig. 2.3b shows Wyngaard's summary of measured vertical velocity skewness, $S \equiv \overline{w^3} / (\overline{w^2})^{3/2}$, versus scaled height (the mean vertical velocity is assumed to be zero, so $w = w'$). Luhar *et al.* (1996) reviewed values of S measured in field and laboratory experiments and found typical values ranged from 0.5 to 0.9, which is consistent with the data plotted in Fig. 2.3b. From Fig. 2.3, it can be seen that for the bulk of the CBL (the mixed layer) vertical velocity statistics are relatively homogeneous.

Mixed layer scaling of the data in Fig. 2.3 is successful even though some of it was collected in conditions that were not horizontally homogeneous or stationary (e.g., in conditions when the boundary layer was growing due to entrainment of air from the overlying stable layer). As discussed by Wyngaard (1988), this success is due to time scales for mixing over the CBL depth being smaller than the time scales for the evolution of the boundary layer due to horizontal advection or entrainment.

The positive skewness of the vertical velocity means that (a) the mode (highest probability value) of the vertical velocity is negative and (b) there are higher probabilities of large magnitude positive velocities (associated with strong updrafts) than large magnitude negative velocities. As will be discussed below, the skewed vertical velocity distribution significantly affects the vertical dispersion of a scalar in the CBL.

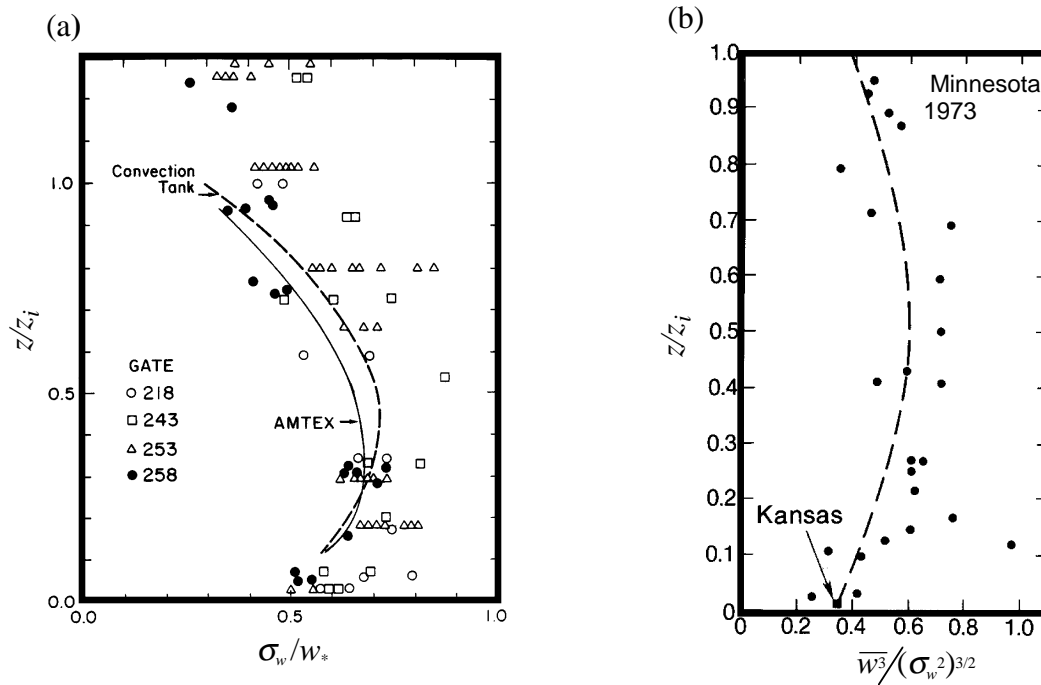


Fig. 2.3. CBL measurements of (a) vertical velocity standard deviation, $\sigma_w \equiv \sqrt{\overline{w^2}}$, scaled by convective velocity scale, w_* , and (b) skewness of vertical velocity skewness versus height scaled by inversion height, z_i , as summarized by Wyngaard (1988).

Scaled variances of horizontal velocity components are approximately homogeneous throughout the CBL with $\sigma_u/w_* = \sigma_v/w_* = 0.6$ (Garratt, 1992). Horizontal and vertical velocity variances are approximately equal in the mixed layer, indicating isotropic turbulence in this layer. However, horizontal velocity distributions in the CBL are not skewed (Deardorff and Willis, 1985).

Boundary layer turbulence scaling relationships have some known limitations. Deardorff (1974b) showed that mixed layer scaling may be limited because it uses only surface fluxes and does not include any information about processes at the top of the boundary layer. In particular, water vapor fluctuations in the CBL are strongly affected by entrainment processes. Panofsky *et al.* (1977) showed that horizontal velocity fluctuations in the unstable surface layer scale with w_* (as mentioned above, mixed layer downdrafts penetrate deep into the surface layer) and not, as predicted by Monin-Obukhov similarity theory, with u_* .

2.3 Small-scale properties of turbulence

Large Reynolds number flows, such as those in the atmospheric boundary layer, contain velocity fluctuations with a wide range of length and time scales. The Reynolds number, Re , can be defined as the ratio of inertia force (e.g., du/dt) to viscous force per unit mass (e.g., $\nu \partial^2 u / \partial z^2$), where ν is the kinematic viscosity of the fluid. The order of magnitude of these forces can be estimated using the characteristic velocity, V , and the characteristic length scale, l , of the turbulent motions. V can be thought of as the root-mean-square of the velocity fluctuations and is proportional to w_* in the mixed layer. The length scale l is, in general, the distance over which the velocity can undergo a change on the order of V , and is proportional to h in the mixed layer. The order of magnitude of the inertia and viscous forces are then V^2/l and $\nu V/l^2$, respectively. The Reynolds number is then

$$Re = \frac{Vl}{\nu}$$

(Monin and Yaglom, 1971).

The largest scale turbulent fluctuations have velocity and length scales that are on the order of V and l . External conditions (e.g., surface heating in the CBL) produce turbulent

kinetic energy at these larger scales. The length scales of the larger scale turbulent motions are often assumed to be proportional to the integral length scale in stationary, homogeneous turbulence (Tennekes and Lumley, 1972). The Eulerian integral length scale, l_E , is the area under the spatial velocity correlation function, and can be defined as follows:

$$l_E \equiv \frac{1}{\sigma_w^2} \int_0^\infty \overline{w'(0)w'(x)} dx,$$

where $w(x)$ is the velocity at position x in the fluid, and σ_w is the velocity standard deviation. The integral length scale provides a measure of the spatial coherence of turbulent motions. Time scales associated with larger scale motions can also be defined using temporal velocity correlation functions. For example, the Lagrangian integral time scale or correlation time, τ , can be defined as follows:

$$\tau \equiv \frac{1}{\sigma_w^2} \int_0^\infty \overline{w'_0 w'(t)} dt.$$

where $w(t)$ is the velocity of a point moving in the fluid (a "fluid particle") at time t , and w_0 is the velocity at $t = 0$.

The larger scale turbulent motions contain most of the turbulent kinetic energy. However, for large Re the viscous force is much weaker than the inertia force associated with these larger scale motions, and, therefore, the viscous force does not act significantly on these larger scales of motion. As a consequence, the larger scale fluctuations are unstable and break down into smaller and smaller scale fluctuations (Monin and Yaglom, 1975). Turbulent kinetic energy cascades to smaller and smaller scales, with most of the turbulent kinetic energy at a given scale coming from the next-largest scale of motion (Tennekes and Lumley, 1972). When the velocity and length scales of the motion becomes small enough that viscous force is comparable to the inertia force (i.e., the

Reynolds number of the motions is of order unity), then kinetic energy is dissipated into internal energy (heat).

So, while external conditions produce turbulent kinetic energy at the larger scales of motion, it is dissipated at the smallest scales of motion. Under steady-state conditions, this production and dissipation occur at the same rate. If there is an imbalance, the turbulent kinetic energy dissipation rate quickly adjusts to match the production rate (Tennekes and Lumley, 1972).

For large Re flows, there is hypothesized to be a "universal" equilibrium range of turbulent velocity fluctuation frequency or wavenumber in which the statistical properties of the smaller scale fluctuations are independent of the properties of the larger scale fluctuations. Kolmogorov's first similarity hypothesis states that the statistical properties of motions in this equilibrium range are determined uniquely by the mean turbulent kinetic energy dissipation rate per unit mass, $\bar{\epsilon}$, and kinematic viscosity, ν (Monin and Yaglom, 1975).

Using Kolmogorov's first similarity hypothesis, the scales of motion in the small-scale end of the equilibrium range, the dissipation range, can be estimated from $\bar{\epsilon}$ and ν by dimensional analysis. These Kolmogorov microscales are length scale $\eta = (\nu^3/\bar{\epsilon})^{1/4}$, velocity scale $u_\eta = (\nu\bar{\epsilon})^{1/4}$, and time scale $\tau_\eta = (\nu/\bar{\epsilon})^{1/2}$. In the convective boundary layer, typical values for τ_η are less than a second, values of η are on the order of a millimeter, and values of u_η are on the order of a hundredth of a meter per second. For example, using typical values of $\bar{\epsilon} \approx 0.4(w_*^3/h)$, $w_* \approx 1 \text{ m s}^{-1}$, $h \approx 1000 \text{ m}$, and $\nu = 1.5 \times 10^{-5} \text{ m}^2 \text{ s}^{-1}$, the values of the Kolmogorov microscales are $\eta \approx 2 \text{ mm}$, $u_\eta \approx 0.009 \text{ m s}^{-1}$, and $\tau_\eta \approx 0.2 \text{ s}$.

At the larger scale end of the equilibrium range, Kolmogorov's second similarity hypothesis states that an inertial subrange exists in which viscous forces are not important and the statistical properties of the motions are determined entirely by $\bar{\epsilon}$. In the inertial subrange, turbulent motions have time scales much smaller than the energy-containing scales (which can be characterized by a Lagrangian velocity correlation time, τ), and much larger than the smaller energy-dissipating scales (characterized by the Kolmogorov microscale, τ_η). In the inertial subrange, statistical properties of the change (in space and time) of fluid velocity are assumed to be approximately stationary, homogeneous and isotropic. This is called "local isotropy".

One of the implications of the second Kolmogorov hypothesis is that the statistical properties of the change of the Lagrangian velocity of a fluid particle, associated with frequencies in the inertial subrange, is a function only of $\bar{\epsilon}$ and the time lag δt . As a consequence, the Lagrangian structure function (considering one component of velocity) is hypothesized to be

$$\overline{(\delta w)^2} = C_0 \bar{\epsilon} \delta t, \quad (2.2.1)$$

where $\delta w \equiv w(t + \delta t) - w(t)$ is a change in the Lagrangian velocity of a fluid particle during a time lag, δt , in the range $\tau_\eta \ll \delta t \ll \tau$, and C_0 is a universal constant (Monin and Yaglom, 1975, p. 359). Similarly, even moments of the velocity change are

$$\overline{(\delta w)^n} \propto (\bar{\epsilon} \delta t)^{n/2} \quad (2.2.2)$$

($n = 2, 4, \dots$). Odd moments are hypothesized to be zero (i.e., the probability distribution of δw is assumed to be symmetric) due to the locally isotropic turbulence in the inertial subrange. These properties have been used in the formulation of Langevin equation models, as will be discussed in Chapter 3.

As stated by Monin and Yaglom (1975, pp. 584-585), Kolmogorov's similarity hypotheses "cannot be regarded as quite exact." This is because the statistical properties of small scale motion may depend not only on the mean dissipation rate, $\bar{\varepsilon}$, but on the probability distribution of ε . The distribution of ε depends on the fluctuations in the velocity field which, in turn, depends on the larger scale properties of the flow. Therefore, the statistical properties of small-scale motion may not be truly universal.

The second Kolmogorov similarity hypothesis has been used successfully to predict some of the statistical properties of velocity fluctuations in the inertial subrange. For example, it has been used successfully to predict the form of the turbulent kinetic energy spectral density in the inertial subrange (e.g., Garratt, 1992). With regard to the Lagrangian structure function, however, Pope (1994) wrote "To date, Lagrangian statistics in high-Reynolds number flows have proven inaccessible both to experiment and to direct numerical simulation. Consequently, a direct test of (the Lagrangian structure function predicted by Kolmogorov's second hypothesis) has not been possible."

2.4 Dispersion phenomena

Willis and Deardorff (1976a, 1976b, 1978 & 1981) simulated downwind advection and vertical dispersion from continuous point sources in the CBL using a laboratory water tank. The observed ensemble-average crosswind-integrated concentration, C , from some of these experiments are summarized in Fig. 2.4. These experimental observations have been made dimensionless using the mixed layer scaling parameters h and w_* . Free-convection-layer and mixed-layer scaling is valid for the water tank experiments because $-L$ is effectively very small (and, correspondingly, $-h/L$, is very large) since there is no mean flow in the water tank. The concentration is made dimensionless through scaling by the concentration value corresponding to a uniform distribution in the vertical, Q/Uh ,

where Q is the continuous point source emission rate, and U is the mean horizontal wind speed.

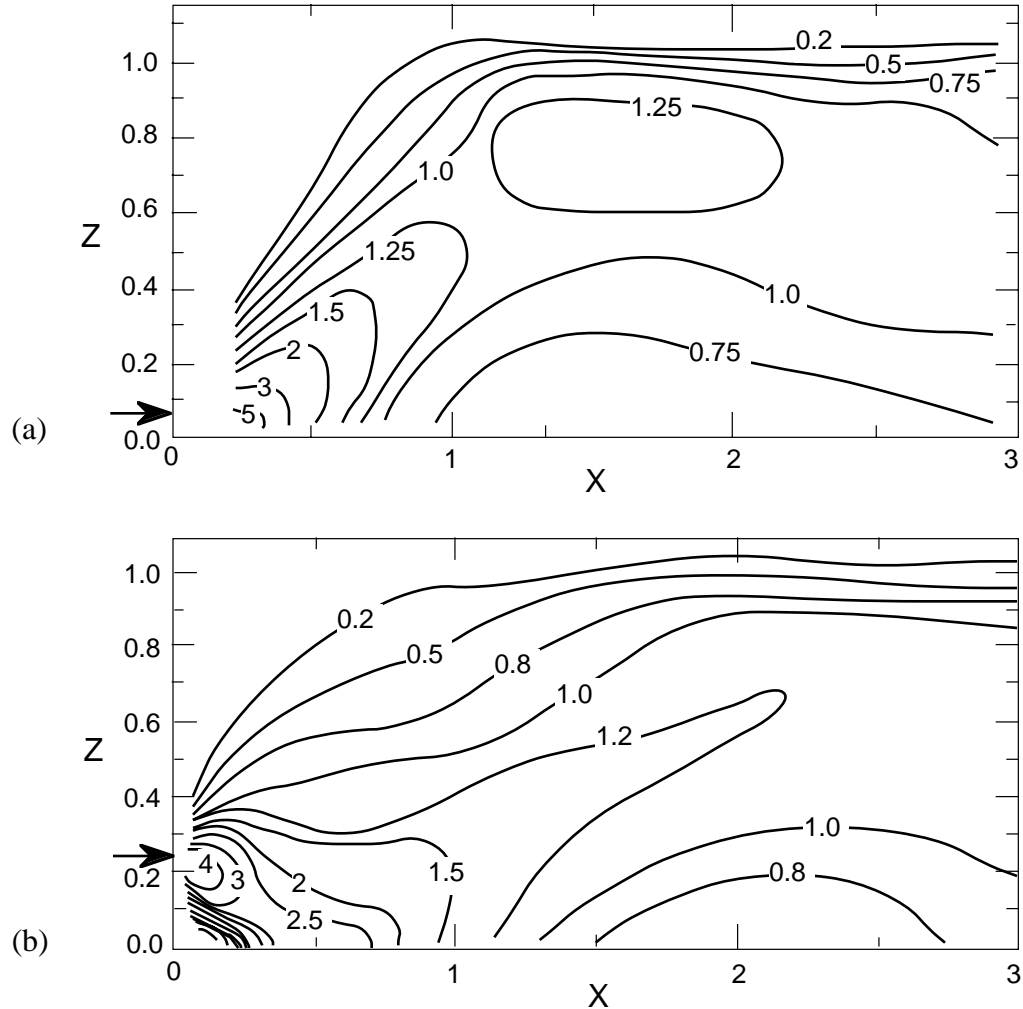


Fig. 2.4. Smoothed contours of dimensionless cross-wind-integrated concentration, CUh/Q , versus dimensionless height, $Z=z/h$, and downwind distance, $X = xw_*/Uh$, from Willis & Deardorff (1976b, 1978) laboratory experiments for dimensionless source heights of (a) $z_s/h = 0.067$ (top figure), (b) $z_s/h = 0.24$ (bottom), where x is downwind distance, w_* is the convective velocity scale, U is the mean horizontal wind speed at the source height, and h is the mean inversion height. Arrows indicate source location.

Most of Willis and Deardorff's experiments used instantaneous line sources (ILS), but some used continuous point sources (CPS). Since there was no mean horizontal flow in the water tank. CPS experiments were conducted by moving the source horizontally, to

simulate a uniform horizontal wind. Concentrations measured from ILS experiments (with the line source oriented in the x direction) were transformed to simulated CPS concentrations (with a mean wind in the x direction). This was done by assuming downwind dispersion relative to the mean horizontal wind U (assumed to be constant with height) is negligible. Using these assumptions, dimensionless time in the experiments, t/t_* , where $t_* \equiv h/w_*$ is the convective time scale, is transformed into a dimensionless downwind distance $X = xw_*/Uh$. This makes use of Taylor's hypothesis that the eddies are advected past a fixed point faster than the time for them to significantly change their characteristics. Willis and Deardorff (1976b) showed that these assumptions were reasonable for $U = 2.8w_*$ by comparing their ILS and CPS observations. They also estimated that these assumptions are valid if $U > 1.2w_*$ or $U > 2\sigma_u$, where σ_u is the standard deviation of the downwind component of the wind velocity.

The first Willis and Deardorff experiments were for near-surface sources. Fig. 2.4a shows that the height of the locus or "line" of the maximum ensemble-average cross-wind-integrated concentration of tracer from a near-surface source stays near the surface initially and then quickly begins to increase with downwind distance starting near $X = 0.5$. Lamb (1978a, 1978b, 1982) studied CBL dispersion using a Lagrangian numerical model, and velocity fields from Deardorff's (1974a) 3-D LES simulations. Lamb's results for near-surface source were similar to Willis and Deardorff's observations.

Lamb also simulated elevated sources and found that the downwind dispersion was significantly different from that from a near-surface source. Lamb's simulations inspired Willis and Deardorff (1978, 1981) to perform the water tank experiments with elevated sources at $z_s = 0.24h$ (observations shown in Fig. 2.4b) as well as $z_s = 0.49h$. The Lamb simulations and the Willis and Deardorff experiments for elevated sources showed

similar results. Fig. 2.4b shows that, for an elevated source, the height of the maximum concentration line initially decreases with downwind distance in the Willis and Deardorff experiments. After encountering the surface near $X = 0.5$, the maximum concentration line stays near the surface until it begins to ascend near $X = 0.8$.

Lamb's and Willis & Deardorff's studies showed that the positive skewness of the vertical velocity distribution, and the long Lagrangian correlation time of the vertical velocity are key to explaining CBL vertical dispersion phenomena. As discussed by Lamb (1982), neutrally buoyant material emitted from an elevated source has a higher probability of encountering a downdraft because of the positively skewed vertical velocity distribution. Lamb (1978a) found that in the middle of the mixed layer the fraction of the horizontal area covered by downdrafts was approximately 60%, with the remaining 40% covered by stronger updrafts. Due to the long-lived, deep convection found in the CBL, material emitted into a downdraft will typically be carried to the surface. Because downdrafts predominate, the most likely event is for emitted material to move relatively slowly toward the surface in downdrafts, and then horizontally into convergence zones of updrafts. Material directly emitted from an elevated source into the strong updrafts is quickly recycled into downdrafts. The combined effect is that the height of the maximum concentration line descends with downwind distance for elevated sources, as shown in Fig. 2.4b.

Material emitted by a near-surface source is either directly incorporated into an updraft or, if it is emitted in a downdraft area, moves horizontally near the surface until it is incorporated in an updraft. Material initially released into an updraft from a surface source doesn't recirculate down near the surface before material released in downdraft areas is swept into updrafts. Because downdrafts cover a majority of the horizontal area, the maximum concentration line initially stays near the surface, but then quickly begins

to ascend, as shown in Fig. 2.4a, when the most likely event is that material is incorporated into updrafts.

Note that at some downwind distances, the near-surface concentration of material emitted from the elevated source (Fig. 2.4b) is greater than from the near-surface source (Fig. 2.4a). Also note that for both source heights the near-surface concentration decreases to a minimum before increasing toward the well-mixed, steady-state concentration value ($CUh/Q \approx 1$) at the furthest downwind distances.

The ability to simulate these phenomena is critical to accurate calculation of tracer concentrations in the CBL. For example, for an elevated source, significant underprediction of ground-level pollutant concentrations can occur in dispersion models if these processes are not taken into account. These underpredictions can be as high as a factor of 2.9 (Briggs, 1993a).

The dispersion phenomena found in these Willis and Deardorff's laboratory experiments and Lamb's numerical experiments have been observed in the atmosphere during a CBL dispersion field study (Kaimal *et al.*, 1986; Briggs, 1993a, 1993b). Briggs (1993b) showed that the field experiment observations were in good agreement with the Willis and Deardorff laboratory observations, as well as Lamb's numerical modeling results.

In the numerical modeling work presented in the next chapters, we shall make use of Willis and Deardorff's simplified conceptual model of dispersion from a continuous point source in the CBL. This conceptual model assumes that (1) mixed-layer scaling is valid, (2) there is a uniform horizontal mean wind velocity, U , and (3) there are velocity fluctuations only in the vertical velocity component, w .

When using these simplifying approximations, the correlation of the vertical and horizontal velocity fluctuations, e.g., $\overline{u'w'}$, is neglected. $\overline{u'w'}$ is non-zero and negative in the CBL (due to the downward turbulent flux of momentum), with a maximum magnitude at the surface (e.g., Stull, 1988). However, as discussed above, the momentum flux is not an important turbulence scaling parameter in the bulk of the CBL ($z > |L|$).

The good agreement between the results of Lamb's simulations (using 3-D LES velocity fields) and Willis and Deardorff's experiments, indicate that the simplifying assumptions used by Willis and Deardorff (that horizontal velocity fluctuations could be neglected and the mean horizontal wind is uniform) are reasonable. The mean wind speed range for which horizontal velocity fluctuations can be neglected, $U > 1.2w_*$ (estimated using the criteria $U > 2\sigma_u$ by Willis and Deardorff, 1976b), appears to be reasonable because the mean wind speed of the LES data used by Lamb was close to the lower end of this range, $U \approx 1.4w_*$.

The range of validity of these assumptions is quite large, and is approximately

$$1.2w_* < U < 6w_*,$$

or

$$2.4 < U < 12 \text{ m s}^{-1},$$

for a typical value of $w_* = 2 \text{ m s}^{-1}$. The upper limit is imposed by the range of validity of mixed layer scaling ($-h/L > 10$). The lower limit is imposed by the assumption that horizontal velocity fluctuations are negligible compared to mean wind advection ($U > 2\sigma_u$).

Because mixed-layer scaling is not valid for $z < 0.1h$, the use of mixed layer scaling will not be valid for source heights, z_s , below $0.1h$ until the vertical spread of material has reached a depth greater than $0.1h$. Nieuwstadt (1980) used observations from the Prairie Grass field experiment (continuous point source at roughly $z_s = 0.0005h$) and the criteria $\sigma_z/h > 0.1$ (where σ_z is the vertical standard deviation of the concentration distribution) to estimate that mixed layer scaling of vertical dispersion is valid for dimensionless downwind distance $X > 0.23$ for a ground-level point source.

3

Langevin Equation Models

In this chapter, Lagrangian stochastic modeling of turbulent dispersion based on the Langevin equation is reviewed, and two Langevin-equation-based models for convective boundary layer dispersion are presented along with “reflection” boundary conditions at the top and bottom of the boundary layer. Pioneering work in the stochastic approach to diffusion was done in the early 1900s by Einstein, Smoluchowski, and Langevin in work on diffusion due to Brownian motion (Gardiner, 1990). Langevin introduced the Lagrangian stochastic approach, with drag and random forces acting on a particle. Taylor (1921) first proposed a Lagrangian statistical approach to turbulent dispersion. Obukhov (1959) proposed that the Lagrangian evolution of fluid particle velocity and position could be described by the Fokker-Planck equation for the probability distribution function of velocity and position. More recently, beginning in the 1970s, considerable progress has been made in the theory and application of Lagrangian stochastic models of fluid particle trajectories in turbulent flows. Reviews of this subject have been written by Durbin (1983), Sawford (1985 & 1993), Thomson (1987), Pope (1987 & 1994), Wilson and Sawford (1996), and Rodean (1996).

The basis of the Lagrangian stochastic approach to turbulent dispersion is reviewed in Section 3.1. The Langevin equation of motion for a fluid particle is presented in Section 3.2. Two forms of the Langevin equation are presented. Section 3.3 presents the Fokker-Planck equation and Kramers-Moyal expansion, which describe the particle velocity probability distribution. These two equations describe the same stochastic processes as

the two forms of the Langevin equation. Section 3.4 presents the development of two Langevin equation models (one used by previous investigators and one new model) for the time evolution of particle velocity assuming homogeneous, skewed fluid velocity distribution. Using some of the properties of these Langevin equation models, Section 3.5 discusses the assumptions inherent in the Langevin equation approach and their justification. Section 3.6 presents the development of methods for integrating the two forms of the Langevin equation to develop an equation for numerically simulating the time evolution of particle velocity. The simulation of particle position is discussed in Section 3.7. The development of methods for selecting new velocities for particles that encounter a boundary (reflection boundary conditions) are discussed in Section 3.8.

3.1 Lagrangian stochastic approach

Lagrangian stochastic models of turbulent dispersion can be used to describe the possible trajectories of fluid particles. A fluid particle represents a small, idealized volume of fluid with spatial dimensions much larger than the average distance between molecules. However, these spatial dimensions are sufficiently small, compared to distances that the fluid properties vary significantly, that the properties in this small volume can be assumed to be uniform. The spatial dimensions of a fluid particle are also small enough that, for the times under consideration, it does not undergo significant deformation, and it can be effectively treated as a “point” moving in the fluid. The effects of molecular diffusion are neglected because they are small compared to the effects of turbulent dispersion in the high Reynolds number flows found in atmospheric boundary layers.

Stochastic models can be used to determine the probability distribution of future particle positions, given initial positions. These probability distributions can be used to calculate ensemble-mean concentration of material at a desired time, given the concentration

distribution at earlier times. Ensemble-mean air concentration, $C(\mathbf{r}, t)$, (mass per unit volume) at position \mathbf{r} and time t can be determined as follows:

$$C(\mathbf{r}, t) = \int_{-\infty}^t dt_0 \int d\mathbf{r}_0 q(\mathbf{r}_0, t_0) P(\mathbf{r}, t ; \mathbf{r}_0, t_0), \quad (3.1.1)$$

where $q(\mathbf{r}_0, t_0)$ represents the source distribution term at position \mathbf{r}_0 at time t_0 (trace material mass emitted per unit time per unit volume), and $P(\mathbf{r}, t ; \mathbf{r}_0, t_0)$ is the probability density function for the particle position \mathbf{r} at time t given it was at position \mathbf{r}_0 at time t_0 (Tennekes and Lumley, 1972). Considering the ensemble of particle trajectories that originate at position \mathbf{r}_0 at time t_0 , $P(\mathbf{r}, t ; \mathbf{r}_0, t_0)$ can be thought of as the fraction of particles per unit volume that are at \mathbf{r} at later time t . If the source distribution term is constant with time and the turbulent flow is stationary (i.e., the statistical properties do not change with time), the ensemble-average concentration can be used as an estimate of the time-average concentration through the ergodic hypothesis (Lumley and Panofsky, 1964).

We will make use of Langevin-equation-based Lagrangian stochastic models that can be used to describe $P(\mathbf{r}, t ; \mathbf{r}_0, t_0)$ through the ensemble of possible particle trajectories, $\{\mathbf{r}_i(t), i = 1, 2, \dots\}$. An individual particle trajectory, $\mathbf{r}_i(t)$, is an independent realization from this ensemble. A Langevin equation model can be used in Monte Carlo simulations to calculate a large sample of particle trajectories, from which the distribution $P(\mathbf{r}, t ; \mathbf{r}_0, t_0)$, its moments, and, using Eq. (3.1.1), the mean concentration $C(\mathbf{r}, t)$ can be estimated.

3.2 Langevin equation

The Langevin equation is a stochastic differential equation that can be used to describe the Lagrangian acceleration of a fluid particle. The generalized Langevin equation can be written as follows:

$$\frac{dw}{dt} = a(w) + \Lambda(t), \quad (3.2.1)$$

where w is the velocity of a fluid particle, and t is time (van Kampen, 1992). (We are studying the case of vertical dispersion, and will restrict our attention to one component of the acceleration.) Eq. (3.2.1) assumes that the net acceleration of a particle is the sum of a deterministic acceleration, $a(w)$, which is a function of w , and a rapidly fluctuating random acceleration, $\Lambda(t)$, which is not a function of w . $\Lambda(t)$ is assumed to be uncorrelated over any time period of interest. It is modeled as delta-function correlated in time, with statistical properties defined by the following autocorrelation functions:

$$\langle\langle \Lambda(t_1)\Lambda(t_2)\Lambda(t_3)\dots\Lambda(t_n) \rangle\rangle = \Gamma_n \delta(t_1 - t_2)\delta(t_1 - t_3)\dots\delta(t_1 - t_n), \quad (3.2.2)$$

where $n = 1, 2, \dots$, and the notation $\langle\langle \rangle\rangle$ denotes the cumulant[#] of a quantity. The set of coefficients $\{\Gamma_n, n = 1, 2, \dots\}$ are to be determined from the statistical properties of the fluid velocity.

The correlation functions defined by Eq. (3.2.2) in cumulant notation can be written in terms of ensemble average quantities. The first three cumulants are the same as the first three central moments, but this is not true of higher cumulants. If the random acceleration

[#] The n th cumulant of a random variable is a function of the moments of order n and lower (Gardiner, 1990). For example, $\langle\langle x \rangle\rangle = \bar{x}$, $\langle\langle x^2 \rangle\rangle = \overline{x^2} - \bar{x}^2$, $\langle\langle x^3 \rangle\rangle = \overline{x^3} - 3\bar{x}\overline{x^2} + \bar{x}^3$, $\langle\langle x^4 \rangle\rangle = \overline{x^4} - 4\bar{x}\overline{x^3} - 3\overline{x^2}^2 + 12\bar{x}^2\overline{x^2} - 6\bar{x}^4$. For a Gaussian distribution, the cumulants for $n = 3, 4, \dots$ are zero. So, the higher order cumulants ($n = 3, 4, \dots$) are a measure of the departure of a probability distribution from a Gaussian distribution.

has zero mean, $\overline{\Lambda(t)} = 0$, the first- through fourth-order correlation functions, for example, defined by (3.2.2) may be written as follows:

$$\langle\langle\Lambda(t)\rangle\rangle = \overline{\Lambda(t)} = 0,$$

$$\langle\langle\Lambda(t_1)\Lambda(t_2)\rangle\rangle = \overline{\Lambda(t_1)\Lambda(t_2)},$$

$$\langle\langle\Lambda(t_1)\Lambda(t_2)\Lambda(t_3)\rangle\rangle = \overline{\Lambda(t_1)\Lambda(t_2)\Lambda(t_3)}, \text{ and}$$

$$\begin{aligned} \langle\langle\Lambda(t_1)\Lambda(t_2)\Lambda(t_3)\Lambda(t_4)\rangle\rangle &= \overline{\Lambda(t_1)\Lambda(t_2)\Lambda(t_3)\Lambda(t_4)} \\ &\quad - 3\overline{\Lambda(t_1)\Lambda(t_2)}^2, \end{aligned}$$

where the notation $\overline{(\quad)}$ denotes the ensemble-average value of a quantity.

We will make use of two forms of the Langevin equation in which the random acceleration, $\Lambda(t)$, has one of the following two properties:

(1) *Gaussian*: $\Lambda(t)$ is a Gaussian process, which means $P(\Lambda(t_1), \Lambda(t_2), \dots, \Lambda(t_n))$ is a multivariate Gaussian distribution completely defined by the means, $\overline{\Lambda(t_i)}$, $i = 1, 2, \dots, n$, and autocovariances, $\overline{\Lambda(t_i)\Lambda(t_j)}$, $i = 1, 2, \dots, n$, $j = 1, 2, \dots, n$. Correspondingly, the third and higher order ($n = 3, 4, \dots$) cumulant autocorrelation functions given by Eq. (3.2.2) are zero.

(2) *Skewed*: $\Lambda(t)$ is a non-Gaussian, skewed process, which means the cumulant autocorrelation functions defined by Eq. (3.2.2) are non-zero for all n ($n = 1, 2, \dots$).

The velocity equation

$$\frac{dz}{dt} = w, \tag{3.2.3}$$

where z is the particle position, along with Eqs. (3.2.1-2) define a stochastic process for the joint evolution of w and z of a fluid particle. In order to calculate the (w, z) phase space trajectory of a particle, we need to obtain an equation for the time evolution of particle velocity, $w(t)$, by integrating the Langevin equation (3.2.1), and, then, integrate the velocity equation (3.2.3) to calculate the time evolution of the particle position, $z(t)$.

3.3 Kramers-Moyal expansion and Fokker-Planck equation

In developing Langevin equation models, it is often very helpful to make use of the equations describing the time evolution of the joint probability density function of particle velocity and position, $P(w, z, t ; w_0, z_0, t_0)$. These are the Kramers-Moyal expansion and the Fokker-Planck equation, which describe the same stochastic processes as the Langevin equations with skewed and Gaussian random accelerations, respectively.

The *Kramers-Moyal expansion* may be written as follows (van Kampen, 1992):

$$\frac{\partial P}{\partial t} = -\frac{\partial}{\partial z}(wP) + \sum_{n=1}^{\infty} \frac{(-1)^n}{n!} \frac{\partial^n}{\partial w^n}(b_n P). \quad (3.3.1)$$

where

$$P = P(w, z, t ; w_0, z_0, t_0)$$

is the joint probability distribution function of velocity w and position z after time interval $\delta t \equiv t - t_0$, given velocity w_0 and position z_0 at the beginning of the time interval. Eq. (3.3.1) with $b_n = 0$ for $n = 3, 4, \dots$ is the *Fokker-Planck equation*, which describes the same process as the Langevin equation with a Gaussian random acceleration.

The coefficients b_n , $n = 1, 2, \dots$, in the Kramers-Moyal expansion (or Fokker-Planck equation for $n = 1, 2$) are defined as follows:

$$b_n = \frac{\overline{(\delta w)^n}}{\delta t}, \text{ as } \delta t \rightarrow 0. \quad (3.3.2)$$

where $\delta t \equiv t - t_0$, $\delta w \equiv w - w_0$, and $\overline{(\delta w)^n}$, $n = 1, 2, \dots$, are the velocity increment moments. The Langevin equation coefficients Γ_n and Kramers-Moyal coefficients b_n are directly related. This can be shown by calculating the small time increment moments of the velocity increment, obtained by integrating the Langevin equation (this will be done later in this chapter). The result, for our case of homogenous statistical properties of the fluid velocity with zero mean, is, for $n = 1$,

$$b_1 = a(w), \quad (3.3.3)$$

and for $n = 2, 3, \dots$,

$$b_n = \Gamma_n. \quad (3.3.4)$$

The Kramers-Moyal expansion (equivalent to the Langevin equation with a skewed random acceleration) may then be written as follows:

$$\frac{\partial P}{\partial t} = -\frac{\partial}{\partial z}(wP) - \frac{\partial}{\partial w}(a(w)P) + \sum_{n=2}^{\infty} \frac{(-1)^n}{n!} \frac{\partial^n}{\partial w^n}(\Gamma_n P). \quad (3.3.5)$$

Similarly, the Fokker-Planck equation (equivalent to the Langevin equation with a Gaussian random acceleration) may then be written as follows:

$$\frac{\partial P}{\partial t} = -\frac{\partial}{\partial z}(wP) - \frac{\partial}{\partial w}(a(w)P) + \frac{1}{2} \frac{\partial^2}{\partial w^2}(\Gamma P), \quad (3.3.6)$$

where $\Gamma \equiv \Gamma_2$.

3.4 Langevin equation models for skewed turbulence

In this section, we will explore two forms of the Langevin equation for turbulent flows with skewed velocity statistics:

- (1) the *nonlinear-Gaussian* Langevin equation with a deterministic term, $a(w)$, that is a *nonlinear* function of w , and a *Gaussian* random term, $\Lambda(t)$; and
- (2) the *linear-skewed* Langevin equation with a deterministic term, $a(w)$, that is a simple *linear* function of w and a *skewed* random term $\Lambda(t)$.

Given the form of the Langevin equation, assumptions and constraints must then be used to determine $a(w)$ and the random acceleration coefficient(s), Γ_n , in terms of known statistical properties of the fluid velocity. In particular, the first three moments of the fluid velocity ($\overline{w_f}$, $\overline{w_f^2}$, and $\overline{w_f^3}$, with $\overline{w_f}$ assumed to be zero) will be used, because they have been shown to be key to CBL dispersion processes, as discussed in Chapter 2. Before describing the development of Langevin equation models for the time evolution of particle velocity in turbulence with a skewed velocity distribution (i.e., non-zero skewness, $S = \overline{w_f^3} / (\overline{w_f^2})^{3/2}$), previous work on these types of models will be reviewed.

3.4.1 Previous studies

The development of Langevin equation dispersion models for skewed turbulence began in the 1980s, sparked by interest in modeling vertical dispersion in the skewed turbulence of the convective boundary layer. Models based on both linear-skewed and nonlinear-Gaussian Langevin equations have been used.

Thomson (1987) demonstrated that the most rigorous constraint, to date, that must be met by a Langevin equation model is the *well-mixed condition*. This condition states that trace material initially well-mixed in a fluid must remain so, and, therefore, the joint probability distribution of position and velocity of tracer particles, $P(w, z)$ will remain the same as that of the fluid, $P_f(w, z)$. Correspondingly, the fluid particles and the tracer will have the same velocity moments, $\overline{w_f^n} = \overline{w^n}$, position moments, $\overline{z_f^m} = \overline{z^m}$, and joint moments $\overline{w_f^n z_f^m} = \overline{w^n z^m}$, for $m = 1, 2, \dots$ and $n = 1, 2, \dots$.

Nonlinear-Gaussian Langevin equation models (e.g., Luhar & Britter, 1989; Weil, 1989 & 1990; Du *et al.*, 1994; Rotach *et al.*, 1996; Luhar *et al.*, 1996) have been successfully developed and applied to the problem of vertical dispersion in the CBL assuming that the vertical velocity distribution is skewed and varies with height (although, the variation of these properties with height in the surface or free convection layers was not resolved in these studies). Hurley and Physick (1993) used a nonlinear-Gaussian Langevin equation model with the simplifying approximation that the skewed vertical velocity distribution is homogeneous in the vertical. They showed fair results compared to laboratory experiments on vertical dispersion in the CBL.

All these nonlinear-Gaussian Langevin models have been developed using an approach introduced by Thomson (1987). In Thomson's approach, the coefficient Γ in the Gaussian random acceleration is chosen so the resulting Lagrangian structure function is consistent with the second Kolmogorov similarity hypothesis (discussed in Chapter 2). The deterministic term, $a(w)$, is then determined from the Fokker-Planck equation using an assumed form for the fluid velocity probability distribution, and applying the well-mixed condition.

The development of *linear-skewed* Langevin equation models (Thomson, 1984; van Dop *et al.*, 1985; de Baas *et al.*, 1986; Sawford, 1986; Sawford and Guest, 1987) has been less successful in meeting the well-mixed constraint for skewed and inhomogeneous turbulence. As discussed by Thomson (1984, 1987), Sawford (1986) and Sawford and Guest (1987), there appear to have been several problems with the formulation and application of these models in bounded flows with strongly inhomogeneous parameterizations of the fluid velocity statistics. In addition, they discuss a fundamental difficulty in applying this type of model: all the cumulants of the random acceleration are non-zero (as noted above), but when higher order cumulants are important it is difficult to generate such a random variable. For inhomogeneous turbulence, it appears this difficulty has not been overcome. However, for the simplified case of *homogeneous* skewed turbulence it will be shown below that a linear-skewed Langevin equation model can be successfully developed, and that it satisfies the well-mixed condition.

3.4.2 Assumptions

In this work, it will be assumed that the ambient turbulence is homogenous and stationary; i.e., the statistical properties of the fluid velocity, w_f , are not a function of time, t , or position, z . It will also be assumed that the mean fluid velocity is zero, $\overline{w_f} = 0$.

These assumptions imply that

- (a) the deterministic acceleration, $a(w)$, depends only on w and not z or t ,
- (b) the random acceleration coefficients $\{\Gamma_n\}$ are also not functions of z or t , and
- (c) the random acceleration $\Lambda(t)$ has a zero mean.

The assumption of homogeneous turbulence allows significantly longer time steps to be used. Time steps must be kept small relative to the Lagrangian velocity correlation time, τ , in typical numerical methods. However, if the turbulence is inhomogeneous with a

Lagrangian time scale that approaches zero at a boundary (as in parameterizations of surface layer turbulence), very small time steps are required. In addition, inhomogeneity in the fluid vertical velocity moments also limits the time step in typical numerical simulations (Thomson, 1987; Wilson and Flesch, 1993). In Langevin equation numerical simulations of CBL dispersion assuming inhomogeneous turbulence, time steps on the order of $\Delta t = 0.01 \tau$ are required for accurate solutions (Luhar and Britter, 1989; Wilson and Flesch, 1993). Hurley and Physick (1993) used a significantly longer time step of $\Delta t = 0.3 \tau$ in their homogenous turbulence simulations. Some numerical error results when using $\Delta t = 0.3 \tau$ with typical numerical methods in homogeneous nonlinear-Gaussian Langevin equation models (as noted by Hurley and Physick and shown in the next chapter), but time steps substantially larger than $\Delta t = 0.01 \tau$ may be used with negligible error.

Using the homogeneous turbulence assumption, Hurley and Physick (1993) developed a CBL dispersion model based on the *nonlinear-Gaussian* Langevin equation. This approach will be presented in the next section, Section 3.4.3. In Section 3.4.4, the development of an alternative model using the *linear-skewed* Langevin equation and the homogeneous turbulence assumption will be presented.

3.4.3 Nonlinear-Gaussian Langevin equation model

As mentioned above, we must integrate the Langevin equation (3.2.1) to obtain an equation for the time evolution of particle velocity. For the case of a nonlinear deterministic acceleration, $a(w)$, it may not be possible to explicitly integrate Eq. (3.2.1). An approximate velocity equation can be developed as follows. Integrating Eq. (3.2.1) results in the following expression for the velocity change:

$$\Delta w = w(\Delta t) - w(0) = \int_0^{\Delta t} a(w) dt + \int_0^{\Delta t} \Lambda(t) dt,$$

where $\Lambda(t)$ is Gaussian for this case. Using a Taylor series expansion for $a(w)$ about $t = 0$,

$$a(w(t)) = a(w_0) + \left. \frac{\partial a(w)}{\partial w} \right|_{t=0} \left. \frac{\partial w}{\partial t} \right|_{t=0} t + O(t^2),$$

where $w_0 \equiv w(0)$, the change in velocity becomes

$$\Delta w = a(w_0)\Delta t + O(\Delta t^2) + \int_0^{\Delta t} \Lambda(t) dt.$$

For $\Delta t \ll 1$, the approximate velocity equation is

$$\Delta w \cong a(w_0)\Delta t + r_G(\Delta t), \quad (3.4.1)$$

where

$$r_G(\Delta t) \equiv \int_0^{\Delta t} \Lambda(t) dt.$$

Since $\Lambda(t)$ is Gaussian for this form of the Langevin equation, the statistical properties of $r_G(\Delta t)$ are determined by its first two moments. Since $\overline{\Lambda(t)} = 0$, the mean is zero,

$$\overline{r_G(\Delta t)} = 0. \quad (3.4.2)$$

The second moment is

$$\begin{aligned} \overline{r_G^2(\Delta t)} &= \overline{\left[\int_0^{\Delta t} \Lambda(t) dt \right]^2} = \int_0^{\Delta t} \int_0^{\Delta t} \overline{\Lambda(t) \Lambda(t')} dt' dt = \int_0^{\Delta t} \int_0^{\Delta t} \Gamma \delta(t - t') dt' dt \\ &= \Gamma \Delta t \end{aligned} \quad (3.4.3)$$

For $\Delta t \ll 1$, the Lagrangian structure function, defined as $\overline{(\Delta w)^2}$, corresponding to this Langevin velocity equation is

$$\begin{aligned}\overline{(\Delta w)^2}_{\Delta t \ll 1} &= \overline{[a(w_0)\Delta t + r_G(\Delta t)]^2} \\ &= \overline{r_G^2(\Delta t)}\end{aligned}\quad (3.4.4)$$

(note that terms of order Δt^2 and higher vanish, that $r_G(\Delta t)$ and $a(w)$ are independent so $\overline{a(w_0)r_G(\Delta t)} = \overline{a(w_0)} \overline{r_G(\Delta t)}$, and that $\overline{r_G(\Delta t)} = 0$). Using Eqs. (3.4.3) and (3.4.4),

$$\overline{(\Delta w)^2}_{\Delta t \ll 1} = \Gamma \Delta t. \quad (3.4.5)$$

The coefficient Γ can be specified for large Reynolds number flows using the Lagrangian structure function predicted by the second Kolmogorov similarity hypothesis, which, as described in Chapter 2, is

$$\overline{(\Delta w)^2} = C_0 \bar{\epsilon} \Delta t \quad (3.4.6)$$

for $\Delta t \ll \tau$. The Langevin equation's Lagrangian structure function given in Eq. (3.4.5) is consistent with Eq. (3.4.6) if

$$\Gamma = C_0 \bar{\epsilon}. \quad (3.4.7)$$

With the random acceleration coefficient, Γ , specified, it only remains to determine the deterministic acceleration, $a(w)$. It can be determined using the Fokker-Planck equation. Using the assumptions that the statistical properties of w are independent of z , the Fokker-Planck equation for velocity alone can be obtained by integrating the Fokker-Planck equation for $P(w, z)$, Eq. (3.3.6), over $z = -\infty$ to ∞ , resulting in:

$$\frac{\partial P(w)}{\partial t} = -\frac{\partial}{\partial w}(a(w)P(w)) + \frac{1}{2} \frac{\partial^2}{\partial w^2}(\Gamma P(w)). \quad (3.4.8)$$

(In performing this integration, the assumption is made that as $w \rightarrow -\infty$, $P(w) \rightarrow 0$ faster than $|a(w)|$ increases.) Assuming stationary conditions, so that the left side of this equation is zero, and integrating in velocity from $-\infty$ to w the following expression for $a(w)$ is obtained:

$$a(w) = \frac{1}{2P(w)} \frac{\partial(\Gamma P(w))}{\partial w}. \quad (3.4.9)$$

The well-mixed constraint ensures that $P(w) = P_f(w)$ is a solution to the Fokker Planck equation. Therefore, given an expression for $P_f(w)$, Eq. (3.4.9) may then be used to obtain an expression for $a(w)$ that satisfies the well-mixed constraint. Since many skewed forms for $P_f(w)$ can potentially be used, this approach does not lead to a unique $a(w)$.

Typically, nonlinear-Gaussian Langevin equation models for the CBL have been developed (e.g., Luhar & Britter, 1989; Weil, 1989 & 1990) using a bi-Gaussian distribution for $P_f(w)$ introduced by Baerentsen and Berkowicz (1984). This distribution is a linear combination of two Gaussian distributions, and can be written as follows:

$$P_f(w) = \lambda_1 P_1(w) + \lambda_2 P_2(w) \quad (3.4.10)$$

where

$$\begin{aligned} P_1(w) &= \frac{1}{\sqrt{2\pi}\sigma_1} \exp\left[-\frac{(w - \bar{w}_1)^2}{2\sigma_1^2}\right] \\ P_2(w) &= \frac{1}{\sqrt{2\pi}\sigma_2} \exp\left[-\frac{(w - \bar{w}_2)^2}{2\sigma_2^2}\right] \end{aligned} \quad (3.4.11, 12)$$

The six parameters of this distribution, $\overline{w_1}$, $\overline{w_2}$, σ_1 , σ_2 , λ_1 , and λ_2 will be specified using the first three moments of the fluid velocity ($\overline{w_f}=0$, $\overline{w_f^2}$, and $\overline{w_f^3}$), which are assumed to be known. These six parameters can be determined from four equations for moments zero through three of this distribution, and two closure assumptions: $\overline{w_1} = \sigma_1$ and $\overline{w_2} = -\sigma_2$ (see Appendix A). The result is

$$\overline{w_2} = -\sigma_2 = \frac{\overline{w_f^3} - \sqrt{\overline{w_f^3}^2 + 8\overline{w_f^2}^3}}{4\overline{w_f^2}}, \quad (3.4.13)$$

$$\overline{w_1} = \sigma_1 = \frac{-\overline{w_f^2}}{2\overline{w_2}} = \frac{\overline{w_f^3} + \sqrt{\overline{w_f^3}^2 + 8\overline{w_f^2}^3}}{4\overline{w_f^2}}, \quad (3.4.14)$$

$$\lambda_1 = \frac{-\overline{w_2}}{\overline{w_1} - \overline{w_2}}, \text{ and} \quad (3.4.15)$$

$$\lambda_2 = \frac{\overline{w_1}}{\overline{w_1} - \overline{w_2}}. \quad (3.4.16)$$

The parameters of the bi-Gaussian distribution are now defined.

Using Eq. (3.4.9), $a(w)$ may be determined using the bi-Gaussian distribution (3.4.10-12) and the well-mixed condition, $P(w) = P_f(w)$. The result is

$$a(w) = \frac{-\Gamma}{2(\lambda_1 P_1(w) + \lambda_2 P_2(w))} \left[\frac{\lambda_1 P_1(w)}{\sigma_1^2} (w - \overline{w_1}) + \frac{\lambda_2 P_2(w)}{\sigma_2^2} (w - \overline{w_2}) \right] \quad (3.4.17)$$

This deterministic acceleration is a complex, non-linear function of velocity, and is not unique, since it depends on the chosen form of the velocity distribution (in this case a bi-Gaussian distribution).

In summary, given the fluid velocity moments $\overline{w_f^2}$ and $\overline{w_f^3}$, and the dissipation rate, $\bar{\epsilon}$ (or, as we shall see below, a Lagrangian correlation time scale of the velocity), this nonlinear-Gaussian model is completely defined by the first-order- Δt accurate velocity equation,

$$\Delta w \cong a(w_0)\Delta t + r_G(\Delta t), \quad (3.4.1)$$

the statistical properties of $r_G(\Delta t)$ given by Eqs. (3.4.2-3) and (3.4.7), and $a(w)$ given by Eqs. (3.4.10-17).

3.4.4 Linear-skewed Langevin equation model

For the linear-skewed Langevin equation, the deterministic acceleration in (3.2.1) is assumed to be a linear function of velocity,

$$a(w) = -\alpha w. \quad (3.4.18)$$

Consistent with our assumption of homogeneous and stationary velocity statistics, α and the set of the random acceleration coefficients $\{\Gamma_n, n = 1, 2, \dots\}$ in (3.2.2) are constant (not a function of z or t). In this case, the Langevin equation (3.2.1) may be integrated explicitly, and has the solution

$$w(t) = w(0)e^{-\alpha t} + \int_0^t e^{\alpha(s-t)} \Lambda(s) ds, \quad (3.4.19)$$

$\Lambda(s) \equiv r_s(t)$

where $\Lambda(t)$ is a non-Gaussian, skewed process for this form of the Langevin equation. The statistical properties of $w(t)$ and $r_s(t)$, and the coefficients α and $\{\Gamma_n, n = 1, 2, 3, \dots\}$ can be determined from an analysis of the velocity moments and autocorrelation function using the Langevin equation solution (3.4.19) with the assumptions above. Using the

Langevin equation, the n th moment of w and r_s can be determined by taking the ensemble-average value of the n th power of the Langevin equation solution for $w(t)$, Eq. (3.4.19), and carrying out the necessary time integration (see Appendix B).

The resulting general equation for the time-dependent velocity moments, using cumulant notation*, is

$$\langle\langle w^n(t) \rangle\rangle = \langle\langle w_0^n \rangle\rangle e^{-n\alpha t} + \langle\langle r_s^n(t) \rangle\rangle, \quad (3.4.20)$$

where $n = 1, 2, \dots$, and $w_0 \equiv w(0)$. The resulting general expression for the time-dependent moments of r_s , using cumulant notation, is

$$\langle\langle r_s^n(t) \rangle\rangle = \frac{\Gamma_n}{n\alpha} (1 - e^{-n\alpha t}). \quad (3.4.21)$$

Alternately, the moments and cumulants of $w(t)$ can also be determined from the Kramers-Moyal expansion for $P(w)$ instead of using the Langevin equation. The n th moment of w can be determined by multiplying this Kramers-Moyal expansion by w^n and integrating over w from $-\infty$ to ∞ and assuming (i) the b_n are not functions of w , and (ii) P_w approaches zero faster than w approaches $+\infty$ or $-\infty$.

Now, from the well-mixed condition we know that an initially well-mixed tracer will have the same velocity distribution, and, correspondingly, the same cumulants and moments as the fluid at all times under stationary conditions. Therefore, under these conditions the well-mixed condition requires that

$$\langle\langle w^n(t) \rangle\rangle = \langle\langle w_0^n \rangle\rangle = \langle\langle w_f^n \rangle\rangle. \quad (3.4.22)$$

* The additivity property shown by Eqs. (3.4.19-20) is the main advantage which cumulants have over moments: i.e., the n th cumulant of the sum of independent variables is equal to the sum of the n th cumulants of the individual variables (Kalbfleisch, 1985).

From Eq. (3.4.20), it can be seen that the cumulants of $r_s(t)$ that meet this constraint are

$$\langle\langle r_s^n(t) \rangle\rangle = \langle\langle w_f^n \rangle\rangle (1 - e^{-n\alpha t}). \quad (3.4.23)$$

From Eqs. (3.4.21) and (3.4.23) it can be seen that

$$\langle\langle w_f^n \rangle\rangle = \frac{\Gamma_n}{n\alpha}, \quad (3.4.24)$$

or

$$\Gamma_n = n\alpha \langle\langle w_f^n \rangle\rangle, \quad n = 1, 2, \dots \quad (3.4.25)$$

For example, $\Gamma_1 = \alpha \overline{w_f} = 0$, $\Gamma_2 = 2\alpha \overline{w_f^2}$, $\Gamma_3 = 3\alpha \overline{w_f^3}$, $\Gamma_4 = 4\alpha (\overline{w_f^4} - 3\overline{w_f^2}^2)$, $\Gamma_5 = 5\alpha (\overline{w_f^5} - 10\overline{w_f^2} \overline{w_f^3})$, and $\Gamma_6 = 6\alpha (\overline{w_f^6} - 15\overline{w_f^2} \overline{w_f^4} - 10\overline{w_f^3}^2 + 30\overline{w_f^2}^3)$. So, the random acceleration cumulant coefficients Γ_n and the random velocity increment $r_s(t)$ are now defined in terms of an infinite number of the fluid velocity cumulants (or moments).

The interpretation of the coefficient α in the deterministic acceleration can be seen from the velocity autocorrelation function. Multiplying the velocity equation (3.4.19) by w_0 and taking the ensemble average results in

$$\overline{w_0 w(t)} = \overline{w_0^2} e^{-\alpha t}. \quad (3.4.26)$$

It can then be seen that the coefficient α is the inverse of the Lagrangian integral time scale or Lagrangian correlation time, τ ,

$$\alpha = \frac{1}{\tau}, \quad (3.4.27)$$

where τ is defined as follows:

$$\tau \equiv \frac{\int_0^\infty \overline{w_0 w(t)} dt}{\overline{w_0^2}}. \quad (3.4.28)$$

The linear-skewed model is now completely defined. Both the deterministic term's α and the set of the random acceleration cumulant coefficients $\{\Gamma_n, n = 1, 2, \dots\}$ are defined in terms of obtainable (in principle) information, namely, the statistical properties of the fluid velocity: the Lagrangian correlation time and the fluid velocity moments.

One of the desirable aspects of this linear-skewed model is that exact expressions for the time-dependent position moments, $\overline{z^m(t)}$, for the joint velocity-position moments, $\overline{w^n(t)z^m(t)}$, and for the autocorrelation functions $\overline{w_0 w^n(t)}$ may be determined as well as for the velocity moments, $\overline{w^n(t)}$, given by the cumulants in Eq. (3.4.20) (under the assumptions, stated above, that the turbulence is homogeneous and stationary, and in the absence of boundaries). Some of these exact, analytic expressions are given in Appendix B. In Chapter 4, we will use these to test numerical simulations using the linear-skewed Langevin model.

In summary, this linear-skewed Langevin equation model assumes that the deterministic acceleration is a simple, linear function of velocity, and that the random acceleration is skewed. For homogeneous turbulence, this Langevin equation may be integrated explicitly to determine an exact equation for the time-evolution of particle velocity,

$$w(t) = w_0 e^{-t/\tau} + r_s(t), \quad (3.4.29)$$

where τ is the Lagrangian correlation time of the velocity, and $r_s(t)$ is a skewed random variable with an infinite number of non-zero cumulants. Using the well-mixed condition,

the statistical properties of $r_s(t)$ are uniquely defined in terms of an infinite number of fluid velocity cumulants by Eq. (3.4.23).

3.4.5 Special case: Gaussian (unskewed) turbulence

For the special case in which the fluid velocity distribution, $P_f(w)$, is Gaussian, and, correspondingly, $\langle\langle w_f^n \rangle\rangle = 0$ for $n = 3, 4, 5, \dots$ (e.g., skewness equals zero), *both* the linear-skewed Langevin equation and the nonlinear-Gaussian Langevin equation collapse to the Langevin equation with a linear deterministic acceleration and a Gaussian random acceleration. This is the classic form of this equation used by Langevin. We shall call it the *linear-Gaussian* Langevin equation. It is also known as the Ornstein-Uhlenbeck process (Gardiner, 1990). In this case, the Langevin equation (3.2.1) may be integrated explicitly (as in the case of the linear-skewed Langevin equation). The velocity equation is

$$w(t) = w(0)e^{-t/\tau} + r_g(t), \quad (3.4.30)$$

where $r_g(t)$ is Gaussian with first two moments defined as follows:

$$\overline{r_g(t)} = 0, \quad (3.4.31)$$

$$\overline{r_g^2(t)} = \overline{w_f^2}(1 - e^{-2t/\tau}). \quad (3.4.32)$$

A relationship between the Lagrangian correlation time scale, τ , the fluid velocity variance, $\overline{w_f^2}$, and the turbulent kinetic energy dissipation rate (per unit mass), $\bar{\epsilon}$, can be obtained using the Lagrangian structure function for this Langevin equation and Kolmogorov's second similarity hypothesis (discussed in Chapter 2). The Langevin-equation Lagrangian structure function for small time increment, δt , is

$$\overline{(\delta w)^2} \approx \frac{2\overline{w_f^2}}{\tau} \delta t, \quad (3.4.33)$$

where $\delta w = w(t + \delta t) - w(t)$. Consistency with the prediction of Kolmogorov's second similarity hypothesis for δt in the inertial subrange, given in Eq. (2.2.1), $\overline{(\delta w)^2} = C_0 \bar{\epsilon} \delta t$, implies that

$$C_0 \bar{\epsilon} = \frac{2\overline{w_f^2}}{\tau}. \quad (3.4.34)$$

This equation shows a relationship between the τ , $\overline{w_f^2}$, and $\bar{\epsilon}$, for Gaussian turbulence. It indicates that the Lagrangian velocity correlation time, τ , associated with the larger scale motions, can, in general, also be thought of as a dissipation time scale for turbulent kinetic energy associated with the larger, energy-containing scales of motion.

3.4.6 Deterministic acceleration, $a(w)$, for the two Langevin equations

The deterministic acceleration, $a(w)$, for the two forms of the Langevin equation – defined using Eqs. (3.4.17) and (3.4.34), for the nonlinear-Gaussian Langevin equation, and using Eqs. (3.4.18) and (3.4.27), for the linear-skewed Langevin equation – can now be compared. The dimensionless deterministic acceleration for both models are plotted in Fig. 3.1 for fluid velocity skewness $S = 0.8$.

For the linear-skewed model, $a(w)$ always acts to slow the speed of the particle. In contrast, the nonlinear $a(w)$ will accelerate particles with velocities in the range $-0.5\sigma_w < w < 0$ in the example shown in Fig. 3.1, where σ_w is the standard deviation of the fluid velocity. Also in contrast to the linear $a(w)$, the magnitude of the nonlinear $a(w)$ does not increase monotonically with the magnitude of the w . In particular, it can be seen

from Fig. 3.1 that for a range of w values near $+0.5\sigma_w$ particles with larger magnitude velocities have a smaller magnitude deceleration.

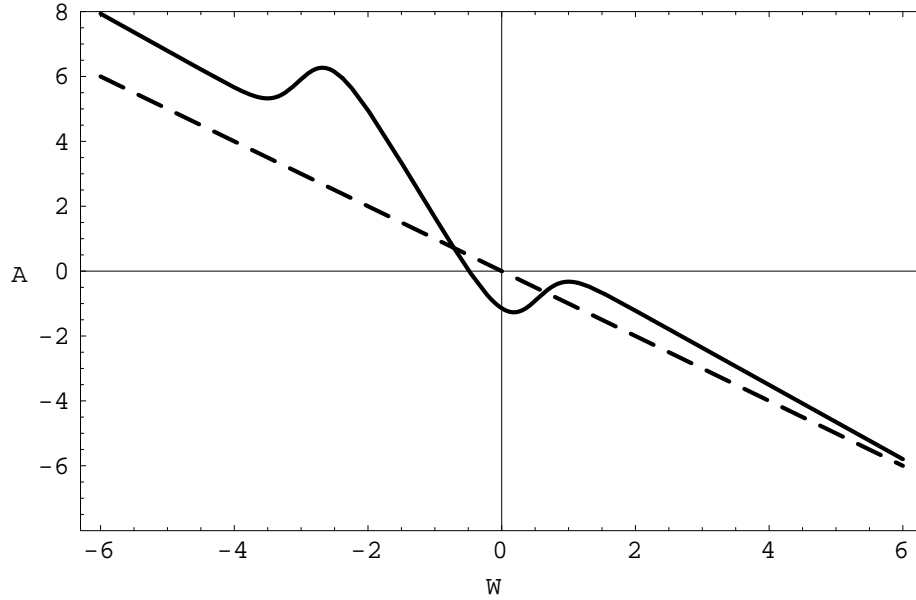


Fig. 3.1. Dimensionless deterministic acceleration, $A(W) = a(w)\tau/\sigma_w$, versus dimensionless velocity $W = w/\sigma_w$ for linear-skewed Langevin equation (dashed line) and nonlinear-Gaussian Langevin equation (solid line) for fluid velocity skewness, $S = 0.8$.

3.5 Assumptions and justification of Langevin equation approach

The justification for the use of the Langevin equation rests solely on its ability to model the statistical properties, observed and hypothesized, of the fluid velocity. Use of the Langevin equation assumes that the time evolution of particle velocity can be modeled by a stochastic process with weakly correlated acceleration, and in which the velocity is a non-differentiable and (in one form of the Langevin equation) a discontinuous function of time, t . This section discusses these assumptions, their implications, and their justification.

The Langevin equation assumes that the particle mean acceleration depends only on its current velocity, and that the random acceleration is uncorrelated over any time period of interest. This assumption that the future particle velocity depends simply on the current velocity, and not the past history of the velocity is called the Markov assumption. These assumptions are justified if the particle acceleration is weakly correlated in time. In large Reynolds number flows, the acceleration is strongly correlated for times on the order of and smaller than the Kolmogorov microscale, τ_η (Monin and Yaglom, 1975, p. 370). As discussed in Chapter 2, τ_η is typically much less than a second in the atmospheric boundary layer. For atmospheric dispersion problems, only times much greater than τ_η are typically of interest, and the Markov assumption is justified.

The statistical properties of the change in velocity predicted by the Langevin equation models over a small time interval can be compared to the predictions of Kolmogorov's second hypothesis. As discussed in Chapter 2, Kolmogorov's second hypothesis implies that $\overline{(\Delta w)^n} \propto (\bar{\epsilon} \Delta t)^{n/2}$ for even n , where $\tau_\eta \ll \Delta t \ll \tau$, and $\overline{(\Delta w)^n} = 0$ for odd n . As discussed by Sawford & Borgas (1994), the nonlinear-Gaussian Langevin equation model is consistent with these predictions. For this model, r_G is Gaussian, and for $\Delta t \ll 1$, $\overline{r_G^2} = C_0 \bar{\epsilon} \Delta t$. Therefore, for even n , $\overline{(\Delta w)^n} = \overline{r_G^n} \propto (C_0 \bar{\epsilon} \Delta t)^{n/2}$, and the moments for odd n are zero. In contrast, the linear-skewed Langevin equation model is not consistent with Kolmogorov's second hypothesis predictions since, for $\Delta t \ll 1$, $\overline{(\Delta w)^n} = \overline{r_s^n} = n \left\langle \left\langle w_f^n \right\rangle \right\rangle \frac{\Delta t}{\tau}$ for all n , as shown in Eq. (3.6.7).

The linear-skewed Langevin equation model does, however, result in reasonable predictions of the velocity autocorrelation for time periods on the order of and smaller than τ . A linear deterministic acceleration results in an exponential autocorrelation function, $c(t) = \overline{w_0 w(t)} / \overline{w_0^2} = e^{-t/\tau}$, as shown by Eqs. (3.4.26-27). The slope of this

function is discontinuous and non-zero at $t = 0$, but the slope of $c(t)$ should be continuous and zero at $t = 0$, due to the inertia of fluid particles. Nevertheless, the exponential autocorrelation function has the correct value of unity at $t = 0$, and, except for $t/\tau \ll 1$, has been shown to be a very good approximation to observations and direct numerical simulation results in homogeneous, isotropic, and stationary turbulence (Pope, 1994). Hanna (1979) found it was a reasonable approximation for $t < 2\tau$ using observations in the unstable, daytime atmospheric boundary layer.

Both forms of the Langevin equation have the property that the velocity is not differentiable with respect to time. Differentiable means the $\lim_{\Delta t \rightarrow 0} (\Delta w / \Delta t)$ exists, where $\Delta w = w(t + \Delta t) - w(t)$. The non-differentiable nature of the Langevin equation velocity can be illustrated by using the Taylor series expansion of the linear-Gaussian velocity equation, Eq. (3.4.30), which yields the following equation for the velocity change, valid for $\Delta t / \tau \ll 1$:

$$\Delta w = -\frac{w(t)}{\tau} \Delta t + \left(\frac{2\overline{w_f^2}}{\tau} \right)^{1/2} \Delta t^{1/2} \zeta$$

where ζ is a Gaussian random variable with zero mean and variance of one. For non-zero values of ζ , the $\lim_{\Delta t \rightarrow 0} (\Delta w / \Delta t) = \pm\infty$, so the velocity is not differentiable.

The linear-skewed Langevin equation (and the corresponding Kramers-Moyal expansion) has the property that the velocity is a discontinuous function of time in a probabilistic sense (although the velocity does have a continuous range of values). This Langevin equation describes what is called a "jump" Markov process. In contrast, the Gaussian-random-acceleration Langevin equation (and the corresponding Fokker-Planck equation) describe a "continuous" Markov process (Gardiner, 1990; Gillespie, 1992). If the velocity is a continuous function of time, then the probability that $w(t + \Delta t)$ is finitely different

from $w(t)$ goes to zero faster than Δt , as Δt goes to zero (Gardiner, 1990). The discontinuous (according to this criterion) nature of the velocity for the skewed-random-force Langevin equation, is illustrated in Appendix C using the linear-skewed Langevin equation model. However, the velocity described by the linear-skewed Langevin equation model is well behaved in the sense that it is *mean-square continuous*, i.e., $\lim_{\Delta t \rightarrow 0} \overline{\Delta w^2} = 0$, where $\Delta w = w(t + \Delta t) - w(t)$. In fact, all the moments of the velocity change for the linear-skewed Langevin equation vanish for vanishing time step, $\lim_{\Delta t \rightarrow 0} \overline{\Delta w^n(\Delta t)} = 0$.

In summary, we expect that physically the fluid particle velocity is a differentiable and continuous function of time, and that the acceleration is strongly correlated over very small time intervals. However, this does not mean that the approximating stochastic mathematical process (described by a form of the Langevin equation) need have these properties. While some of the statistical properties of the change in velocity over short time increments predicted by the different forms of the Langevin equation may be physically unrealistic, as just discussed, the ensemble average properties (e.g., velocity moments, autocorrelation) of the Langevin equation velocity are realistic. This makes these equations useful for making predictions at the times of interest for atmospheric dispersion problems.

3.6 Numerical simulation of $w(t)$

To perform numerical simulations of particle motion using the equations for the time evolution of particle velocity, $w(t)$, determined from the Langevin equation, we need a method of obtaining random velocity increments, $r(t)$, from a probability distribution, $P(r)$, with moments $\overline{r^n(t)}$. For the nonlinear-Gaussian model, $P(r)$ is Gaussian and the first two moments of r completely define this distribution (the third and higher order

cumulants are zero). However, for the linear-skewed model, $P(r)$ is non-Gaussian and the cumulants of all orders are non-zero.

3.6.1 Nonlinear-Gaussian Langevin equation model

The nonlinear-Gaussian Langevin equation model for the time evolution of velocity, accurate to first order in Δt , was defined in Section 3.4 by

$$w(t + \Delta t) = w(t) + a(w(t))\Delta t + r_G(\Delta t), \quad (3.6.1)$$

$$\overline{r_G(\Delta t)} = 0, \quad (3.6.2)$$

$$\overline{r_G^2(\Delta t)} = \frac{2\overline{w_f^2}}{\tau} \Delta t \quad (3.6.3)$$

where $w(t+\Delta t)$ is the numerically-calculated velocity of a particle after time step Δt given velocity $w(t)$ at the beginning of the time step, and the functional form for the nonlinear $a(w)$ was defined in Eq. (3.4.17). Values of $r_G(\Delta t)$ can be generated from a Gaussian distribution using standard methods. Initial values of w are chosen from the bi-Gaussian fluid velocity distribution given by Eqs. (3.4.10-16).

3.6.2 Linear-skewed Langevin equation model

For the linear skewed Langevin equation model, the statistical properties of $r_s(t)$ are functions of an infinite number of fluid velocity moments. However, the velocity moments of most fluids are not known with sufficient accuracy beyond the first few. This is because the higher moments are highly dependent on the low-probability tails of the velocity probability distribution where experimental statistics are poorest. However,

information on only the first few velocity moments has been shown to explain tracer dispersion in the CBL. For example, the first three velocity moments were used to define the fluid velocity distribution for the nonlinear-Gaussian model above, and have been used in most previous applications of Langevin equation models to CBL dispersion.

A practical difficulty, for the linear skewed model, is that even if all of the cumulants of the fluid velocity were known, it is mathematically difficult (if not impossible) to obtain $P(r_s(t))$ from an infinite number of cumulants. In addition, the form of $P(r_s(t))$ continually changes with time increment t , due to the time-dependent behavior of the moments of $P(r_s(t))$ (see Eq. (3.4.23) and Appendix B). For example, the second and third moments of $r_s(t)$, $\overline{r_s^2(t)}$ and $\overline{r_s^3(t)}$, are proportional to t at small t , and, therefore, the skewness, $\overline{r_s^3(t)} / (\overline{r_s^2(t)})^{3/2}$ is proportional to $t^{-1/2}$. So, $P(r_s(t))$ becomes more highly skewed as t decreases. Therefore, it does not seem possible to obtain an analytic form for $P(r_s)$ from which individual values of $r_s(t)$ can be selected in a numerical simulation. (In contrast, for the nonlinear-Gaussian model, $P(r_G)$ retains the same form, a Gaussian distribution, for all t .)

This practical difficulty will be addressed by using a simple, known functional form, $P_a(r_s)$, as an approximation to the probability distribution $P(r_s)$. $P_a(r_s)$ will be defined using the exact first three moments of r_s . The higher moments ($n = 4, 5, \dots$) of $r_s(t)$ are, then, defined from the functional form of $P_a(r_s)$, and can be calculated. Through the relationship (3.4.23) between the moments of $r_s(t)$ and w_f , the higher moments of the fluid velocity are, then, implicitly defined.

For the linear-skewed Langevin model, the equation we will use to numerically simulate the particle velocity is

$$w(t + \Delta t) = w(t)e^{-\Delta t/\tau} + r_{sa}(\Delta t), \quad (3.6.4)$$

where $w(t + \Delta t)$ is the numerically-calculated velocity of a particle after time step Δt given velocity $w(t)$ at the beginning of the time step. $r_{sa}(\Delta t)$ is a random velocity increment obtained from a probability distribution $P_a(r_s)$ which has the first three moments which are the same as the exact first three moments of $r_s(\Delta t)$,

$$\overline{r_{sa}(\Delta t)} = 0, \quad (3.6.5a)$$

$$\overline{r_{sa}^2(\Delta t)} = \overline{w_f^2} \left(1 - e^{-2\Delta t/\tau}\right), \text{ and} \quad (3.6.5b)$$

$$\overline{r_{sa}^3(\Delta t)} = \overline{w_f^3} \left(1 - e^{-3\Delta t/\tau}\right) \quad (3.6.5c)$$

(see Appendix B). Eqs. (3.6.5a, b, and c) define $P_a(r_s)$ since it will have a functional form defined by the first three moments. Since the first three moments of $w(t + \Delta t)$ depend only on the first three moments of r_s and $w(t)$, this approximation is exact for the first three moments of w .

The distribution $P_a(r_s)$ that we use here is a combination of two overlapping uniform probability distributions, and shall henceforth be referred to as a "double-block" distribution. The form of this distribution and the determination of its parameters using the known first three moments of r is given in Appendix C.

The higher moments of r_{sa} resulting from $P_a(r_s)$ for very small times, $\Delta t / \tau \ll 1$, are

$$\overline{r_{sa}^n(\Delta t)}_{\Delta t/\tau \ll 1} = \frac{\left(\overline{w_f^3}\right)^{n-2}}{\left(\overline{w_f^2}\right)^{n-3}} \left[\frac{4(3)^{n-2}}{n+1} \right] \frac{\Delta t}{\tau}, \quad n = 4, 5, \dots \quad (3.6.6)$$

(see Appendix C). Using (3.4.23), the moments of $r_s(\Delta t)$ in terms of the fluid velocity moments for very small times, $\Delta t / \tau \ll 1$, are

$$\overline{r_s^n(\Delta t)}_{\Delta t / \tau \ll 1} = \langle \langle r_s^n(\Delta t) \rangle \rangle_{\Delta t / \tau \ll 1} = \Gamma_n \Delta t = n \langle \langle w_f^n \rangle \rangle \frac{\Delta t}{\tau}, \quad (3.6.7)$$

where $n = 1, 2, \dots$ (note that the property that the moments of r_s approach the cumulants of r_s for very small time was used in obtaining Eq. (3.6.7)). Equating (3.6.6) and (3.6.7), i.e., $\overline{r_s^n(\Delta t)}_{\Delta t / \tau \ll 1} = \overline{r_{sa}^n(\Delta t)}_{\Delta t / \tau \ll 1}$, we can now specify the higher fluid velocity cumulants,

$$\langle \langle w_f^n \rangle \rangle = \frac{(\overline{w_f^3})^{n-2}}{(\overline{w_f^2})^{n-3}} \left[\frac{4(3)^{n-2}}{n(n+1)} \right], \quad n = 4, 5, \dots \quad (3.6.8)$$

(the fourth through sixth velocity moments corresponding to this equation are given in Appendix C). So, using this approach, the higher fluid velocity cumulants (and moments) can be defined implicitly in terms of the first three fluid velocity moments. (Note: this is also true of the non-linear Gaussian model described earlier, for which the parameters of the bi-Gaussian velocity distribution were defined using the first three moments of the fluid velocity and the remaining moments are defined implicitly.)

In general, $P_a(r_s)$ is only an approximation to $P(r_s)$, although they have the exact same first three moments. For a finite time step there is numerical error in the higher ($n \geq 4$) moments of $r_s(\Delta t)$ and, correspondingly in the higher moments of $w(t)$. However, the higher ($n \geq 4$) moments of w_f have limiting values for small time step. These limiting values are used to define the exact higher velocity moments for the linear-skewed Langevin model. Then, for sufficiently small time steps ($\Delta t / \tau \ll 1$), the numerical simulation results will approach the exact solution.

This approach to simulating and defining the Langevin equation model has some desirable aspects. First, we have a well-defined system with specified values for the

random term coefficients $\{\Gamma_n\}$ that are in agreement with the known turbulence properties of the fluid, namely, the first few velocity moments. Second, the first three moments of velocity can be simulated exactly for any time step, while the higher moments are exact in the limit of small time steps.

In order to compare calculations made with this linear-skewed Langevin equation model directly with those made with the nonlinear-Gaussian model described above, it would be desirable to use the same fluid velocity distribution with both models. However, while the first three moments of the fluid velocity distribution are explicitly specified for both these models (and, therefore, can be made the same for both models), the higher moments are only implicitly defined for both models. In addition, while the form of the fluid velocity distribution is explicitly specified (the bi-Gaussian distribution) for the nonlinear-Gaussian model, it is not specified for the linear-skewed model, rather, it is the result of the chosen form of the Langevin equation.

3.7 Numerical simulation of $z(t)$

The velocity equation, $w = dz/dt$, must be integrated to obtain an equation for the time evolution of particle position. In integrating this equation, it is assumed that the particle velocity varies linearly between the value calculated by the Langevin velocity equation at the beginning of the time step, $w(t)$, and the value at the end of the time step, $w(t + \Delta t)$. This yields the following approximate position equation

$$z(t + \Delta t) = z(t) + \frac{1}{2}[w(t + \Delta t) + w(t)]\Delta t \quad (3.7.1)$$

Eq. (3.7.1) results in a mean displacement that is correct through $O(\Delta t^2)$, which is

$$\overline{[z(t + \Delta t) - z(t)]} = w(t)\Delta t - \frac{1}{2}a(w(t))\Delta t^2 + O(\Delta t^3).$$

(In contrast, the often-used first-order position equation, $z(t + \Delta t) = z(t) + w(t)\Delta t$, results in a mean displacement that is correct through $O(\Delta t)$.)

We now have methods for simulating the joint evolution of particle velocity and position, $(w(t), z(t))$, and can calculate particle trajectories in (w, z) space in an unbounded flow (no boundaries). A Monte Carlo simulation of a sample of N independent particle trajectories (each representing a realization from the ensemble of possible trajectories) can be used to estimate ensemble average quantities such as position moments, velocity moments, velocity autocorrelation, as well as velocity probability distributions and position probability distributions (needed to calculate average air concentration). Next, we will address the case of bounded flow, and the selection of new velocities when a boundary is encountered.

3.8 Reflection boundary conditions

In a homogenous model, the interaction with boundaries must be treated with some type of “reflection” of the vertical velocity. In the homogeneous, two-dimensional conceptual model of the CBL that we are using, there are horizontal boundaries at the ground surface and at the average height of the capping inversion, the horizontal mean wind is uniform, and the statistical properties of the fluid vertical velocity fluctuations are homogeneous. Consequently, this model does not resolve the variation of the statistical properties of the fluid velocity in the surface layer near the bottom of the CBL and in the entrainment layer near the top, and, correspondingly, does not model the details of possible trajectories in these layers. Reflection boundary conditions for approximating the effect of interactions with these layers were investigated. Three reflection boundary conditions were compared in this work, one each in which the incident and reflected speeds are (I) positively correlated, (II) negatively correlated and (III) uncorrelated.

Reflection methods that assume that the magnitude of the reflected vertical velocity is *positively* correlated with the magnitude of the incident velocity have been used in all previous Langevin equation models of dispersion in the CBL. In a homogeneous model, this would imply that air approaching the surface from the mixed layer with a strong downdraft velocity spends relatively little time near the surface, because it is given a relatively strong updraft velocity when it encounters the surface and, given the long velocity correlation time, is quickly returned to the mixed layer. The observed circulation patterns in the CBL indicate that positively correlated incident and reflected speeds may not be the best choice for a homogeneous model.

As discussed in Chapter 2 and by Williams and Hacker (1992, 1993), air in the core of a strong downdraft region has relatively strong downward velocity, penetrates deep into the surface layer, spreads out away from its center, and stays near the surface while it moves horizontally toward convergence zones that feed the updrafts (thermals) in the mixed layer. In contrast, air in relatively weak, smaller downdraft regions or near the edges of strong downdraft regions has relatively weaker downward velocity, will approach the surface closer to convergence zones, and is likely to be returned to the mixed layer faster.

The effect of the observed near-surface circulation patterns might be represented best by a method using a reflected speed which is *negatively* correlated with the incident speed. This would result in relatively fast descending particles being given a relatively low magnitude reflected velocity when they encounter the surface, and remaining near the surface for a longer time. In contrast, slower descending particles would be given a relatively higher magnitude reflected velocity, and remain near the surface for a shorter time.

A third approach to reflection assumes that the reflected speed is *uncorrelated* with the incident speed. In other words, a particle leaves the surface with no memory of its incoming velocity. In a homogeneous model, this approach might be justified if mixed layer downdrafts are not coupled with updrafts in a coherent circulation, and if turbulent motions nearer the surface have very small velocity correlation times.

As discussed by Weil (1990), Wilson and Flesch (1993), Hurley and Physick (1993), and Thomson and Montgomery (1994), reflection methods used previously in Langevin equation simulations of CBL dispersion have been unable to maintain a well-mixed position and velocity distribution in a skewed, homogenous turbulent fluid. However, Thomson and Montgomery presented a sound basis for such methods, and successfully tested one method versus the well-mixed condition in homogeneous, skewed turbulence.

Thomson and Montgomery (1994) based their approach to velocity reflection at boundaries on the criterion that if a trace material is well mixed in a fluid it must remain so. Based on this criterion, the joint velocity and position probability density function of the tracer is, therefore, the same as that of the fluid, $P_f(w, z)$. Thomson and Montgomery (and also an anonymous reviewer of the paper by Hurley and Physick, 1993) recognized that a well-mixed spatial and velocity distribution will be maintained if at the height of a boundary, just as at any other height z , the ensemble-average flux of particles with velocity in $(w, w + dw)$ through z is proportional to

$$\phi(w, z) \equiv w P_f(w, z) dw.$$

$\phi(w, z)$ is the fraction of all particles (in an ensemble) with velocity in $(w, w + dw)$ crossing z per unit time. Since we are assuming the velocity distribution is independent of height so that $P_f(w, z) = n_f(z) P_f(w; z) = n_f(z) P_f(w)$, where $n_f(z)$ and $P_f(w)$ are the fluid spatial and velocity distributions, respectively, this flux may be written as follows:

$$\phi(w, z) = w n_f(z) P_f(w) dw .$$

The probability density function for positive velocities crossing any height z is proportional to $\phi(w, z)$, and is

$$P_+(w) = \frac{w n_f(z) P_f(w)}{\int_0^{\infty} w n_f(z) P_f(w) dw} ,$$

or

$$P_+(w) = \frac{w P_f(w)}{\int_0^{\infty} w P_f(w) dw} , \quad w > 0. \quad (3.8.1)$$

Similarly, the probability density function for negative velocities crossing any height is

$$P_-(w) = \frac{w P_f(w)}{\int_{-\infty}^0 w P_f(w) dw} , \quad w < 0. \quad (3.8.2)$$

The distributions $P_-(w)$ and $P_+(w)$ can be used to describe the distribution of the ensemble of incident and reflected velocities, respectively, at a lower boundary (the reverse relationship holds at the upper boundary). However, they do not provide the relationship between a specific w_i and the resultant w_r . Any relationship between w_i and w_r that results in these distributions will satisfy the well-mixed condition.

One method of implementing reflection, which will be referred to as *reflection method I*, that results in a positive correlation between the magnitudes of w_i and w_r , is to choose w_r at the lower boundary, for example, such that

$$\int_0^{w_r} P_+(w) dw = \int_{w_i}^0 P_-(w) dw , \quad w_r > 0, \quad w_i < 0, \quad (3.8.3)$$

for a given $w_i < 0$. This makes use of the fact that the incident particle velocities w_i crossing the boundary are distributed according to $P_-(w)$. If $P_f(w)$ is Gaussian or any other symmetric distribution, this method reduces to the simple, so-called perfect reflection method: $w_r = -w_i$.

The net flux at the boundary must be zero. This means that

$$-\int_{-\infty}^0 \phi(w, z) dw = \int_0^{\infty} \phi(w, z) dw.$$

Using the definition of $\phi(w, z)$, this becomes

$$-\int_{-\infty}^0 w P_f(w) dw = \int_0^{\infty} w P_f(w) dw.$$

This criterion is met if the fluid velocity distribution has zero mean. If the mean velocity is zero, then the normalizing constants for both P_+ and P_- , are the same, and reflection method I, given in Eq. (3.8.3), simplifies to

$$\int_0^{w_r} w P_f(w) dw = -\int_{w_i}^0 w P_f(w) dw, \quad w_r > 0, \quad w_i < 0.$$

This is not the only method of selecting reflected velocities that are distributed according to P_{\pm} . Two other methods will be investigated. A method that results in a negative correlation between the magnitude of w_i and w_r , which we will refer to as *reflection method II*, is to chose w_r such that at the lower boundary, for example,

$$\int_0^{w_r} P_+(w) dw = \int_{-\infty}^{w_i} P_-(w) dw, \quad w_r > 0, \quad w_i < 0, \quad (3.8.4)$$

Another method, *reflection method III*, is to randomly select a reflected velocity value from the distribution P_+ at the lower boundary (P_- at the upper boundary).

It is convenient to introduce cumulative probability distribution functions defined as follows:

$$F_+(w) = \int_0^w P_+(w_+) dw_+, \quad w > 0, \text{ and} \quad (3.8.5)$$

$$F_-(w) = \int_{-\infty}^w P_-(w_-) dw_-, \quad w < 0. \quad (3.8.6)$$

The three reflection methods for selecting a new, reflected velocity w_r after a boundary is encountered with incident velocity w_i can then be described as follows:

- *Method I – Positively correlated w_i and w_r magnitudes*

Lower boundary:

$$\text{Given } w_i < 0, \text{ select } w_r > 0 \text{ such that } F_+(w_r) = 1 - F_-(w_i) \quad (3.8.7)$$

Upper boundary:

$$\text{Given } w_i > 0, \text{ select } w_r < 0 \text{ such that } F_-(w_r) = 1 - F_+(w_i) \quad (3.8.8)$$

- *Method II – Negatively correlated w_i and w_r magnitudes*

Lower boundary:

$$\text{Given } w_i < 0, \text{ select } w_r > 0 \text{ such that } F_+(w_r) = F_-(w_i) \quad (3.8.9)$$

Upper boundary:

$$\text{Given } w_i > 0, \text{ select } w_r < 0 \text{ such that } F_-(w_r) = F_+(w_i) \quad (3.8.10)$$

- *Method III – Random w_r chosen from $P_{\pm}(w)$*

Lower boundary:

Obtain uniform random number u on $(0,1)$

$$\text{Select } w_r \text{ such that } F_+(w_r) = u \quad (3.8.11)$$

Upper boundary:

Obtain uniform random number u on $(0,1)$

Select w_r such that $F_-(w_r) = u$ (3.8.12)

If analytic expressions are available for $P_f(w)$, $F_+(w)$ and $F_-(w)$ it might be possible to solve Eqs. (3.8.7-12) for w_r explicitly. For the linear-skewed Langevin model, we do not have an analytic expression for $P_f(w)$. For the nonlinear-Gaussian Langevin model, we have an analytic, bi-Gaussian $P_f(w)$, but it may not be possible to solve Eqs. (3.8.7-12) explicitly for w_r (Hurley and Physick, 1993; Thomson and Montgomery, 1994).

To implement the reflection methods, we first construct tables of $F_+(w_j)$ or $F_-(w_j)$ versus w_j , for $j = 1$ to n bins, using $P_f(w)$ calculated numerically from a Langevin equation simulation. Given incident velocity w_i , the corresponding value of $F_{\pm}(w_i)$ is approximated by linear interpolation between the closest two table values. Then, using the value of $F_{\pm}(w_r)$ determined from one of the three reflection methods, the reflected velocity w_r is approximated by linear interpolation between table values. In the numerical simulations performed in this work, tables were constructed of $F_-(w)$ versus w using $n = 128$ bins from $w = -12\sigma_w$ to 0 and of $F_+(w)$ versus w for $n = 128$ bins from $w = 0$ to $+12\sigma_w$, using evenly spaced intervals of w .

In order to improve the numerical accuracy of the reflection calculation, over Thomson & Montgomery's implementation, the time step was split at the point a boundary is encountered. In this implementation, the following steps are used when a boundary is encountered:

- (1) Assuming the velocity varied linearly between $w(t)$ and $w(t + \Delta t)$ during Δt , the incident velocity and time when a boundary was encountered are calculated.

- (2) The reflected velocity is calculated using method I, II or III.
- (3) The Langevin velocity equation is used with the reflected velocity and the remainder of the time step to re-compute the final velocity at the end of the time step.
- (4) The final position is calculated, starting at the boundary, by assuming the velocity varied linearly between the reflected velocity and the final velocity over the remainder of the time step.

In this method, particles follow curved (quadratic) $z(t)$ trajectories, and are re-reflected if they again encounter the boundary during the remainder of the time step.

4

Model Evaluation

In this chapter, the two Langevin equation models and three reflection boundary conditions presented in Chapter 3 are tested and evaluated. Results are presented from simulations of idealized cases for which exact, analytic statistical properties of w and z are known, including simulations of well-mixed spatial and velocity distributions. These simulations are used to evaluate the statistical properties and numerical accuracy of the models. Results are then presented from simulations of Willis and Deardorff's laboratory water tank experiments discussed in Chapter 2. These are used to test the ability of the models to calculate dispersion in the convective boundary layer.

4.1 Tests in unbounded turbulence

The idealized case of dispersion in unbounded, stationary, homogeneous, skewed turbulence was used to test the accuracy of numerical simulations versus several known analytic results for the statistical properties of velocity and position, and to determine the size of the numerical integration time step required for accurate solutions. One of these analytic results is that if tracer particle initial velocities are distributed with the fluid velocity distribution, $P_f(w)$, then tracer particle velocity distribution will remain the same as $P_f(w)$ at all times, and, correspondingly, the tracer particle velocity moments will remain the same as the ambient fluid velocity moments, $\overline{w_f^n}$, at all times. These velocity moments are known for both the linear-skewed and nonlinear-Gaussian Langevin equation models. In addition, for the nonlinear-Gaussian model, the velocity

distribution $P_f(w)$ is a known analytic function (the bi-Gaussian distribution given in Chapter 3). For the linear-skewed model, there are also known analytic expressions for the time-dependent position moments, joint velocity-position moments, and velocity autocorrelation functions (given in Appendix B).

The sources of numerical error differ somewhat between the two Langevin equation models. Error in the calculated velocity is introduced in simulations with the nonlinear-Gaussian Langevin equation model because the approximate velocity update equation is accurate only through $O(\Delta t)$, where Δt is the size of the numerical integration time step. In this equation, both the deterministic term and the moments of the random term are accurate through order $O(\Delta t)$. In contrast, the linear-skewed Langevin equation uses a more accurate velocity equation, which is exact for the first three moments of velocity, because the deterministic term and the first three moments of the random term are exact. However, for a finite time step the linear-skewed model does yield error in the fourth and higher moments, due to the approximate distribution used for the random velocity increment, as discussed in Chapter 3. Error in the particle position (additional to the error in the velocity) is introduced because of the approximate position update equation, which is accurate through $O(\Delta t^2)$ for the mean displacement, as discussed in Chapter 3.

Simulations were performed assuming steady state conditions with no boundaries and a skewed velocity distribution. Particle initial velocities were chosen from a fluid velocity distribution, $P_f(w)$, with zero mean, standard deviation σ_w , and skewness $S \equiv \overline{w_f^3} / \sigma_w^3 = 1$. Particle positions were all initialized to $z=0$. Trajectories, $\{(w_i(t), z_i(t)), i = 1, 2, \dots, N\}$, for $N = 5 \times 10^5$ particles were calculated from $t = 0$ to 4τ . The results are presented in the following dimensionless coordinates: $T = t/\tau$, $W = w/\sigma_w$, and $Z = z/(\sigma_w \tau)$. Simulations with different size time steps, $\Delta T = 0.2, 0.05$, and 0.01 , were completed with each model in order to determine the time step size required for accurate numerical solutions.

For the nonlinear-Gaussian model, initial velocities were selected from the known bi-Gaussian distribution for $P_f(w)$. For the linear-skewed model, an analytic expression for $P_f(w)$ is not available from which to select initial velocities (although, analytic expressions exist for all the moments). Therefore, initial guess velocity values with the correct first three velocity moments were assigned using a double-block distribution, and then adjusted using simulations with the linear-skewed velocity equation for a period of 2τ (in retrospect, a period of 1τ is sufficient) prior to the start of the simulations in order to reach an initial velocity distribution as close as possible to the steady-state fluid velocity distribution.

The velocity distributions calculated by the nonlinear-Gaussian model at $T = 4$ using three different time steps, $\Delta T = 0.2, 0.05$, and 0.01 are shown in Fig. 4.1, along with the exact, analytic distribution. The calculated velocity distributions for the unbounded case, show a strong time step dependence, due to the $O(\Delta t)$ velocity update equation. For $\Delta T = 0.01$, there is excellent agreement between the numerically-calculated distribution and the exact distribution. There is a small departure from the correct velocity distribution when $\Delta T = 0.05$, and large departures when $\Delta T = 0.2$.

The velocity distributions calculated by the linear-skewed Langevin equation model at $T = 4$ using $\Delta T = 0.2, 0.05$, and 0.01 are shown in Fig. 4.2. The shape of this distribution depends on the parameters, A and B , of the double-block distribution, $P_a(r_s)$, (see Appendix C) used for the random term in the linear-skewed model's velocity equation. Values of $A = B = 1$ were used because they resulted in reasonable agreement between the model-predicted velocity distributions and the measured CBL velocity distributions

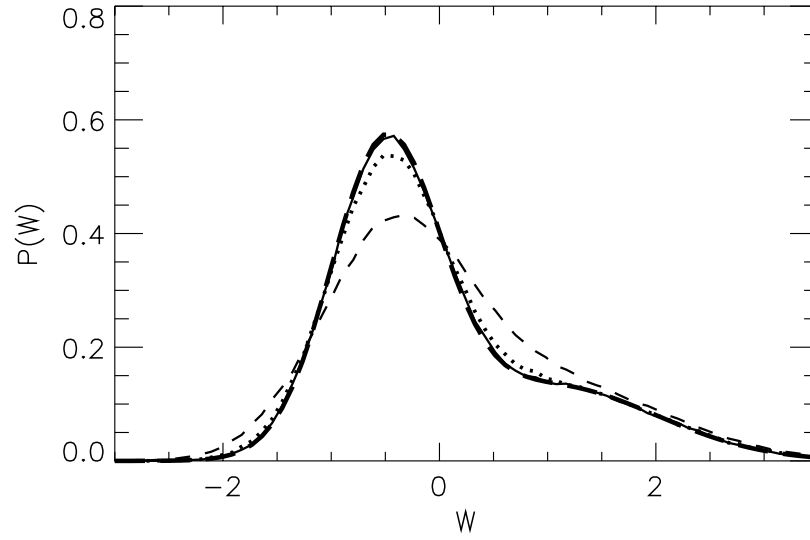


Fig. 4.1. Dimensionless velocity distribution from *nonlinear-Gaussian* model simulation at $T=4$ using three different time steps, $\Delta T = 0.2$ (short-dash line), 0.05 (dotted line), and 0.01 (solid line), along with analytic velocity distribution (long-dash line), for the unbounded turbulence case.

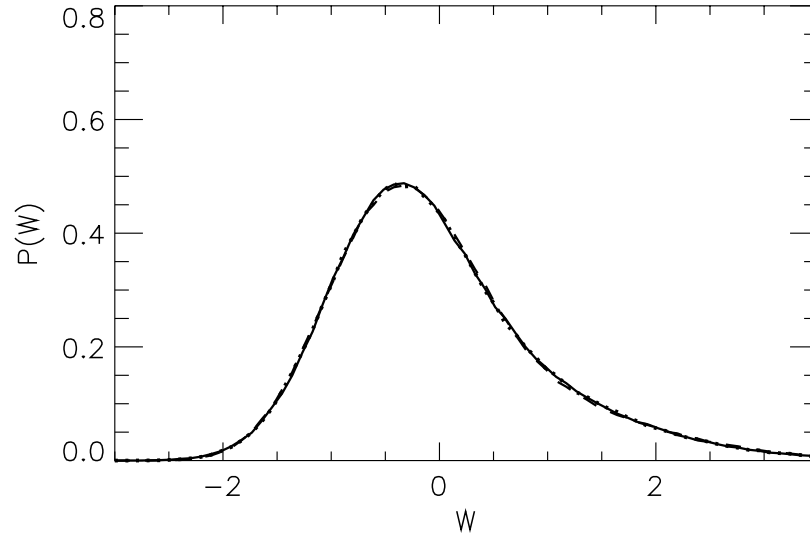


Fig. 4.2. Dimensionless velocity distribution from *linear-skewed* model simulation at $T=4$ using three different time steps, $\Delta T = 0.2$ (short-dash line), 0.05 (dotted line), and 0.01 (solid line), for the unbounded turbulence case.

(shown later in this chapter). There is very little difference in the velocity distributions (Fig. 4.2) from the simulations using the three different time steps. This shows that the numerical accuracy of the linear-skewed model velocity equation is significantly better than the nonlinear-Gaussian model, as expected, because the linear-skewed model uses a velocity equation exact for the first three velocity moments.

The departures in the higher moments of velocity, which are affected by small departures in the tails of the distributions, are not easily detected in the curves in Figs. 4.1 and 4.2. These departures can be seen directly in the numerically calculated higher moments. Table 4.1 gives the values for the first six velocity moments calculated by the nonlinear-Gaussian model at $T = 4$ using time steps of $\Delta T = 0.2, 0.05$, and 0.01 , as well as the corresponding exact values for the fluid velocity moments. Table 4.2 presents the same results corresponding to the linear-skewed model. The first three moments are explicitly controlled for both models, and have the same exact values. The values of the exact fourth and higher moments, given in Tables 4.1 and 4.2, differ between the two models, because they use different $P_f(W)$ distributions. For both models, decreasing the time step has the expected effect of increasing the accuracy of the velocity moments calculated.

The nonlinear-Gaussian model requires smaller time steps than the linear-skewed model to achieve comparable accuracy in the calculated velocity moments. For example, the results in Table 4.2 show that for the largest time step used, $\Delta T = 0.2$, the linear-skewed model's calculated first three moments are the same as the exact values, within the statistical uncertainty (due to the finite number of particles used to estimate ensemble averages) as measured by the standard error. The nonlinear-Gaussian model results in Table 4.1 show that the smallest time step, $\Delta T = 0.01$, is required to obtain comparable accuracy in the first three moments. For the fourth and higher moments of velocity, a

time step of approximately $\Delta T = 0.01$ is required to reduce the error to approximately 1% or less for both models.

Table 4.1. Dimensionless velocity moments (\pm standard error) calculated using *nonlinear-Gaussian* Langevin equation model at dimensionless time $T=4$ from three simulations with $S=1$ and three different time step values; and exact fluid velocity moments.

	<i>Numerical value</i>			<i>Exact value</i>
	$\Delta t/\tau = 0.2$	$\Delta t/\tau = 0.05$	$\Delta t/\tau = 0.01$	
\overline{W}	0.094 ± 0.002	0.016 ± 0.001	0.003 ± 0.001	0.
$\overline{W^2}$	1.179 ± 0.003	1.027 ± 0.002	1.004 ± 0.002	1.
$\overline{W^3}$	1.182 ± 0.008	1.020 ± 0.007	1.001 ± 0.007	1.
$\overline{W^4}$	4.867 ± 0.026	3.921 ± 0.023	3.777 ± 0.022	3.75
$\overline{W^5}$	10.164 ± 0.097	8.432 ± 0.082	8.159 ± 0.078	8.125
$\overline{W^6}$	35.772 ± 0.380	27.590 ± 0.325	26.296 ± 0.296	26.125

Table 4.2. Dimensionless velocity moments (\pm standard error) calculated using *linear-skewed* Langevin equation model at dimensionless time $T=4$ from three simulations with $S=1$ and three different time step values; and exact fluid velocity moments.

	<i>Numerical value</i>			<i>Exact value</i>
	$\Delta t/\tau = 0.2$	$\Delta t/\tau = 0.05$	$\Delta t/\tau = 0.01$	
\overline{W}	0.000 ± 0.001	0.000 ± 0.001	0.000 ± 0.001	0.
$\overline{W^2}$	1.002 ± 0.003	1.000 ± 0.003	0.999 ± 0.003	1.
$\overline{W^3}$	1.012 ± 0.010	0.995 ± 0.010	0.995 ± 0.011	1.
$\overline{W^4}$	4.711 ± 0.045	4.712 ± 0.047	4.780 ± 0.050	4.8
$\overline{W^5}$	12.884 ± 0.233	13.022 ± 0.252	13.456 ± 0.283	13.6
$\overline{W^6}$	53.421 ± 1.369	55.359 ± 1.532	58.790 ± 1.816	59.714

The time-step dependence of the fourth and higher moments calculated by the linear-skewed model is evident in the results in Table 4.2. As discussed in Chap. 3, this is a result of the fact that the fourth and higher cumulants of the random velocity increment in

this Langevin equation model are not exact. However, from the values in Table 4.2, it can be seen that the higher velocity moments quickly approach the limiting values (given in Chapter 3) as the time step is decreased.

The model-predicted particle position distributions for the unbounded case were also evaluated. Accurate prediction of position probability density is important because it is proportional to concentration. Figure 4.3 shows the distribution of dimensionless particle position, $P(Z)$, at $T = 1$ calculated by the nonlinear-Gaussian model using three different time steps, $\Delta T = 0.2, 0.05$, and 0.01 . Figure 4.4 shows the same for the linear-skewed model. These distributions were calculated by sampling particle positions within bins of width $\Delta Z = 0.25$. For the nonlinear-Gaussian model, the distributions for the simulations with the two smaller time steps, $\Delta T = 0.05$ and 0.01 , show only small differences, indicating the numerical solutions are converging at these time step values. For $\Delta T = 0.2$, there are significant departures from the limiting distribution (for example, a 6% difference between the peak probability of the $\Delta T = 0.2$ distribution and the $\Delta T = 0.01$ distribution). In contrast, for the linear-skewed Langevin equation model there is very little change in the model simulated $P(Z)$ distributions for the different time steps. This again reflects the better numerical accuracy of the linear-skewed Langevin equation model. These results indicate that the approximate position update equation used in both these models is quite accurate at these time steps.

The effect of the positively-skewed velocity distribution is evident in the skewed position distribution at $T = 1$ in Figs. 4.3 and 4.4. There is a larger positive- Z tail to the distribution, and the mode of the distribution is negative. The difference in the shapes of the $P(Z)$ distributions reflects the different $P_f(W)$ distributions (shown in Figs. 4.1 and 4.2) used by the two models. However, the different forms of the Langevin equation used in these models must also contribute to the difference.

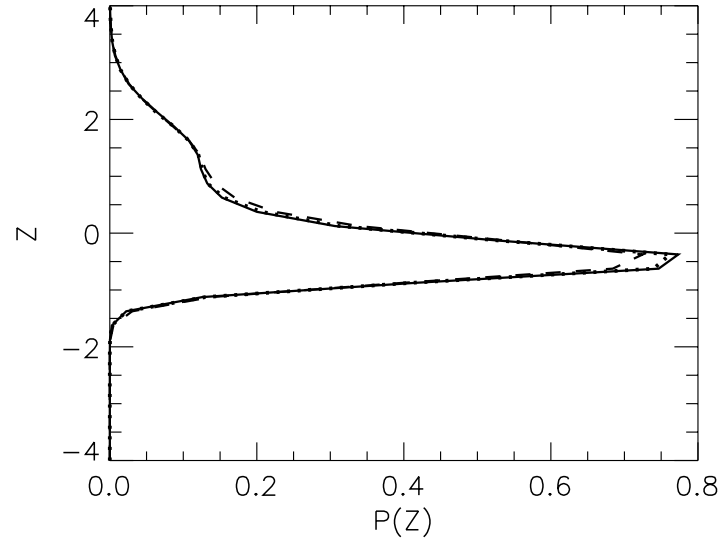


Fig. 4.3. Particle position distribution, $P(Z)$, versus dimensionless height, Z , at $T = 1$ from *nonlinear-Gaussian* model simulation using three different time steps, $\Delta T = 0.2$ (dashed line), 0.05 (dotted line), and 0.01 (solid line), for the unbounded turbulence case.

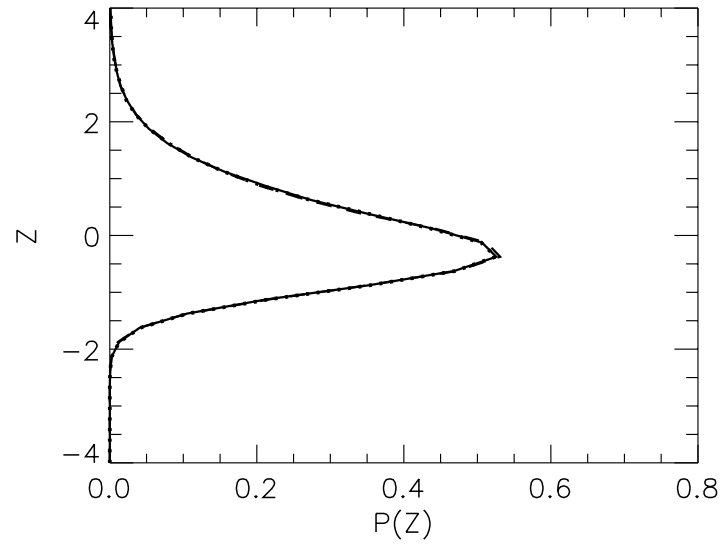


Fig. 4.4. Same as Fig. 4.3, except from *linear-skewed* model simulation.

The mean fluid velocity is zero, so the mean position should remain zero in these simulations. For the nonlinear-Gaussian model, Fig. 4.5 shows that the numerical error in the mean position is probably acceptable for $\Delta T = 0.05$. The error in the mean position is at least partially due to error in the mean velocity (noted above) for the nonlinear-Gaussian model. For $\Delta T = 0.01$, the error is extremely small. For $\Delta T = 0.2$, it is much larger.

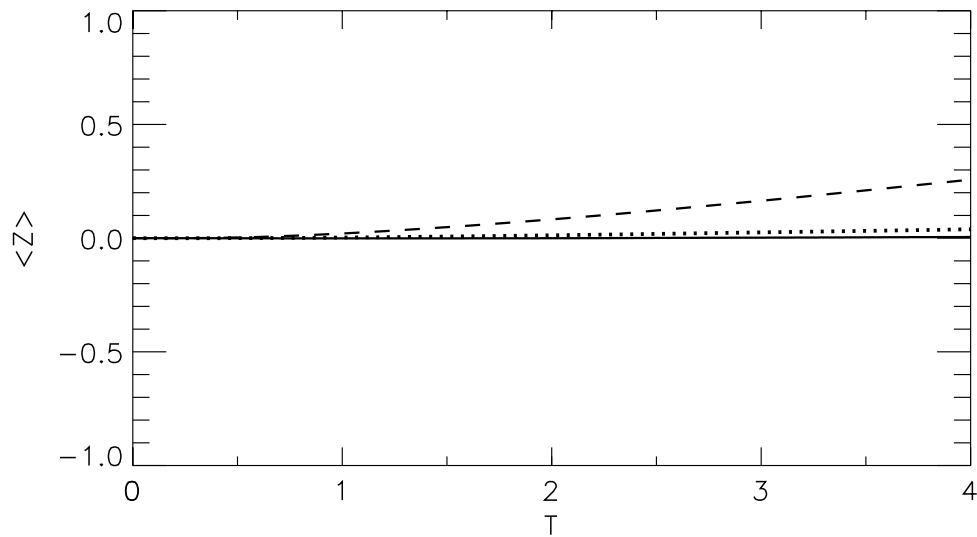


Fig. 4.5. Particle dimensionless mean position, $\overline{(Z(T) - Z(0))}$, as a function of dimensionless time, T , from the *nonlinear-Gaussian* model simulations using three different time steps, $\Delta T = 0.2$ (dashed line), 0.05 (dotted line), and 0.01 (solid line), for the unbounded turbulence case.

For the linear-skewed model, position moments can be calculated analytically and used to evaluate the model results. Figure 4.6 shows the dimensionless mean position, $\overline{(Z(T) - Z(0))}$; standard deviation, $\sigma_z \equiv \overline{(Z(T) - Z(0))^2}^{1/2}$; and third moment, $\overline{(Z(T) - Z(0))^3}$, as a function of T from the linear-skewed model simulation with time step $\Delta T = 0.2$, along with the corresponding analytic solutions (see Appendix A). Fig. 4.6 shows there is excellent agreement between the numerical and analytic results even for the longest time step used.

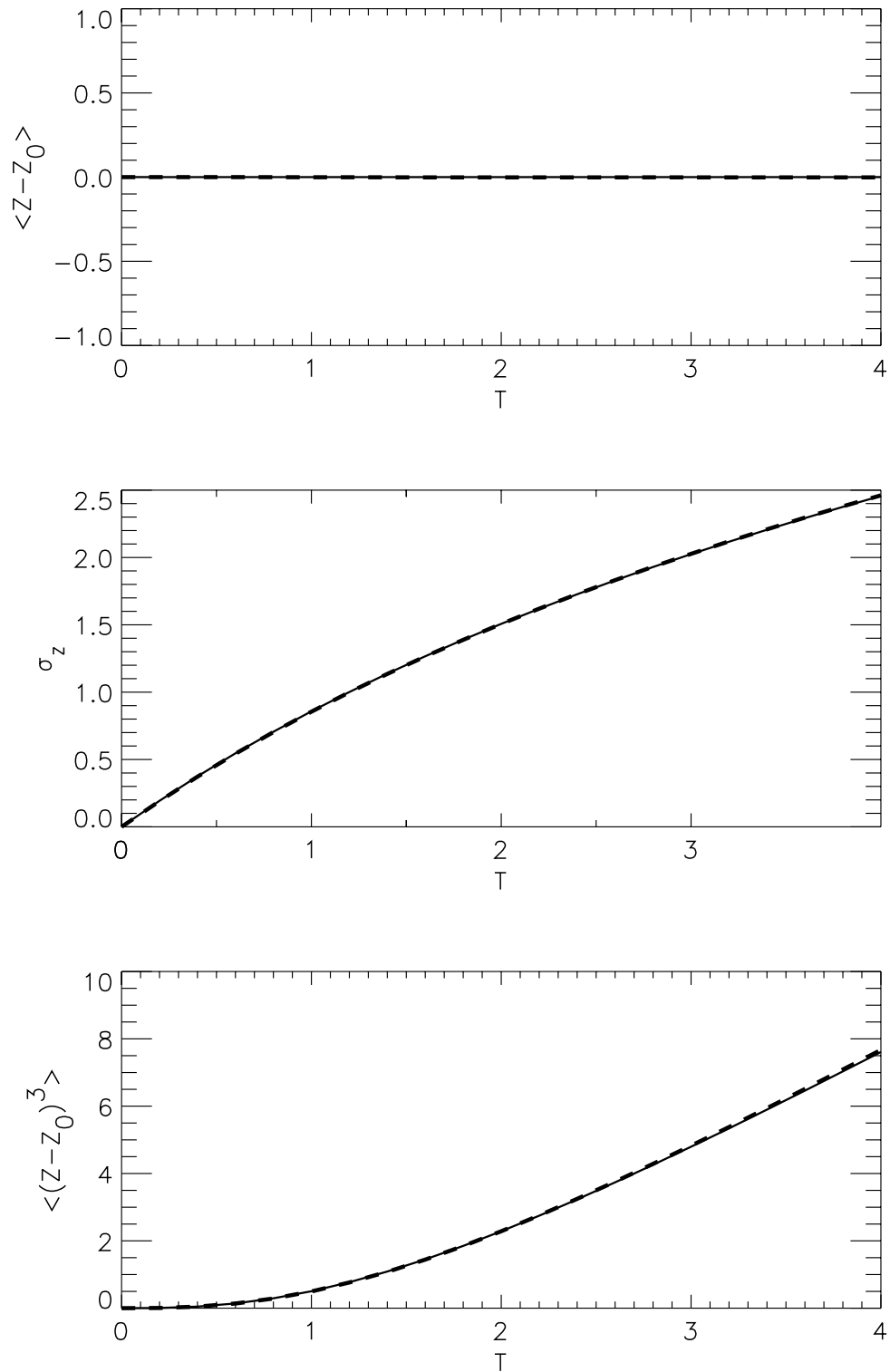


Fig. 4.6. Mean, standard deviation and third moment (about initial position) of dimensionless particle position as a function of dimensionless time, T , from the *linear-skewed* model simulation with time step $\Delta T = 0.2$ (dashed line), and the corresponding analytic values (solid line) for the unbounded turbulence case.

For the linear-skewed model, there are also analytic solutions for velocity autocorrelation functions and joint velocity-position moments (see Appendix A), and these were used to further evaluate this model. Fig. 4.7 shows plots of three velocity autocorrelation functions, $\overline{W(T)W(0)}$, $\overline{W^2(T)W(0)}$, and $\overline{W^3(T)W(0)}$, as a function of T from the linear-skewed model simulation with time step $\Delta T = 0.05$, along with the corresponding analytic functions. There is excellent agreement between the numerical and analytic results. (This is true for $\Delta T = 0.2$ also, except for a small departure from the analytic curve for $\overline{W^3(T)W(0)}$, which depends on the fourth moment of velocity.) Fig. 4.8 shows plots of the three velocity-position joint moments, $\overline{W(T)(Z(T) - Z(0))}$, $\overline{W^2(T)(Z(T) - Z(0))}$, and $\overline{W(T)(Z(T) - Z(0))^2}$, as a function of T from the linear-skewed model simulation with time step $\Delta T = 0.2$, along with the corresponding analytic functions. These results show the model is accurately simulating the evolution of particle velocity and position as measured by these autocorrelation functions and joint moments.

In summary, both Langevin equation models can accurately simulate known statistical properties of velocity and position for this unbounded case if sufficiently small time steps are used. Results of tests varying the size of the numerical integration time step reflect the increased accuracy of the velocity update equation in the linear-skewed model, compared to the nonlinear-Gaussian model. For linear-skewed model simulations, a time step of $\Delta T = 0.2$ results in negligible error in the velocity and position distributions for this unbounded case. For nonlinear-Gaussian model simulations, a time step of $\Delta T = 0.05$ results in acceptable error.

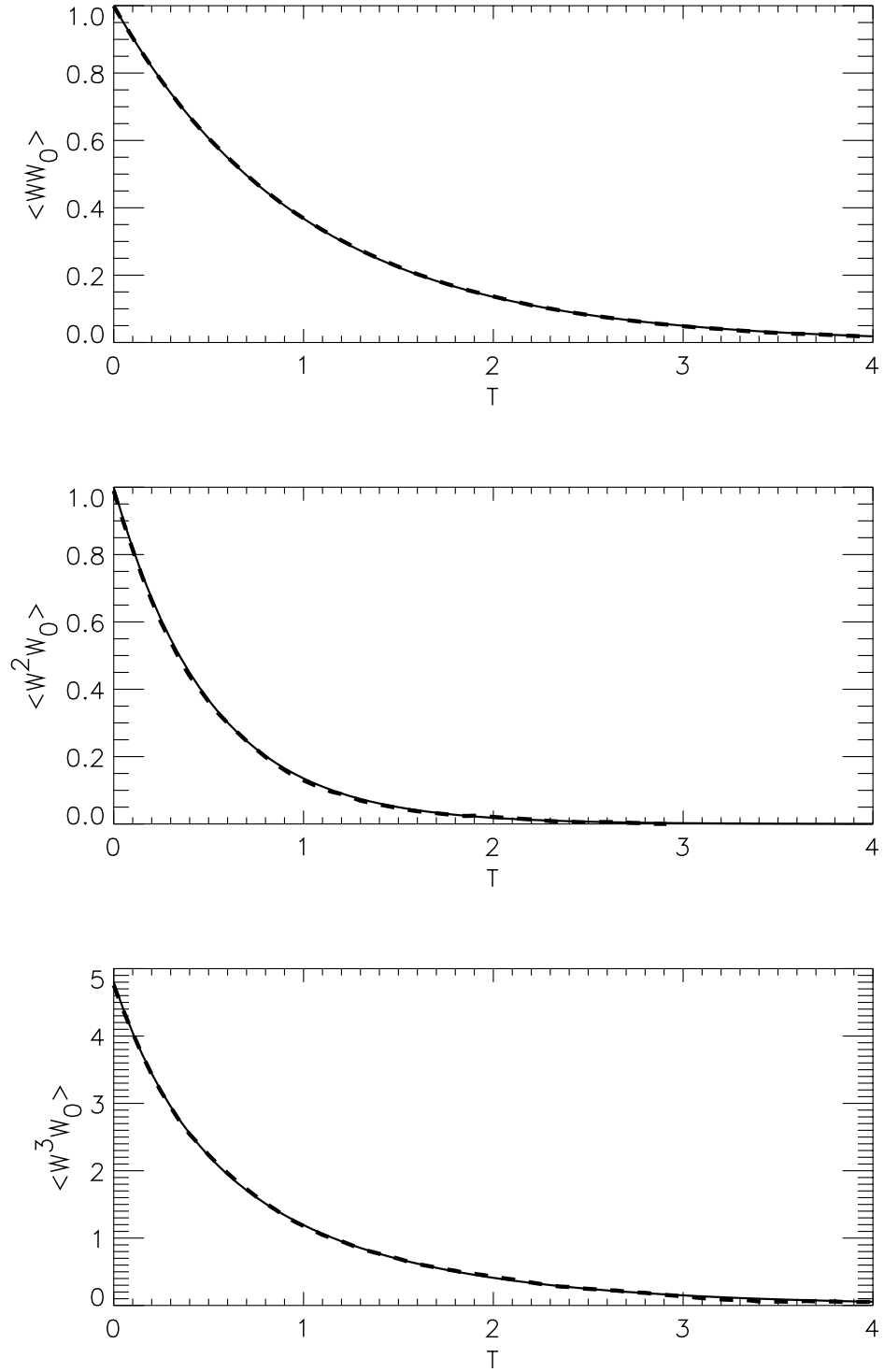


Fig. 4.7. Velocity autocorrelation functions, $\overline{W(T)W(0)}$, $\overline{W^2(T)W(0)}$, and $\overline{W^3(T)W(0)}$, as a function of T from the *linear-skewed* model simulation with time step $\Delta T = 0.05$ (dashed line), along with the corresponding analytic functions (solid line) for the unbounded turbulence case.

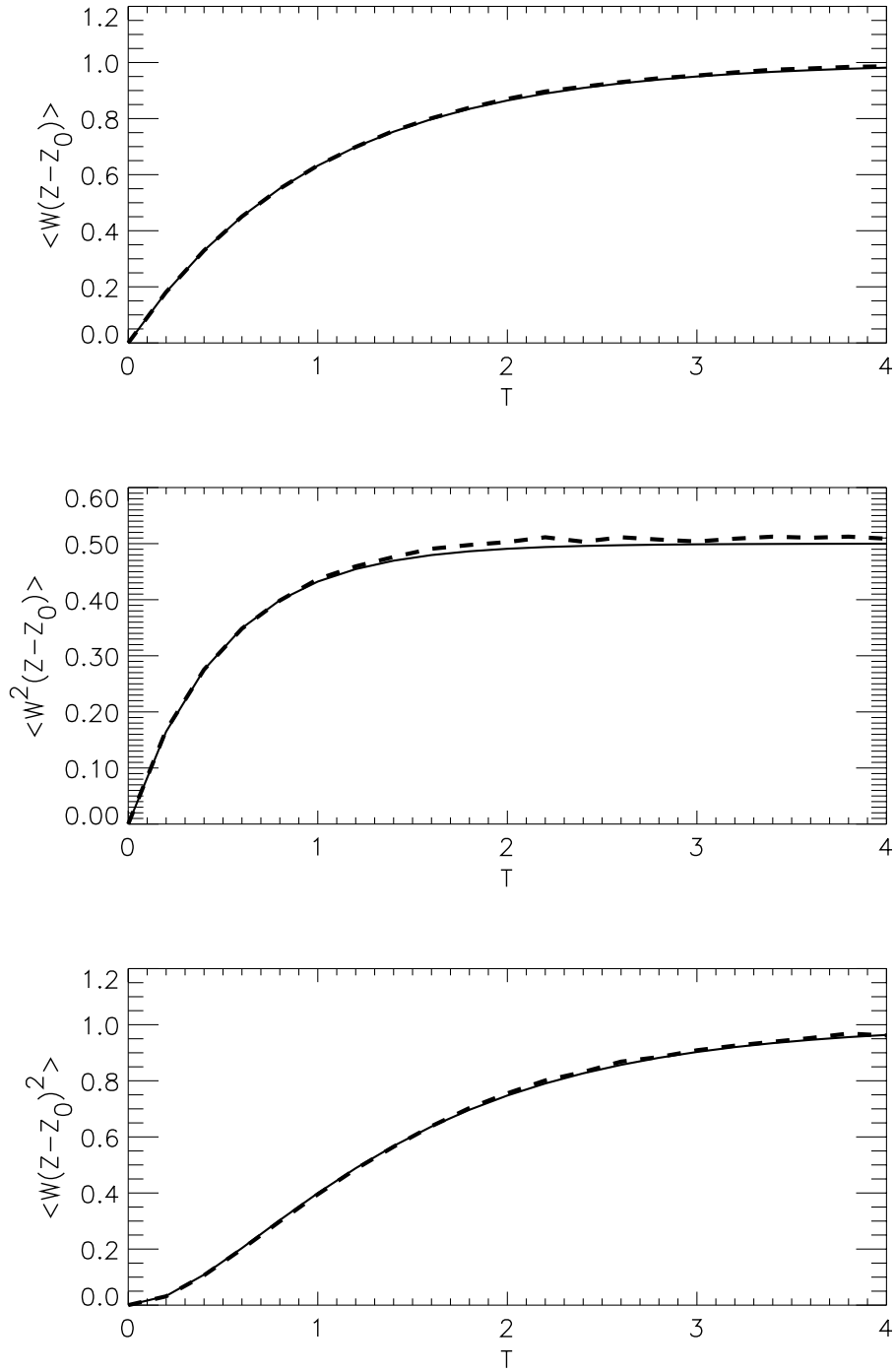


Fig. 4.8. Velocity-position joint moments, $\overline{W(T)(Z(T)-Z(0))}$, $\overline{W^2(T)(Z(T)-Z(0))}$, and $\overline{W(T)(Z(T)-Z(0))^2}$, as a function of T from the linear-skewed model simulation with time step $\Delta T = 0.2$ (dashed line), along with the corresponding analytic functions (solid line) for the unbounded turbulence case.

4.2 Well-mixed tests in bounded turbulence

Each of the three reflection boundary conditions discussed in Chapter 3, and both Langevin equation models, were tested to determine the time step required for accurate numerical simulations of well-mixed spatial and velocity distributions in an idealized homogeneous, stationary, skewed, bounded flow. The presence of boundaries introduces additional sources of numerical error (in addition to those discussed in Section 4.1) because the incident velocity is calculated by using an approximation that the velocity varies linearly in time over the time step in which the boundary is encountered, and because the reflected velocity is determined using an approximate table look-up method, as described in Chapter 3.

Simulations were performed in which particle velocities were initialized, as in the unbounded simulations above, from a fluid velocity distribution having a skewness $S = 1$. Initial positions were distributed uniformly between boundaries at $z = 0$ and $z = h$. A Lagrangian time scale value of $\tau = 0.5(h / \sigma_w)$ was used. Simulations were performed for a time period of $2(h / \sigma_w)$. The results from these simulations will be presented in the following dimensionless coordinates: $T = t\sigma_w/h$, $W = w/\sigma_w$, and $Z = z/h$. In these simulations, $N = 5 \times 10^5$ particles were used. Position distributions were calculated using 20 bins between the top and bottom boundary, and were averaged from $T = 0.5$ to 2.

To determine tables of $F_+(w)$ and $F_-(w)$ used in the reflection methods described Chapter 3, a preliminary simulation was performed for a period of (h / σ_w) before the start of final simulation from $T = 0$ to 2. The average velocity distribution over this period was used to compute tables of $F_+(w)$ and $F_-(w)$. The resulting initial $P(w)$ was approximate, just as the velocity distribution is at any time after a steady state is reached in a numerical simulation.

Particle position distributions, $P(Z)$, from simulations with different size time steps, $\Delta t = 0.01 \tau$, 0.05τ and 0.2τ , were completed using both models in order to determine the time step size required for accurate numerical solutions. Fig. 4.9 shows the results for reflection method III (results from simulations using the other two reflection methods were similar) and the nonlinear-Gaussian model using $\Delta t = 0.05 \tau$ and 0.2τ . These results show that a time step of $\Delta t = 0.05 \tau$ results in error in the position distribution of less than 3% (the correct uniform position distribution is $P(Z) = 1$), while for $\Delta t = 0.2 \tau$, there is error of up to approximately 10%. For the linear-skewed model simulations using reflection method III, Fig. 4.10 shows that there are only minor departures of less than 1% from the correct uniform distribution, for both $\Delta t = 0.2 \tau$ and 0.05τ . The better accuracy of the linear-skewed model results, compared to the nonlinear-Gaussian model, is, again, an indication of the smaller numerical error in the linear-skewed model velocity update equation.

The initial and final velocity distributions, $P(W)$, from simulations using $\Delta t = 0.05 \tau$ were compared to determine if the steady-state velocity distribution is maintained. Figs. 4.11 and 4.12 show that for $\Delta t = 0.05 \tau$ and reflection method III (similar results were obtained with the other two reflection methods), both models maintain the initial velocity distribution very well.

Figs. 4.13 and 4.14 show well-mixed test results for the two models and for all three reflection methods using a time step $\Delta t = 0.05 \tau$. The nonlinear-Gaussian model results in Fig. 4.13 show that the departures from the well-mixed spatial distribution are less than approximately 3% for this time step. For the linear-skewed model, Fig. 4.14 shows that all three reflection methods result in departures of approximately 1% or less for this time step. Results from simulations using a smaller time step, $\Delta t = 0.01 \tau$, (not shown)

produced excellent results, with less than 0.5% departure from the well-mixed spatial distribution for both models and all three reflection methods.

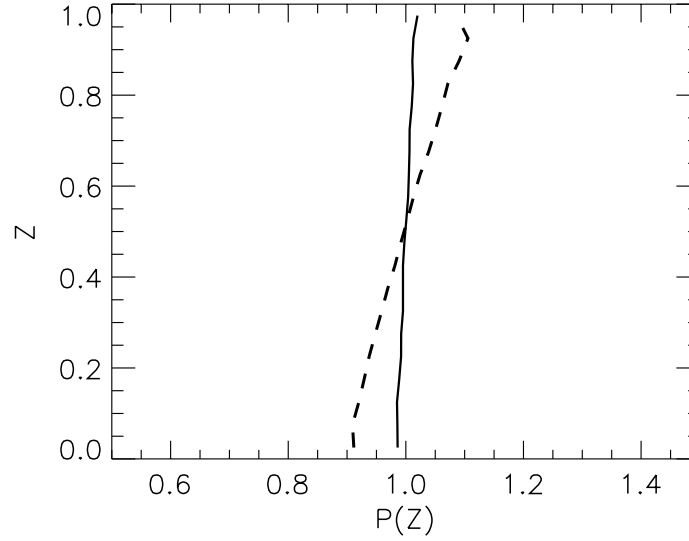


Figure 4.9. Position distributions, $P(Z)$, from two *nonlinear-Gaussian* model simulations of a well-mixed distribution using numerical time steps of $\Delta t = 0.2 \tau$ (dashed line) and 0.05τ (solid line), and reflection method III.

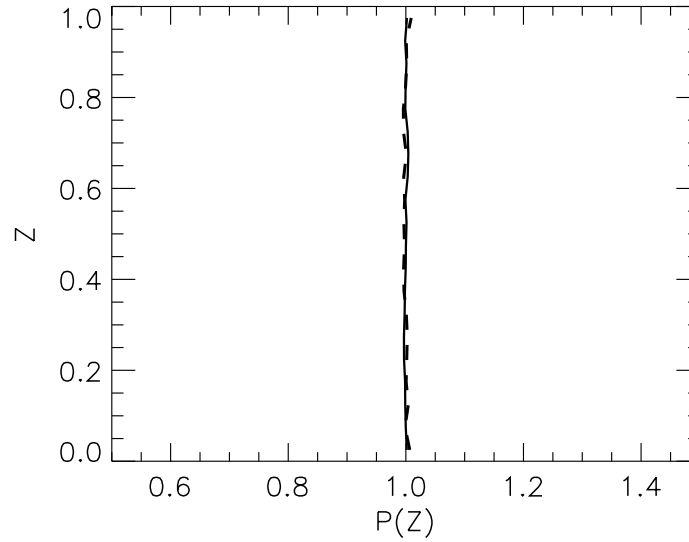


Figure 4.10. Same as Fig. 4.9, except from *linear-skewed* model.

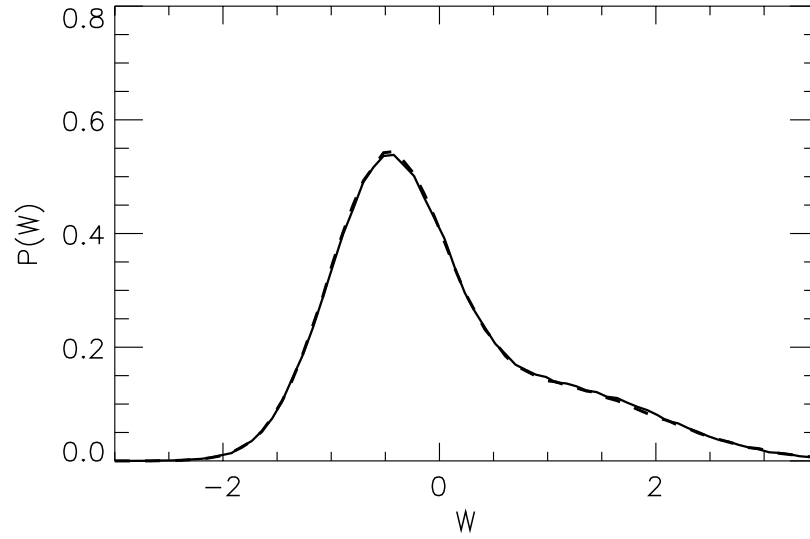


Figure 4.11. Velocity distributions, $P(W)$, at $T = 0$ (solid line) and $T = 2$ (dashed line) from *nonlinear-Gaussian* model simulation of a well-mixed distribution using reflection method III and numerical time step of $\Delta t = 0.05 \tau$.

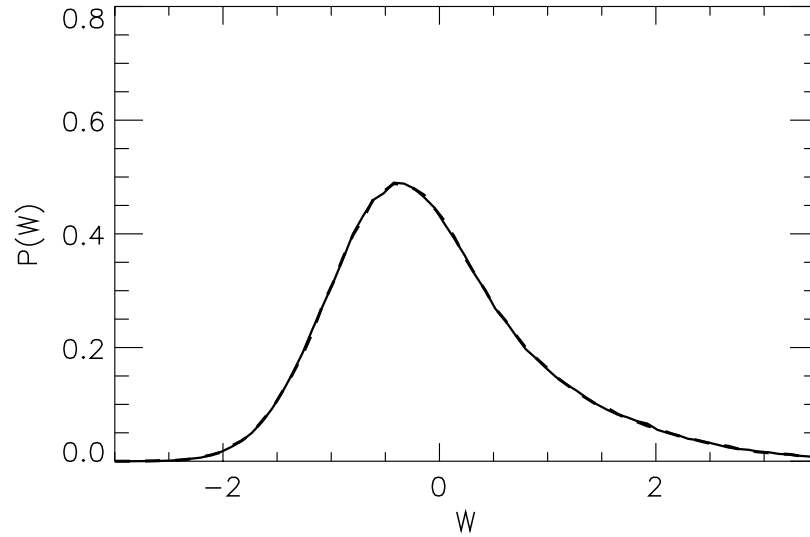


Figure 4.12. Same as Fig. 4.11, except for *linear-skewed* model simulation.

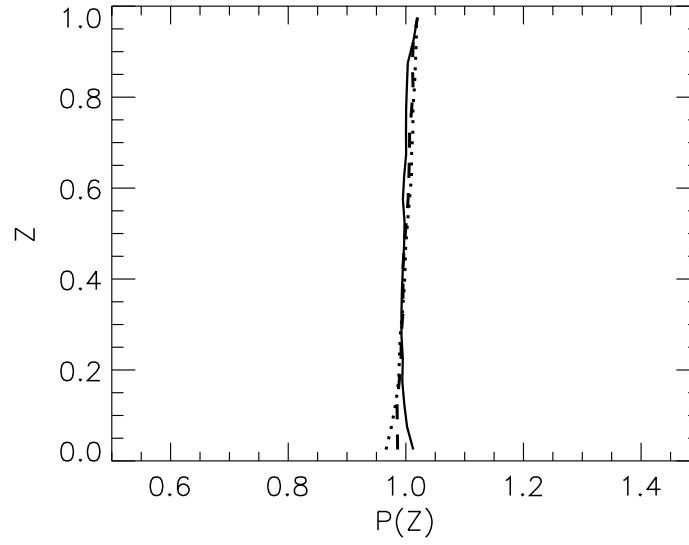


Figure 4.13. Position distributions, $P(Z)$, from three *nonlinear-Gaussian* model simulations of a well-mixed distribution using reflection method I (solid line), method II (dotted line) and method III (dashed line), and numerical time step of $\Delta t = 0.05 \tau$.

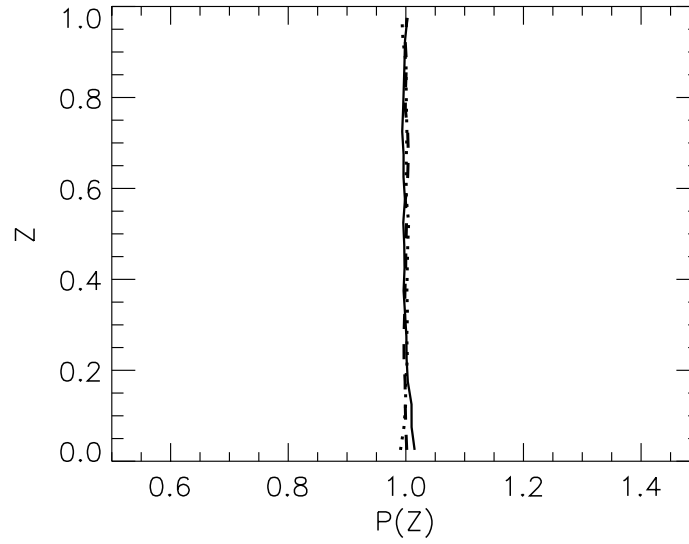


Figure 4.14. Same as Fig. 4.13, except from three *linear-skewed* model simulations.

In summary, both Langevin models and all three reflection methods can maintain well-mixed spatial and velocity distributions. For nonlinear-Gaussian model simulations, numerical error in the spatial distribution is acceptably small (less than 3%) when a time step of $\Delta t = 0.05 \tau$ is used. The linear-skewed model again exhibited better numerical accuracy than the nonlinear-Gaussian model for the same time step. For linear-skewed model simulations, numerical error in the spatial distribution is acceptably small (1% or less) for time steps as large as $\Delta t = 0.2 \tau$.

4.3 CBL simulation

Willis and Deardorff's laboratory experiments, discussed in Chapter 2, were used to evaluate the ability of the two homogeneous Langevin equation models and three reflection methods to simulate vertical dispersion in the CBL. This experimental dataset was used because it is unique in that (a) detailed measurements of *both* the tracer concentration field (Willis and Deardorff, 1976a, 1976b, 1978 & 1981) and the fluid velocity statistics (Deardorff and Willis, 1985) were made, and (b) ensemble averages were computed from several experiments under the same conditions. In addition, the Willis and Deardorff experimental results have been found to be in substantial agreement with both numerical and field experiments (Briggs, 1993b).

Section 4.3.1, presents the two-dimensional conceptual model that will be used in simulations of the CBL. In section 4.3.2, Deardorff and Willis' measured vertical velocity distributions will be used to determine the fluid velocity variance and skewness needed as input to the models, and to evaluate the Langevin equation models' simulated velocity distributions. Section 4.3.3 discusses the estimation of the Lagrangian velocity correlation time. In section 4.3.4, Willis and Deardorff's tracer dispersion measurements will be used as an indirect method of evaluating the modeled velocity distributions and the other

modeling assumptions: i.e., the form of the Langevin equation and the reflection boundary conditions. (As discussed in Chapter 3, a controlled comparison of the effects of the different forms of the Langevin equation alone would require the same velocity distribution be used for both models. However, while the first three moments of the distribution can be made the same, it is not clear how the velocity distributions can be made the same for both types of Langevin models.) Section 4.3.5 presents a discussion of the sensitivity of the simulation results to the values of the input parameters.

4.3.1 Two-dimensional conceptual model

A simplified 2-D conceptual model of vertical dispersion and horizontal mean wind advection in the CBL is used in this work. As discussed in Chapters 2 and 3, in this model it is assumed that there is (1) a horizontal, impermeable boundary at the average height of the capping inversion ($z = h$), (2) a horizontal, impermeable boundary at the surface ($z = 0$), (3) a uniform horizontal (x direction) mean wind, and (4) velocity fluctuation only in the vertical velocity component, w . The last two assumptions are consistent with Willis and Deardorff's transformation of their dispersion observations. In addition, we assume that the statistical properties of the fluid vertical velocity fluctuations are homogeneous, and that mixed-layer scaling of the vertical velocity statistics is valid.

This conceptual model can be used to simplify the expression for the cross-wind-integrated air concentration. Using Eq. (3.1.1), the ensemble-mean cross-wind-integrated air concentration, $c(x, z, t)$, can be expressed as follows:

$$c(x, z, t) = \int_{-\infty}^t dt_0 \int_{-\infty}^{\infty} dz_0 \int_{-\infty}^{\infty} dx_0 q(x_0, z_0, t_0) P(x, z, t ; x_0, z_0, t_0), \quad (4.3.1)$$

For a continuous point source, $q(x_0, z_0, t_0) = Q\delta(x_0 - x_s)\delta(z_0 - z_s)$, where Q is the source strength (mass emitted per unit time) and (x_s, z_s) is the location of the source. Eq. (4.3.1), then, simplifies to

$$c(x, z, t) = Q \int_{-\infty}^t dt_0 P(x, z, t; x_s, z_s, t_0). \quad (4.3.2)$$

Displacements in the x and z directions are assumed to be independent, therefore $P(x, z, t) = P(x, t)P(z, t)$. Displacements in the x direction are assumed to be due only to the mean wind velocity, and, therefore, $P(x, t; x_s, t_0) = \delta((x - x_s) - U(t - t_0))$. Using these assumptions and transforming to relative spatial coordinates $\hat{x} = x - x_s$ and $\hat{z} = z - z_s$ and time coordinate $\hat{t} = \frac{\hat{x}}{U}$ (downwind travel time from the source), Eq. (4.3.2) simplifies to

$$c(\hat{x}, \hat{z}) = \frac{Q}{U} P(\hat{z}, \hat{t}). \quad (4.3.3)$$

The Langevin equation models described in Chapter 3 are used to calculate the time evolution of particle velocity, $w(t)$, and position, $z(t)$. Monte Carlo simulations of a sample of N particle trajectories, $\{z_i(t), i = 1, 2, \dots, N\}$, will be used to estimate $P(\hat{z}, \hat{t})$, and, through Eq. (4.3.3), $c(\hat{x}, \hat{z})$.

Mixed-layer scaling parameters (boundary layer depth, h , and convective velocity scale, w_*) are used to scale the numerical simulation results, as done by Willis and Deardorff for their experimental results. Results are presented as functions of the following dimensionless variables: downwind distance $X = \hat{x}w_*/Uh$, velocity $W = w/w_*$, and height $Z = z/h$. Since the mean horizontal wind velocity, U , is assumed to be constant, dimensionless downwind distance X is the same as dimensionless downwind travel time $\hat{t}w_*/h$. The cross-wind-integrated concentration is made dimensionless by scaling it by

the concentration that would be found if material were uniformly distributed in the vertical, $C = cUh/Q$.

4.3.2 Vertical velocity distribution

The observed dimensionless vertical velocity distributions, $P_f(W)$, published by Deardorff and Willis (1985) were analyzed to determine velocity variance and skewness used as input to the Langevin equation models. The $P_f(W)$ curves for various heights published in Deardorff and Willis' Fig. 16 were digitized and used to compute the variance and skewness. The probability of the highest- W ($W \approx 1.95$) point plotted in these curves (the histogram bin at the end of the positive tail of the distribution) included the probability of that bin and all higher W values (as a result, the probability density unrealistically increased with W at the end of the positive- W tail of the distribution plotted in the figure). Therefore, this probability value was lowered by multiplying it by $\frac{1}{4}$. The remainder was distributed uniformly between $W = 2.015$ and $W = 2.535$. Small adjustments were then made to this data to ensure that the mean velocity was zero and the total probability equaled one. However, all of these adjustments to the digitized data did not significantly change the values of the velocity moments calculated. The values calculated were very similar to those calculated by M.F. Hibberd (personal communication, 1997) from these same published curves.

Table 4.3 lists the dimensionless velocity statistics calculated from the Deardorff and Willis (1985) velocity distribution curves. At each dimensionless height, $Z = z/h$, dimensionless values are given for the velocity variance, $\sigma_{w_f}^2 / w_*^2$; velocity skewness S ; probability of negative velocity, \mathbf{P}_- ; probability of positive velocity, \mathbf{P}_+ ; mean negative velocity, \bar{w}_- / w_* ; mean positive velocity, \bar{w}_+ / w_* ; variance of negative velocity, $\sigma_{w_-}^2 / w_*^2$; and variance of positive velocity, $\sigma_{w_+}^2 / w_*^2$.

Table 4.3. Dimensionless velocity statistics versus dimensionless height, calculated from velocity distributions published by Deardorff and Willis (1985) .

$\frac{z}{h}$	$\frac{\sigma_{w_f}^2}{w_*^2}$	S	\mathbf{P}_-	\mathbf{P}_+	$\frac{\overline{w_-}}{w_*}$	$\frac{\overline{w_+}}{w_*}$	$\frac{\sigma_{w_-}^2}{w_*^2}$	$\frac{\sigma_{w_+}^2}{w_*^2}$
0.21	0.315	0.428	0.58	0.42	-0.39	0.53	0.086	0.14
0.40	0.376	0.731	0.62	0.38	-0.39	0.64	0.080	0.20
0.48	0.350	0.798	0.53	0.47	-0.43	0.49	0.064	0.23
0.62	0.397	0.814	0.61	0.39	-0.40	0.63	0.088	0.24
0.79	0.233	1.250	0.53	0.47	-0.34	0.38	0.038	0.18
0.89	0.210	0.640	0.60	0.40	-0.29	0.43	0.064	0.12

Deardorff and Willis also plotted measured values of variance (in their Fig. 4) and third moment of velocity (in their Fig. 15). The variance values are similar but not identical to those calculated from their Fig. 16 and listed in Table 4.3 here. The skewness corresponding to the third moment values from Deardorff and Willis' Fig. 15 are significantly higher than those listed in Table 4.3, even though Deardorff and Willis stated that they were calculated from the same data plotted in their Fig. 16. The original investigator did not recall any possible explanations for these differences (J.W. Deardorff, personal communication, 1997).

The variance and skewness values in Table 4.3 were used in this work. They are consistent with other published values for the CBL (see Luhar *et al.*, 1996, for a review). Velocity variance and skewness values for use in homogeneous Langevin equation model simulations were obtained by averaging the values in Table 4.3. The resulting average values of $\sigma_{w_f}^2 / w_*^2 = 0.31$ and $S = \overline{w_f^3} / \sigma_{w_f}^3 = 0.78$ were used in this work. The sensitivity of the dispersion simulation results to the choice of values for these parameters will be discussed later in this chapter.

Velocity distributions from simulations with both Langevin models using these average variance and skewness values were compared to the measured velocity distributions published by Deardorff and Willis (1985). Figs. 4.15 and 4.16 show the velocity distribution resulting from the simulations with the nonlinear-Gaussian model and linear-skewed model, respectively, along with the measured distributions published by Deardorff and Willis for three different heights. These calculated distributions are averaged over a period of 5τ from simulations without boundaries using $\Delta t = 0.05\tau$ (for the nonlinear-Gaussian, this time step results in small departures from the analytic velocity distribution, as noted in Sec. 4.1 above). Compared to the measured velocity distributions, the calculated distributions in Figs. 4.15 and 4.16 both appear to be reasonable representations.

4.3.3 Lagrangian correlation time

Lagrangian velocity statistics and correlation time scale, τ , are typically not measured. This is true of the Willis and Deardorff experiments. Estimates of τ are typically made with indirect methods, in which best fit values are determined by comparing model predictions to experimental dispersion measurements. The relationship $\tau = 2\sigma_w^2/C_0\varepsilon$, presented in Chapter 3, is often used to estimate τ along with measurements and/or parameterizations of σ_w^2 and ε . However, even if σ_w^2 and ε are known there is uncertainty in the value of C_0 .

Estimates of the value of C_0 range from 2 to 10, with some of the latest near 3 (Du *et al.*, 1995). Sawford (1993) proposed that part of this variation in estimates of C_0 is due to the fact that C_0 has been estimated indirectly using data from experiments (for example, the Willis and Deardorff experiments) in which the Reynolds number was not large enough to reach the large Reynolds number limit, for which C_0 is truly a universal constant.

Previous Langevin equation modeling studies using the Willis and Deardorff experiments typically used $C_0 = 2$ (e.g., Luhar and Britter, 1989; Weil, 1989).

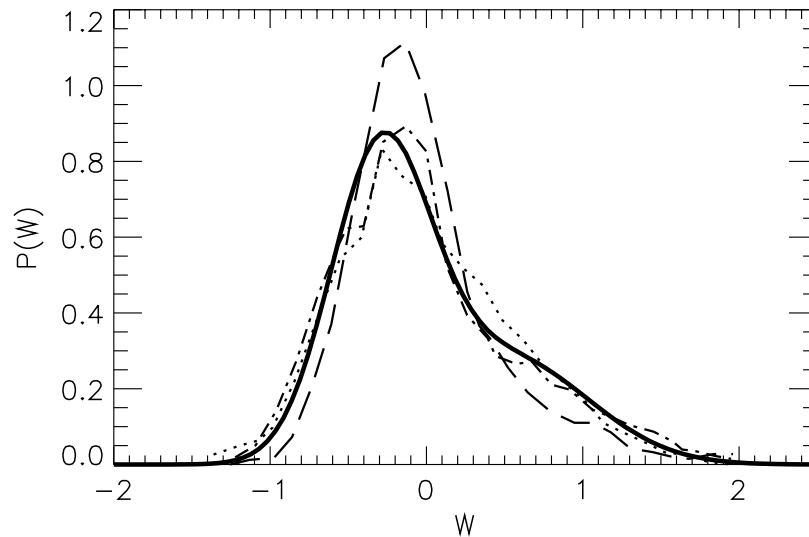


Fig. 4.15. Dimensionless velocity distribution from the *nonlinear-Gaussian* model simulation (solid line) along with the velocity distributions observed by Deardorff and Willis (1985) at $Z=0.21$ (dotted line), $Z=0.48$ (dash-dot line), and $Z=0.79$ (dashed line).

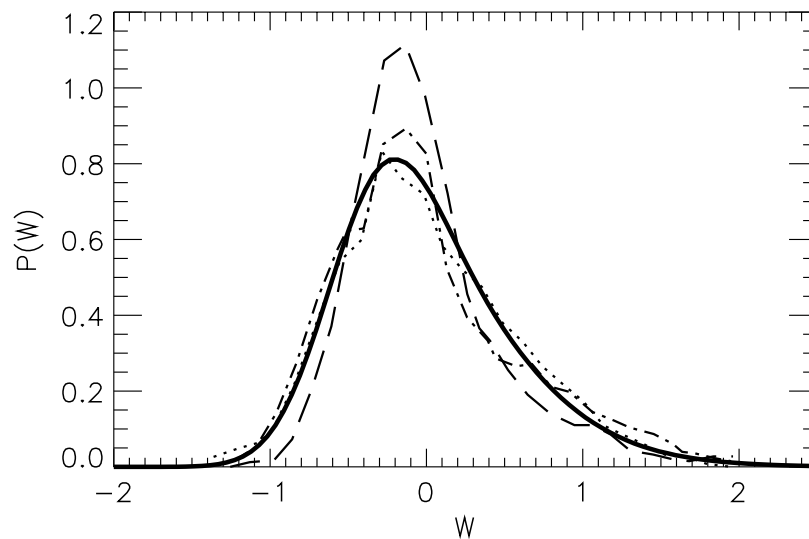


Fig. 4.16. Same as Fig. 4.15, but from *linear-skewed* model simulation.

The height averaged value of the turbulent kinetic energy dissipation rate data published by Deardorff and Willis (1985) is approximately $\varepsilon = 0.4(w_*^3/h)$. Using the average value of $\sigma_w^2 = 0.31w_*^2$ determined above from the same study and $C_0 = 2$, this corresponds to a value of $\tau = 0.8(h/w_*)$. This value was used in this work. The sensitivity of the dispersion simulations to the value of τ will be discussed below.

4.3.4 Cross-wind-integrated concentration

Simulations of dispersion for the Willis and Deardorff experiments were made with both Langevin equation models. Simulations were performed with each model using each of the three reflection methods (the same reflection method was applied at both the top and bottom boundaries, although they could be different, e.g., negatively correlated incident and reflected speed at the bottom, positively correlated at the top). A time step of $\Delta t = 0.05\tau$; 10^5 particles (sensitivity tests with 5×10^5 particles did not result in noticeable differences in the concentration distribution) and 20 vertical particle-position sampling bins were used in each simulation.

For comparison with the numerical simulation results below, Fig. 4.17 shows contours of the dimensionless cross-wind-integrated concentration, $C(X,Z)$, versus dimensionless height, Z , and downwind distance, X , determined from Willis and Deardorff's (1976b, 1978 and 1981) laboratory experiment observations for three dimensionless source heights: (a) $Z_s = 0.067$, (b) $Z_s = 0.24$, and (c) $Z_s = 0.49$.

Contours of cross-wind-integrated concentration $C(X,Z)$ calculated by the nonlinear-Gaussian model for all three source heights using the three reflection methods are presented in Fig. 4.18 (reflection method I), Fig. 4.19 (method II) and Fig. 4.20 (method III). Contours of $C(X,Z)$ calculated using the linear-skewed model are shown in Fig. 4.21 (reflection method I), Fig. 4.22 (method II) and Fig. 4.23 (method III).

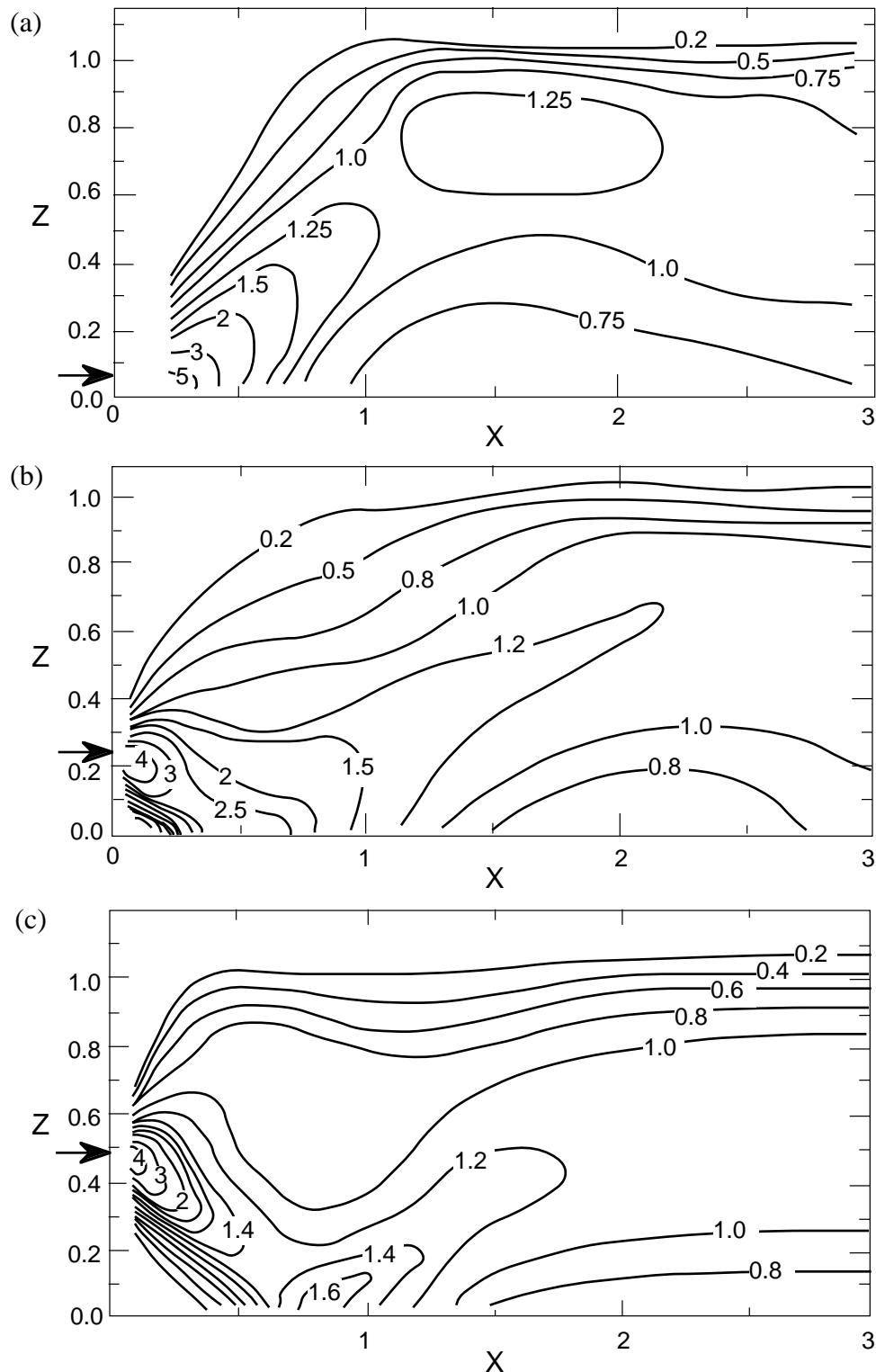


Fig. 4.17. Smoothed contours of dimensionless cross-wind-integrated concentration, $C(X, Z)$, versus dimensionless height, Z , and downwind distance, X , from Willis & Deardorff (1976b, 1978, 1981) laboratory experiments for dimensionless source heights of (a) $Z_s=0.067$ (top figure), (b) $Z_s=0.24$ (middle), and (c) $Z_s=0.49$ (bottom). Arrows indicate source location.

For both Langevin models, the choice of reflection boundary condition has the largest effect on the simulations for the source height closest to the boundary ($Z_s=0.067$), as might be expected. For $Z_s=0.067$, the simulations with reflection method II (shown in Fig. 4.19 for the nonlinear-Gaussian model, and in Fig. 4.22 for the linear-skewed model) produce initial ($X < 1$) concentrations patterns that are in noticeably better agreement with the observed patterns (shown in Fig. 4.17) than the simulations with reflection method I. For all source heights, reflection method II (negatively-correlated-speed reflection) appears to simulate the near-surface concentration more accurately than the other two reflection methods. The results of simulations with reflection method III are intermediate between those of reflection methods I and II.

For both Langevin equation models, reflection method II is better able to simulate the observed behavior of the maximum concentration line than the other two reflection methods. The observed height of the maximum concentration remains near the surface for a time after it first encounters the surface, and, then, increases in height. For $Z_s = 0.067$ and 0.24, the experimentally observed maximum concentration line stays near the surface for a distance, ΔX , of approximately 0.3 to 0.4 after it encounters the surface, and then increases in height (see observed $C(X,Z)$ contours in Figs. 4.17a and 4.17b). For $Z_s = 0.49$, this distance is approximately $\Delta X = 0.2$ (see Fig. 4.17c) and is associated with a secondary maximum in the observed near-surface concentration near $X = 0.8$, after which the height of maximum concentration increases with X . These observed features are simulated best by reflection method II for both Langevin models (see Figs. 4.19 and 4.22). The linear-skewed model using reflection method II is best able to simulate the increasing height of the maximum concentration with downwind distance after it reaches the surface (Figs. 4.22a, b & c).

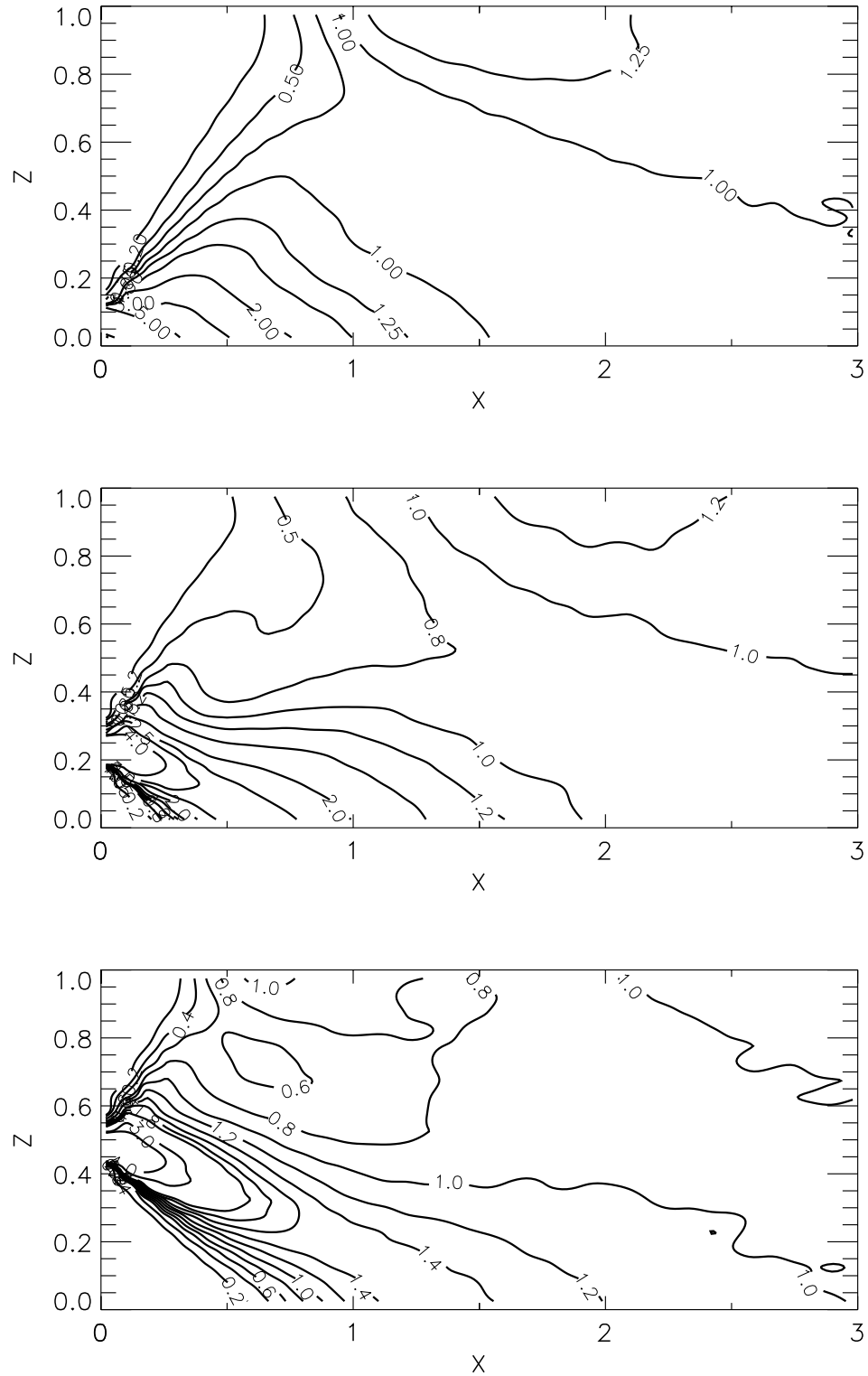


Fig. 4.18. Contours of dimensionless cross-wind-integrated concentration, $C(X, Z)$, versus dimensionless height, Z , and downwind distance, X , from *nonlinear Gaussian Langevin equation model, reflection method I* simulations of the Willis & Deardorff experiments for dimensionless source heights (a) $Z_s=0.067$ (top figure), (b) $Z_s=0.24$ (middle), and (c) $Z_s=0.49$ (bottom).

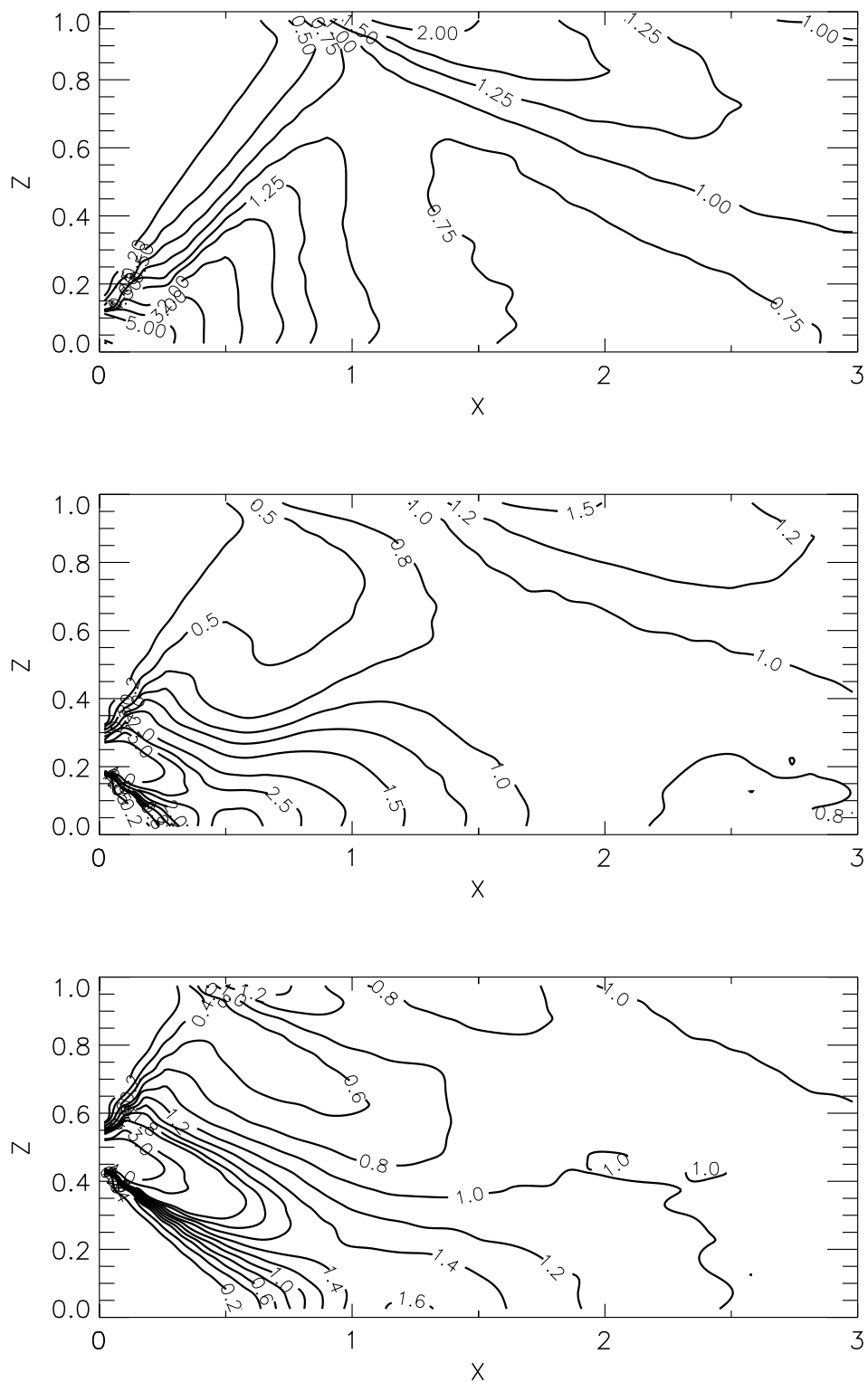


Fig. 4.19. Same as Fig. 4.18, except from *nonlinear-Gaussian* Langevin equation model, *reflection method II* simulations.

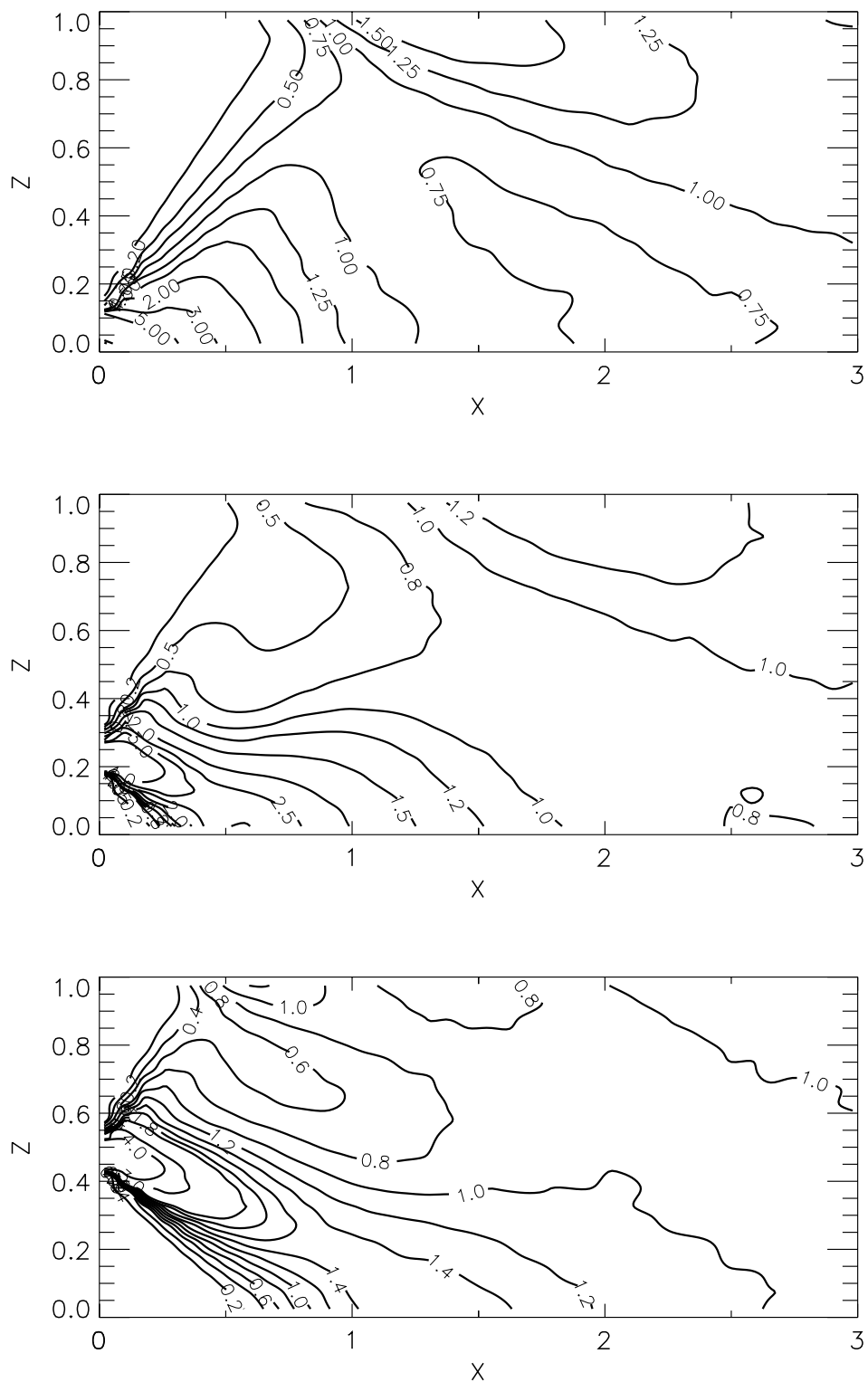


Fig. 4.20. Same as Fig. 4.18, except from *nonlinear-Gaussian* Langevin equation model, *reflection method III* simulations.

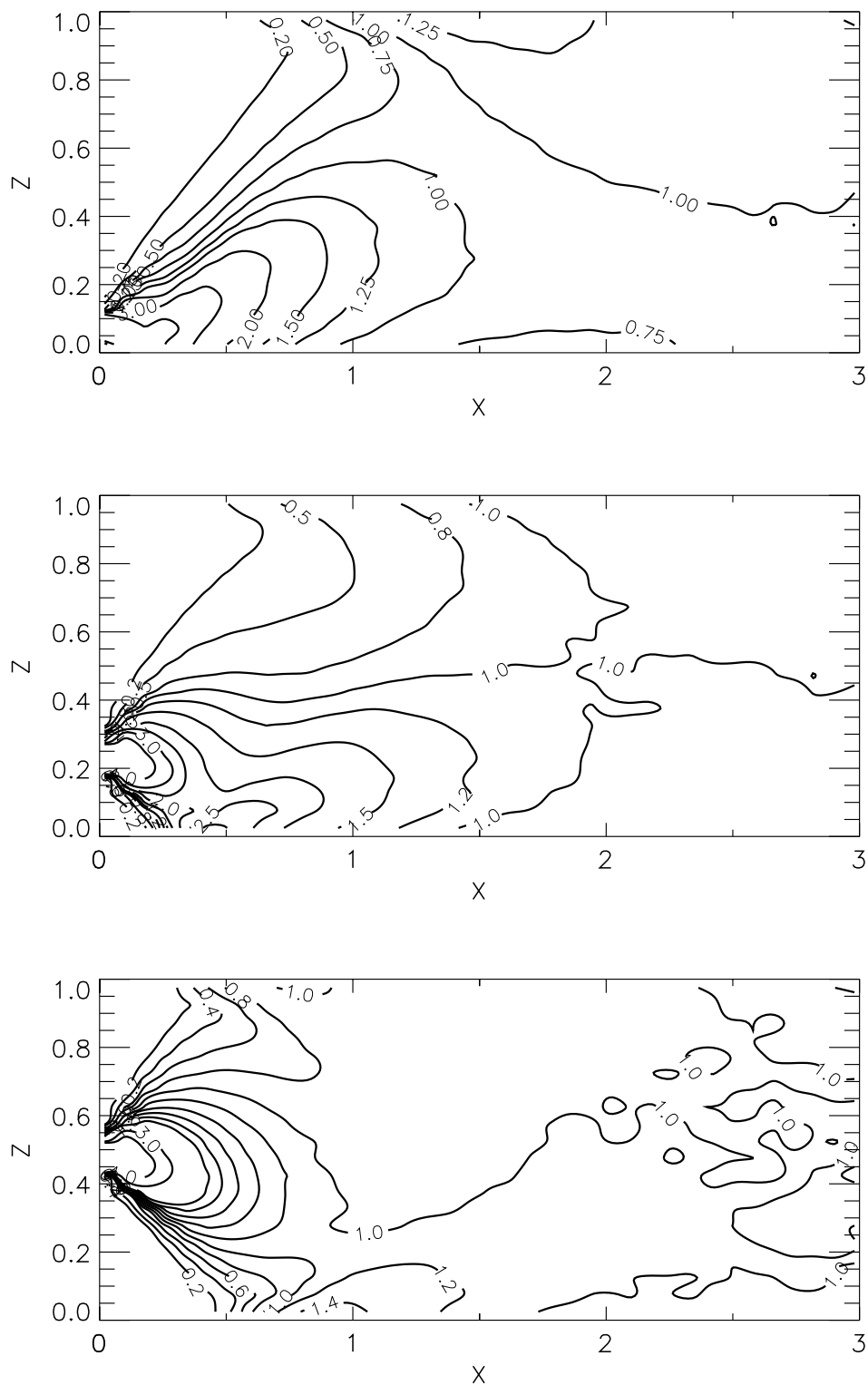


Fig. 4.22. Same as Fig. 4.18, except from *linear skewed* Langevin equation model, *reflection method II* simulations.

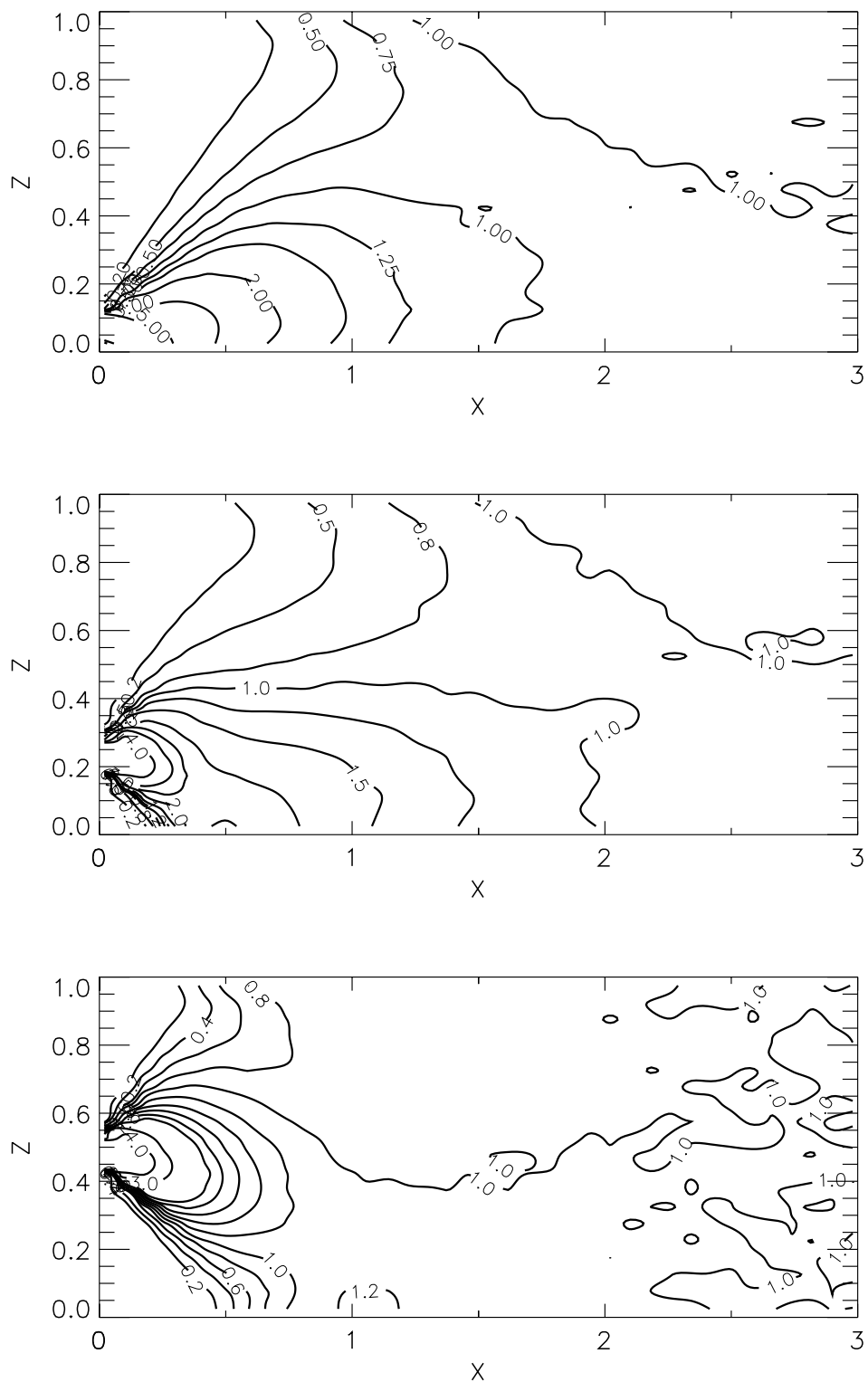


Fig. 4.23. Same as Fig. 4.18, except from *linear-skewed* Langevin equation model, *reflection method III* simulations.

The calculated concentrations shown in Figs. 4.18-23 approach a uniform distribution, $C = 1$, for large X . This is the correct behavior when fixed, impermeable boundaries are used at both the top and the bottom of the boundary layer, as in these calculations. In effect, this results in concentration changing discontinuously at the boundary layer height ($Z = 1$). In the CBL, concentrations decrease smoothly with height over the entrainment layer (roughly $0.8 < Z < 1.2$) as seen in Fig. 4.17. Correspondingly, while the calculated concentrations approach $C = 1$ at $Z = 1$ for large X , the observed concentrations in the Willis and Deardorff experiments approach approximately $C = 0.5$ at $Z = 1$. Near the top of the boundary layer, the nonlinear-Gaussian model results (Figs. 4.18-20) show overly high concentrations for all three reflection methods. Possible reasons for these overly high concentrations will be discussed in Section 4.3.6. Overly high concentrations are not present at the top of the boundary layer in the linear-skewed model results (Figs. 4.21-23).

Dimensionless near-surface concentration versus downwind distance, $C(X,0)$, from simulations using the nonlinear-Gaussian model and the three reflection methods is compared to observations from the Willis and Deardorff experiments in Fig. 4.24. The mean square error of this nonlinear-Gaussian model simulated near-surface concentration is plotted in Fig. 4.25 for each reflection method and each source height. The mean square error (MSE) is defined here as $MSE = \frac{1}{n_{obs}} \sum_{i=1}^{n_{obs}} (p_i - o_i)^2$, where o_i is a observed value, p_i is the model predicted value interpolated to the point of the observation, and n_{obs} is the number of observations. The standard error of the MSE (a measure of the uncertainty in the estimate of the MSE) is shown as error bars in Fig. 4.25. A similar comparison of the linear-skewed model simulation results to observations is shown in Fig. 4.26. The MSE of these linear-skewed model results is plotted in Fig. 4.27.

For both models, the choice of reflection method can noticeably affect near-surface concentration. The best overall results are obtained using reflection method II for both models. However, changing the reflection method results in more significant changes in the linear-skewed model results (Fig. 4.27) than in the nonlinear-Gaussian model results (Fig. 4.25). The linear-skewed model and reflection method II results (shown in Fig. 4.26, dotted line) show the best overall agreement with the experimental observations for near-surface concentration. This can be seen in the lower mean square error values (shown in Fig. 4.27) for the linear-skewed/reflection-method-II (LS/II) simulation results. For $Z_s = 0.49$, the linear-skewed model predicts the location of the peak concentration better than the nonlinear-Gaussian model, and also better than previous inhomogeneous Langevin equation model simulations summarized by Du *et al.* (1994). For both Langevin models, reflection method I results in the poorest agreement overall.

Dimensionless mean height of the concentration distribution, \bar{Z} , versus downwind distance from simulations using the nonlinear-Gaussian model and the three reflection methods is compared to observations from the Willis and Deardorff experiments in Fig. 4.28. The mean square error of the nonlinear-Gaussian model simulated \bar{Z} is plotted in Fig. 4.29 for each reflection method and each source height. Fig. 4.30 shows the same comparison using the linear-skewed model. The *MSE* of these linear-skewed model results are plotted in Fig. 4.31. The choice of model and reflection method has the largest effect when the release is closest to the lower boundary, $Z_s = 0.067$. For $Z_s = 0.067$, reflection method II significantly improves the results compared to reflection method I for both models. The nonlinear-Gaussian model results are closer to the observations than the linear-skewed model results for $Z_s = 0.067$. For $Z_s = 0.24$, both models perform well, with the choice of reflection method causing only small differences. For $Z_s = 0.49$, the nonlinear-Gaussian model performs better and the choice of reflection method has little effect.

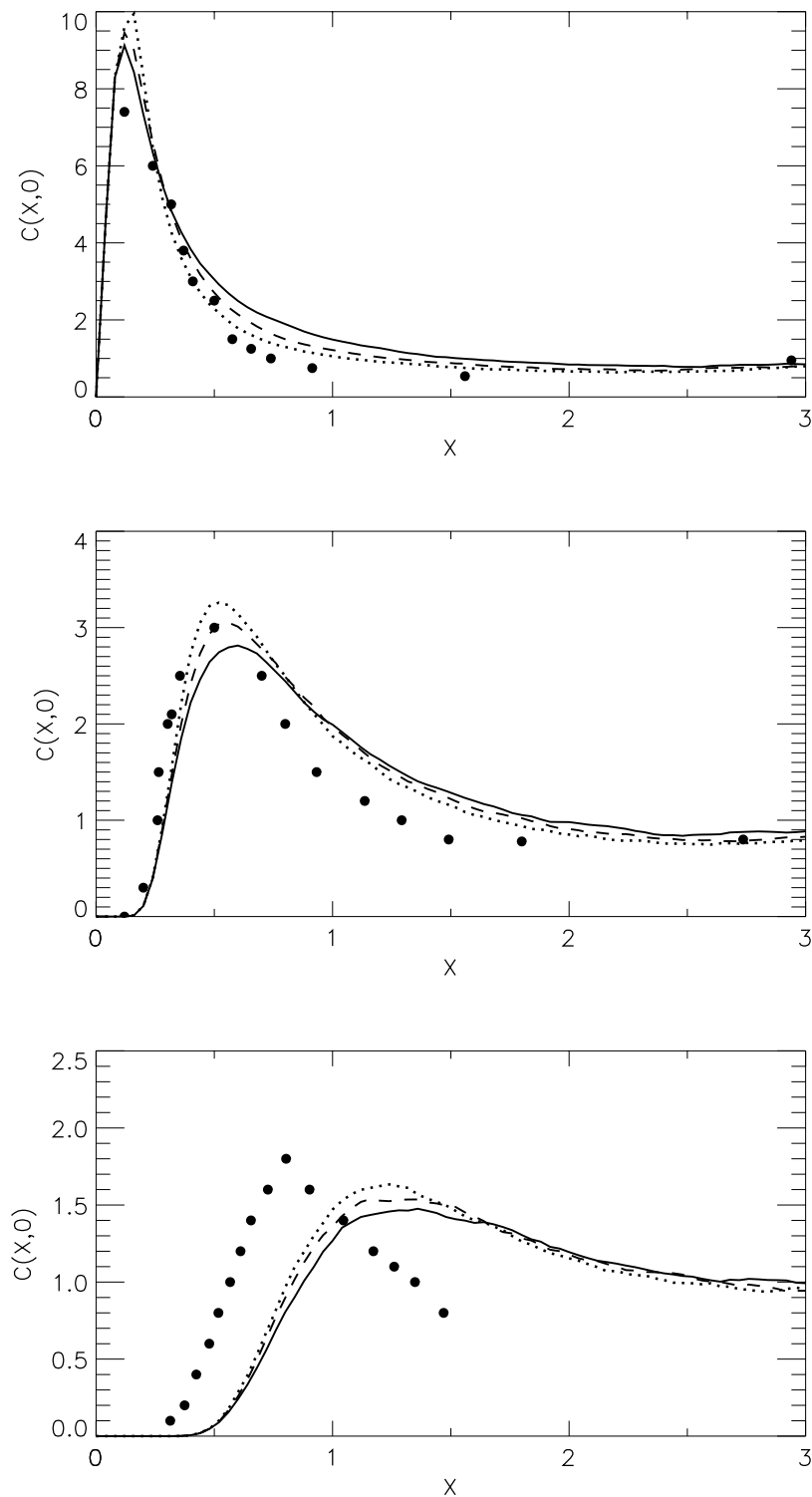
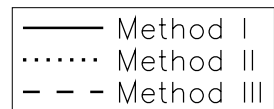


Fig. 4.24. Calculations of dimensionless near-ground concentration for dimensionless source height of (a) $Z_s = 0.067$ (top figure), (b) $Z_s = 0.24$ (middle), and (c) $Z_s = 0.49$ (bottom) using the nonlinear-Gaussian Langevin equation model and the three reflection methods: method I (solid line), method II (dotted line), method III (dashed line). Circles are data from Willis & Deardorff experiments.



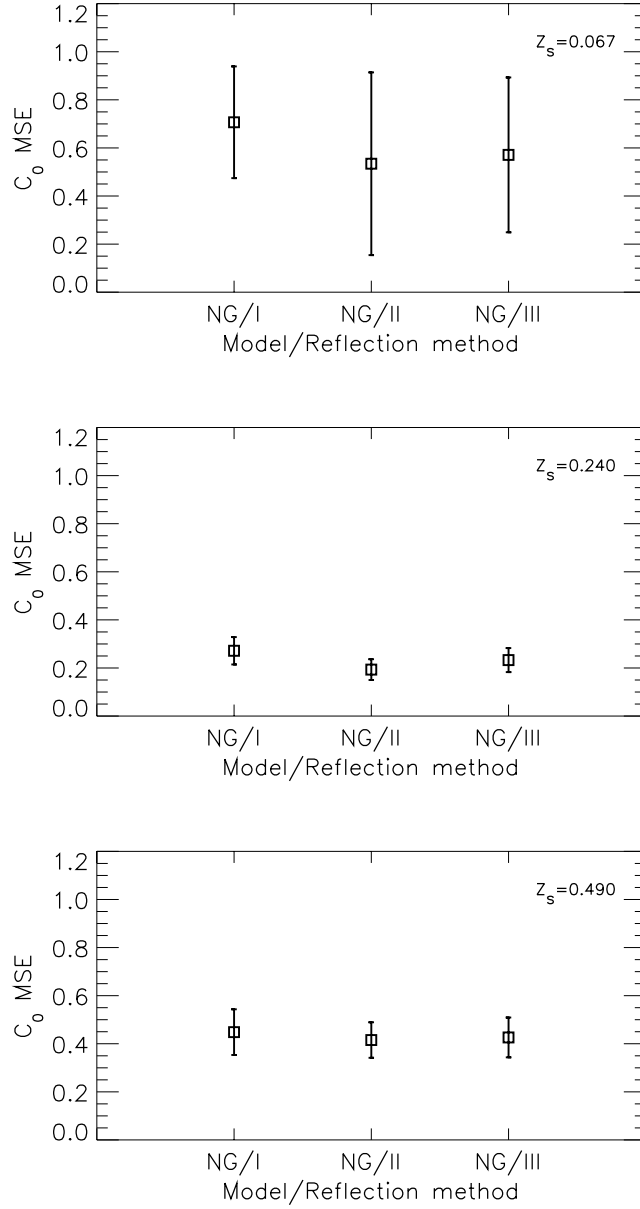


Fig. 4.25. Mean square error (MSE) of dimensionless near-ground concentration predicted by the *nonlinear-Gaussian* (NG) Langevin equation model using reflection methods I, II, and III, estimated using observations from the Willis & Deardorff experiments for dimensionless source height of (a) $Z_s = 0.067$ (top figure), (b) $Z_s = 0.24$ (middle), and (c) $Z_s = 0.49$ (bottom). Error bars indicate plus and minus standard error.

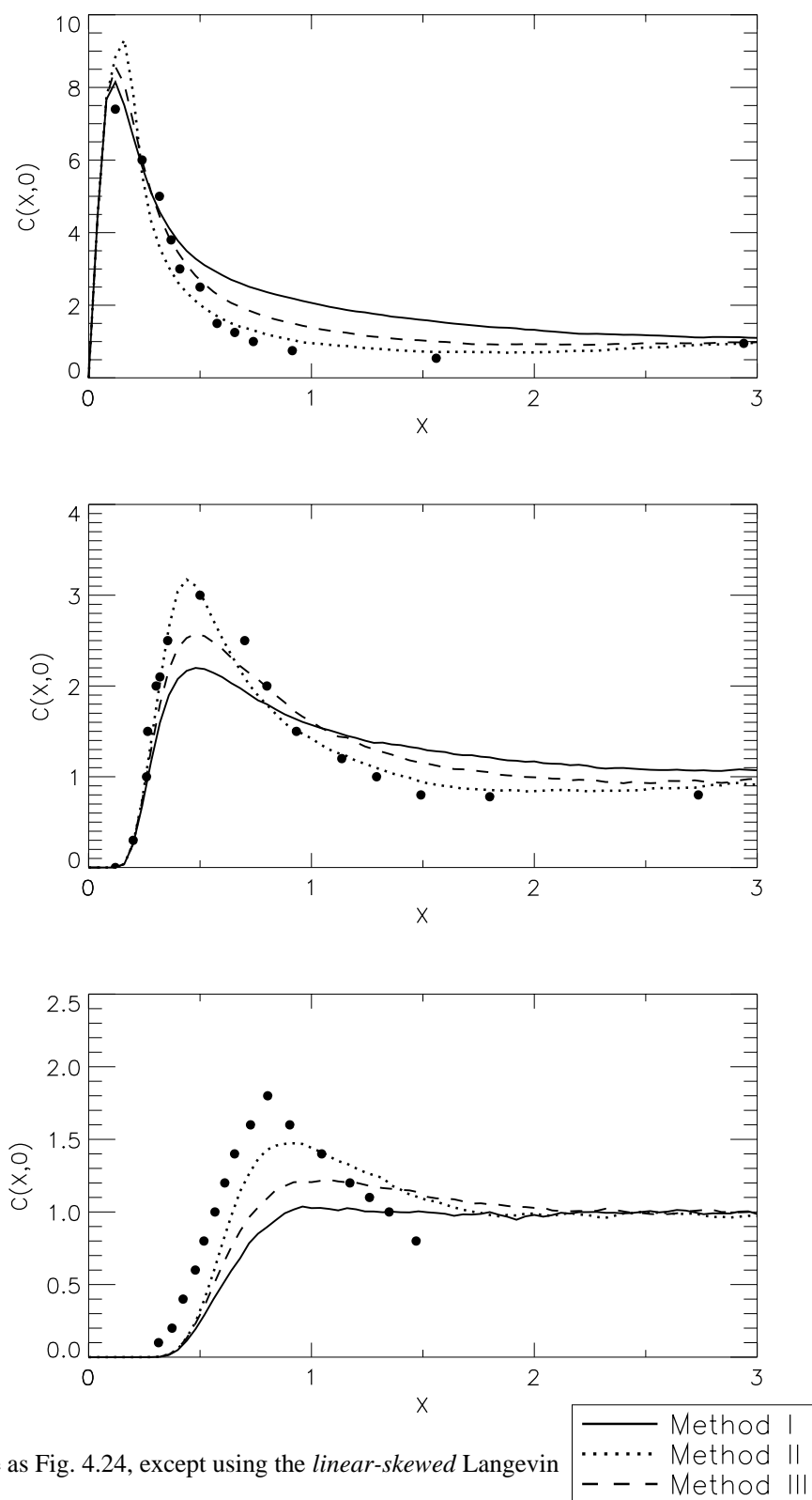


Fig. 4.26. Same as Fig. 4.24, except using the *linear-skewed* Langevin equation model.

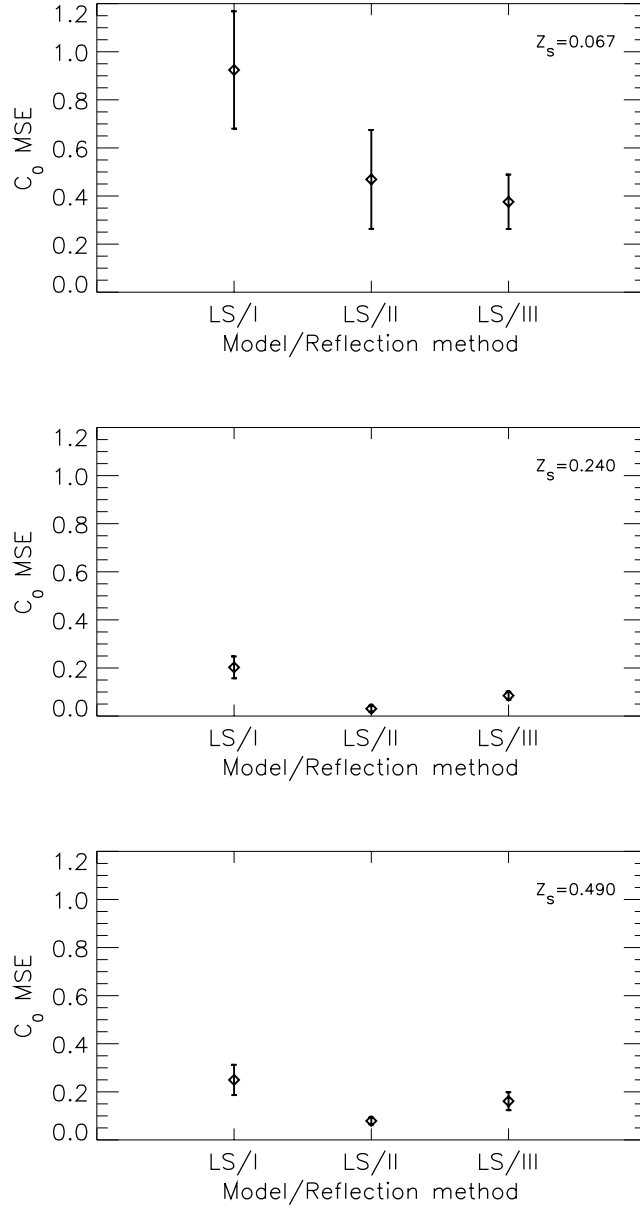


Fig. 4.27. Mean square error (MSE) of dimensionless near-ground concentration predicted by the *linear-skewed* (LS) Langevin equation model using reflection methods I, II, and III, estimated using observations from the Willis & Deardorff experiments for dimensionless source height of (a) $Z_s = 0.067$ (top figure), (b) $Z_s = 0.24$ (middle), and (c) $Z_s = 0.49$ (bottom). Error bars indicate plus and minus standard error.

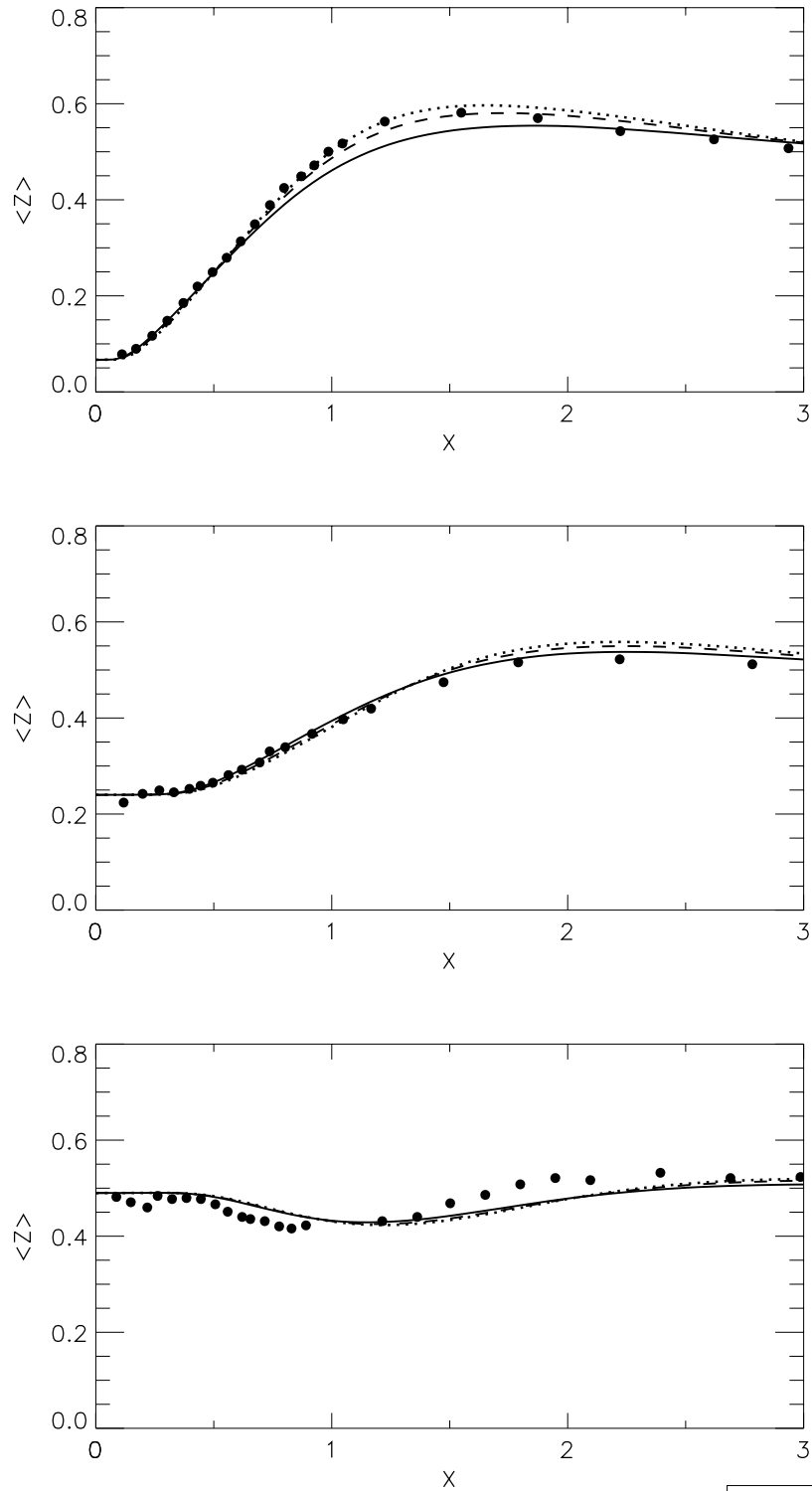


Fig. 4.28. Calculations of dimensionless mean height of concentration distribution for dimensionless source height of (a) $Z_s = 0.067$ (top figure), (b) $Z_s = 0.24$ (middle), and (c) $Z_s = 0.49$ (bottom) using the *nonlinear-Gaussian* Langevin equation model and the three reflection methods: method I (solid line), method II (dotted line), method III (dashed line). Circles are data from Willis & Deardorff water tank experiments.



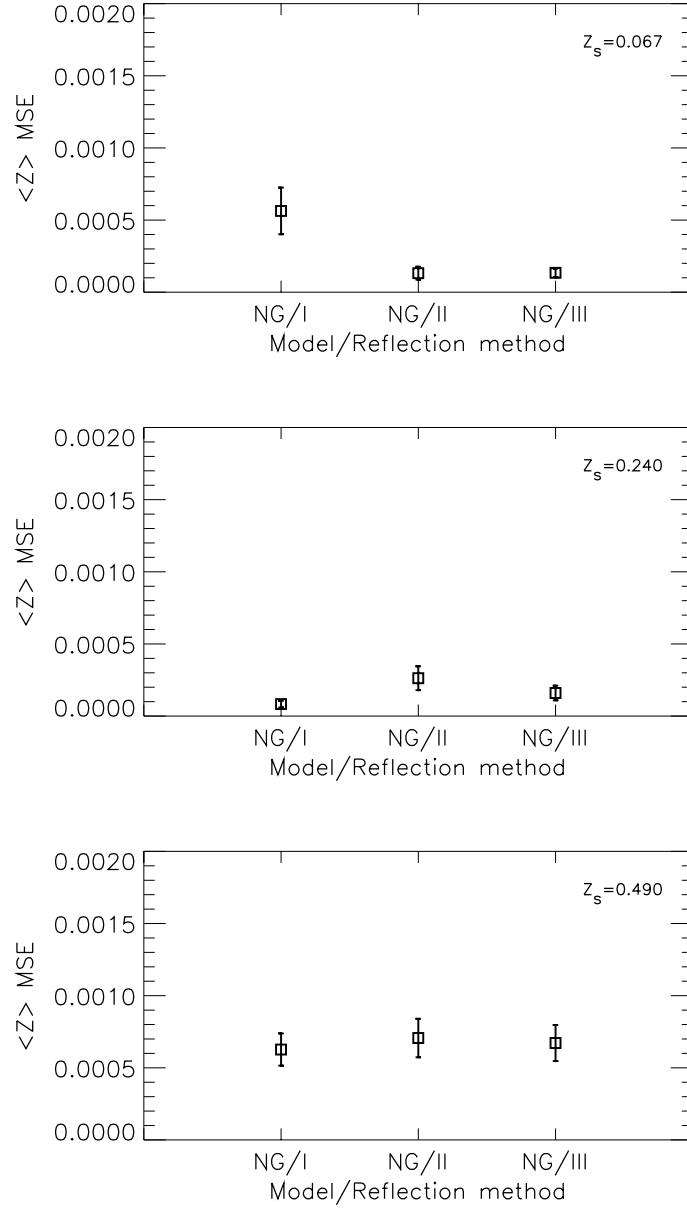


Fig. 4.29. Mean square error (MSE) of dimensionless mean height of concentration distribution predicted by the *nonlinear-Gaussian* (NG) Langevin equation model using reflection methods I, II, and III, estimated using observations from the Willis & Deardorff experiments for dimensionless source height of (a) $Z_s = 0.067$ (top figure), (b) $Z_s = 0.24$ (middle), and (c) $Z_s = 0.49$ (bottom). Error bars indicate plus and minus standard error.

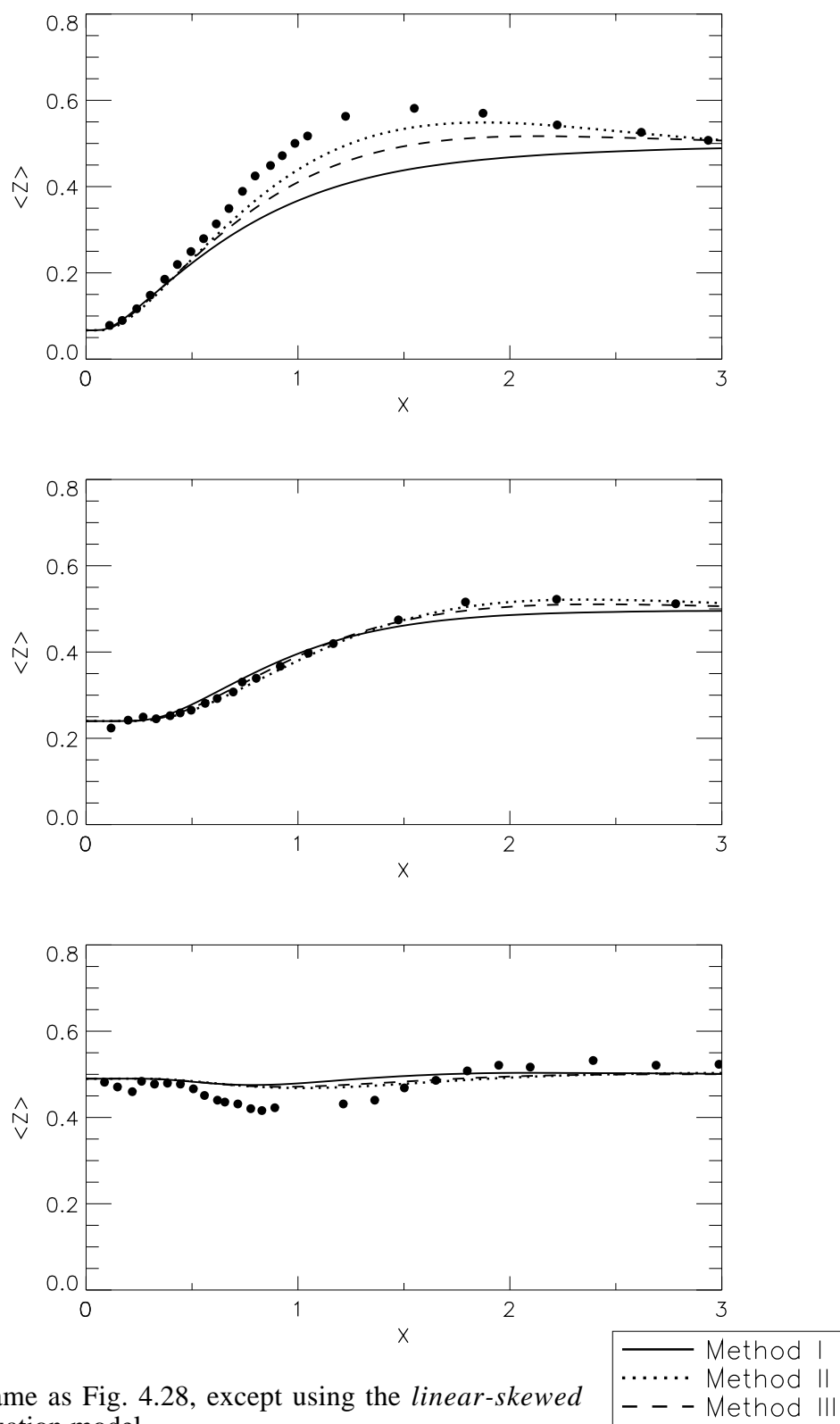


Fig. 4.30. Same as Fig. 4.28, except using the *linear-skewed* Langevin equation model.

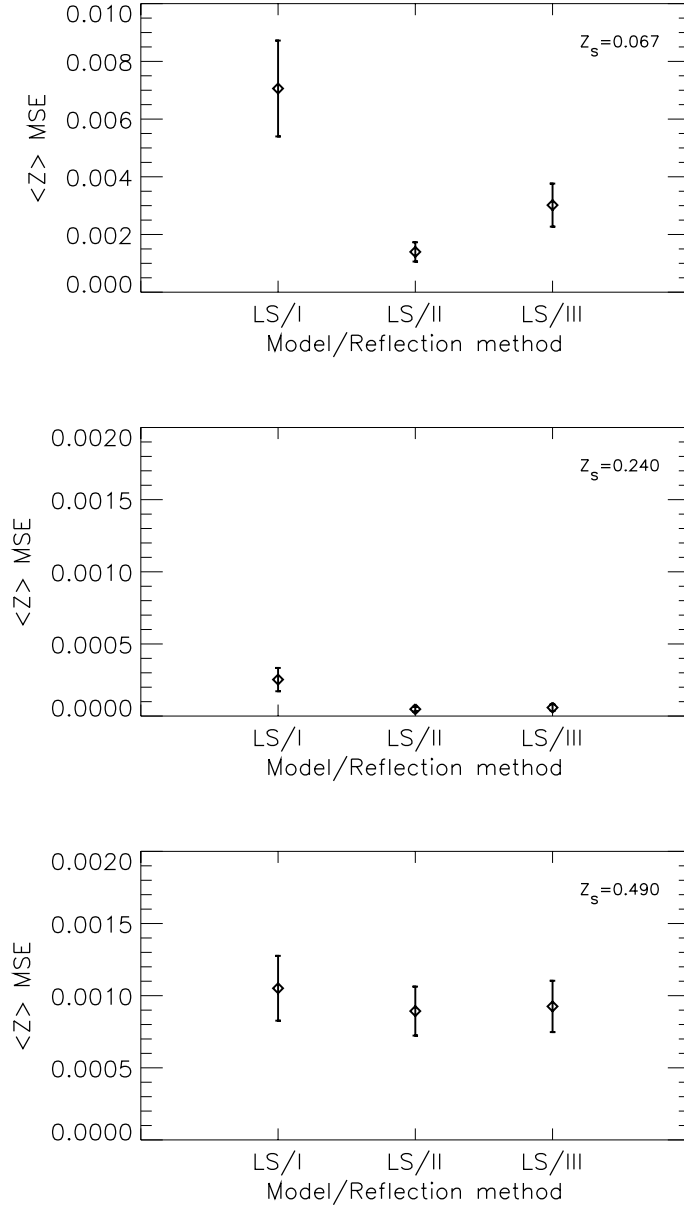


Fig. 4.31. Mean square error (MSE) of dimensionless mean height of concentration distribution predicted by the *linear-skewed* (LS) Langevin equation model using reflection methods I, II, and III, estimated using observations from the Willis & Deardorff experiments for dimensionless source height of (a) $Z_s = 0.067$ (top figure), (b) $Z_s = 0.24$ (middle), and (c) $Z_s = 0.49$ (bottom). Error bars indicate plus and minus standard error.

The dimensionless standard deviation (about the source height) of the vertical distribution of material, $\sigma_z \equiv \overline{(Z - Z_s)^2}^{1/2}$, versus downwind distance from simulations using the nonlinear-Gaussian model and the three reflection methods is compared to observations from the Willis and Deardorff experiments in Fig. 4.32. The mean square error of the nonlinear-Gaussian model simulated σ_z is plotted in Fig. 4.33 for each reflection method and each source height. Fig. 4.34 shows a comparison of the linear-skewed model results and observations. The *MSE* of these linear-skewed model results are plotted in Fig. 4.35. For the $Z_s = 0.067$ case, the nonlinear-Gaussian model results are in better agreement with observations, with the choice of reflection method causing small differences. Reflection method II significantly improves the performance of the linear-skewed model for the $Z_s = 0.067$ case. For $Z_s = 0.24$, the linear-skewed model results are more accurate. Both the standard deviation and the mean height of the concentration distribution are, naturally, not affected as strongly by the choice of boundary condition in the two cases where the sources are farther from the boundaries, $Z_s = 0.24$ and 0.49 .

Table 4.4 presents the mean square error and mean fractional error of the predictions of \bar{z}/h , σ_z/h , and $C(X,0)$ from simulations with nonlinear-Gaussian (N-G) and linear-skewed (L-S) Langevin equation model using reflection methods I, II, and III. The mean square error, *MSE*, was defined and discussed above. The mean fractional error, *MFE*, is defined here as $MFE = \frac{1}{n_{obs}} \sum_{i=1}^{n_{obs}} \frac{(p_i - o_i)}{o_i}$, and is a measure of the bias of the predictions.

Table 4.4 also presents the standard error (a measure of the uncertainty in the estimated mean value) of the *MSE* and *MFE* for each simulation. Considering all results for all the experiments, there is no systematic bias in the predictions. The *MFE* values do indicate that there is a tendency for observed $C(X,0)$ to be over predicted for $Z_s = 0.067$, and under predicted for $Z_s = 0.49$. For the nonlinear-Gaussian model using reflection method II, the observed near-surface concentration is over predicted by an average of 15% (*MFE*

= 0.1476) for $Z_s = 0.067$, under predicted by 0.5% ($MFE = -0.00508$) for $Z_s = 0.24$, and under predicted by 32% for $Z_s = 0.49$. For the linear-skewed model using reflection method II, the observed near-surface concentration is over predicted by an average of 5% for $Z_s = 0.067$, under predicted by 1% for $Z_s = 0.24$, and under predicted by 27% for $Z_s = 0.49$.

In summary, both Langevin equation models can simulate the observed concentration distributions reasonably well. For both Langevin equation models, simulations with reflection method II (negatively correlated incident and reflected speeds) result in the best agreement with the observed concentration distributions. This improved agreement is most notable for the experiment in which the source is closest to the boundary. When reflection method II is used, neither Langevin equation model's results are significantly better (compared to observations) than the other. The nonlinear-Gaussian model simulations predict the mean height and standard deviation of the vertical concentration distribution better than the linear-skewed model simulations for two out of the three experiments. However, the linear-skewed model simulations predict the near-surface concentration better than the nonlinear-Gaussian model simulations for most of the observations. Possible reasons for the differences between the results of simulations using the two models and the three reflection methods will be discussed in Section 4.3.6.

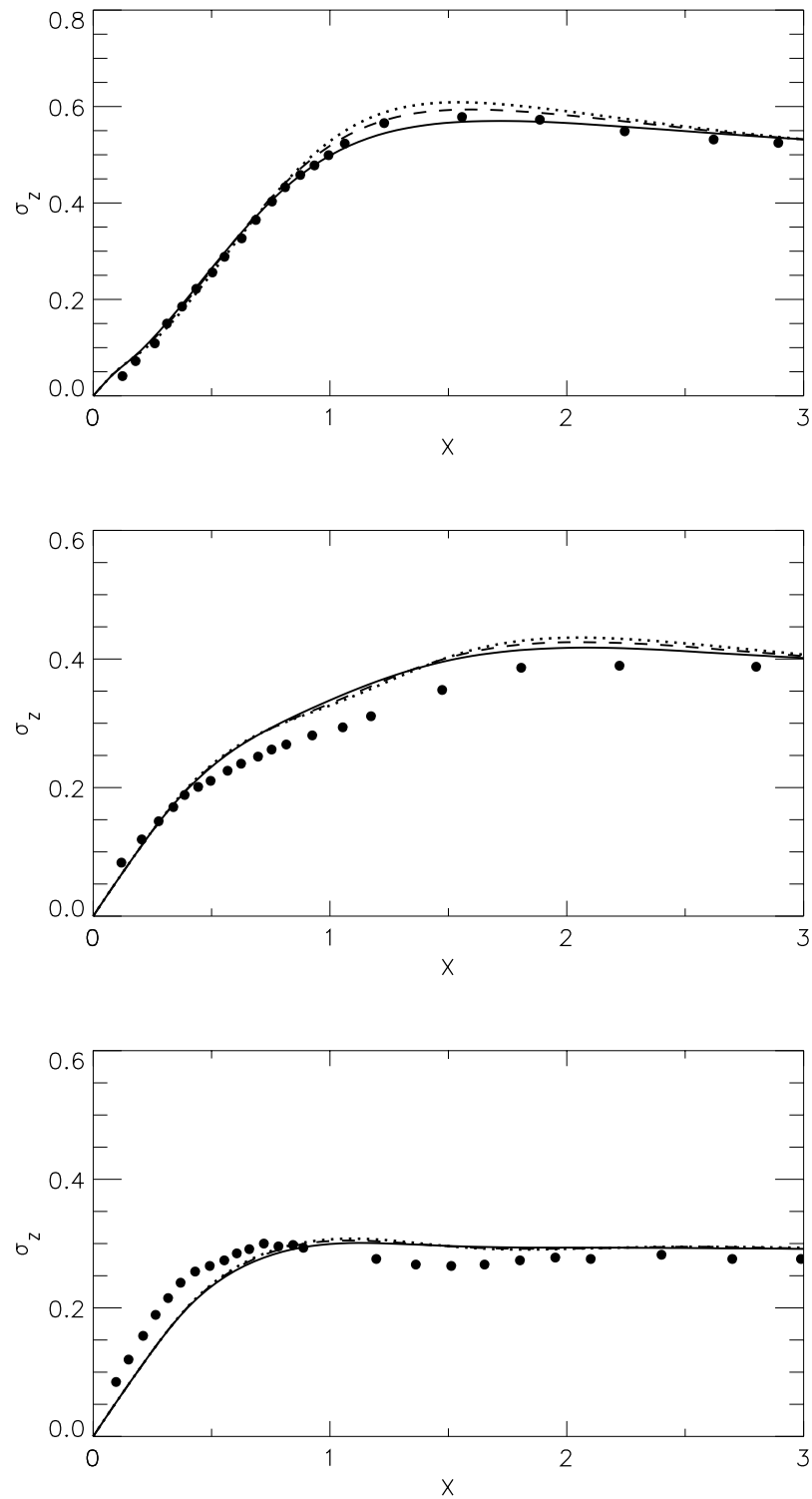


Fig. 4.32. Calculations of dimensionless standard deviation of concentration distribution for dimensionless source height Z_s of (a) 0.067, (b) 0.24, and (c) 0.49 using the *nonlinear-Gaussian* Langevin equation model and the three reflection methods: method I (solid line), method II (dotted line), method III (dashed line). Circles are data from Willis & Deardorff water tank experiments.

— Method I
 Method II
 --- Method III

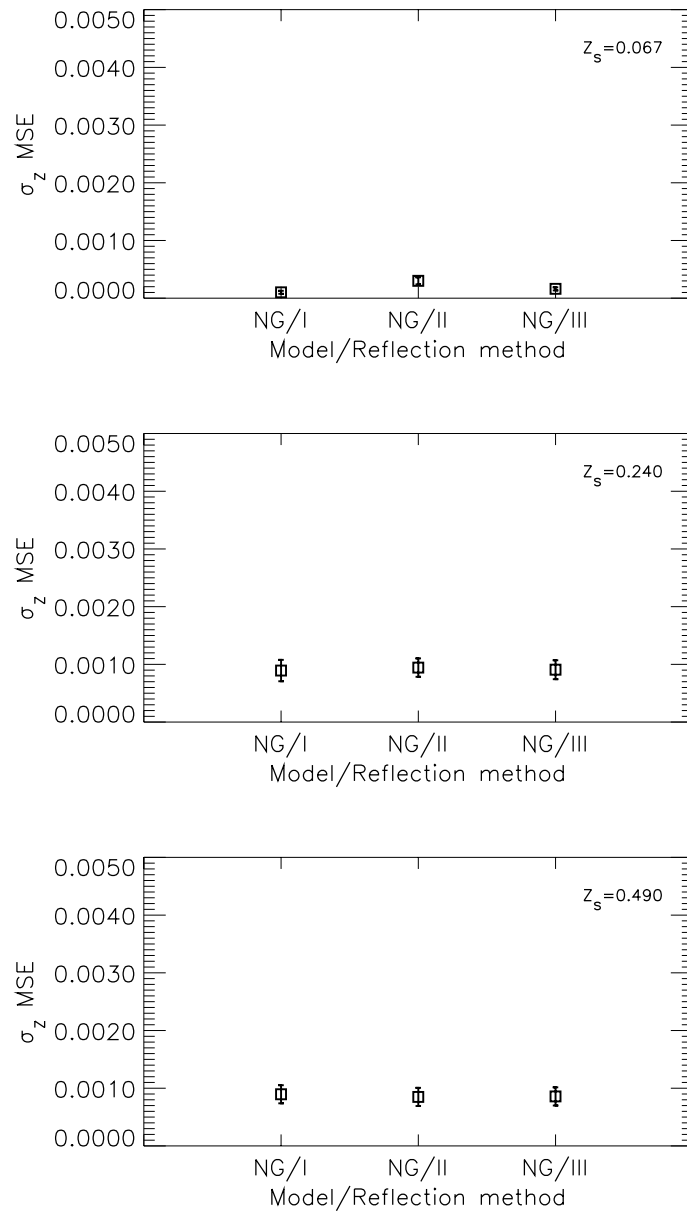


Fig. 4.33. Mean square error (MSE) of dimensionless standard deviation of concentration distribution predicted by the nonlinear-Gaussian (NG) Langevin equation model using reflection methods I, II, and III, estimated using observations from the Willis & Deardorff experiments for dimensionless source height of (a) $Z_s = 0.067$ (top figure), (b) $Z_s = 0.24$ (middle), and (c) $Z_s = 0.49$ (bottom). Error bars indicate plus and minus standard error.

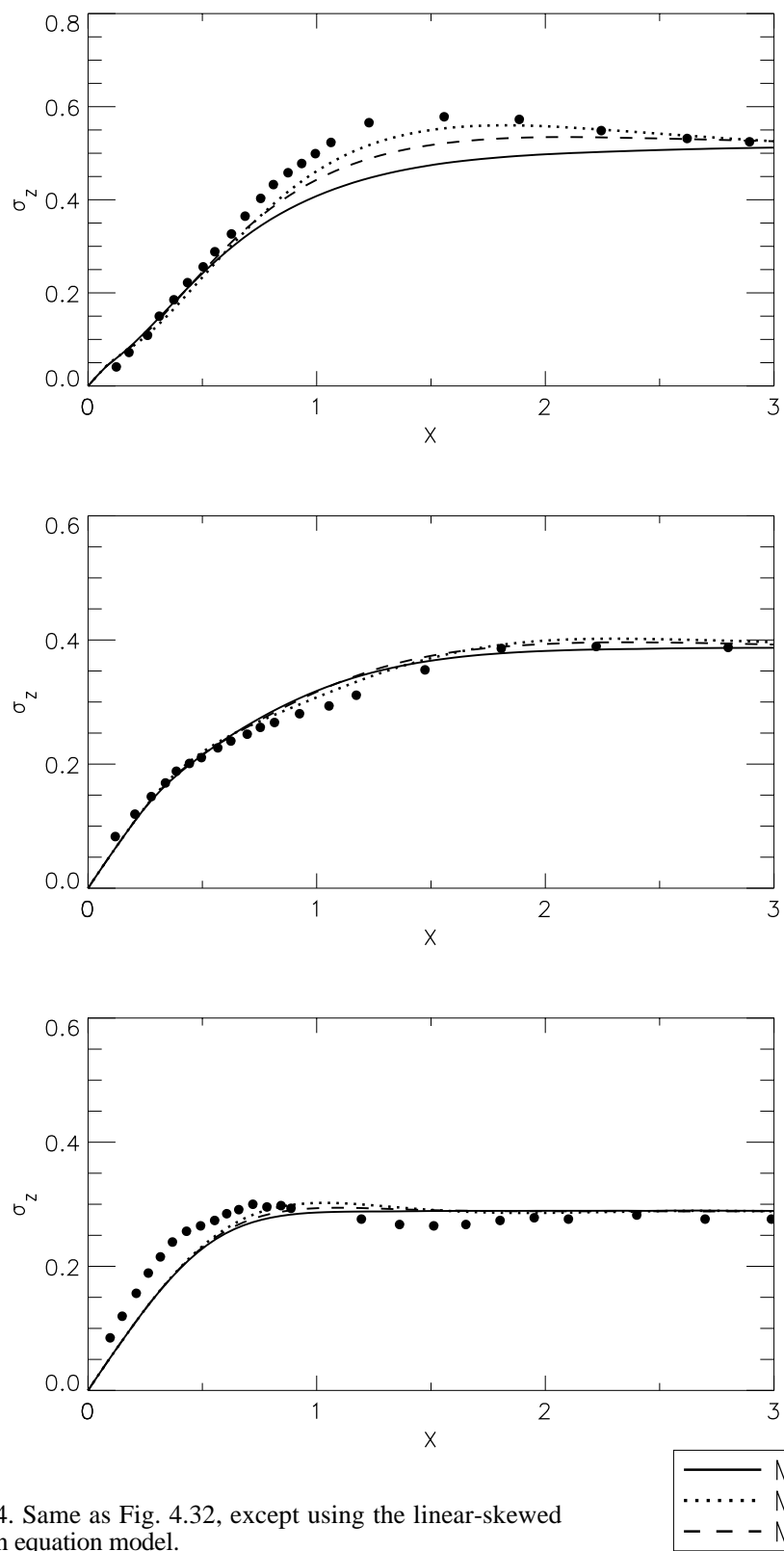


Fig. 4.34. Same as Fig. 4.32, except using the linear-skewed Langevin equation model.

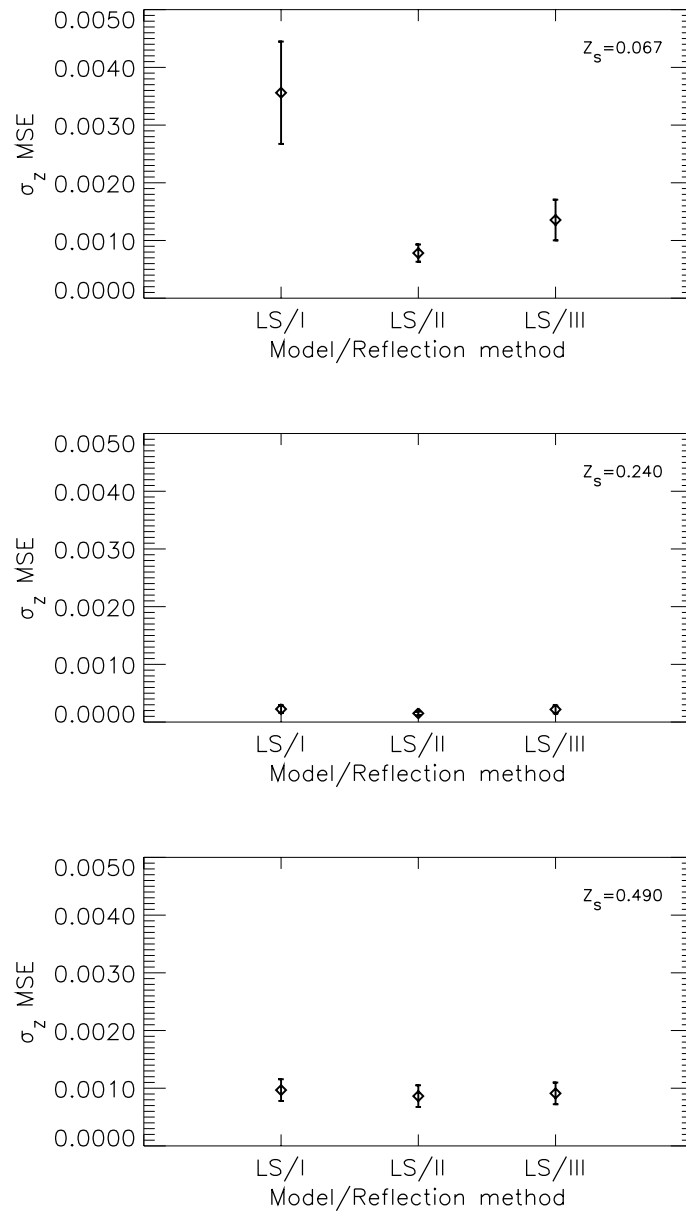


Fig. 4.35. Mean square error (MSE) of dimensionless standard deviation of concentration distribution predicted by the *linear-skewed* (LS) Langevin equation model using reflection methods I, II, and III, estimated using observations from the Willis & Deardorff experiments for dimensionless source height of (a) $Z_s = 0.067$ (top figure), (b) $Z_s = 0.24$ (middle), and (c) $Z_s = 0.49$ (bottom). Error bars indicate plus and minus standard error.

Table 4.4. Error in model predictions estimated using observations from the Willis & Deardorff experiments for dimensionless source heights of $z_s/h = 0.067, 0.24$ and 0.49 . Mean square error (*MSE*), standard error of *MSE* (*SE MSE*), mean fractional error (*MFE*), standard error of *MFE* (*SE MFE*) of predictions of \bar{z}/h , σ_z/h , and $C(X,0)$ from simulations with nonlinear-Gaussian (N-G) and linear-skewed (L-S) Langevin equation model using reflection methods I, II, and III.

Model	$\frac{z_s}{h}$	S	$\frac{\sigma_{w_f}^2}{w_*^2}$	$\frac{\tau w_*}{h}$	Ref. Meth	\bar{z}/h				σ_z/h				$C(X,0)$			
						<i>MSE</i>	<i>SE MSE</i>	<i>MFE</i>	<i>SE MFE</i>	<i>MSE</i>	<i>SE MSE</i>	<i>MFE</i>	<i>SE MFE</i>	<i>MSE</i>	<i>SE MSE</i>	<i>MFE</i>	<i>SE MFE</i>
N-G	0.067	0.78	0.31	0.8	I	0.00056	0.00016	-0.03709	0.00777	0.00010	0.00003	0.04404	0.02334	0.70675	0.23245	0.44514	0.12330
N-G	0.067	0.78	0.31	0.8	II	0.00013	0.00004	-0.01263	0.00852	0.00030	0.00006	0.05092	0.02387	0.53436	0.37998	0.14760	0.06701
N-G	0.067	0.78	0.31	0.8	III	0.00013	0.00003	-0.01874	0.00623	0.00016	0.00003	0.05439	0.02248	0.57114	0.32196	0.29275	0.08442
N-G	0.240	0.78	0.31	0.8	I	0.00008	0.00002	0.00962	0.00552	0.00089	0.00019	0.07047	0.02140	0.27160	0.05680	0.00098	0.10276
N-G	0.240	0.78	0.31	0.8	II	0.00026	0.00008	-0.00207	0.00934	0.00094	0.00016	0.07514	0.02077	0.19335	0.04337	-0.00508	0.08754
N-G	0.240	0.78	0.31	0.8	III	0.00016	0.00005	0.00278	0.00745	0.00091	0.00016	0.07239	0.02090	0.23290	0.04990	0.00391	0.09623
N-G	0.490	0.78	0.31	0.8	I	0.00063	0.00011	0.00654	0.01048	0.00090	0.00016	-0.06412	0.02912	0.44834	0.09510	-0.39118	0.14740
N-G	0.490	0.78	0.31	0.8	II	0.00071	0.00013	0.00715	0.01121	0.00085	0.00016	-0.05693	0.02930	0.41548	0.07392	-0.32165	0.15860
N-G	0.490	0.78	0.31	0.8	III	0.00067	0.00013	0.00679	0.01090	0.00086	0.00016	-0.05961	0.02917	0.42633	0.08282	-0.35114	0.15423
L-S	0.067	0.78	0.31	0.8	I	0.00706	0.00166	-0.15052	0.01987	0.00356	0.00089	-0.06532	0.03102	0.92419	0.24416	0.67294	0.20864
L-S	0.067	0.78	0.31	0.8	II	0.00140	0.00033	-0.08362	0.00859	0.00078	0.00015	-0.03153	0.02643	0.46914	0.20576	0.05067	0.06425
L-S	0.067	0.78	0.31	0.8	III	0.00302	0.00075	-0.10458	0.01256	0.00136	0.00035	-0.03214	0.02634	0.37587	0.11317	0.34067	0.10907
L-S	0.240	0.78	0.31	0.8	I	0.00025	0.00008	0.01204	0.00925	0.00023	0.00007	0.00673	0.01723	0.20258	0.04539	0.01843	0.08180
L-S	0.240	0.78	0.31	0.8	II	0.00005	0.00002	-0.00852	0.00507	0.00015	0.00003	0.01130	0.01542	0.03051	0.01275	-0.00986	0.02920
L-S	0.240	0.78	0.31	0.8	III	0.00006	0.00002	0.00307	0.00535	0.00022	0.00007	0.01119	0.01672	0.08519	0.01626	0.03093	0.05566
L-S	0.490	0.78	0.31	0.8	I	0.00105	0.00022	0.04424	0.01184	0.00097	0.00019	-0.08405	0.02821	0.24964	0.06297	-0.45376	0.08031
L-S	0.490	0.78	0.31	0.8	II	0.00089	0.00017	0.03416	0.01160	0.00086	0.00019	-0.07107	0.02870	0.07912	0.01411	-0.26640	0.09479
L-S	0.490	0.78	0.31	0.8	III	0.00093	0.00018	0.03613	0.01168	0.00091	0.00019	-0.07760	0.02845	0.16120	0.03747	-0.34961	0.09155

4.3.5 Sensitivity tests

As mentioned above, there is some variability and uncertainty in the observed values of the fluid velocity variance, $\sigma_{w_f}^2$, and, in particular, in the observed values of velocity skewness, S , and the estimated value of the Lagrangian correlation time, τ , used in the CBL dispersion simulations just presented. Therefore, the sensitivity of the dispersion simulation results to the values of τ , $\sigma_{w_f}^2$, and S was investigated. Additional simulations for the three source heights ($Z_s = 0.067, 0.24$, and 0.49) used in the Willis and Deardorff experiments were performed with both Langevin equation models using reflection method II and two alternative values for each of the three parameters, τ , $\sigma_{w_f}^2$, and S , one near the low end and one near the high end of the range of values found in the CBL. These low-end and high-end values are $\tau w_*/h = 0.5$ and 1.2 , $\sigma_{w_f}^2/w_*^2 = 0.2$ and 0.4 , and $S = 0.4$ and 1.2 , respectively. The "best-estimate" values, used in the simulations shown above, are $\tau w_*/h = 0.8$, $\sigma_{w_f}^2/w_*^2 = 0.31$, and $S = 0.78$. Simulations were completed for each of the three source heights with each model in which only one of these three parameters was changed (first to the low-end and then to the high-end value) and the other two parameters were kept at their best-estimate values (this resulted in 18 additional simulations with each model). The results of these sensitivity tests are shown and discussed in Appendix D. In addition, two simulations were made for each of the three source heights with each model in which all three parameters were changed together in the following two combinations: (1) $\tau w_*/h = 1.2$, $\sigma_{w_f}^2/w_*^2 = 0.4$, and $S = 1.2$; and (2) $\tau w_*/h = 0.5$, $\sigma_{w_f}^2/w_*^2 = 0.2$, and $S = 0.4$ (this resulted in 6 additional simulations with each model). These may be physically realistic combinations because larger values of τ , $\sigma_{w_f}^2$, and S occur together (e.g., in the middle of the CBL), while lower values occur together (e.g., toward the bottom of the CBL).

The simulation results are sensitive to some changes in certain input parameter values. The results indicate that for the source height near the middle of the boundary layer ($Z_S = 0.49$) higher values of τ and/or $\sigma_{w_f}^2$ consistently improve results for both models. This is consistent with the higher measured values for $\sigma_{w_f}^2$ and the higher estimated values for τ that occur in the middle of the CBL. The sensitivity tests show that the overall agreement with observations (for all three source heights) is significantly worse for both models when the lowest $\sigma_{w_f}^2$ value ($0.2w_*^2$) is used, as well as when the lowest τ value ($0.5h/w_*$) is used. For the nonlinear-Gaussian model, agreement is significantly worse when the highest S value (1.2) is used.

Considering all the simulation results for both models (the sensitivity tests shown in Appendix D, and the original simulations shown above), the original, best-estimate values for $\tau=0.8h/w_*$, $\sigma_{w_f}^2=0.31w_*^2$, and $S=0.78$ result in relatively good agreement with observations for all three source heights, and appear to be good values for use in a homogeneous Langevin equation model of the CBL. However, the overall results of the nonlinear-Gaussian model can be improved by using a smaller value of S (between 0.4 and 0.78), along with a larger value of τ (between $0.8h/w_*$ and $1.2h/w_*$). The overall results of the linear-skewed model can be improved by using a larger value of τ (between $0.8h/w_*$ and $1.2h/w_*$), and were not significantly changed when using a smaller value of S (except for the $C(X,0)$ results for $Z_S = 0.49$, which improved using a smaller skewness). Given the uncertainty in these parameter values, modified values within these ranges could be justified (for example, $\tau = 1.0h/w_*$, $S = 0.6$), and would improve some of the predictions of the models.

4.3.6 Discussion

In this section, possible reasons for the differences between the results of the two Langevin equation models and the three reflection methods used in the CBL simulations

will be discussed. One notable difference between the results of simulations using different reflection methods is that method II (negatively correlated incident and reflected speeds) generally results in the best agreement with the observed dispersion of material near the surface. As discussed in Chapter 3, the variation of the statistical properties of the fluid velocity in the surface layer are not resolved in the homogenous model being used in this work. Correspondingly, the details of possible fluid trajectories near the surface are not simulated (e.g., the translation of vertical to horizontal motion as air in a downdraft approaches the surface is not simulated). The CBL simulation results indicate that reflection method II results in the best approximation (of the three methods tested) for the trajectories of particles near the surface for a homogeneous model.

Reflection method II seems best able to simulate the time that descending particles, with different velocity, spend near the surface. Relatively fast descending air in the core of a strong, organized mixed-layer downdraft penetrates all the way through the surface layer, as discussed in Chapter 2. Upward motion is suppressed in the downdraft. Air flows radially outward along the surface, away from the center of the downdraft area. Therefore, it is very plausible that air approaching the surface from the mixed layer with a relatively *high* downward velocity will, on average, remain near the surface longer since it must move horizontally from the center of the downdraft before reaching the convergence zones that feed updrafts. Reflection method II has this effect, by assigning a relatively weak upward velocity when a particle with a strong downward velocity encounters the surface. Now, air approaching the surface with a relatively *low* speed (e.g., in a relatively weak, narrow downdraft or near the edge of a strong downdraft where downward speeds are smaller than in the core) will likely approach the surface closer to a convergence line that feeds an updraft, be more quickly swept into an updraft, and, therefore, spend relatively little time in the surface layer. Reflection method II has this

effect, by assigning a relatively strong upward velocity when a particle with a weak downward velocity encounters the surface.

These arguments for reflection method II are supported by previous numerical simulations and observational studies. Lamb (1981) noted that Lagrangian simulations, using 3-D LES velocity fields, of the trajectories of fluid particles released continuously into downdrafts at approximately $0.5h$ showed that particles in the core of downdrafts descend fastest, enter the surface layer, and, on average, tend to remain in the surface layer initially while slower descending particles enter the surface layer. As a result, particles tend to accumulate in the surface layer for a time before moving upward, out of the surface layer. This process is responsible for the secondary concentration maximum at the surface observed in Lamb's (1982) LES simulations for a source in the middle of the CBL, as well as in Willis & Deardorff's observations shown in Fig. 4.17c. The effect of this process is also seen in the behavior, shown in Fig. 4.17, of the observed maximum concentration line remaining near the surface for a time after it reaches the surface, and before it begins to increase in height. This phenomena is best simulated using reflection method II for both Langevin equation models.

Schmidt and Schumann's (1989) LES simulations showed that, on average, fluid moves radially outward from the centers of downdrafts along the surface and upward motion is suppressed in the downdraft area. This fluid moves horizontally near the surface toward convergence lines (these are "spokes" in a wheel-like pattern) and then continues to flow horizontally along these spokes toward "hubs" before beginning to move upward in to the mixed layer. This indicates that air approaching the surface with a relatively strong downward velocity (in the core of a downdraft) spends a relatively longer time, on average, near the surface (as implied by negatively-correlated-speed reflection, method II), and is not returned relatively quickly to the mixed layer (as implied by positively-

correlated-speed reflection, method I). Schmidt and Schumann's simulations showed that this circulation pattern is spatially coherent over large spatial scales (on the order of h). Vertical motion in the middle of the CBL has a maximum correlation with horizontal motion very close to the surface, where fluid flows into the bottom of the mixed layer updrafts and out of the bottom of mixed layer downdrafts. This horizontal surface flow connects mixed layer downdrafts to updrafts, which are separated, on average, by horizontal distances of $0.5h$ to h .

Williams and Hacker (1992, 1993) presented the results of observational studies, and developed a conceptual model of the interaction of the surface and mixed layers. Their schematic diagram of this conceptual model includes wide downdraft regions in the mixed layer penetrating into the surface layer, and, also, narrower, weak downdraft regions that do not penetrate deep into the surface layer. This diagram indicates that both the air in weaker downdrafts and the air near the edges of strong downdrafts can be more quickly re-circulated into updrafts. This is consistent with the effect of reflection method II.

Based on these previous studies, it is plausible that, for particles released into downdrafts in the mixed layer, the particles with a strong downward velocity (e.g., in the core of a downdraft) are swept to the surface faster and then move horizontally along the surface while slower descending particles (e.g., near the edges of downdraft areas) are still approaching the surface. The faster-descending and slower-descending particles can then converge near the edges of downdraft areas near the surface. Reflection method II has this effect, since it allows the high speed descending particles to remain closer to the surface after reflection until slower descending particles approach the surface.

In light of these arguments, positively-correlated-speed reflection (method I) does not appear to be a good approximation to particle trajectories near the surface. Using reflection method I, a particle encountering the surface with a relatively strong downward velocity will be assigned a relatively strong upward velocity and, given the long velocity correlation time, will unrealistically result in the particle spending relatively little time near the surface.

Reflection method III results are intermediate between the best results, obtained using method II, and the worst results, obtained with method I. This indicates that uncorrelated-speed reflection is a better approximation than positively-correlated-speed reflection. Reflection method III assigns a randomly selected reflected velocity (from the proper distribution). Reflection method III might be a reasonable approach if the downdrafts were not coupled to updrafts in a coherent circulation pattern. However, the observational and numerical studies discussed above, and the better results obtained with negatively-correlated-speed reflection (method II), indicate that this is not the case.

The results of the two Langevin equation models using the same reflection method are significantly different in some cases. This must be due to one or both of the fundamental differences between the two models: the form of the velocity distribution and the form of the Langevin equation. The fluid velocity distributions for the two models were shown in Figs. 4.15 and 4.16. The two forms of the Langevin equation were discussed in Chapter 3, and their deterministic terms compared in Fig. 3.1. The fluid velocity distribution (which is used to assign initial particle velocities) completely determines the dispersion for times much less than τ (in the simulations shown above, the velocity correlation time is $0.8h / w_*$, corresponding to a dimensionless travel time and dimensionless downwind distance, X , of 0.8). However, at later times, it is not possible to isolate the reasons for the differences between models from these results because the different forms of the

Langevin equation affect the results, in addition to the different fluid velocity distributions.

One of the differences between the results of the two Langevin equation models is found near the top of the boundary layer. The nonlinear-Gaussian model results (Figs. 4.18-20) show overly high concentrations for all three reflection methods. These overly high concentrations are not present in the linear-skewed model results (Figs. 4.21-23). A definitive explanation for this difference cannot be determined from these results. However, the difference must be due to one or both of the fundamental differences between the two models: the shape of the velocity distribution (shown in Figs. 4.15 and 4.16) and the form of the Langevin equation. While the overly high concentrations for the nonlinear-Gaussian model would be decreased if a realistic entrainment layer were resolved, similar features have been present in results from previous nonlinear-Gaussian model studies that used more realistic inhomogeneous turbulence parameterizations (Luhar and Britter, 1989; Weil, 1989; Du *et al.*, 1994). It has been suggested (Weil, 1989; Du *et al.*, 1994) that these high concentrations may be due to unrealistic aspects of the inhomogeneous turbulence parameterizations used in these previous studies. However, the fact that the overly high concentrations at the top of the boundary layer do not appear in the simulations with the linear-skewed model presented here, nor in Sawford and Guest's (1987) simulations using an inhomogeneous linear-skewed Langevin model, suggests that these features may also be the result of an inherent property of at least some nonlinear-Gaussian Langevin equation models.

5

Summary and Conclusions

This dissertation presents the development and evaluation of a Langevin equation model for vertical dispersion of trace material in the convective boundary layer, CBL. This model simulates the possible trajectories of fluid particles in turbulent flows that have skewed velocity distributions and large scale turbulent structures, such as in the CBL. A new model based on a "linear-skewed" form of the Langevin equation, which has a linear (in velocity) deterministic acceleration and a skewed random acceleration, was introduced. This model was developed using the simplifying assumption that the vertical velocity distribution is spatially homogeneous, as well as skewed. Comparisons were made between this new linear-skewed Langevin equation model and another homogeneous model, used by previous investigators, that is based on a "nonlinear-Gaussian" form of the Langevin equation. This nonlinear-Gaussian Langevin equation has a nonlinear (in velocity) deterministic acceleration and a Gaussian random acceleration. The well-mixed condition—the constraint that initially well-mixed tracer spatial and velocity distributions must remain so—was used to develop both models.

In a homogeneous Langevin equation model, the properties of turbulence near boundaries are not resolved, and interactions with boundaries must be handled with "reflection" of the velocity. Three reflection boundary conditions that meet the well-mixed condition in homogeneous, skewed turbulence were presented. These include one using the standard assumption that the magnitudes of the incident and reflected velocities are positively

correlated, and two alternatives in which the magnitude of these velocities are either negatively correlated or uncorrelated.

The linear-skewed and nonlinear-Gaussian Langevin equation models were first tested using the idealized case of unbounded, stationary, homogeneous turbulence. These simulations were used to help determine the numerical integration time step size, Δt , required for accurate simulations of particle velocity, w , and position, z , using each model. Comparison of the simulated first six velocity moments to the exact moments (and, for the nonlinear-Gaussian model, the simulated and exact velocity probability density function) showed that both models can accurately simulate particle velocity for a sufficiently small time step. Examination of the particle position distributions and position moments showed that both models can also accurately simulate particle position for a sufficiently small time step.

While both models can accurately simulate the (w, z) phase space trajectory of a particle, the linear-skewed model was shown to be more accurate than the nonlinear-Gaussian model for the same size time step. This is because the linear-skewed form of the Langevin equation can be integrated explicitly for the case of homogeneous fluid velocity statistics. The resulting linear-skewed model's velocity update equation is exact through the first three moments of velocity. In contrast, the corresponding nonlinear-Gaussian model equation is accurate only through $O(\Delta t)$.

A comparison of the first six velocity moments calculated by the linear-skewed model to the exact fluid velocity moments shows that the method of defining the fourth and higher fluid velocity moments for this model using the small-time-step limit is practical; that is, for practical values of the time step size, the calculated fourth and higher moments approach these exact limiting values. This indicates that this is a successful approach to

handling the problem of the time step dependence of these higher-order moments, which arises because the linear-skewed Langevin equation model's random term has non-zero fourth and higher order cumulants that are not explicitly controlled. In contrast, the nonlinear-Gaussian model does not have this problem, because it uses a Gaussian random term, for which the third and higher order cumulants are zero. However, the nonlinear-Gaussian model does have non-zero third and higher moments of the random term, and *all* the moments (first and higher) are approximate, because of the $O(\Delta t)$ approximate velocity update equation used here.

In spite of the approximate higher moments of the linear-skewed model's random term, the absence of numerical error in the deterministic term and in the first three moments of the random term for this model, makes the overall error in the velocity and position distributions much smaller than for the nonlinear-Gaussian model. This is because the nonlinear-Gaussian model uses an $O(\Delta t)$ approximate deterministic term and $O(\Delta t)$ approximations for all the moments of the random term.

For the linear-skewed Langevin equation model, exact, analytic expressions for the time-dependent position moments, $\overline{z^m(t)}$, for the joint velocity-position moments, $\overline{w^n(t)z^m(t)}$, and for the autocorrelation functions $\overline{w_0 w^n(t)}$ can be determined, and were used to show that for $m = 1, 2, 3$ and $n = 1, 2$ and 3 the linear-skewed model calculations for these quantities are very accurate. These results indicate that the velocity update equation and the approximate position update equation simulate the joint evolution of particle velocity and position quite accurately.

Well-mixed spatial and velocity distributions for the idealized case of bounded, stationary, homogeneous turbulence, were used to evaluate both models. It was shown that calculations using both models and all three reflection methods approach the correct

well-mixed distributions as the time step is decreased. These results again showed that the linear-skewed model can be used with longer time steps than the nonlinear-Gaussian model and achieve the same accuracy. Acceptably small errors of 3% or less in the spatial distribution were obtained with the linear-skewed model with $\Delta t = 0.2 \tau$, while the nonlinear-Gaussian model required a smaller time step of $\Delta t = 0.05 \tau$ to achieve this accuracy. Inhomogeneous Langevin models used by previous investigators have used a time step on the order of $\Delta t = 0.01 \tau$ for accurate numerical solutions (e.g., less than 3% error in the concentration from simulations of a well-mixed tracer in a bounded flow). The homogeneous linear-skewed model, therefore, is more efficient than the homogeneous nonlinear-Gaussian model, and considerably more efficient than inhomogeneous models.

Observations from Willis and Deardorff's (1976a, 1976b, 1978 & 1981) laboratory experiments were used to evaluate the ability of the two homogeneous Langevin equation models and three reflection methods to simulate velocity distributions and tracer dispersion in the CBL. The measured velocity distributions published by Deardorff and Willis (1985) for several heights in the CBL were analyzed to obtain height-averaged velocity variance and skewness values for use in these simulations. The resulting simulated velocity distributions were reasonable representations of the observed distributions.

The simulations of the Willis and Deardorff experiments confirmed that homogeneous Langevin equation models can capture important aspects of dispersion from sources in the CBL. Some aspects of the observed tracer dispersion were simulated better by the linear-skewed model, and some simulated better by the nonlinear-Gaussian model. It was also found that the choice of reflection boundary condition can significantly affect the predicted concentration distribution.

One of the main conclusions of this work is that the application of the negatively correlated incident and reflected speed boundary condition (reflection method II) provides a significantly better representation of dispersion within the CBL than the standard assumption that the speeds are correlated. For both of the homogeneous-turbulence Langevin equation models, which do not resolve the variation of the statistical properties of the fluid velocity in the surface layer, this negatively-correlated-speed reflection method simulates the observed dispersion of material near the surface significantly better than either of the other two reflection methods. The effect of this reflection method is consistent with the observed behavior of air in the core of strong downdrafts, which penetrates deep into the surface layer, spreads out along the surface, and spends more time near the surface than air in weaker downdrafts, on average. It is also consistent with air in weaker downdrafts approaching the surface closer to convergence lines that feed into updrafts, being more quickly swept into updrafts, and spending less time near the surface. Results using the uncorrelated-speed reflection (method III) are intermediate between the best results, obtained using reflection method II, and the poorest results, obtained using positively-correlated-speed reflection method I.

Using reflection method II, both the nonlinear-Gaussian and linear-skewed Langevin equation models' results are in good agreement with observations from Willis and Deardorff's experiments. Neither model is clearly superior. Some features of the concentration field are predicted better by one model and some by the other. The nonlinear-Gaussian model results agree better with the observed mean height and standard deviation of the vertical concentration distribution for the sources at $z_s = 0.067h$ and $0.49h$. The linear-skewed model results agree better with these observed values for $z_s = 0.24h$. The linear-skewed model predicts more accurately the near-surface concentration versus downwind distance, and predicts more accurately a related feature:

the increasing height of the maximum concentration, with downwind distance, after it reaches the surface for all three source heights. The nonlinear-Gaussian model predicts overly high concentrations near the top of the boundary layer. This may be partly due to unrealistic treatment of the entrainment layer. However, the fact that these features do not appear in the simulations with a linear-skewed model suggests that these features may also be the result of an inherent property of the nonlinear-Gaussian Langevin equation model.

A definitive explanation for the difference in the results of the two Langevin equation models cannot be determined from this study. However, the difference must be due to one or both of the related differences between the two models: (1) the different shapes of the velocity distribution (which, however, were specified to have the same first three moments), and (2) the different forms of the Langevin equation. For the linear-skewed model, the velocity distribution, $P_f(w)$, is a result of the assumed form of the Langevin equation. In contrast, for the nonlinear-Gaussian model, the final form of the Langevin equation is a result of the assumed analytic form of $P_f(w)$. It is not clear how the two models could be formulated to use the same fluid velocity distribution (to do a more direct comparison of the two forms of the Langevin equation), but this is an area of possible future work.

In the future, other fluid velocity distributions, $P_f(w)$, could also be explored to determine if they are superior for use in homogeneous-turbulence Langevin equation models of CBL dispersion. While the velocity distributions used in this work are in reasonable agreement with the experimental data, they are not unique, and alternatives could be investigated.

A possible future extension of this homogeneous-turbulence Langevin equation modeling approach is to simulate dispersion across the interface between the boundary layer and the free atmosphere, when these two layers are assumed to have different homogeneous turbulent properties. Thomson *et al.* (1997) have proposed an approach to this problem. This extension might allow better simulation of concentrations in, as well as above, the interfacial/entrainment layer.

Of the two Langevin equation models and three reflection methods evaluated, the linear-skewed Langevin equation model with a negatively-correlated-speed reflection boundary condition (method II) is recommended. The results with the linear-skewed model are comparable overall to the nonlinear-Gaussian model results, but the linear-skewed model is significantly more efficient and predicts near-surface concentration, which is of primary importance for many dispersion-modeling applications, more accurately than the nonlinear-Gaussian model.

Appendices

Appendix A: Bi-Gaussian velocity distribution

The bi-Gaussian distribution for $P_f(w)$ used by Baerentsen and Berkowicz (1984) is a linear combination of two Gaussian distributions, and can be written as follows:

$$P_f(w) = \lambda_1 P_1(w) + \lambda_2 P_2(w), \quad (3.4.10)$$

where

$$\begin{aligned} P_1(w) &= \frac{1}{\sqrt{2\pi}\sigma_1} \exp\left[-\frac{(w - \bar{w}_1)^2}{2\sigma_1^2}\right] \\ P_2(w) &= \frac{1}{\sqrt{2\pi}\sigma_2} \exp\left[-\frac{(w - \bar{w}_2)^2}{2\sigma_2^2}\right] \end{aligned} \quad (3.4.11, 12)$$

The six parameters of this distribution, \bar{w}_1 , \bar{w}_2 , σ_1 , σ_2 , λ_1 , and λ_2 will be specified assuming the first three moments of the fluid velocity ($\bar{w}_f=0$, \bar{w}_f^2 , and \bar{w}_f^3) are known.

The six parameters can be determined from the following four equations for moments zero through three of this distribution,

$$\lambda_1 + \lambda_2 = 1, \quad (A.1)$$

$$\lambda_1 \bar{w}_1 + \lambda_2 \bar{w}_2 = \bar{w}_f = 0, \quad (\text{A.2})$$

$$\lambda_1 (\bar{w}_1^2 + \sigma_1^2) + \lambda_2 (\bar{w}_2^2 + \sigma_2^2) = \bar{w}_f^2, \quad (\text{A.3})$$

$$\lambda_1 (3\bar{w}_1 \sigma_1^2 + \bar{w}_1^3) + \lambda_2 (3\bar{w}_2 \sigma_2^2 + \bar{w}_2^3) = \bar{w}_f^3, \quad (\text{A.4})$$

along with two closure equations,

$$\bar{w}_1 = \sigma_1, \quad (\text{A.5})$$

$$\bar{w}_2 = -\sigma_2. \quad (\text{A.6})$$

Solving the six equations (A.1-6) for the six parameters yields

$$\bar{w}_2 = -\sigma_2 = \frac{\bar{w}_f^3 - \sqrt{\bar{w}_f^3{}^2 + 8\bar{w}_f^2{}^3}}{4\bar{w}_f^2}, \quad (3.4.13)$$

$$\bar{w}_1 = \sigma_1 = \frac{-\bar{w}_f^2}{2\bar{w}_2} = \frac{\bar{w}_f^3 + \sqrt{\bar{w}_f^3{}^2 + 8\bar{w}_f^2{}^3}}{4\bar{w}_f^2}, \quad (3.4.14)$$

$$\lambda_1 = \frac{-\bar{w}_2}{\bar{w}_1 - \bar{w}_2}, \text{ and} \quad (3.4.15)$$

$$\lambda_2 = \frac{\bar{w}_1}{\bar{w}_1 - \bar{w}_2}. \quad (3.4.16)$$

The higher moments of the bi-Gaussian distribution are not explicitly controlled, but can be calculated. For example, the fourth through sixth moments are

$$\bar{w}_f^4 = \lambda_1 (3\sigma_1^4 + 6\bar{w}_1^2 \sigma_1^2 + \bar{w}_1^4) + \lambda_2 (3\sigma_2^4 + 6\bar{w}_2^2 \sigma_2^2 + \bar{w}_2^4), \quad (\text{A.7})$$

$$\overline{w}_f^5 = \lambda_1 \overline{w}_1 (15\sigma_1^4 + 10\overline{w}_1^2 \sigma_1^2 + \overline{w}_1^4) + \lambda_2 \overline{w}_2 (15\sigma_2^4 + 10\overline{w}_2^2 \sigma_2^2 + \overline{w}_2^4), \quad (\text{A.8})$$

$$\overline{w}_f^6 = \lambda_1 (15\sigma_1^6 + 45\overline{w}_1^2 \sigma_1^4 + 15\overline{w}_1^4 \sigma_1^2 + \overline{w}_1^6) + \lambda_2 (15\sigma_2^6 + 45\overline{w}_2^2 \sigma_2^4 + 15\overline{w}_2^4 \sigma_2^2 + \overline{w}_2^6). \quad (\text{A.9})$$

Appendix B: Linear-skewed Langevin equation model velocity moments, autocorrelation functions, position moments and joint velocity-position moments

In Chapter 3 it was shown that for the linear-skewed Langevin equation, the general equation for the time-dependent velocity cumulants is

$$\langle\langle w^n(t) \rangle\rangle = \langle\langle w_0^n \rangle\rangle e^{-n\alpha t} + \langle\langle r^n(t) \rangle\rangle, \quad (3.4.20)$$

where $n = 1, 2, \dots$, and $w_0 \equiv w(0)$. (Note that r is the same as r_s in Chapter 3.) The general expression for the time-dependent cumulants of r is

$$\langle\langle r^n(t) \rangle\rangle = \frac{\Gamma_n}{n\alpha} (1 - e^{-n\alpha t}). \quad (3.4.21)$$

Using the definition in Eq. (3.4.27),

$$\alpha = 1/\tau,$$

the corresponding first six moment of $w(t)$ are,

$$\overline{w(t)} = \overline{w_0} e^{-t/\tau},$$

$$\overline{w^2(t)} = \overline{w_0^2} e^{-2t/\tau} + \overline{r^2(t)},$$

$$\overline{w^3(t)} = \overline{w_0^3} e^{-3t/\tau} + 3\overline{w_0} e^{-t/\tau} \overline{r^2(t)} + \overline{r^3(t)},$$

$$\overline{w^4(t)} = \overline{w_0^4} e^{-4t/\tau} + 6\overline{w_0^2} e^{-2t/\tau} \overline{r^2(t)} + 4\overline{w_0} e^{-t/\tau} \overline{r^3(t)} + \overline{r^4(t)},$$

$$\overline{w^5(t)} = \overline{w_0^5} e^{-5t/\tau} + 10\overline{w_0^3} e^{-3t/\tau} \overline{r^2(t)} + 10\overline{w_0^2} e^{-2t/\tau} \overline{r^3(t)} + 5\overline{w_0} e^{-t/\tau} \overline{r^4(t)} + \overline{r^5(t)}, \text{ and}$$

$$\overline{w^6(t)} = \overline{w_0^6} e^{-6t/\tau} + 15\overline{w_0^4} e^{-4t/\tau} \overline{r^2(t)} + 20\overline{w_0^3} e^{-3t/\tau} \overline{r^3(t)} + 15\overline{w_0^2} e^{-2t/\tau} \overline{r^4(t)} + 6\overline{w_0} e^{-t/\tau} \overline{r^5(t)} + \overline{r^6(t)},$$

where

$$\overline{r(t)} = 0,$$

$$\overline{r^2(t)} = \overline{w_f^2} (1 - e^{-2t/\tau}),$$

$$\overline{r^3(t)} = \overline{w_f^3} (1 - e^{-3t/\tau}),$$

$$\overline{r^4(t)} = (\overline{w_f^4} - 3\overline{w_f^2}^2) (1 - e^{-4t/\tau}) + 3\overline{w_f^2}^2 (1 - e^{-2t/\tau})^2,$$

$$\overline{r^5(t)} = (\overline{w_f^5} - 10\overline{w_f^2} \overline{w_f^3}) (1 - e^{-5t/\tau}) + 10\overline{w_f^2} \overline{w_f^3} (1 - e^{-2t/\tau}) (1 - e^{-3t/\tau}), \text{ and}$$

$$\begin{aligned} \overline{r^6(t)} = & \left[\overline{w_f^6} - 15\overline{w_f^2} \overline{w_f^4} - 10\overline{w_f^3}^2 + 30\overline{w_f^2}^3 \right] (1 - e^{-6t/\tau}) + 10\overline{w_f^3}^2 (1 - e^{-3t/\tau})^2 \\ & + 15\overline{w_f^2} (\overline{w_f^4} - 3\overline{w_f^2}^2) (1 - e^{-2t/\tau} - e^{-4t/\tau} + e^{-6t/\tau}) + 15\overline{w_f^2}^3 (1 - e^{-2t/\tau})^3 \end{aligned}$$

The second cumulant of r , for example, is determined as follows:

$$z(t) = z(0) + \frac{w(0)}{\alpha} (1 - e^{-\alpha t}) + \frac{1}{\alpha} \int_0^t [1 - e^{\alpha(s-t)}] \Lambda(s) ds. \quad (\text{B.1})$$

$\alpha \equiv \frac{1}{\tau} \frac{4}{4} \frac{4}{4} \frac{2}{4} \frac{4}{4} \frac{4}{4} \frac{3}{3}$
 $\equiv r_z(t)$

The moments of $(z(t) - z_0)$ and $r_z(t)$ can be determined from Eq. (B.1) and the definitions of $\alpha = 1/\tau$ in Eq. (3.4.27) and $\{\Gamma_n\}$ in Eq. (3.4.25). The first three moments of $(z(t) - z_0)$ are

$$\overline{(z(t) - z_0)} = \overline{w_0} \tau (1 - e^{-t/\tau}),$$

$$\overline{(z(t) - z_0)^2} = \overline{w_0^2} \tau^2 (1 - e^{-t/\tau})^2 + \overline{r_z^2(t)}, \text{ and}$$

$$\overline{(z(t) - z_0)^3} = \overline{w_0^3} \tau^3 (1 - e^{-t/\tau})^3 + 3 \overline{w_0} \tau (1 - e^{-t/\tau}) \overline{r_z^2(t)} + \overline{r_z^3(t)}$$

where $z_0 \equiv z(0)$, and

$$\overline{r_z(t)} = 0,$$

$$\overline{r_z^2(t)} = \overline{w_f^2} \tau^2 \left[2 \frac{t}{\tau} + 4e^{-t/\tau} - e^{-2t/\tau} - 3 \right], \text{ and}$$

$$\overline{r_z^3(t)} = \frac{\overline{w_f^3} \tau^3}{2} \left[6 \frac{t}{\tau} + 18e^{-t/\tau} - 9e^{-2t/\tau} + 2e^{-3t/\tau} - 11 \right].$$

The expression for $\overline{(z(t) - z_0)^2}$ is the same as that obtained by Taylor (1921) using an exponential velocity autocorrelation function (which, as discussed in Chapter 3, is a property of a Langevin equation with a linear deterministic acceleration).

Similarly, joint moments of $w(t)$ and $(z(t) - z_0)$ can be determined from Eqs. (3.4.19) and (B.1). For example,

$$\begin{aligned}\overline{w(t)(z(t) - z_0)} &= \overline{w_0^2} \tau e^{-t/\tau} (1 - e^{-t/\tau}) + \overline{r(t)r_z(t)}, \\ \overline{w^2(t)(z(t) - z_0)} &= 2\overline{w_0} \overline{r(t)r_z(t)} e^{-t/\tau} + \overline{w_0} \tau \overline{r^2(t)} (1 - e^{-t/\tau}) + \\ &\quad \overline{w_0^3} \tau (e^{-2t/\tau} - e^{-3t/\tau}) + \overline{r^2(t)r_z(t)}, \text{ and} \\ \overline{w(t)(z(t) - z_0)^2} &= \overline{w_0} \overline{r_z^2(t)} e^{-t/\tau} + 2\overline{w_0} \tau \overline{r(t)r_z(t)} (1 - e^{-t/\tau}) + \\ &\quad \overline{w_0^3} \tau^2 (e^{-3t/\tau} - 2e^{-2t/\tau} + e^{-t/\tau}) + \overline{r(t)r_z^2(t)},\end{aligned}$$

where

$$\begin{aligned}\overline{r(t)r_z(t)} &= \overline{w_f^2} \tau (1 - e^{-t/\tau})^2, \\ \overline{r^2(t)r_z(t)} &= \frac{\overline{w_f^3} \tau}{2} (1 - e^{-t/\tau})^2 (1 + 2e^{-t/\tau}), \\ \overline{r(t)r_z^2(t)} &= \overline{w_f^3} \tau^2 (1 - e^{-t/\tau})^3, \text{ and}\end{aligned}$$

$\overline{r^2(t)}$ and $\overline{r_z^2(t)}$ were given above.

These exact expressions for the position moments and joint velocity-position moments, can be used to examine the accuracy of the approximate position equation, $z(t + \Delta t) = z(t) + \frac{1}{2}[w(t + \Delta t) + w(t)]\Delta t$, (described in Chapter 3) by comparing series expansions of the exact and approximate expressions. The result is that for the first two position moments the exact and approximate expressions are the same through $O(\Delta t^2)$:

$$\overline{[z(t + \Delta t) - z(t)]} = \overline{w(t)}\Delta t - \frac{\overline{w(t)}\Delta t^2}{2\tau} + O(\Delta t^3),$$

$$\overline{[z(t + \Delta t) - z(t)]^2} = \overline{w^2(t)}\Delta t^2 + O(\Delta t^3).$$

The exact and approximate expressions for the following joint moments are also the same through $O(\Delta t^2)$:

$$\overline{w(t)[z(t + \Delta t) - z(t)]} = \overline{w^2(t)}\Delta t + \left(\frac{\overline{w_f^2}}{\tau} - \frac{3\overline{w^2(t)}}{2\tau} \right) \Delta t^2 + O(\Delta t^3),$$

$$\overline{w^2(t)[z(t + \Delta t) - z(t)]} = \overline{w^3(t)}\Delta t + \left(\frac{4\overline{w_f^2 w(t)}}{\tau} - \frac{5\overline{w^3(t)}}{2\tau} + \frac{3\overline{w_f^3}}{2\tau} \right) \Delta t^2 + O(\Delta t^3),$$

$$\overline{w(t)[z(t + \Delta t) - z(t)]^2} = \overline{w^3(t)}\Delta t^2 + O(\Delta t^3).$$

Appendix C: Linear-skewed model random velocity increment distribution

Double-block distribution

An example of the skewed "double-block" distribution used for the random velocity increment, $r(\Delta t)$, in the linear-skewed Langevin equation model is shown in Fig. C.1-2. (Note that r is the same as r_s used in Chapter 3.) Fig. C1 shows the two separate scaled uniform distributions, $f_1(r)$ and $f_2(r)$, defined by six parameters: the means m_1 and m_2 ; half-widths, Δ_1 and Δ_2 ; and probability densities, p_1 and p_2 , respectively. Fig. C2 shows the double-block probability density function, $P_a(r)$, which is a linear combination of the two distributions:

$$P_a(r) = f_1(r) + f_2(r), \quad (\text{C.1})$$

where

$$f_1(r) = \begin{cases} p_1, & \text{if } (m_1 - \Delta_1) \leq r \leq (m_1 + \Delta_1) \\ 0, & \text{elsewhere} \end{cases} \quad (\text{C.2})$$

and

$$f_2(r) = \begin{cases} p_2, & \text{if } (m_2 - \Delta_2) \leq r \leq (m_2 + \Delta_2) \\ 0, & \text{elsewhere} \end{cases} \quad (\text{C.3})$$

Using (C.1-3), the general equation for the moments is

$$\begin{aligned} \overline{r_a^n} &\equiv \int_{-\infty}^{\infty} r^n P_a(r) dr \\ &= \frac{p_1}{n+1} \left[(m_1 + \Delta_1)^{n+1} - (m_1 - \Delta_1)^{n+1} \right] + \frac{p_2}{n+1} \left[(m_2 + \Delta_2)^{n+1} - (m_2 - \Delta_2)^{n+1} \right] \end{aligned} \quad (\text{C.4})$$

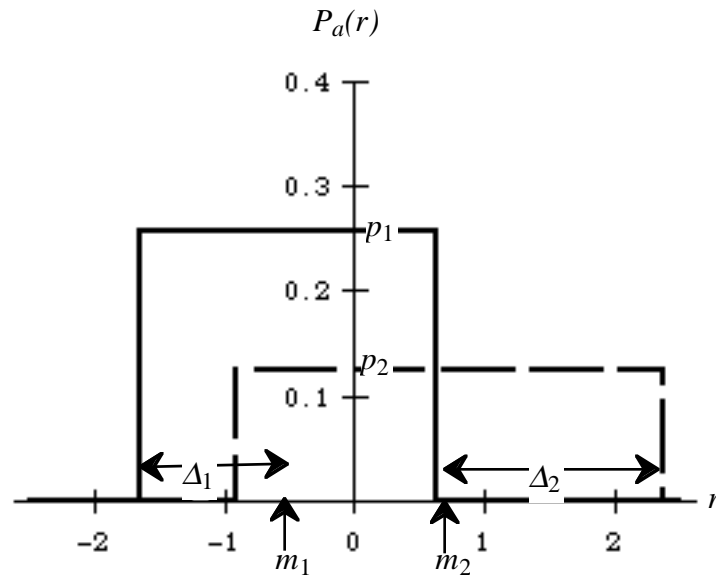


Fig. C.1. Example of two overlapping uniform probability density functions: $f_1(r_a)$ (solid line) and $f_2(r_a)$ (dashed line) with means m_1 and m_2 ; half-widths Δ_1 and Δ_2 ; and probability densities p_1 and p_2 , respectively.

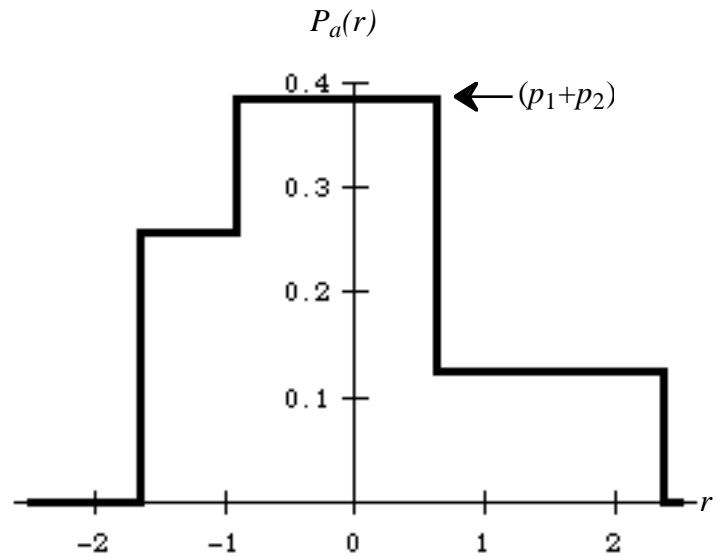


Fig. C.2. Example of double-block probability density function which is the sum of the two overlapping uniform distributions in Fig. 1a. This distribution has a mean of zero, a variance of 1 and a skewness of 0.5.

Since we know that skewness is of fundamental importance to CBL dispersion, we will derive the six parameters of this distribution so that the desired first moment (the mean, assumed to be zero), second moment (σ_r^2), and third moment (ζ_r^3) are obtained.

Moments zero through three then provide us with four equations:

$$\overline{r_a^0} = 2p_1\Delta_1 + 2p_2\Delta_2 = 1, \quad (C.5)$$

$$\overline{r_a} = m_1p_1\Delta_1 + m_2p_2\Delta_2 = 0, \quad (C.6)$$

$$\overline{r_a^2} = \frac{2}{3}p_1\Delta_1^3 + 2\Delta_1m_1^2p_1 + \frac{2}{3}p_2\Delta_2^3 + 2\Delta_2m_2^2p_2 = \sigma_r^2, \text{ and} \quad (C.7)$$

$$\overline{r_a^3} = 2[\Delta_1^3m_1p_1 + \Delta_1m_1^3p_1 + \Delta_2^3m_2p_2 + \Delta_2m_2^3p_2] = \zeta_r^3. \quad (C.8)$$

Since there are four equations and six unknowns, two more equations are required for closure. We use the following two equations:

$$\Delta_1^2 = A^2m_1^2 + B^2\sigma_r^2 \text{ and} \quad (C.9)$$

$$\Delta_2^2 = A^2m_2^2 + B^2\sigma_r^2. \quad (C.10)$$

A and B are positive constants which must be specified.

Solving (C.5-10) for m_1 , m_2 , p_1 and p_2 results in

$$m_{1,2} = \frac{C}{2D\sigma_r^2} \left[\frac{\zeta_r^3}{E} \operatorname{m} \left(\frac{\zeta_r^6}{E^2} + \frac{4D^3\sigma_r^6}{C^3} \right)^{1/2} \right] \quad (C.11)$$

$$p_1 = \frac{m_2}{2\Delta_1(m_2 - m_1)}, \text{ and} \quad (\text{C.12})$$

$$p_2 = \frac{-m_1}{2\Delta_2(m_2 - m_1)}, \quad (\text{C.13})$$

where

$$C = 1 + \frac{A^2}{3},$$

$$D = 1 - \frac{B^2}{3}, \text{ and}$$

$$E = 1 + A^2.$$

From these expressions it can be seen that the coefficient B must be less than $\sqrt{3}$.

Four parameters then define the double-block distribution: the constants A and B , and the desired second and third moments, σ_r^2 and ζ_r^3 . Through Eqs. (C.9-13) these four parameters completely define m_1 , m_2 , p_1 , p_2 , Δ_1 , and Δ_2 and, correspondingly, the double-block distribution, $P_a(r)$.

As a result of this procedure to define $P_a(r)$, the first, second, and third moments of the distribution are explicitly specified, while the higher moments are implicitly defined through m_1 , m_2 , p_1 , p_2 , Δ_1 , and Δ_2 , and can be calculated using the general moment equation (C.4). The higher ($n = 4, 5, \dots$) moments of $P_a(r)$ for $\Delta t/\tau \ll 1$ are

$$\overline{r_a^n(\Delta t)}_{\Delta t/\tau \ll 1} = \left(\frac{\Delta t}{\tau}\right) \frac{\left(\overline{w_f^3}\right)^{n-2}}{\left(\overline{w_f^2}\right)^{n-3}} \left\{ \frac{3^{n-2}[(1+A)^{n+1} - (1-A)^{n+1}]C^{n-3}}{2^{n-2}(n+1)AD^{n-3}E^{n-2}} \right\}, \quad n = 4, 5, \dots$$

Fluid velocity moments

The moments of $r(\Delta t)$ in the linear-skewed Langevin equation model's velocity equation are related to the fluid velocity moments, for $\Delta t/\tau \ll 1$, through Eq. (3.6.7):

$$\overline{r^n(\Delta t)}_{\Delta t/\tau \ll 1} = \langle \langle r^n(\Delta t) \rangle \rangle_{\Delta t/\tau \ll 1} = \Gamma_n \Delta t = n \langle \langle w_f^n \rangle \rangle \frac{\Delta t}{\tau},$$

where $n=1, 2, \dots$ (note that we have used the property that the moments of r approach the cumulants of r in the small time limit).

Equating $\overline{r^n(\Delta t)}_{\Delta t/\tau \ll 1} = \overline{r_a^n(\Delta t)}_{\Delta t/\tau \ll 1}$, the higher fluid velocity cumulants corresponding to the double-block distribution are

$$\langle \langle w_f^n \rangle \rangle = \frac{(\overline{w_f^3})^{n-2}}{(\overline{w_f^2})^{n-3}} \left\{ \frac{3^{n-2} [(1+A)^{n+1} - (1-A)^{n+1}] C^{n-3}}{2^{n-2} n(n+1) A D^{n-3} E^{n-2}} \right\}, \quad n = 4, 5, \dots$$

The constants A and B were assigned values of $A = B = 1$. These values resulted in reasonable agreement between the linear-skewed Langevin equation model predicted velocity distributions and experimentally determined velocity distributions published by Deardorff and Willis (1985) and shown in Chapter 4. With $A = B = 1$, the fourth, fifth, and sixth fluid velocity moments are

$$\overline{w_f^4} = \frac{9\overline{w_f^3}^2}{5\overline{w_f^2}^2} + 3\overline{w_f^2}^2,$$

$$\overline{w_f^5} = \frac{18\overline{w_f^3}^3}{5\overline{w_f^2}^2} + 10\overline{w_f^2}\overline{w_f^3},$$

$$\overline{w_f^6} = \frac{54\overline{w_f^3}^4}{7\overline{w_f^2}^3} + 10\overline{w_f^3}^2 + 15\overline{w_f^2}\overline{w_f^4} - 30\overline{w_f^2}^3.$$

Continuity of $w(t)$

As discussed in Chapter 3, the velocity described by the linear-skewed Langevin equation model is well behaved in the sense that it is mean-square continuous, that is $\lim_{\Delta t \rightarrow 0} \overline{\Delta w^2(\Delta t)} = 0$. In fact, all the moments of the velocity change for the linear-skewed Langevin equation vanish for vanishing time step, $\lim_{\Delta t \rightarrow 0} \overline{\Delta w^n(\Delta t)} = \lim_{\Delta t \rightarrow 0} \overline{r^n(\Delta t)} = 0$, as shown by Eq. (3.6.7). However, the linear-skewed Langevin equation describes a process in which the possible realizations of $w(t)$, or "sample paths", are not continuous functions of time.

The possible realizations of $w(t)$ are continuous functions of time if, for any $\varepsilon > 0$,

$$\lim_{\Delta t \rightarrow 0} \frac{\int_{|w_{\Delta t} - w_0| > \varepsilon} P(w_{\Delta t}; w_0) dw_{\Delta t}}{\Delta t} = 0 \quad (\text{C.14})$$

where $P(w_{\Delta t}; w_0)$ is the probability of velocity $w_{\Delta t}$ at $t = \Delta t$, given velocity w_0 at $t = 0$ (Gardiner, 1990). For convenience, define

$$F_\varepsilon \equiv \int_{|w_{\Delta t} - w_0| > \varepsilon} P(w_{\Delta t}; w_0) dw_{\Delta t}.$$

F_ε is the probability that the absolute value of the difference between $w_{\Delta t}$ and w_0 is greater than ε . Therefore, Eq. (C.14) can be re-written as follows:

$$\lim_{\Delta t \rightarrow 0} \frac{F_\varepsilon}{\Delta t} = 0.$$

Eq. (C.14) states that probability that the velocity at $t = \Delta t$ is finitely different than the velocity at $t = 0$ goes to zero faster than Δt , as Δt goes to zero.

We will now examine the continuity condition given by Eq. (C.14) for the linear-skewed Langevin equation model using the double-block distribution. Consider the case where $w_0 = 0$, so that

$$P(w_{\Delta t}; w_0) = P_a(r)$$

(see Eq. (3.6.4)). For the continuity condition, we are interested in the small time limiting behavior of $P_a(r)$. For $\Delta t/\tau \ll 1$, the parameters of double-block distribution, $P_a(r)$, (with $A = B = 1$) become (retaining only lowest order $\Delta t/\tau$ terms)

$$m_1 = -\frac{2\overline{w_f^2}^2}{3\overline{w_f^3}} \frac{\Delta t}{\tau},$$

$$\Delta_1 = \sqrt{2\overline{w_f^2}}^{1/2} \left(\frac{\Delta t}{\tau} \right)^{1/2},$$

$$m_2 = \frac{3\overline{w_f^3}}{2\overline{w_f^2}} + \frac{2\overline{w_f^2}^2}{3\overline{w_f^3}} \left(\frac{\Delta t}{\tau} \right),$$

$$\Delta_2 = \left[\left(\frac{3\overline{w_f^3}}{2\overline{w_f^2}} \right)^2 + 4\overline{w_f^2} \left(\frac{\Delta t}{\tau} \right) \right]^{1/2}.$$

Therefore, for $\Delta t/\tau \ll 1$

$$m_1 = O(\Delta t),$$

$$\Delta_1 = O(\Delta t^{1/2}),$$

$$m_2 = \frac{3\overline{w_f^3}}{2\overline{w_f^2}} = \text{constant},$$

$$\Delta_2 = \frac{\overline{3w_f^3}}{2\overline{w_f^2}} = \text{constant},$$

and

$$p_1 = O(\Delta t^{-1/2}),$$

$$p_2 = O(\Delta t).$$

So the continuity condition (C.14) becomes

$$\begin{aligned} \lim_{\Delta t \rightarrow 0} \frac{F_\varepsilon}{\Delta t} &= \lim_{\Delta t \rightarrow 0} \frac{\int_{|r|>\varepsilon} P_a(r) dr}{\Delta t} \\ &= \lim_{\Delta t \rightarrow 0} \frac{\int_{|r|>\varepsilon} [f_1(r) + f_2(r)] dr}{\Delta t} \\ &= \lim_{\Delta t \rightarrow 0} \left(\frac{1}{\Delta t} \right) \left\{ \int_{\substack{\mathbb{T} \setminus \mathbb{A} \times \mathbb{A} \\ \equiv F_{-\varepsilon 1}}} f_1(r) dr + \int_{\substack{\mathbb{T} \setminus \mathbb{A} \times \mathbb{A} \\ \equiv F_{-\varepsilon 2}}} f_2(r) dr + \int_{\substack{\mathbb{T} \times \mathbb{A} \\ \equiv F_{+\varepsilon 1}}} f_1(r) dr + \int_{\substack{\mathbb{T} \times \mathbb{A} \\ \equiv F_{+\varepsilon 2}}} f_2(r) dr \right\} \end{aligned}$$

where

$$F_{-\varepsilon 1} = \begin{cases} (-\varepsilon - (m_1 - \Delta_1))p_1, & \text{if } (m_1 - \Delta_1) < -\varepsilon \\ 0, & \text{if } (m_1 - \Delta_1) > -\varepsilon \end{cases}$$

$$F_{-\varepsilon 2} = \begin{cases} (-\varepsilon - (m_2 - \Delta_2))p_2, & \text{if } (m_2 - \Delta_2) < -\varepsilon \\ 0, & \text{if } (m_2 - \Delta_2) > -\varepsilon \end{cases}$$

$$F_{+\varepsilon 1} = \begin{cases} (m_1 + \Delta_1 - \varepsilon)p_1, & \text{if } (m_1 + \Delta_1) > \varepsilon \\ 0, & \text{if } (m_1 + \Delta_1) < \varepsilon \end{cases}$$

$$F_{+\varepsilon 2} = \begin{cases} (m_2 + \Delta_2 - \varepsilon)p_2, & \text{if } (m_2 + \Delta_2) > \varepsilon \\ 0, & \text{if } (m_2 + \Delta_2) < \varepsilon \end{cases}$$

Note that $\lim_{\Delta t \rightarrow 0} m_2 = \lim_{\Delta t \rightarrow 0} \Delta_2 = \text{constant}$, so that $\lim_{\Delta t \rightarrow 0} (m_2 - \Delta_2) = 0$ and $\lim_{\Delta t \rightarrow 0} F_{-\varepsilon 2} = 0$. For positive values of $F_{+\varepsilon 1}$ and $F_{-\varepsilon 1}$, both $\frac{F_{+\varepsilon 1}}{\Delta t}$ and $\frac{F_{-\varepsilon 1}}{\Delta t}$ depend on Δt as follows:

$$O(\Delta t^{-1}) - O(\Delta t^{-3/2}),$$

where small time behavior of the double-block parameters, m_1 , m_2 , Δ_1 , Δ_2 , p_1 , and p_2 , given above, has been used (recall that these parameters are all positive except $m_1 < 0$). So, for small $\varepsilon < \lim_{\Delta t \rightarrow 0} (m_2 + \Delta_2)$,

$$\lim_{\Delta t \rightarrow 0} \frac{F_{-\varepsilon 1}}{\Delta t} = 0$$

$$\lim_{\Delta t \rightarrow 0} \frac{F_{-\varepsilon 2}}{\Delta t} = 0$$

$$\lim_{\Delta t \rightarrow 0} \frac{F_{+\varepsilon 1}}{\Delta t} = 0$$

$$\lim_{\Delta t \rightarrow 0} \frac{F_{+\varepsilon 2}}{\Delta t} = \text{constant}$$

Therefore,

$$\lim_{\Delta t \rightarrow 0} \frac{F_\varepsilon}{\Delta t} = \text{constant}$$

and *not* zero for all $\varepsilon > 0$ as required for continuity. Therefore, the process described by the skewed double-block distribution is *not* continuous in this sense. This discontinuous property is due to the probability of a value of $r > \varepsilon$ from block 2, $F_{+\varepsilon 2}$, decreasing linearly in Δt , and not faster than Δt , as required to meet the continuity condition (C.14). Note, however, that the probability of selecting a value of r from block 2 does decrease to zero as Δt goes to zero,

$$\lim_{\Delta t \rightarrow 0} (2\Delta_2 p_2) = 0,$$

while the probability of selecting a value from block 1 goes to one,

$$\lim_{\Delta t \rightarrow 0} (2\Delta_1 p_1) = 1.$$

In this sense, the change in velocity is well behaved.

In contrast, for the special case in which $P_a(r)$ is *not* skewed (i.e., $\langle\langle w_f^3 \rangle\rangle = 0$ so that $\overline{r^3} = 0$), the small- Δt behavior of the double-block parameters is

$$m_2 = -m_1 = O(\Delta t^{1/2}),$$

$$\Delta_2 = \Delta_1 = O(\Delta t^{1/2}),$$

$$p_2 = p_1 = O(\Delta t^{-1/2}),$$

and

$$\lim_{\Delta t \rightarrow 0} \frac{F_{-\varepsilon 1}}{\Delta t} = \lim_{\Delta t \rightarrow 0} \frac{F_{-\varepsilon 2}}{\Delta t} = \lim_{\Delta t \rightarrow 0} \frac{F_{+\varepsilon 1}}{\Delta t} = \lim_{\Delta t \rightarrow 0} \frac{F_{+\varepsilon 2}}{\Delta t} = 0.$$

Therefore, if the random term is not skewed, the process *is* continuous.

Appendix D: CBL simulation sensitivity tests

As discussed in Section 4.3.5, additional CBL dispersion simulations were performed to test the sensitivity of results to values of the input parameters τ , $\sigma_{w_f}^2$, and S . Additional simulations for the three source heights ($Z_s = 0.067, 0.24$, and 0.49) used in the Willis & Deardorff experiments were performed with both Langevin equation models using reflection method II and two alternative values of τ , $\sigma_{w_f}^2$, and S , one near the low end and one near the high end of the range of values found in the CBL. These low-end and high-end values are $\tau w_*/h = 0.5$ and 1.2 , $\sigma_{w_f}^2/w_*^2 = 0.2$ and 0.4 , and $S = 0.4$ and 1.2 , respectively. The "best-estimate" values, used in the simulations shown in Chapter 4, are $\tau w_*/h = 0.8$, $\sigma_{w_f}^2/w_*^2 = 0.31$, and $S = 0.78$. Results from simulations for each of the three source heights with each of the two Langevin equation models are shown below. The mean height and standard deviation of the vertical concentration distribution, \bar{Z} and σ_Z , and the near-surface concentration, $C(X,0)$, calculated from the simulations using the three different values (low, best-estimate, and high) for each parameter (τ , $\sigma_{w_f}^2$, or S) are plotted along with observations from Willis & Deardorff's experiments in Figs. D.1 through D.18.

The mean square error (MSE) and mean fractional error (MFE) of the simulated values of \bar{z}/h , σ_z/h , and $C(X,0)$ were estimated using observations from the Willis & Deardorff experiments. The mean square error (MSE) is defined here as $MSE = \frac{1}{n_{obs}} \sum_{i=1}^{n_{obs}} (p_i - o_i)^2$, where o_i is a observed value, p_i is the model predicted value interpolated to the point of the observation, and n_{obs} is the number of observations. MSE is a measure of the absolute error in the predictions. The mean fractional error (MFE) is defined here as $MFE = \frac{1}{n_{obs}} \sum_{i=1}^{n_{obs}} \frac{(p_i - o_i)}{o_i}$, and is a measure of the bias of the predictions. Table D.1 presents the MSE and MFE , and the standard error (a measure of uncertainty in the estimated mean value) of the MSE and MFE for each simulation. Considering all the

results, the *MFE* values indicate that there is no systematic bias in predictions. The *MFE* values do indicate that there is a tendency for observed $C(X,0)$ to be over predicted for $Z_s = 0.067$, and under predicted for $Z_s = 0.49$. Table D.2 presents the model-predicted maximum near-surface concentration, $C(X,0)$, from each simulation, and the observed maximum $C(X,0)$ from the Willis & Deardorff experiments.

The simulation results indicate that \bar{Z} , σ_z and $C(X,0)$, varied with different values of τ , $\sigma_{w_f}^2$, and S in a similar manner for both Langevin equation models. As the value of τ is increased, the rate at which \bar{Z} and σ_z increases with downwind distance (travel time) is significantly greater for $Z_s = 0.067$ and $0 < X < 1.5$. For $Z_s = 0.24$, this effect was also present, but less pronounced. For $Z_s = 0.49$, larger values of τ result in a slightly faster initial ($0 < X < 1$) rate of decrease of \bar{Z} and slightly faster initial rate of increase of σ_z with downwind distance. For $Z_s = 0.49$, larger values of τ also result in higher maximum $C(X,0)$, as well as smaller X at which the maximum $C(X,0)$ occurs. This effect was also present for $Z_s = 0.24$, but was less pronounced. For $Z_s = 0.49$, higher values of τ consistently improve results for both models.

Larger values of $\sigma_{w_f}^2$ result in a more rapid initial ($0 < X < 1$) rate of increase of \bar{Z} with downwind distance for $Z_s = 0.067$ and 0.24 . For $Z_s = 0.49$, larger values of $\sigma_{w_f}^2$ result in a more rapid initial rate of decrease of \bar{Z} with downwind distance. Larger values of $\sigma_{w_f}^2$ also result in a more rapid increase in σ_z with downwind distance, as expected, for all three source heights, Z_s . Larger values of $\sigma_{w_f}^2$ also result in smaller X at which the peak $C(X,0)$ occurs for all Z_s (and also some tendency for higher peak $C(X,0)$ values). This effect might be explained by the increase in the magnitude of the mean negative fluid velocity, for the modeled fluid velocity distributions, with increasing $\sigma_{w_f}^2$. The only consistent improvement in the overall results of both models (compared to the original

simulations using the best-estimate values) was found for $Z_S = 0.49$ when using the largest value of $\sigma_{w_f}^2$.

Larger values of S result in a more rapid initial ($0 < X < 1$) rate of decrease in \bar{Z} with downwind distance for $Z_S = 0.49$. For $Z_S = 0.24$, larger values of S result in a smaller initial rate of increase in \bar{Z} with downwind distance. For $Z_S = 0.067$, larger values of S result in a faster initial rate of increase in \bar{Z} and σ_z with downwind distance. Larger values of S tended to result in higher peak $C(X,0)$. For $Z_S = 0.49$ and 0.24 , larger S results in larger X at which the peak $C(X,0)$ occurs. These effects might be explained by the decrease in the magnitude of the mean negative fluid velocity, the decrease in the variance of the negative velocity, and the increase in the total probability of a negative velocity with increasing S for the modeled fluid velocity distributions. Changes in S have a larger effect on the results of the nonlinear-Gaussian model than the linear-skewed model (for the range of S tested). The only overall improvement on the results of simulations using the original best-estimate parameter values was found for the nonlinear-Gaussian model when using the lowest value of $S = 0.4$ (in particular, results for $Z_S = 0.24$ and 0.49 significantly improved).

For a particular source height and a particular model, some combinations of input parameter values significantly improve some of the results. For $Z_S = 0.067$, the linear-skewed model results for \bar{Z} and σ_z improve when using the largest values of τ , $\sigma_{w_f}^2$ or S . For $Z_S = 0.24$ and 0.49 , the nonlinear-Gaussian model results for $C(X,0)$ improve significantly, and the \bar{Z} and σ_z results also tend to improve, using the smallest value of S . For $Z_S = 0.49$, nonlinear-Gaussian model results for \bar{Z} , σ_z , and $C(X,0)$ improve using the largest values of τ or $\sigma_{w_f}^2$; results for the location of the maximum $C(X,0)$ improve using the smallest value of S ; and results for the maximum $C(X,0)$ improve using the largest value of S . For $Z_S = 0.49$, linear-skewed model results for \bar{Z} and

$C(X,0)$ improve significantly when the largest values of τ , $\sigma_{w_f}^2$, and S were used together.

Lagrangian time scale sensitivity tests

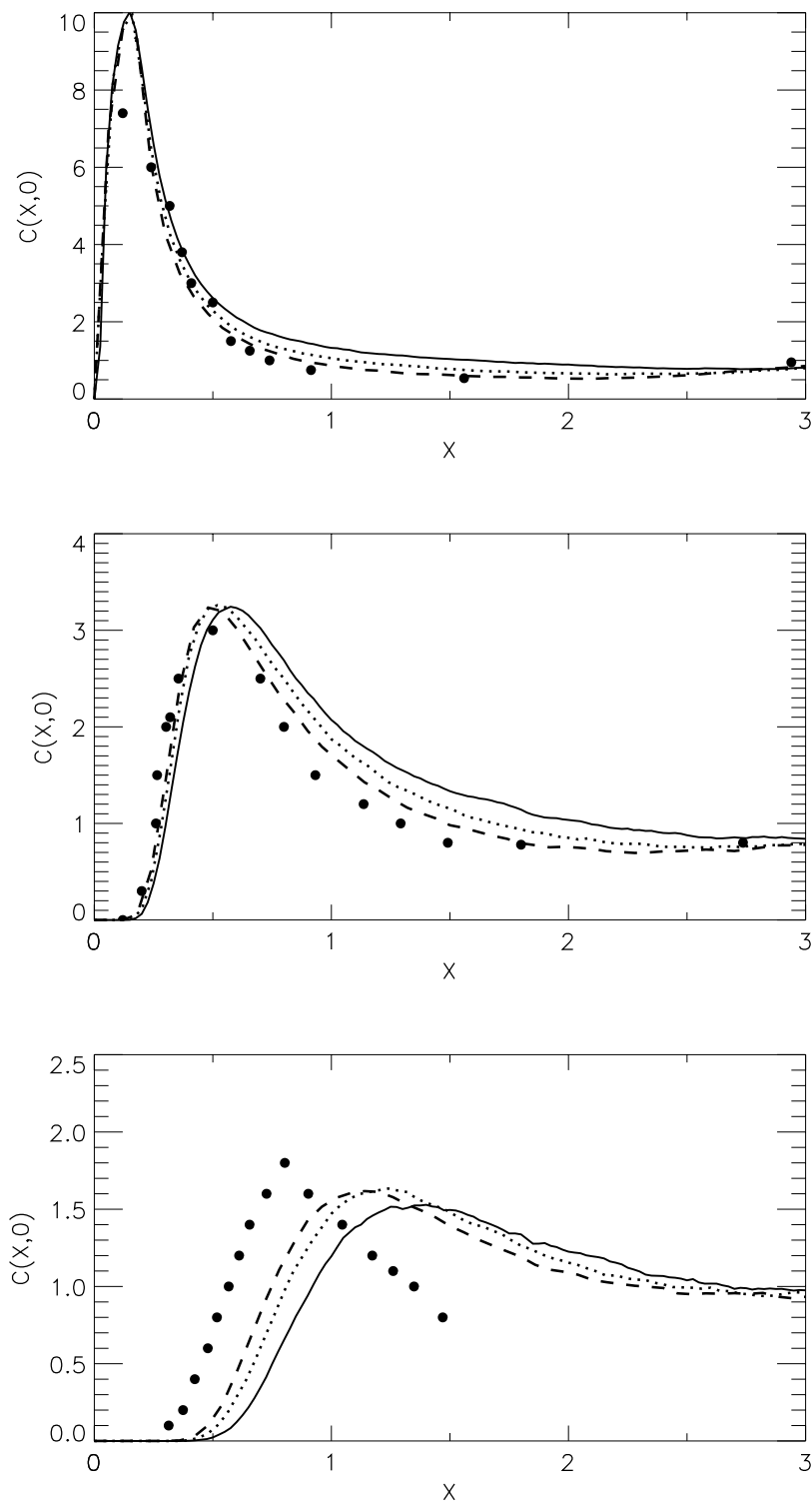


Fig. D.1. Calculations of dimensionless near-ground concentration for dimensionless source height of (a) $Z_s = 0.067$ (top figure), (b) $Z_s = 0.24$ (middle), and (c) $Z_s = 0.49$ (bottom) using the nonlinear-Gaussian Langevin equation model and three values for the Lagrangian velocity correlation time: $\tau_{w_*}/h = 0.5$ (solid line), 0.8 (dotted line), 1.2 (dashed line). Circles are data from Willis & Deardorff experiments.

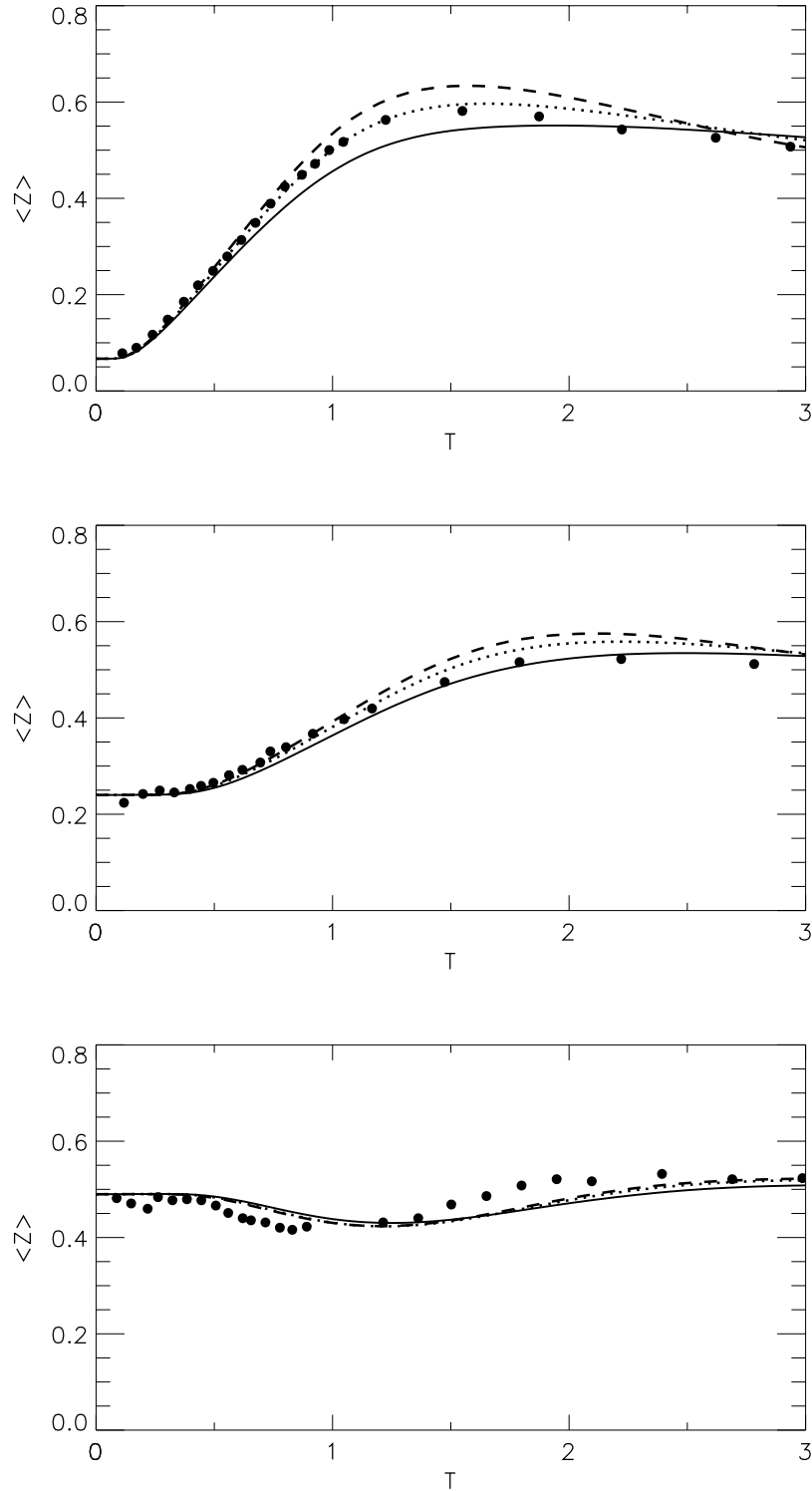


Fig. D.2. Calculations of dimensionless mean height of concentration distribution for dimensionless source height of (a) $Z_s = 0.067$ (top figure), (b) $Z_s = 0.24$ (middle), and (c) $Z_s = 0.49$ (bottom) using the nonlinear-Gaussian Langevin equation model and three values for the Lagrangian velocity correlation time: $\tau_{w_s}/h = 0.5$ (solid line), 0.8 (dotted line), 1.2 (dashed line). Circles are data from Willis & Deardorff water tank experiments.

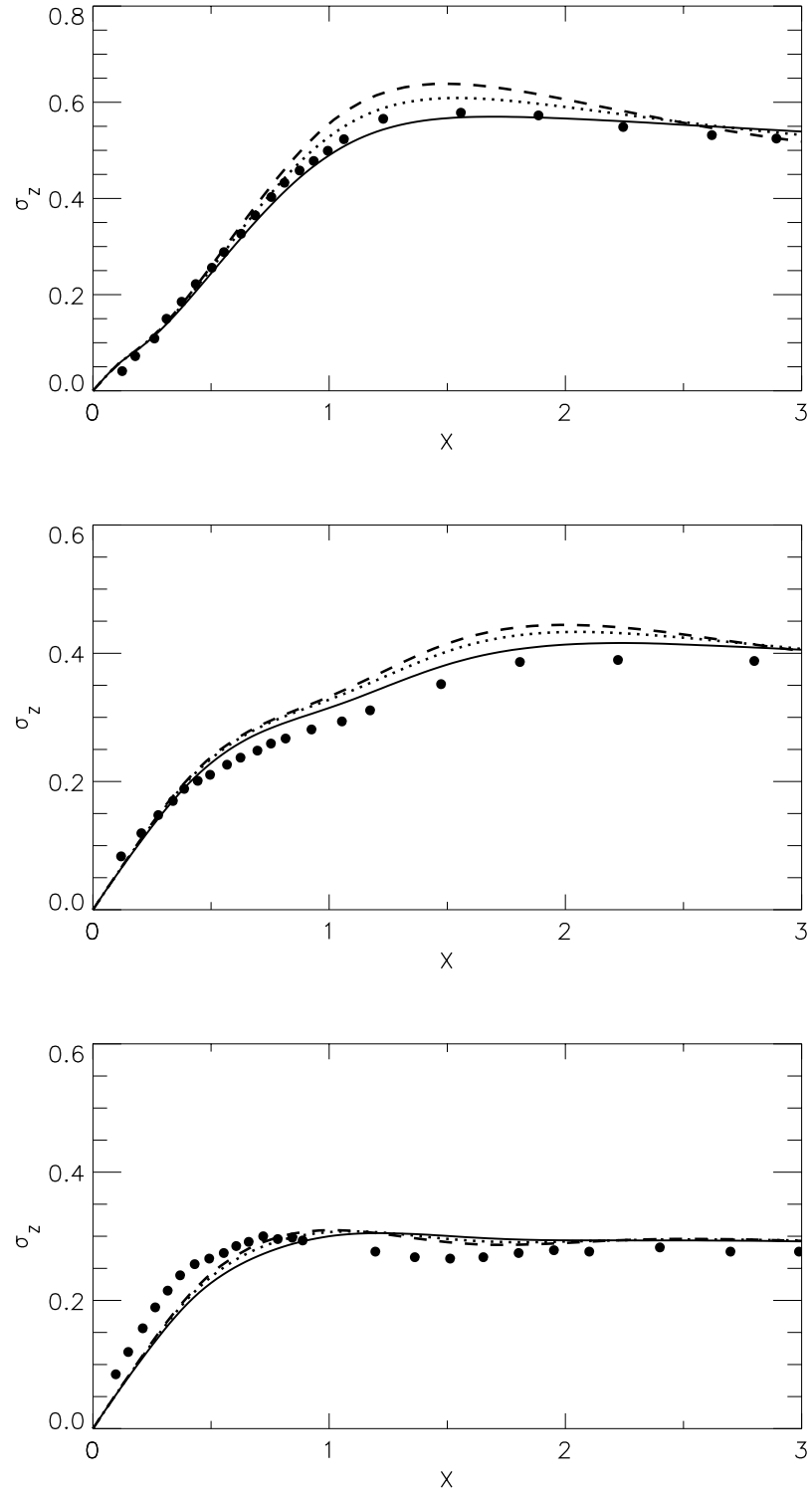


Fig. D.3. Calculations of dimensionless standard deviation of concentration distribution for dimensionless source height Z_s of (a) 0.067 (top figure), (b) 0.24 (middle), and (c) 0.49 (bottom) using the *nonlinear-Gaussian* Langevin equation model and *three values for the Lagrangian velocity correlation time*: $\tau_{w*}/h = 0.5$ (solid line), 0.8 (dotted line), 1.2 (dashed line). Circles are data from Willis & Deardorff water tank experiments.

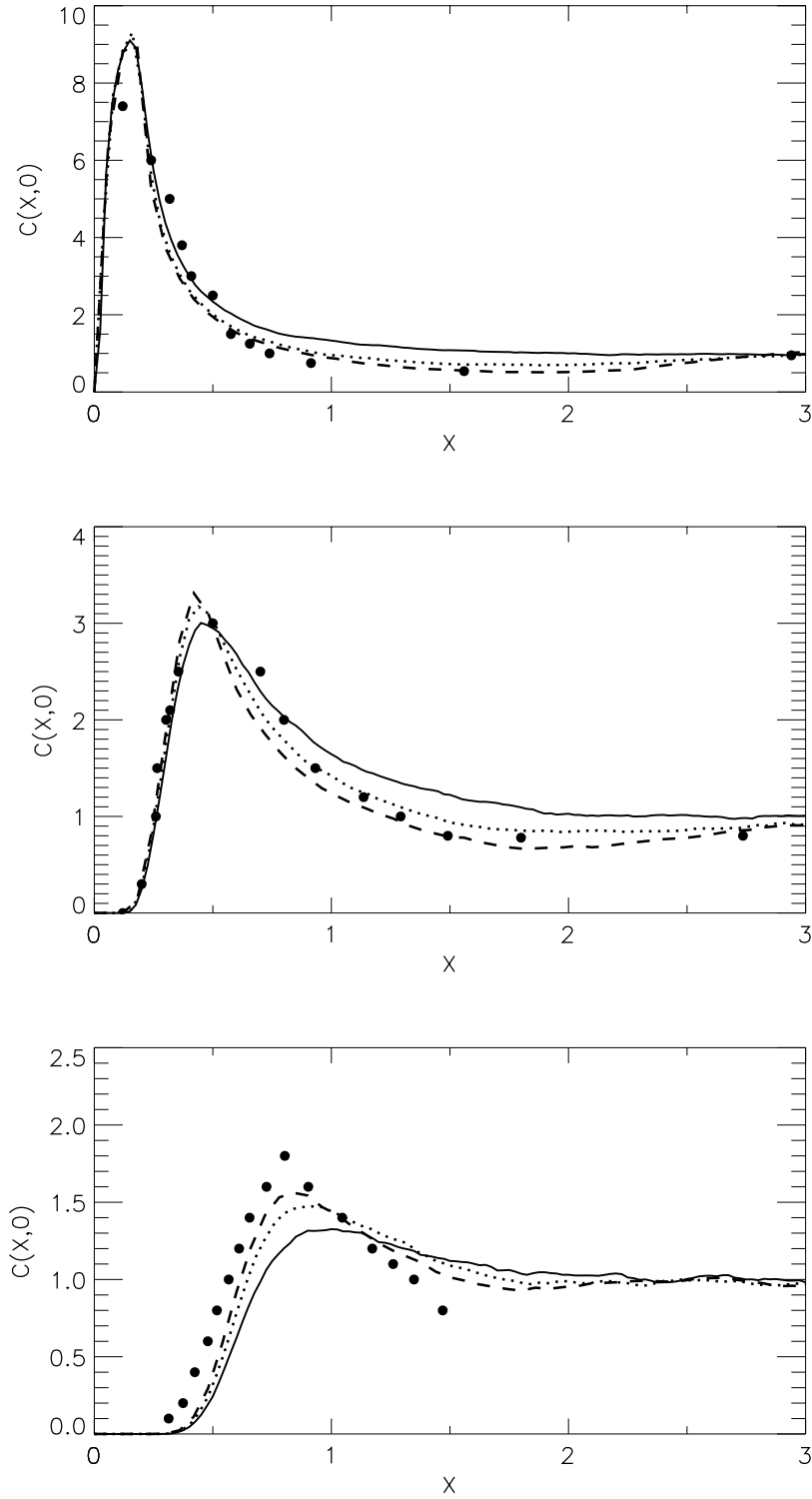


Fig. D.4. Calculations of dimensionless near-ground concentration for dimensionless source height of (a) $Z_s = 0.067$ (top figure), (b) $Z_s = 0.24$ (middle), and (c) $Z_s = 0.49$ (bottom) using the *linear-skewed* Langevin equation model and *three* values for the *Lagrangian velocity correlation time*: $\tau w_*/h = 0.5$ (solid line), 0.8 (dotted line), 1.2 (dashed line). Circles are data from Willis & Deardorff experiments.

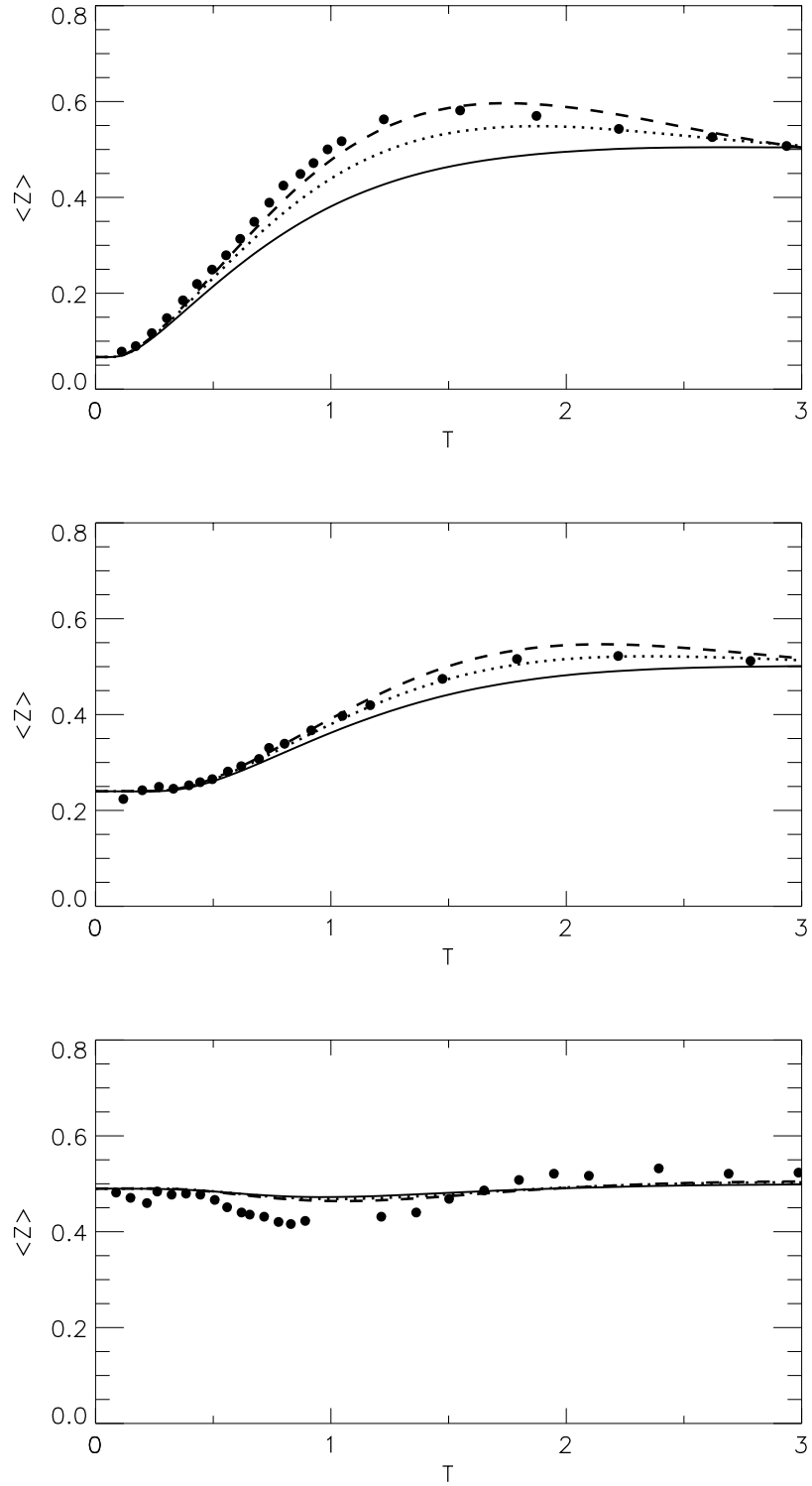


Fig. D.5. Calculations of dimensionless mean height of concentration distribution for dimensionless source height of (a) $Z_s = 0.067$ (top figure), (b) $Z_s = 0.24$ (middle), and (c) $Z_s = 0.49$ (bottom) using the linear-skewed Langevin equation model and three values for the Lagrangian velocity correlation time: $\tau_{w_e}/h = 0.5$ (solid line), 0.8 (dotted line), 1.2 (dashed line). Circles are data from Willis & Deardorff water tank experiments.

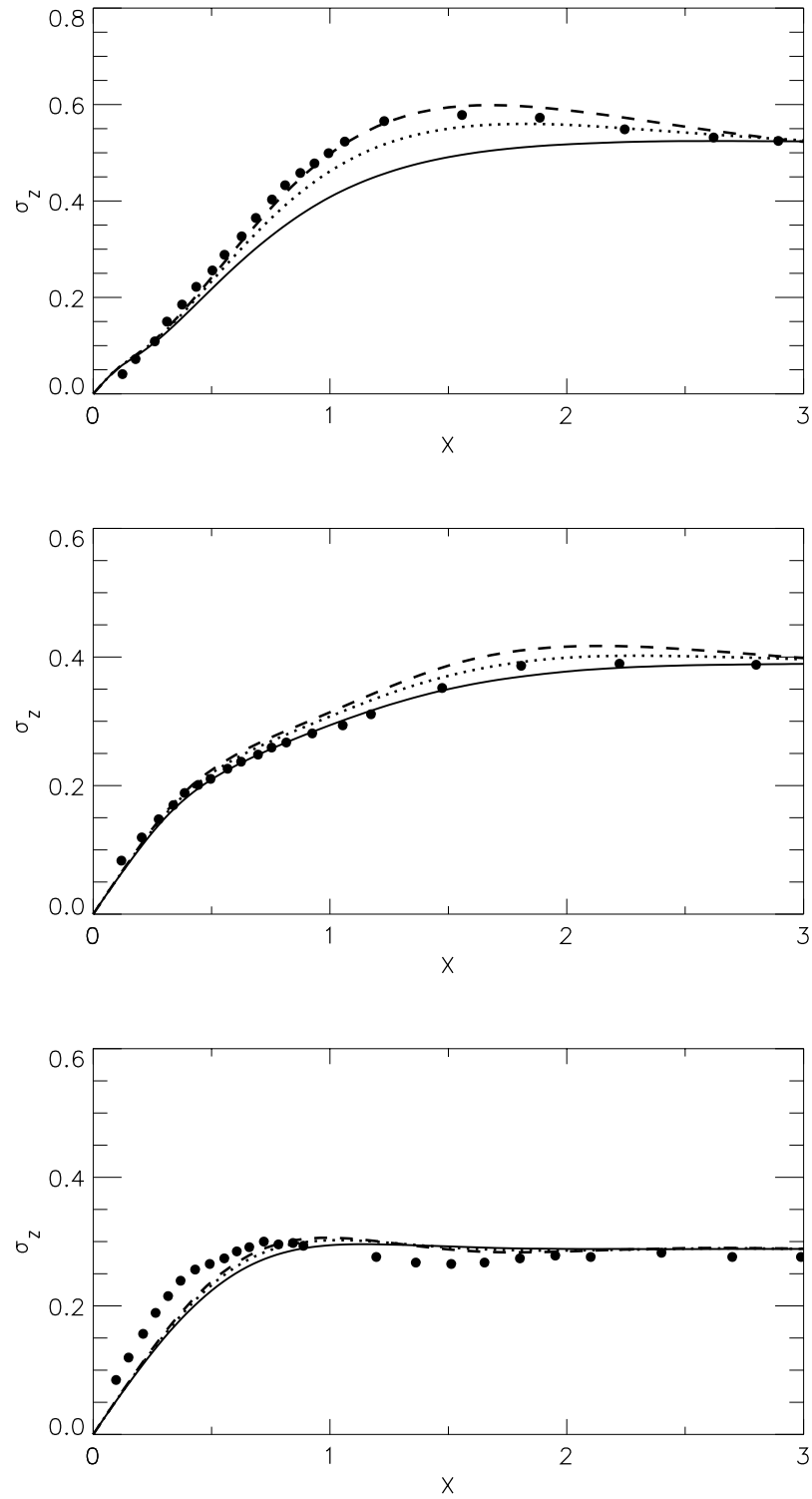


Fig. D.6. Calculations of dimensionless standard deviation of concentration distribution for dimensionless source height Z_s of (a) 0.067 (top figure), (b) 0.24 (middle), and (c) 0.49 (bottom) using the *linear-skewed* Langevin equation model and *three values for the Lagrangian velocity correlation time*: $\tau_{w*}/h = 0.5$ (solid line), 0.8 (dotted line), 1.2 (dashed line). Circles are data from Willis & Deardorff water tank experiments.

Velocity skewness sensitivity tests

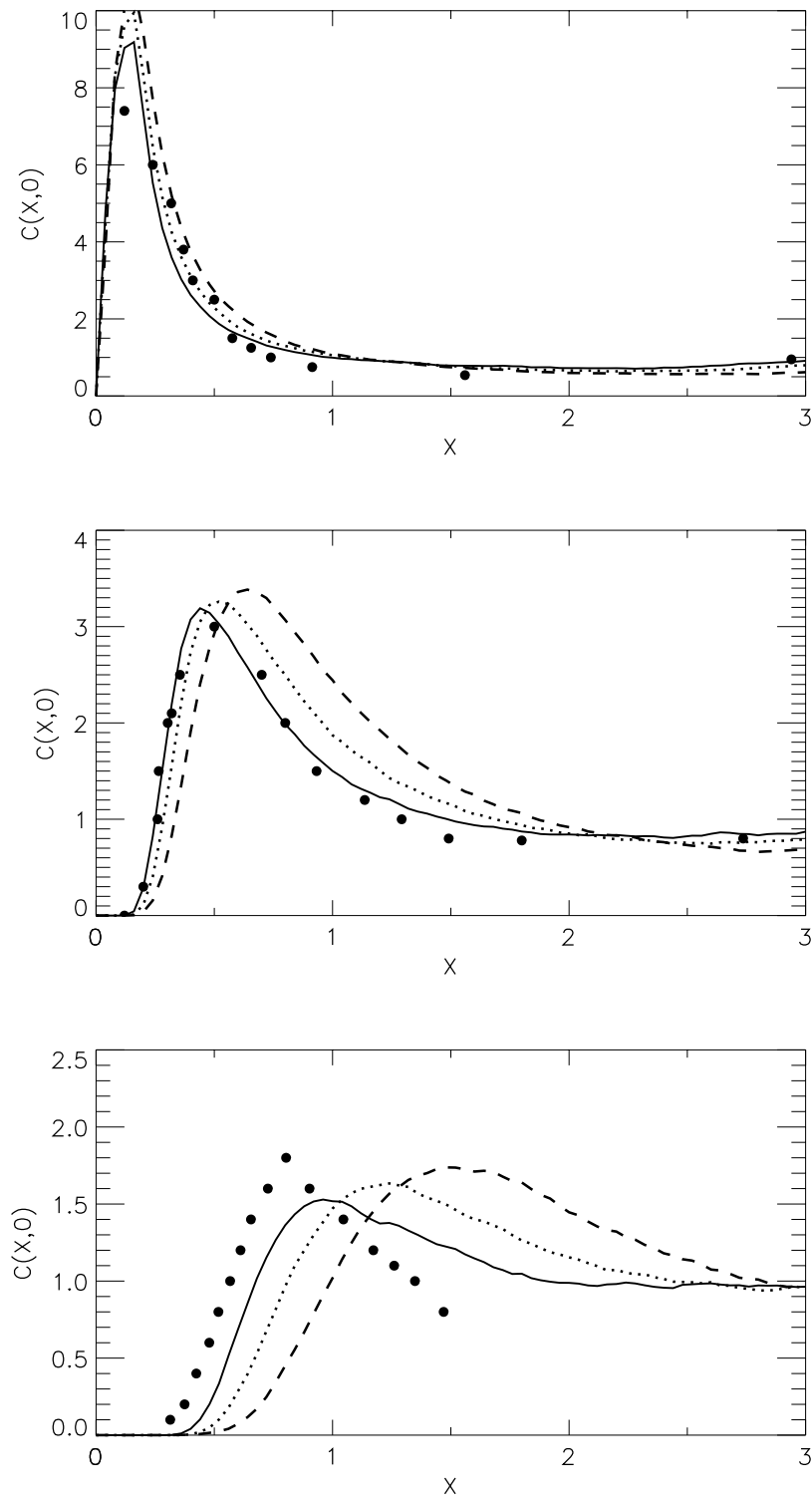


Fig. D.7. Calculations of dimensionless near-ground concentration for dimensionless source height of (a) $Z_s = 0.067$ (top figure), (b) $Z_s = 0.24$ (middle), and (c) $Z_s = 0.49$ (bottom) using the *nonlinear-Gaussian* Langevin equation model and three values for fluid velocity skewness : $S = 0.4$ (solid line), 0.78 (dotted line), 1.2 (dashed line). Circles are data from Willis & Deardorff experiments.

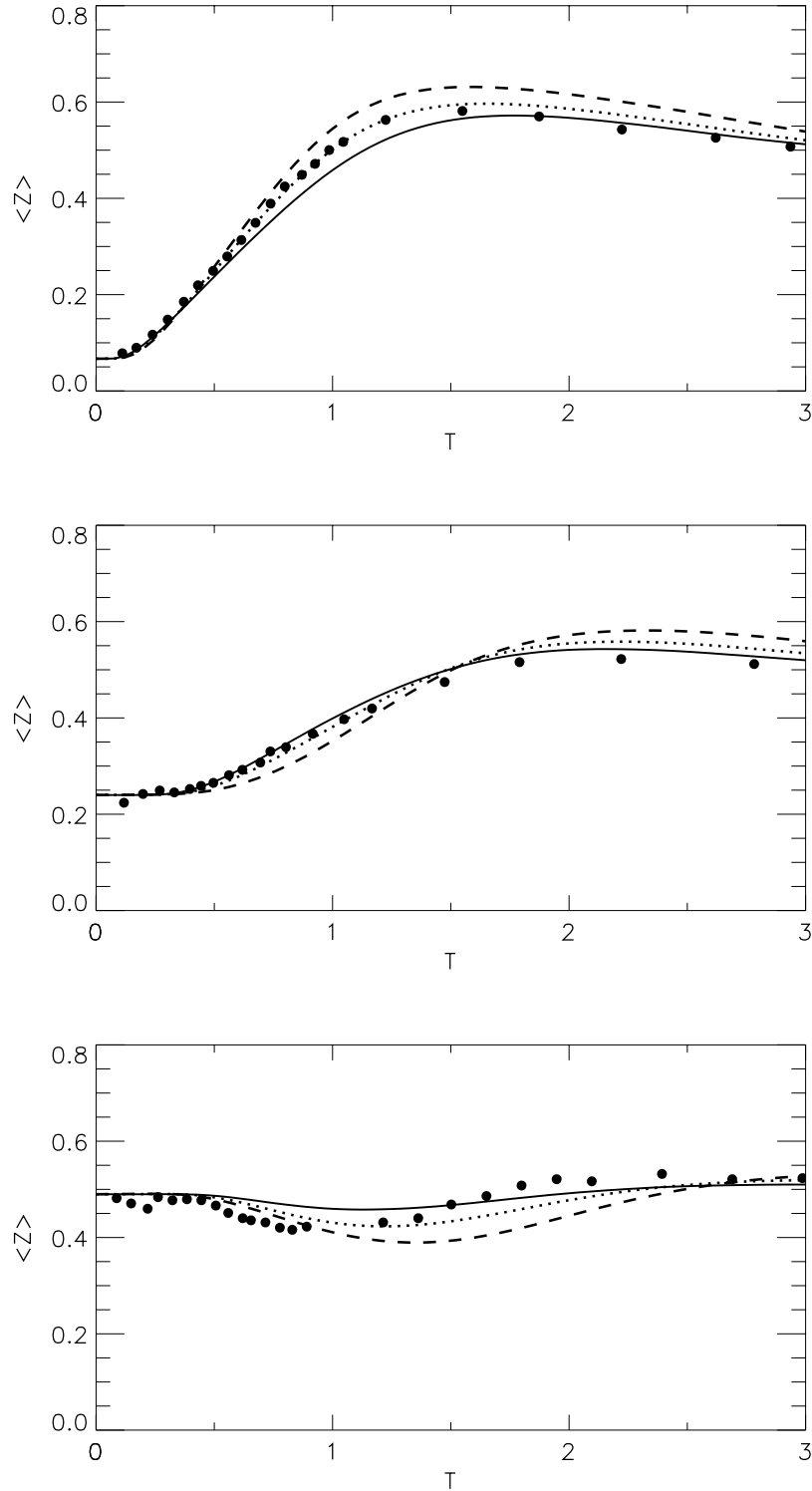


Fig. D.8. Calculations of dimensionless mean height of concentration distribution for dimensionless source height of (a) $Z_s = 0.067$ (top figure), (b) $Z_s = 0.24$ (middle), and (c) $Z_s = 0.49$ (bottom) using the *nonlinear-Gaussian* Langevin equation model and *three values for fluid velocity skewness* : $S = 0.4$ (solid line), 0.78 (dotted line), 1.2 (dashed line). Circles are data from Willis & Deardorff water tank experiments.

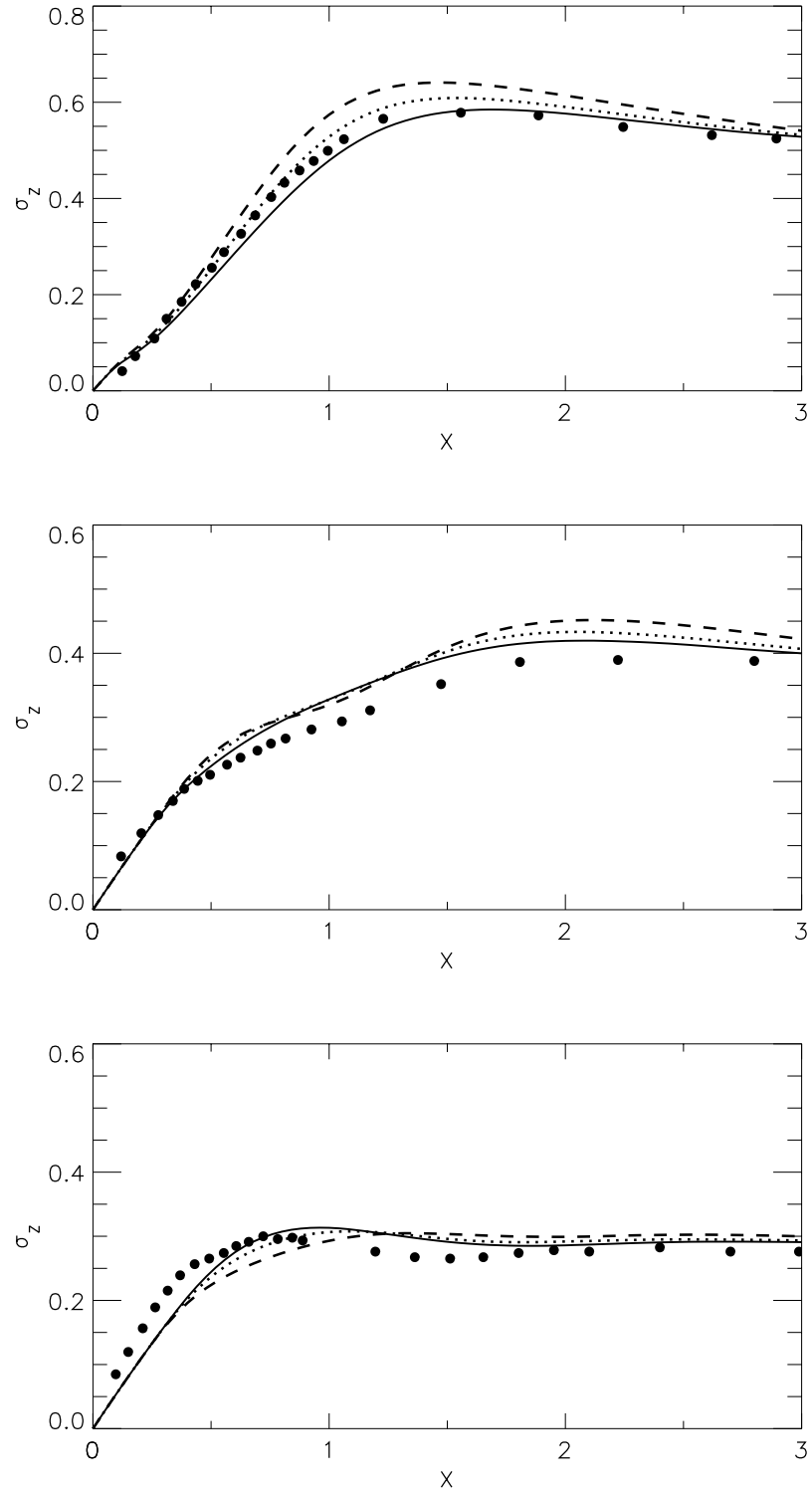


Fig. D.9. Calculations of dimensionless standard deviation of concentration distribution for dimensionless source height Z_s of (a) 0.067 (top figure), (b) 0.24 (middle), and (c) 0.49 (bottom) using the *nonlinear-Gaussian* Langevin equation model and *three values for fluid velocity skewness* : $S = 0.4$ (solid line), 0.78 (dotted line), 1.2 (dashed line). Circles are data from Willis & Deardorff water tank experiments.

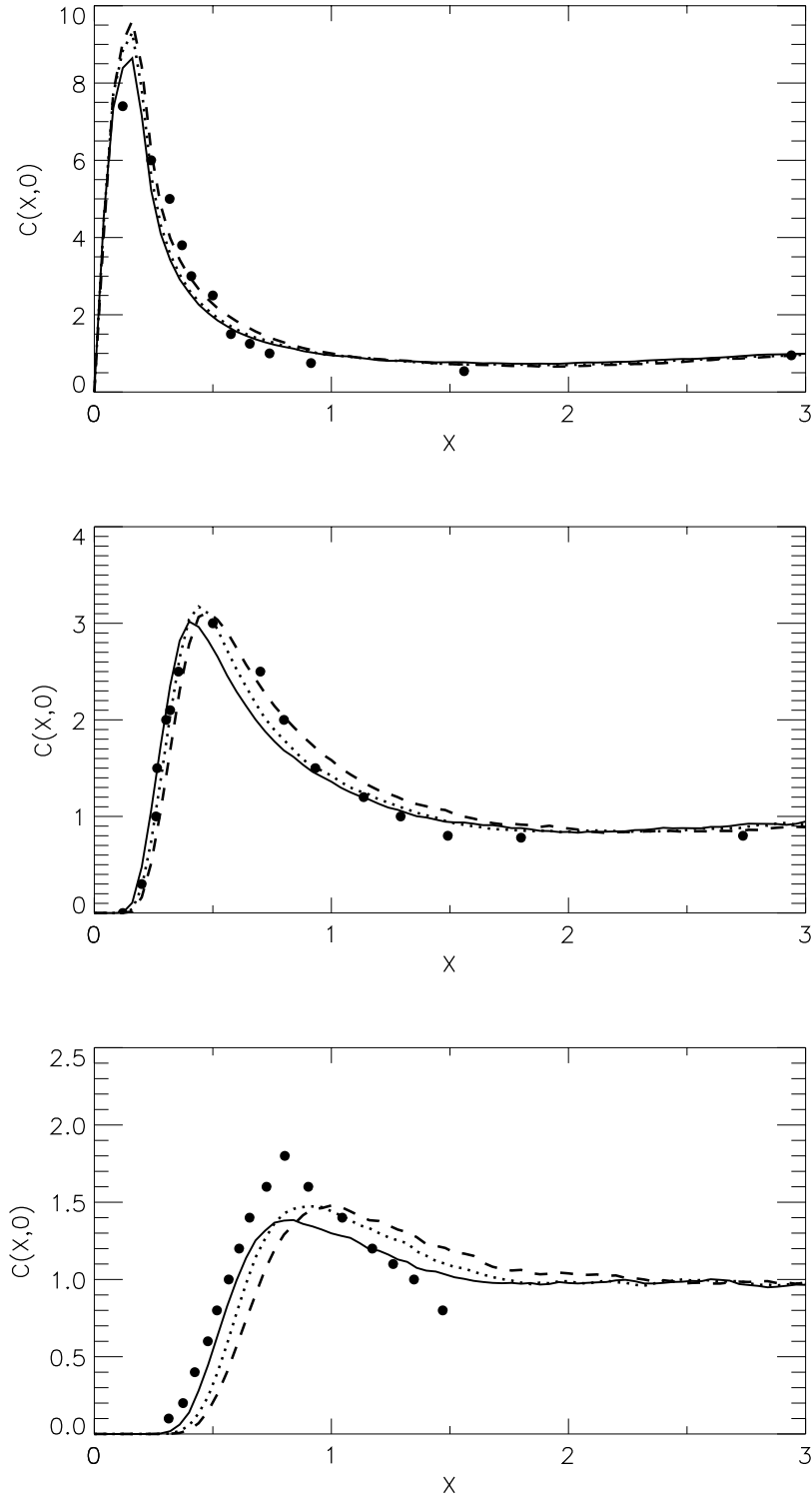


Fig. D.10. Calculations of dimensionless near-ground concentration for dimensionless source height of (a) $Z_s = 0.067$ (top figure), (b) $Z_s = 0.24$ (middle), and (c) $Z_s = 0.49$ (bottom) using the *linear-skewed* Langevin equation model and *three values for fluid velocity skewness* : $S = 0.4$ (solid line), 0.78 (dotted line), 1.2 (dashed line). Circles are data from Willis & Deardorff experiments.

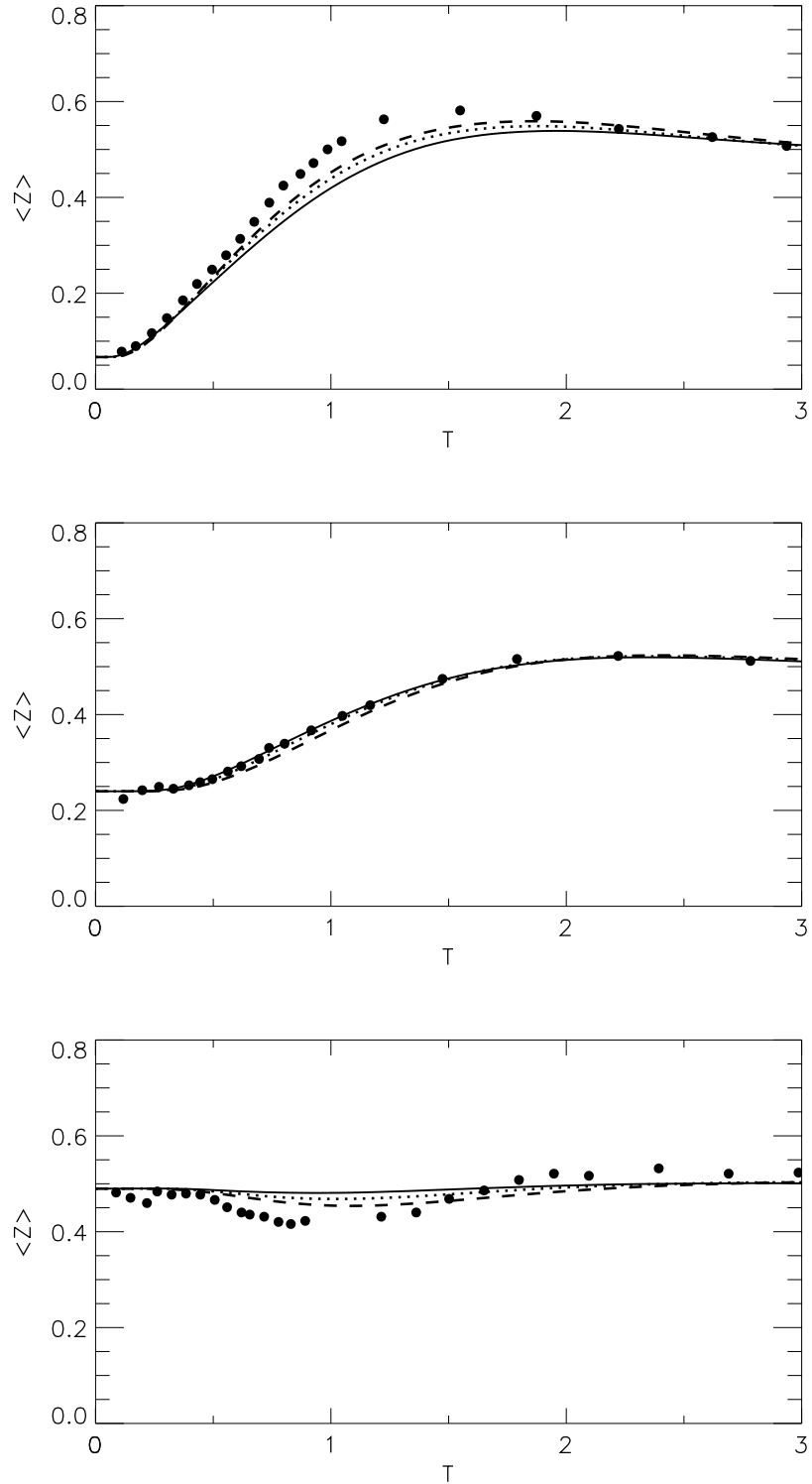


Fig. D.11. Calculations of dimensionless mean height of concentration distribution for dimensionless source height of (a) $Z_s = 0.067$ (top figure), (b) $Z_s = 0.24$ (middle), and (c) $Z_s = 0.49$ (bottom) using the *linear-skewed* Langevin equation model and *three values for fluid velocity skewness* : $S = 0.4$ (solid line), 0.78 (dotted line), 1.2 (dashed line). Circles are data from Willis & Deardorff water tank experiments.

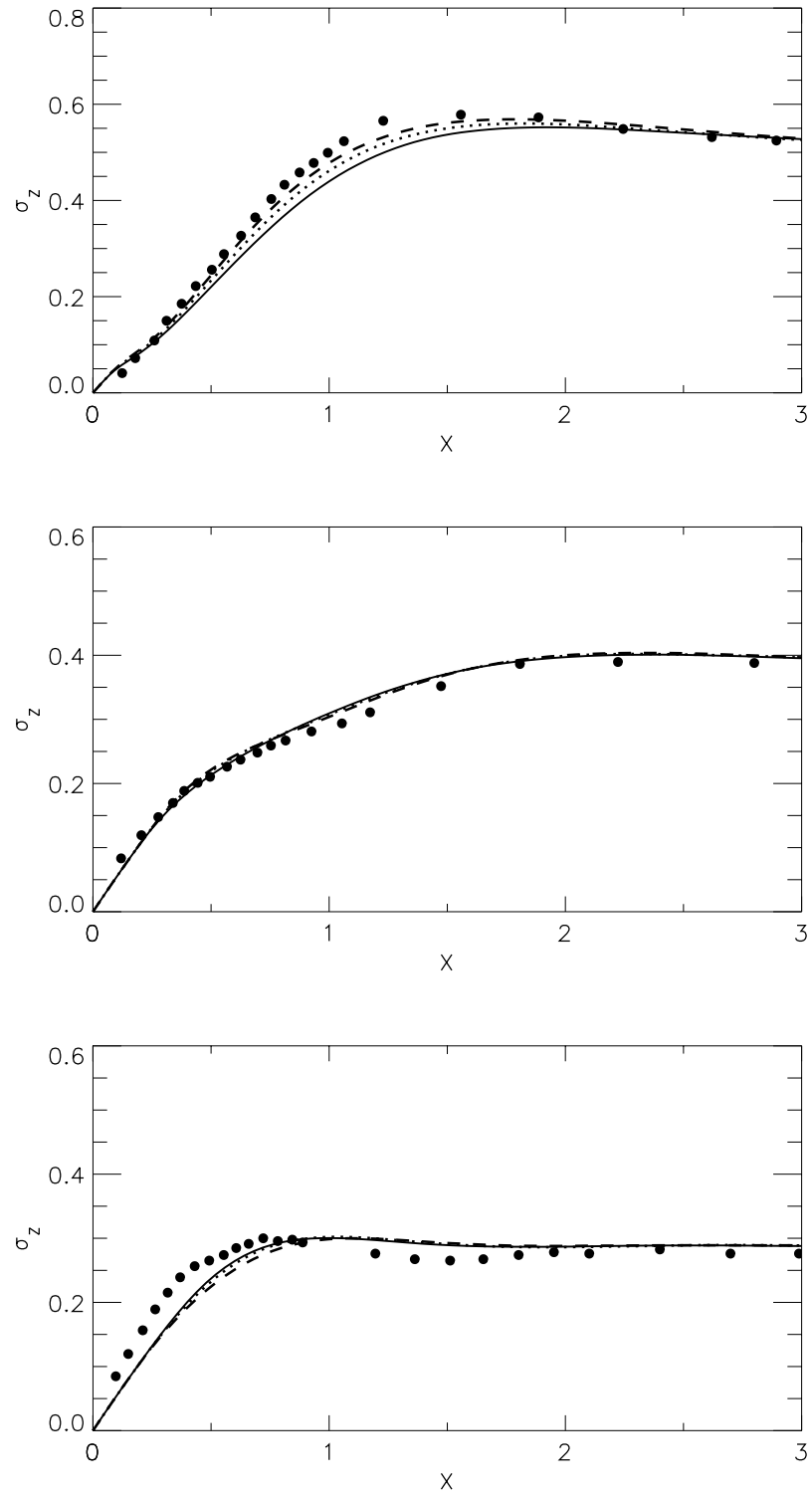


Fig. D.12. Calculations of dimensionless standard deviation of concentration distribution for dimensionless source height Z_s of (a) 0.067 (top figure), (b) 0.24 (middle), and (c) 0.49 (bottom) using the *linear-skewed* Langevin equation model and *three values for fluid velocity skewness* : $S = 0.4$ (solid line), 0.78 (dotted line), 1.2 (dashed line). Circles are data from Willis & Deardorff water tank experiments.

Velocity variance sensitivity tests

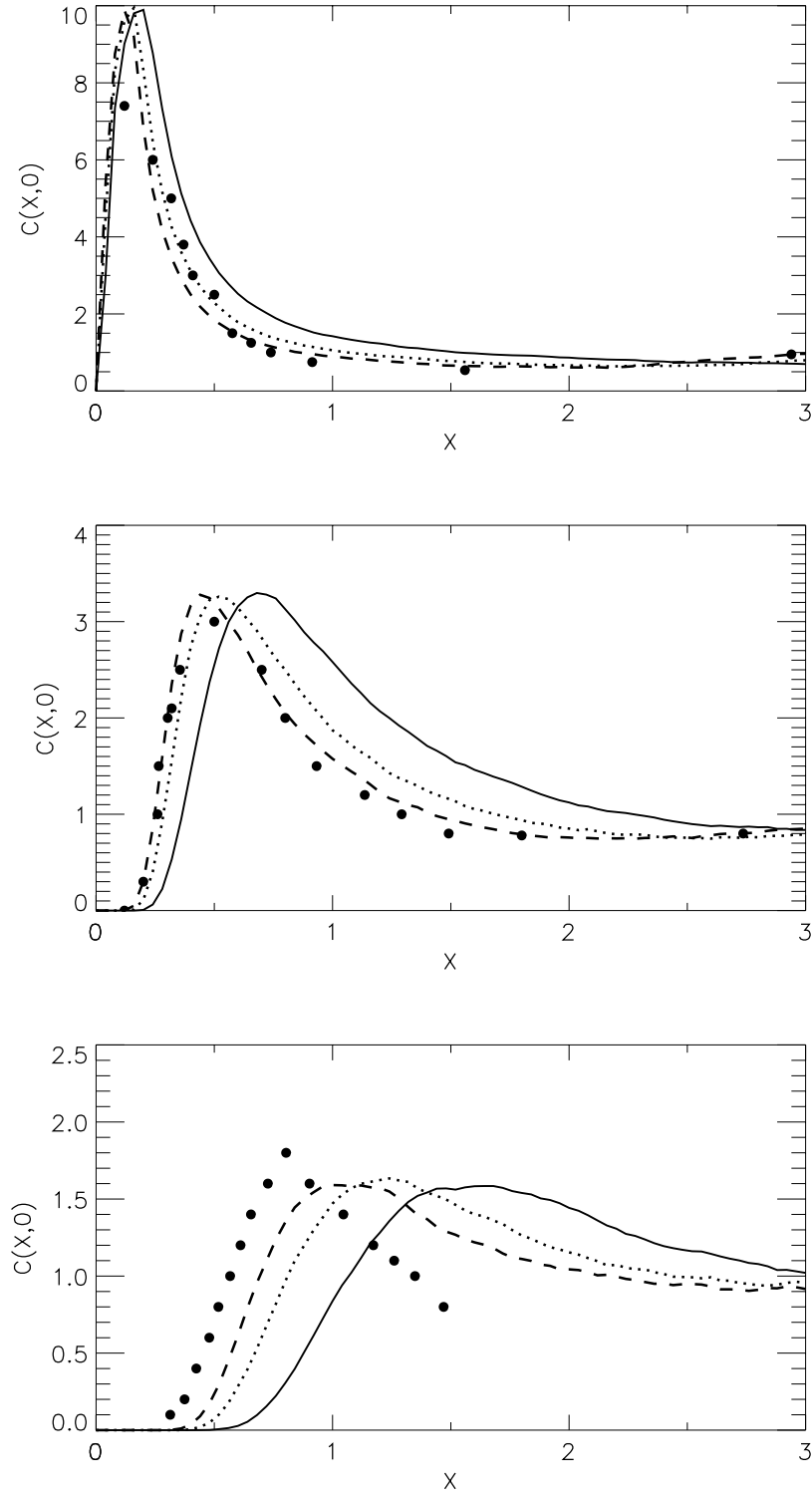


Fig. D.13. Calculations of dimensionless near-ground concentration for dimensionless source height of (a) $Z_s = 0.067$ (top figure), (b) $Z_s = 0.24$ (middle), and (c) $Z_s = 0.49$ (bottom) using the *nonlinear-Gaussian* Langevin equation model and *three values for fluid velocity variance* : $\sigma_{w_f}^2/w_*^2 = 0.2$ (solid line), 0.31 (dotted line), 0.4 (dashed line). Circles are data from Willis & Deardorff experiments.

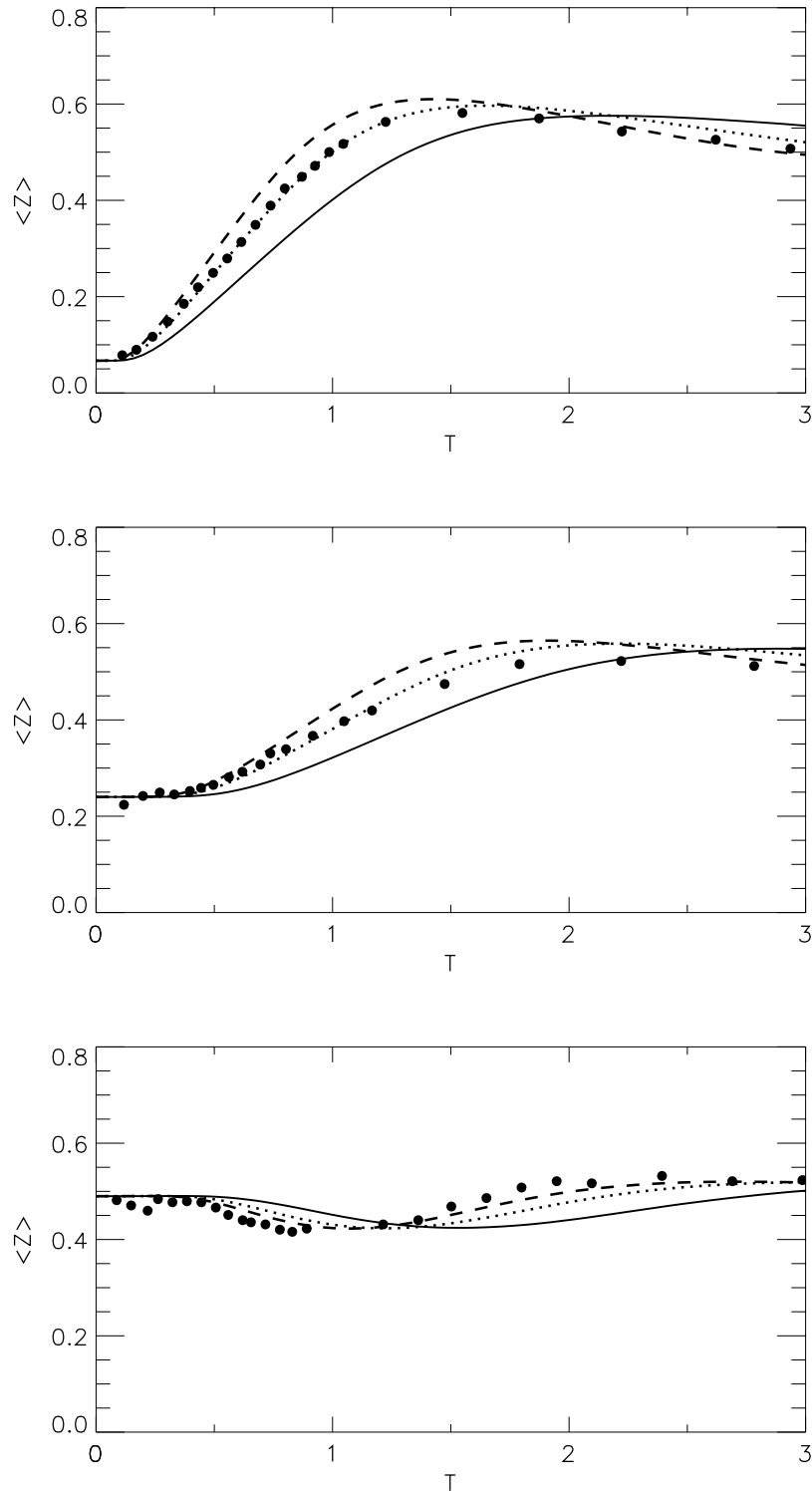


Fig. D.14. Calculations of dimensionless mean height of concentration distribution for dimensionless source height of (a) $Z_s = 0.067$ (top figure), (b) $Z_s = 0.24$ (middle), and (c) $Z_s = 0.49$ (bottom) using the *nonlinear-Gaussian* Langevin equation model and *three values for fluid velocity variance* : $\sigma_{w_f}^2/w_*^2 = 0.2$ (solid line), 0.31 (dotted line), 0.4 (dashed line). Circles are data from Willis & Deardorff water tank experiments.

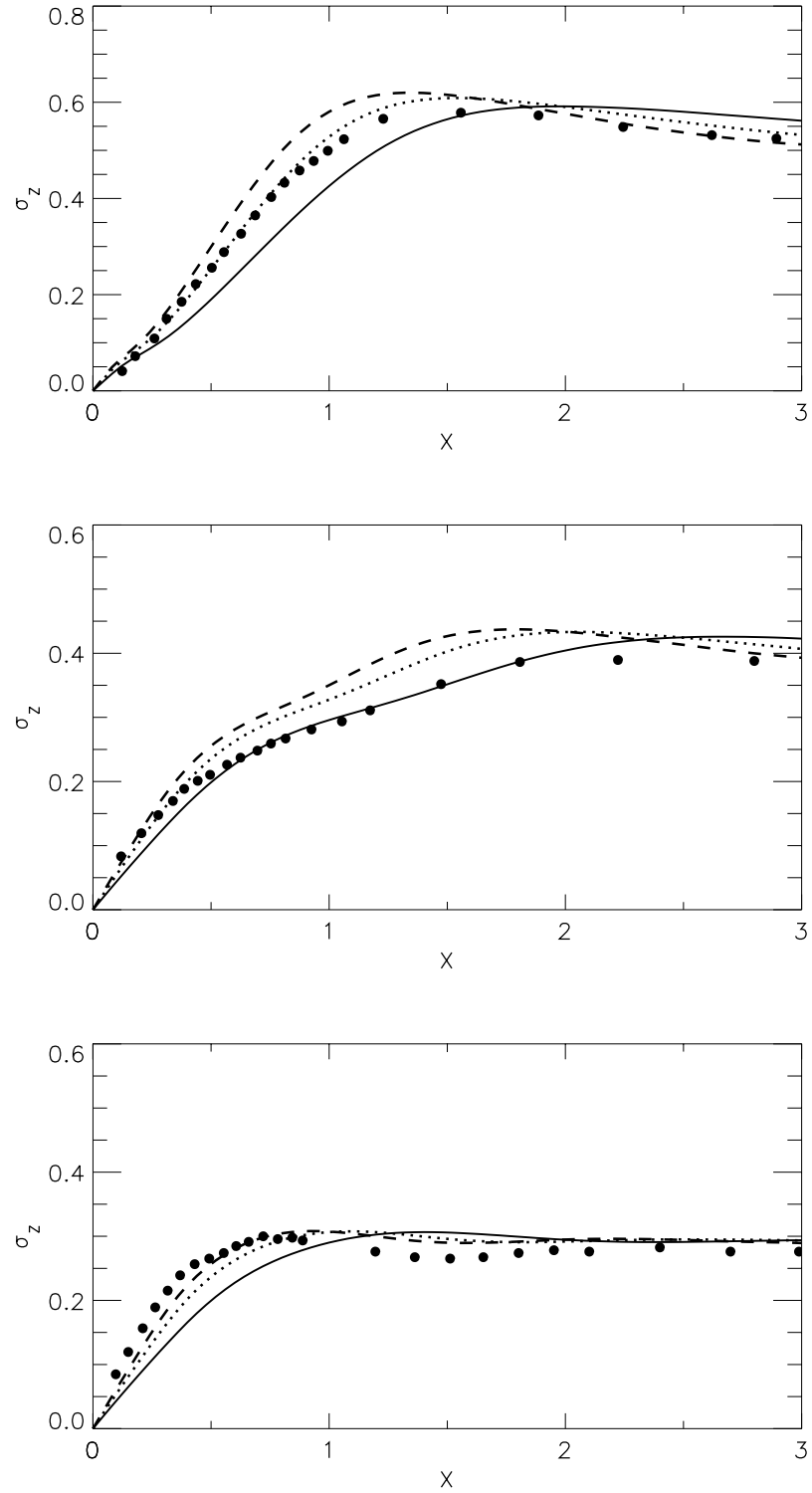


Fig. D.15. Calculations of dimensionless standard deviation of concentration distribution for dimensionless source height Z_s of (a) 0.067 (top figure), (b) 0.24 (middle), and (c) 0.49 (bottom) using the *nonlinear-Gaussian* Langevin equation model and *three values for fluid velocity variance* : $\sigma_{w_f}^2 / w_*^2 = 0.2$ (solid line), 0.31 (dotted line), 0.4 (dashed line). Circles are data from Willis & Deardorff water tank experiments.

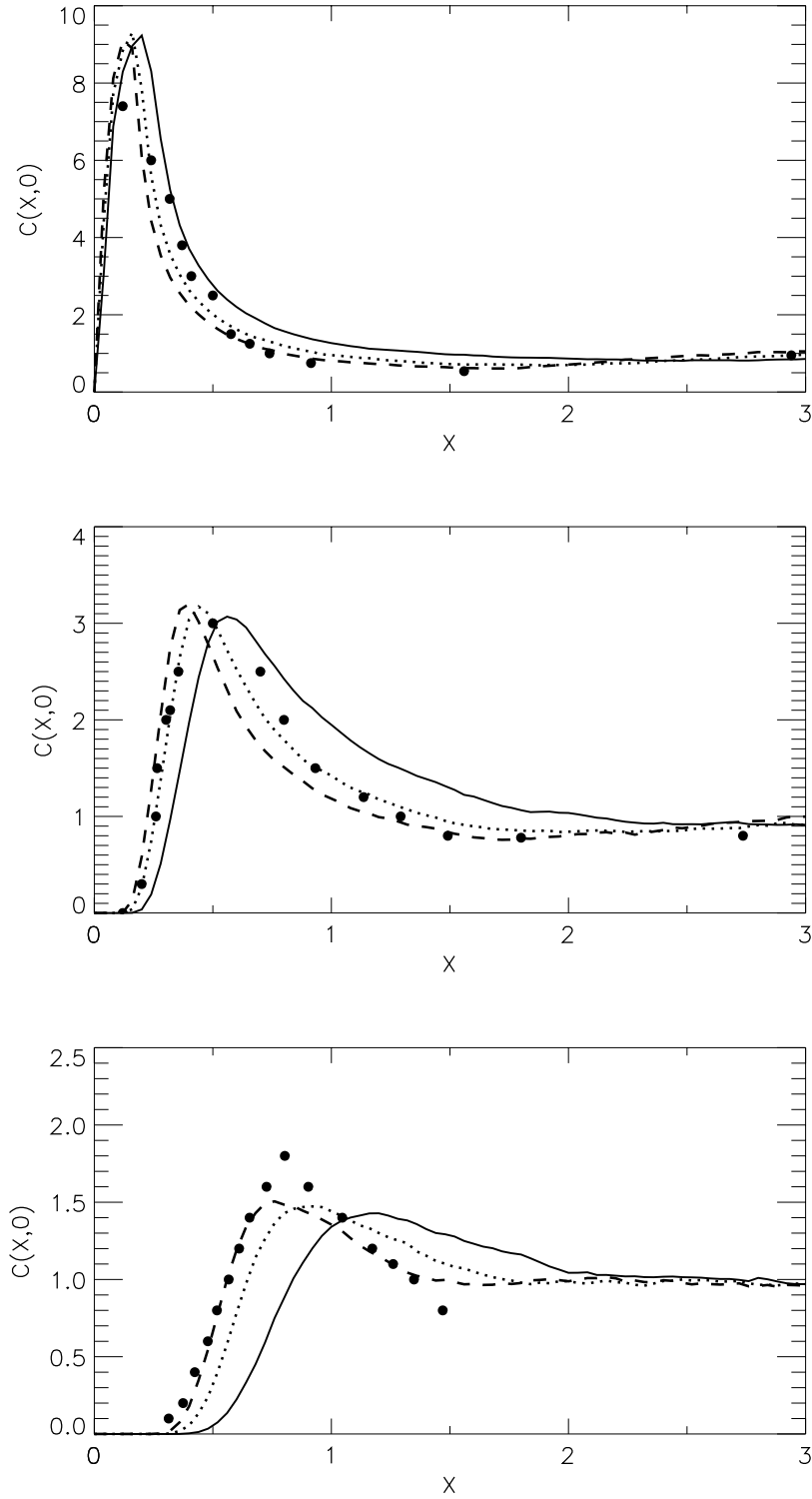


Fig. D.16. Calculations of dimensionless near-ground concentration for dimensionless source height of (a) $Z_s = 0.067$ (top figure), (b) $Z_s = 0.24$ (middle), and (c) $Z_s = 0.49$ (bottom) using the *linear-skewed* Langevin equation model and *three values for fluid velocity variance* : $\sigma_{w_f}^2 / w_*^2 = 0.2$ (solid line), 0.31 (dotted line), 0.4 (dashed line). Circles are data from Willis & Deardorff experiments.

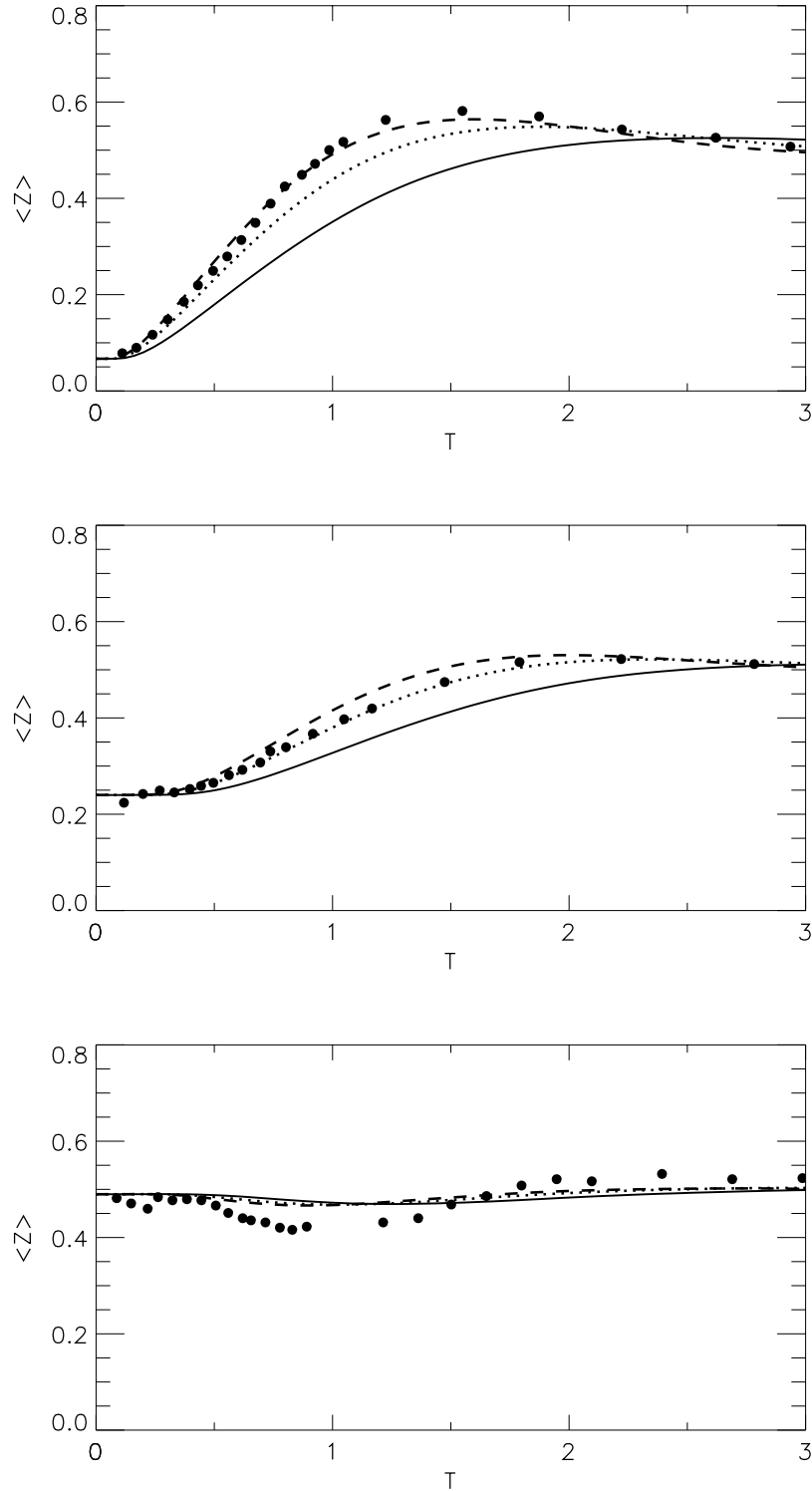


Fig. D.17. Calculations of dimensionless mean height of concentration distribution for dimensionless source height of (a) $Z_s = 0.067$ (top figure), (b) $Z_s = 0.24$ (middle), and (c) $Z_s = 0.49$ (bottom) using the *linear-skewed* Langevin equation model and *three values for fluid velocity variance* : $\sigma_{w_f}^2 / w_*^2 = 0.2$ (solid line), 0.31 (dotted line), 0.4 (dashed line). Circles are data from Willis & Deardorff water tank experiments.

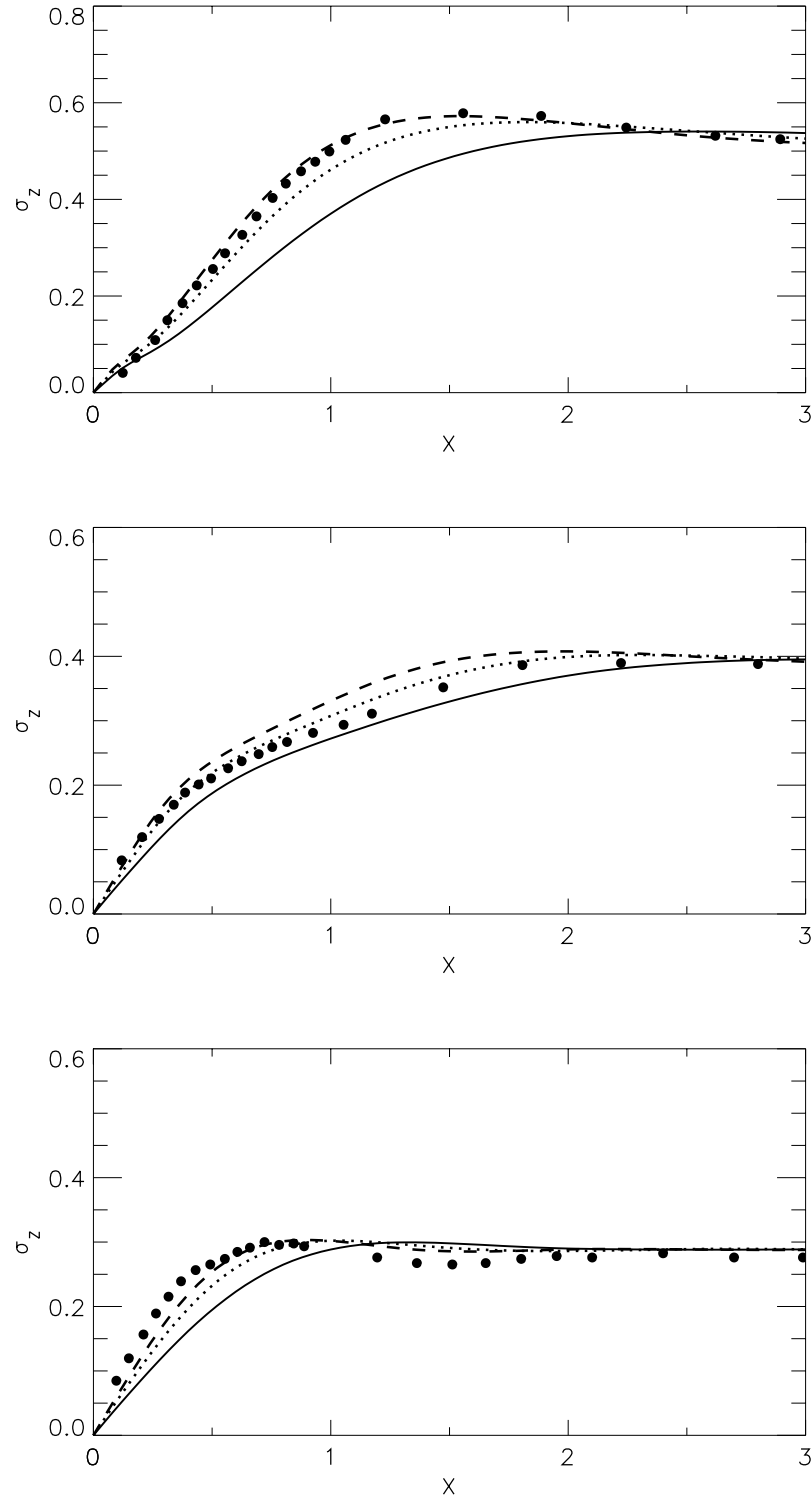


Fig. D.18. Calculations of dimensionless standard deviation of concentration distribution for dimensionless source height Z_s of (a) 0.067 (top figure), (b) 0.24 (middle), and (c) 0.49 (bottom) using the *linear-skewed* Langevin equation model and *three values for fluid velocity variance* : $\sigma_{w_f}^2 / w_*^2 = 0.2$ (solid line), 0.31 (dotted line), 0.4 (dashed line). Circles are data from Willis & Deardorff water tank experiments.

Table D.1. Error in model predictions estimated using observations from the Willis & Deardorff experiments for dimensionless source heights of $z_s/h = 0.067, 0.24$ and 0.49 . Mean square error (MSE), standard error of MSE ($SE\ MSE$), mean fractional error (MFE), standard error of MFE ($SE\ MFE$) of predictions of \bar{z}/h , σ_z/h , and $C(X,0)$ from simulations with nonlinear-Gaussian (N-G) and linear-skewed (L-S) Langevin equation model using reflection method II and a range of input values for the fluid velocity skewness, S , the dimensionless fluid velocity variance, $\sigma_{w_f}^2/w_*^2$, and the dimensionless Lagrangian correlation time, $\tau w_*/h$.

						\bar{z}/h				σ_z/h				$C(X,0)$			
Model	$\frac{z_s}{h}$	S	$\frac{\sigma_{w_f}^2}{w_*^2}$	$\frac{\tau w_*}{h}$	Ref. Meth.	MSE	$SE\ MSE$	MFE	$SE\ MFE$	MSE	$SE\ MSE$	MFE	$SE\ MFE$	MSE	$SE\ MSE$	MFE	$SE\ MFE$
N-G	0.067	0.40	0.20	0.5	II	0.01223	0.00246	-0.25432	0.02261	0.01120	0.00211	-0.23210	0.03356	1.17170	0.26440	0.61216	0.14355
N-G	0.067	0.40	0.31	0.8	II	0.00069	0.00017	-0.05523	0.00814	0.00049	0.00008	-0.02140	0.02537	0.52778	0.23753	0.05405	0.07073
N-G	0.067	0.78	0.20	0.8	II	0.00470	0.00081	-0.16347	0.02471	0.00365	0.00059	-0.11775	0.03122	1.61104	0.56178	0.50906	0.10503
N-G	0.067	0.78	0.31	0.5	II	0.00083	0.00018	-0.06442	0.00862	0.00019	0.00003	0.00888	0.02576	0.69548	0.38372	0.32951	0.10120
N-G	0.067	0.78	0.31	0.8	II	0.00013	0.00004	-0.01263	0.00852	0.00030	0.00006	0.05092	0.02387	0.53436	0.37998	0.14760	0.06701
N-G	0.067	0.78	0.31	1.2	II	0.00062	0.00018	0.02192	0.01121	0.00101	0.00025	0.07706	0.02360	0.55335	0.37201	0.03602	0.05078
N-G	0.067	0.78	0.40	0.8	II	0.00144	0.00028	0.08334	0.01418	0.00251	0.00050	0.15570	0.02915	0.91359	0.49614	-0.00690	0.06140
N-G	0.067	1.20	0.31	0.8	II	0.00105	0.00021	0.03009	0.01579	0.00200	0.00037	0.12234	0.02328	1.02037	0.56249	0.27480	0.07695
N-G	0.067	1.20	0.40	1.2	II	0.00645	0.00130	0.16012	0.02580	0.00840	0.00168	0.25167	0.03438	0.86436	0.67226	0.00381	0.05013
N-G	0.240	0.40	0.20	0.5	II	0.00184	0.00043	-0.08946	0.01488	0.00068	0.00009	-0.12609	0.02123	0.72655	0.15443	0.01134	0.16603
N-G	0.240	0.40	0.31	0.8	II	0.00014	0.00004	0.01703	0.00587	0.00063	0.00014	0.05038	0.01954	0.01890	0.00434	0.04957	0.02586
N-G	0.240	0.78	0.20	0.8	II	0.00154	0.00034	-0.07724	0.01733	0.00039	0.00010	-0.05870	0.02698	1.10645	0.22402	0.00825	0.19037
N-G	0.240	0.78	0.31	0.5	II	0.00026	0.00005	-0.02979	0.00899	0.00043	0.00006	0.04111	0.01877	0.39351	0.07641	0.01549	0.12392
N-G	0.240	0.78	0.31	0.8	II	0.00026	0.00008	-0.00207	0.00934	0.00094	0.00016	0.07514	0.02077	0.19335	0.04337	-0.00508	0.08754
N-G	0.240	0.78	0.31	1.2	II	0.00049	0.00019	0.01435	0.01067	0.00125	0.00024	0.08958	0.02157	0.08230	0.02578	-0.01935	0.05202
N-G	0.240	0.78	0.40	0.8	II	0.00075	0.00025	0.04801	0.01026	0.00208	0.00036	0.15035	0.01936	0.02630	0.00708	0.06842	0.02281
N-G	0.240	1.20	0.31	0.8	II	0.00094	0.00023	-0.02855	0.01723	0.00120	0.00024	0.08621	0.02136	0.78266	0.15711	-0.00960	0.15871

N-G	0.240	1.20	0.40	1.2	II	0.00112	0.00045	0.03408	0.01467	0.00268	0.00049	0.17145	0.01980	0.10643	0.02678	0.00767	0.05746
N-G	0.490	0.40	0.20	0.5	II	0.00139	0.00025	0.02977	0.01534	0.00266	0.00052	-0.13959	0.04237	0.75209	0.17856	-0.44991	0.15828
N-G	0.490	0.40	0.31	0.8	II	0.00079	0.00015	0.03125	0.01097	0.00072	0.00016	-0.04888	0.02865	0.12320	0.02068	-0.27350	0.11002
N-G	0.490	0.78	0.20	0.8	II	0.00186	0.00038	0.00310	0.01803	0.00240	0.00044	-0.12665	0.04164	0.83612	0.19389	-0.48684	0.17093
N-G	0.490	0.78	0.31	0.5	II	0.00087	0.00016	0.00834	0.01244	0.00111	0.00019	-0.07194	0.03103	0.57256	0.12599	-0.42790	0.16002
N-G	0.490	0.78	0.31	0.8	II	0.00071	0.00013	0.00715	0.01121	0.00085	0.00016	-0.05693	0.02930	0.41548	0.07392	-0.32165	0.15860
N-G	0.490	0.78	0.31	1.2	II	0.00062	0.00012	0.00791	0.01049	0.00072	0.00015	-0.05103	0.02814	0.26746	0.04472	-0.30872	0.14086
N-G	0.490	0.78	0.40	0.8	II	0.00026	0.00005	0.00958	0.00667	0.00038	0.00006	-0.01868	0.02141	0.17627	0.02373	-0.21061	0.12179
N-G	0.490	1.20	0.31	0.8	II	0.00164	0.00048	-0.02102	0.01612	0.00126	0.00015	-0.07024	0.03172	0.68193	0.15278	-0.46803	0.17159
N-G	0.490	1.20	0.40	1.2	II	0.00059	0.00017	-0.01506	0.00978	0.00052	0.00006	-0.02670	0.02249	0.33356	0.05644	-0.29660	0.15267
L-S	0.067	0.40	0.20	0.5	II	0.01761	0.00344	-0.29996	0.02370	0.01593	0.00291	-0.27970	0.03312	0.94383	0.20340	0.61231	0.15330
L-S	0.067	0.40	0.31	0.8	II	0.00245	0.00057	-0.10497	0.01164	0.00179	0.00034	-0.07001	0.02679	0.47595	0.19313	0.03079	0.06835
L-S	0.067	0.78	0.20	0.8	II	0.00919	0.00183	-0.22684	0.02257	0.00790	0.00146	-0.19307	0.03167	0.75719	0.40307	0.36150	0.08951
L-S	0.067	0.78	0.31	0.5	II	0.00558	0.00126	-0.15656	0.01460	0.00372	0.00078	-0.09934	0.03050	0.38061	0.14003	0.25250	0.10888
L-S	0.067	0.78	0.31	0.8	II	0.00140	0.00033	-0.08362	0.00859	0.00078	0.00015	-0.03153	0.02643	0.46914	0.20576	0.05067	0.06425
L-S	0.067	0.78	0.31	1.2	II	0.00033	0.00006	-0.03832	0.00829	0.00020	0.00003	0.00974	0.02464	0.53312	0.22055	-0.00670	0.05490
L-S	0.067	0.78	0.40	0.8	II	0.00015	0.00003	0.00752	0.00847	0.00022	0.00004	0.07104	0.02889	1.03843	0.38838	-0.07628	0.06296
L-S	0.067	1.20	0.31	0.8	II	0.00090	0.00021	-0.07288	0.00850	0.00031	0.00006	0.00094	0.02651	0.38959	0.21588	0.13512	0.06261
L-S	0.067	1.20	0.40	1.2	II	0.00121	0.00021	0.06830	0.01402	0.00220	0.00041	0.15077	0.03030	0.87121	0.35487	-0.04591	0.05919
L-S	0.240	0.40	0.20	0.5	II	0.00236	0.00063	-0.09465	0.01594	0.00136	0.00011	-0.16855	0.01725	0.40000	0.08493	0.02327	0.13097
L-S	0.240	0.40	0.31	0.8	II	0.00003	0.00001	0.00438	0.00477	0.00015	0.00004	0.00245	0.01557	0.05768	0.02096	0.08349	0.05106
L-S	0.240	0.78	0.20	0.8	II	0.00149	0.00036	-0.07966	0.01414	0.00059	0.00008	-0.11773	0.02077	0.47713	0.13340	-0.07474	0.12811
L-S	0.240	0.78	0.31	0.5	II	0.00042	0.00013	-0.03711	0.00792	0.00007	0.00002	-0.03036	0.01319	0.06986	0.01702	0.06396	0.06039
L-S	0.240	0.78	0.31	0.8	II	0.00005	0.00002	-0.00852	0.00507	0.00015	0.00003	0.01130	0.01542	0.03051	0.01275	-0.00986	0.02920
L-S	0.240	0.78	0.31	1.2	II	0.00012	0.00004	0.01097	0.00599	0.00036	0.00007	0.03523	0.01669	0.04716	0.02225	-0.03465	0.03161
L-S	0.240	0.78	0.40	0.8	II	0.00032	0.00008	0.03945	0.00740	0.00073	0.00015	0.08598	0.01404	0.17359	0.04762	0.11803	0.08470
L-S	0.240	1.20	0.31	0.8	II	0.00018	0.00004	-0.02660	0.00718	0.00014	0.00002	0.01257	0.01504	0.08586	0.03162	-0.04710	0.05782
L-S	0.240	1.20	0.40	1.2	II	0.00052	0.00018	0.03990	0.00880	0.00102	0.00019	0.10475	0.01442	0.10640	0.03437	0.02488	0.06300
L-S	0.490	0.40	0.20	0.5	II	0.00135	0.00028	0.04360	0.01420	0.00278	0.00055	-0.15797	0.04068	0.36454	0.09070	-0.49562	0.11102

L-S	0.490	0.40	0.31	0.8	II	0.00120	0.00025	0.04451	0.01302	0.00077	0.00018	-0.06708	0.02803	0.03721	0.01043	-0.18648	0.06396
L-S	0.490	0.78	0.20	0.8	II	0.00117	0.00022	0.03377	0.01372	0.00248	0.00049	-0.14053	0.04073	0.41395	0.09410	-0.40969	0.13896
L-S	0.490	0.78	0.31	0.5	II	0.00099	0.00019	0.03493	0.01235	0.00110	0.00022	-0.08612	0.03002	0.14386	0.03055	-0.34041	0.09820
L-S	0.490	0.78	0.31	0.8	II	0.00089	0.00017	0.03416	0.01160	0.00086	0.00019	-0.07107	0.02870	0.07912	0.01411	-0.26640	0.09479
L-S	0.490	0.78	0.31	1.2	II	0.00080	0.00015	0.03094	0.01110	0.00074	0.00017	-0.06302	0.02770	0.04094	0.00823	-0.22814	0.08364
L-S	0.490	0.78	0.40	0.8	II	0.00079	0.00015	0.03311	0.01078	0.00036	0.00007	-0.03279	0.02097	0.01401	0.00616	-0.11363	0.05826
L-S	0.490	1.20	0.31	0.8	II	0.00070	0.00011	0.02064	0.01086	0.00104	0.00021	-0.08065	0.02946	0.16133	0.03167	-0.32542	0.11326
L-S	0.490	1.20	0.40	1.2	II	0.00040	0.00007	0.01857	0.00806	0.00036	0.00008	-0.03942	0.02037	0.01696	0.00490	-0.15786	0.06594

Table D.2. Comparison of model predicted maximum near-surface concentration, $C(X,0)$, and observed maximum $C(X,0)$ from the Willis & Deardorff experiments for dimensionless source heights of $z_s/h = 0.067, 0.24$ and 0.49 . Results are shown from simulations with the nonlinear-Gaussian (N-G) and linear-skewed (L-S) Langevin equation models using reflection method I, II, and III, and a range of input values for the fluid velocity skewness, S , the dimensionless fluid velocity variance, $\sigma_{w_f}^2/w_*^2$, and the dimensionless Lagrangian correlation time, $\tau w_*/h$.

Model	$\frac{z_s}{h}$	S	$\frac{\sigma_{w_f}^2}{w_*^2}$	$\frac{\tau w_*}{h}$	Refl. Meth.	Max. $C(X,0)$ predicted	Max. $C(X,0)$ observed	X of max. $C(X,0)$ predicted	X of max. $C(X,0)$ observed
N-G	0.067	0.40	0.20	0.5	II	9.29080	7.40000	0.17500	0.12000
N-G	0.067	0.40	0.31	0.8	II	9.18560	7.40000	0.16000	0.12000
N-G	0.067	0.78	0.20	0.8	II	9.89380	7.40000	0.20000	0.12000
N-G	0.067	0.78	0.31	0.5	II	10.02140	7.40000	0.15000	0.12000
N-G	0.067	0.78	0.31	0.8	I	9.12720	7.40000	0.12000	0.12000
N-G	0.067	0.78	0.31	0.8	II	9.94640	7.40000	0.16000	0.12000
N-G	0.067	0.78	0.31	0.8	III	9.45460	7.40000	0.12000	0.12000
N-G	0.067	0.78	0.31	1.2	II	9.57060	7.40000	0.12000	0.12000
N-G	0.067	0.78	0.40	0.8	II	9.89060	7.40000	0.12000	0.12000
N-G	0.067	1.20	0.31	0.8	II	10.60440	7.40000	0.16000	0.12000
N-G	0.067	1.20	0.40	1.2	II	10.32020	7.40000	0.12000	0.12000
N-G	0.240	0.40	0.20	0.5	II	3.01700	3.00000	0.60000	0.50000
N-G	0.240	0.40	0.31	0.8	II	3.19140	3.00000	0.44000	0.50000
N-G	0.240	0.78	0.20	0.8	II	3.29760	3.00000	0.68000	0.50000
N-G	0.240	0.78	0.31	0.5	II	3.24420	3.00000	0.57500	0.50000
N-G	0.240	0.78	0.31	0.8	I	2.81420	3.00000	0.60000	0.50000
N-G	0.240	0.78	0.31	0.8	II	3.25980	3.00000	0.52000	0.50000
N-G	0.240	0.78	0.31	0.8	III	3.05180	3.00000	0.56000	0.50000

N-G	0.240	0.78	0.31	1.2	II	3.23520	3.00000	0.48000	0.50000
N-G	0.240	0.78	0.40	0.8	II	3.27880	3.00000	0.44000	0.50000
N-G	0.240	1.20	0.31	0.8	II	3.38480	3.00000	0.64000	0.50000
N-G	0.240	1.20	0.40	1.2	II	3.26200	3.00000	0.54000	0.50000
N-G	0.490	0.40	0.20	0.5	II	1.37040	1.80000	1.37500	0.80367
N-G	0.490	0.40	0.31	0.8	II	1.52920	1.80000	0.96000	0.80367
N-G	0.490	0.78	0.20	0.8	II	1.58440	1.80000	1.68000	0.80367
N-G	0.490	0.78	0.31	0.5	II	1.52880	1.80000	1.40000	0.80367
N-G	0.490	0.78	0.31	0.8	I	1.47600	1.80000	1.36000	0.80367
N-G	0.490	0.78	0.31	0.8	II	1.63380	1.80000	1.24000	0.80367
N-G	0.490	0.78	0.31	0.8	III	1.53820	1.80000	1.16000	0.80367
N-G	0.490	0.78	0.31	1.2	II	1.61720	1.80000	1.14000	0.80367
N-G	0.490	0.78	0.40	0.8	II	1.59060	1.80000	1.00000	0.80367
N-G	0.490	1.20	0.31	0.8	II	1.73760	1.80000	1.48000	0.80367
N-G	0.490	1.20	0.40	1.2	II	1.67720	1.80000	1.20000	0.80367
L-S	0.067	0.40	0.20	0.5	II	8.51560	7.40000	0.17500	0.12000
L-S	0.067	0.40	0.31	0.8	II	8.64280	7.40000	0.16000	0.12000
L-S	0.067	0.78	0.20	0.8	II	9.23060	7.40000	0.20000	0.12000
L-S	0.067	0.78	0.31	0.5	II	9.10380	7.40000	0.15000	0.12000
L-S	0.067	0.78	0.31	0.8	I	8.14900	7.40000	0.12000	0.12000
L-S	0.067	0.78	0.31	0.8	II	9.30480	7.40000	0.16000	0.12000
L-S	0.067	0.78	0.31	0.8	III	8.56980	7.40000	0.12000	0.12000
L-S	0.067	0.78	0.31	1.2	II	8.99040	7.40000	0.18000	0.12000
L-S	0.067	0.78	0.40	0.8	II	9.10880	7.40000	0.12000	0.12000
L-S	0.067	1.20	0.31	0.8	II	9.61100	7.40000	0.16000	0.12000
L-S	0.067	1.20	0.40	1.2	II	9.30020	7.40000	0.12000	0.12000
L-S	0.240	0.40	0.20	0.5	II	2.70380	3.00000	0.55000	0.50000
L-S	0.240	0.40	0.31	0.8	II	3.01800	3.00000	0.40000	0.50000
L-S	0.240	0.78	0.20	0.8	II	3.06920	3.00000	0.56000	0.50000

L-S	0.240	0.78	0.31	0.5	II	3.00460	3.00000	0.45000	0.50000
L-S	0.240	0.78	0.31	0.8	I	2.19920	3.00000	0.48000	0.50000
L-S	0.240	0.78	0.31	0.8	II	3.17260	3.00000	0.44000	0.50000
L-S	0.240	0.78	0.31	0.8	III	2.57500	3.00000	0.48000	0.50000
L-S	0.240	0.78	0.31	1.2	II	3.31160	3.00000	0.42000	0.50000
L-S	0.240	0.78	0.40	0.8	II	3.20020	3.00000	0.40000	0.50000
L-S	0.240	1.20	0.31	0.8	II	3.11460	3.00000	0.48000	0.50000
L-S	0.240	1.20	0.40	1.2	II	3.24040	3.00000	0.42000	0.50000
L-S	0.490	0.40	0.20	0.5	II	1.19340	1.80000	1.27500	0.80367
L-S	0.490	0.40	0.31	0.8	II	1.38500	1.80000	0.84000	0.80367
L-S	0.490	0.78	0.20	0.8	II	1.42860	1.80000	1.20000	0.80367
L-S	0.490	0.78	0.31	0.5	II	1.32600	1.80000	1.00000	0.80367
L-S	0.490	0.78	0.31	0.8	I	1.03740	1.80000	0.96000	0.80367
L-S	0.490	0.78	0.31	0.8	II	1.47280	1.80000	0.92000	0.80367
L-S	0.490	0.78	0.31	0.8	III	1.22160	1.80000	1.08000	0.80367
L-S	0.490	0.78	0.31	1.2	II	1.56160	1.80000	0.84000	0.80367
L-S	0.490	0.78	0.40	0.8	II	1.50560	1.80000	0.76000	0.80367
L-S	0.490	1.20	0.31	0.8	II	1.47920	1.80000	1.00000	0.80367
L-S	0.490	1.20	0.40	1.2	II	1.53880	1.80000	0.78000	0.80367

References

- Baerentsen, J.H. and R. Berkowicz (1984) Monte Carlo simulation of plume dispersion in the convective boundary layer, *Atmos. Env.*, **18**, 701-712.
- Briggs, G.A. (1988) Analysis of diffusion field experiments. In *Lectures on Air Pollution Modeling* (A. Venkatram and J.C. Wyngaard, eds.), pp. 63-117. Am. Met. Soc., Boston.
- Briggs, G.A. (1993a) Final results of the CONDORS convective diffusion experiment. *Bound.-Layer Meteorol.*, **62**, 315-328.
- Briggs, G.A. (1993b) Plume Dispersion in the Convective Boundary Layer. Part II: Analysis of CONDORS field experiment data. *J. Appl. Meteorol.*, **32**, 1388-1425.
- Deardorff, J.W. (1970a) Preliminary results from numerical integrations of the unstable planetary boundary layer. *J. Atmos. Sci.*, **27**, 1209-1211.
- Deardorff, J.W. (1970b) Convective velocity and temperature scales for the unstable planetary boundary layer and for Rayleigh convection. *J. Atmos. Sci.*, **27**, 1211-1213.
- Deardorff, J.W. (1972) Numerical investigation of neutral and unstable planetary boundary layers. *J. Atmos. Sci.*, **29**, 91-115.
- Deardorff, J.W. (1974a) Three-dimensional numerical study of the height and mean structure of a heated planetary boundary layer. *Bound.-Layer Met.*, **7**, 81-106.
- Deardorff, J.W. (1974b) Three-dimensional numerical study of turbulence in an entraining mixed layer. *Bound.-Layer Meteorol.*, **7**, 199-226.
- Deardorff, J.W. (1978) Closure of second- and third-moment rate equations for diffusion in homogeneous turbulence. *Phys. Fluids*, **21**, 525-530.
- Deardorff, J.W., and G.E. Willis (1974) Physical modeling of diffusion in the mixed layer. Preprint, *Symposium on Atmospheric Diffusion and Air Pollution.*, Santa Barbara, CA, September 9-13, 1974. American Meteorological Society, 45 Beacon St., Boston, MA, pp. 387-391.
- Deardorff, J.W., and G.E. Willis (1985) Further results from a laboratory model of the convective planetary boundary layer. *Bound.-Layer Meteorol.*, **32**, 205-236

- De Baas, van Dop and Nieuwstadt (1986) An application of the Langevin equation for inhomogeneous conditions to dispersion in a convective boundary layer, *Quart. J. R. Met. Soc.*, **112**, 165-180.
- Du, S., J.D. Wilson and E. Yee (1994) Probability density functions for velocity in the convective boundary layer and implied trajectory models, *Atmos. Env.*, **28**, 1211-1217.
- Du, S., B.L. Sawford, J.D. Wilson and D.J. Wilson (1995) Estimation of the Kolmogorov constant for the Lagrangian structure function, using a second-order Lagrangian model of grid turbulence. *Phys. Fluids*, **7**, 3083-3089.
- Durbin, P.A. (1983) *Stochastic differential equations and turbulent dispersion*. NASA Reference Publication 1103, 69 pp. (Available from NTIS as N8322546)
- Ermak, D.L. and J.S. Nasstrom (1995) Numerical simulation of the Langevin equation for skewed turbulence. Preprint, *11th Symposium on Boundary Layers and Turbulence*, Charlotte, NC, 27-31 March 1995. American Meteorological Society, Boston.
- Gardiner, C.W. (1990) *Handbook of stochastic methods for physics, chemistry and the natural sciences*, Second edition, Springer-Verlag, N.Y., 442 pp.
- Garratt, J.R. (1992) *The Atmospheric Boundary Layer*, Cambridge University Press, Cambridge, UK, 316 pp.
- Gillespie, D.T. (1992) *Markov Processes: An Introduction for Physical Scientists*, Academic Press, Inc., Harcourt Brace Jovanovich, Publishers, Boston, 565 pp.
- Hanna, S.R. (1979) Some Statistics of Lagrangian and Eulerian Wind Fluctuations. *J. Appl. Meteorol.*, **18**, 518-525.
- Holtslag, A.A.M., and F.T.M. Nieuwstadt (1986) Scaling the atmospheric boundary layer. *Bound.-Layer Meteorol.*, **36**, 201-209.
- Hurley, P. and W. Physick (1993) A skewed homogeneous Lagrangian particle model for convective conditions. *Atmos. Environ.*, **27A**, 619-624.
- Kaimal, J.C., W.L. Eberhard, W.R. Moninger, J.E. Gaynor, S.W. Troxel, T. Uttal, G.A. Briggs, and G.E. Start (1986) *Project Condors – Convective Diffusion Observed by Remote Sensors*, Report Number Seven, NOAA/ERL, Boulder, CO 80303, 305 pp..
- Kalbfleisch, J.G. (1985) *Probability and statistical inference – Volume 1: Probability*, Second edition, Springer-Verlag, N.Y.
- Lamb, R.G. (1978a) A numerical simulation of dispersion from an elevated point source in the convective planetary boundary layer. *Atmos. Environ.*, **12**, 1297-1304.

- Lamb, R.G. (1978b) The effects of release height on material dispersion in the convective planetary boundary layer. In preprints of *Fourth Symposium on Turbulence, Diffusion, and Air Pollution*, Jan. 15-18, 1979, pp. 27-33. Am. Met. Soc., Boston.
- Lamb, R.G. (1981) A numerical investigation of tetraon versus fluid particle dispersion the convective planetary boundary layer. *J. Appl. Meteorol.*, **20**, 391-403.
- Lamb, R.G. (1982) Diffusion in the convective boundary layer. In *Atmospheric Turbulence and Air Pollution Modelling* (F.T.M. Nieuwstadt and H. van Dop, eds.), pp. 159-229. D. Reidel, Boston.
- Lange, R. (1978) ADPIC—A three-dimensional particle-in-cell model for the dispersal of atmospheric pollutants and its comparison to regional tracer studies. *J. Appl. Meteorol.*, **17**, 320-329.
- Luhar, A.K. and R.E. Britter (1989) A random walk model for dispersion in inhomogeneous turbulence in a convective boundary layer. *Atmos. Environ.*, **23**, 1911-1924.
- Luhar, A.K., M.F. Hibberd, and P.F. Hurley (1996) Comparison of closure schemes used to specify the velocity PDF in Lagrangian stochastic dispersion models for convective conditions. *Atmos. Environ.*, **30**, 1407-1418.
- Lumley, J.L. and H.A. Panofsky (1964) *The Structure of Atmospheric Turbulence*. John Wiley and Sons, Inc., New York.
- Monin, A.S., and A.M. Yaglom (1971) *Statistical Fluid Mechanics: Mechanics of Turbulence, Volume 1* (J.L. Lumley, ed.), The MIT Press, Cambridge, Mass., 769 pp.
- Monin, A.S., and A.M. Yaglom (1975) *Statistical Fluid Mechanics: Mechanics of Turbulence, Volume 2* (J.L. Lumley, ed.), The MIT Press, Cambridge, Mass., 874 pp.
- Nasstrom, J.S., and D.L. Ermak, 1997: Comparison of reflection boundary conditions for Langevin equation modeling of convective boundary layer dispersion, Preprint, *12th Symposium on Boundary Layers and Turbulence*, Vancouver, B.C., 28 July-1 Aug, 1997. American Meteorological Society, Boston.
- Nasstrom, J.S., and D.L. Ermak, 1998: Langevin equation modeling of convective boundary layer dispersion assuming homogeneous, skewed turbulence, Preprint, *Tenth Joint Conference on the Applications of Air Pollution Meteorology*, Phoenix, AZ, Jan. 11-16, 1998. American Meteorological Society, Boston.
- Nieuwstadt, F.T.M. (1980) Application of mixed-layer similarity to the observed dispersion from a ground-level source, *J. Appl. Meteorol.*, **19**, 157-162.

- Obukhov, A.M. (1946) Turbulence in an atmosphere with a non-uniform temperature, *Tr. Akad. Nauk. SSSR Inst. Teorel. Geofis.*, No. 1 (translation in *Bound.-Layer Meteor.*, **2**, 7-29, 1971)
- Obukhov, A.M. (1959) Description of turbulence in terms of Lagrangian variables, *Atmospheric Diffusion and Air Pollution* (F.N. Frenkiel and P.A. Sheppard, eds.), Proceedings of symposium held at Oxford, August 24-29, 1958, pp. 113-116. Academic Press, New York.
- Panofsky, H.A., H. Tennekes, D.H. Lenschow, and J.C. Wyngaard (1977) The characteristics of turbulent velocity components in the surface layer under convective conditions. *Bound.-Layer Meteorol.*, **11**, 355-361.
- Pope, S.B. (1987) Consistency conditions for random-walk models of turbulent dispersion. *Phys. Fluids*, **30**, 2374-2379.
- Pope, S.B. (1994) Lagrangian PDF methods for turbulent flows. *Annu. Rev. Fluid Mech.*, **26**, 23-63.
- Rodean, H.C. (1996) *Stochastic Lagrangian Models of Turbulent Diffusion*. Meteorological Monograph No. 48, Am. Meteor. Soc., Boston, MA.
- Rotach, M.W., S.-E. Gryning, and C. Tassone (1996) A two-dimensional Lagrangian stochastic dispersion model for daytime conditions, *Quart. J. R. Met. Soc.*, **122**, 367-389.
- Sawford, B.L. (1985) Lagrangian statistical simulation of concentration mean and fluctuation fields, *J. Climate and Appl. Meteor.*, **24**, 1152-1166.
- Sawford, B.L. (1986) Generalized random forcing in random-walk turbulent dispersion models, *Phys. Fluids*, **29**, 3582-3585.
- Sawford, B.L. and F.M. Guest (1987) Lagrangian stochastic analysis of flux-gradient relationships in the convective boundary layer, *J. Atmos. Sci.*, **44**, 1152-1165.
- Sawford, B.L. (1993) Recent developments in the Lagrangian stochastic theory of turbulent dispersion, *Boundary-Layer Meteorol.*, **62**, 197-215.
- Sawford, B.L., and B.S. Borgas (1994) On the continuity of stochastic models for the Lagrangian velocity in turbulence, *Physica D*, **76**, 297-311.
- Schmidt, H., and U. Schumann (1989) Coherent structure of the convective boundary layer derived from large-eddy simulations, *J. Fluid Mech.*, **200**, 511-562.
- Seinfeld, J.H. (1988) Ozone air quality models: A critical review. *Air Pollution Control Assoc., Journal*, **38**, 616-645.

- Stull, R.B. (1988) *An Introduction to Boundary Layer Meteorology*. Kluwer Academic Publishers, Boston, MA. 666 pp.
- Taylor, G.I. (1921) Diffusion by continuous movements, *Proc. Lond. Math. Soc. Ser. 2*, **20**, 196-211.
- Tennekes H., and J.L. Lumley (1972) *A First Course in Turbulence*. The MIT Press, Cambridge, MA.
- Thomson, D.J. (1984) Random walk modelling of diffusion in inhomogeneous turbulence, *Quart. J. R. Met. Soc.*, **110**, 1107-1120.
- Thomson, D.J. (1987) Criteria for the selection of stochastic models of particle trajectories in turbulent flows. *J. Fluid Mech.*, **180**, 529-556.
- Thomson, D.J. and M.R. Montgomery (1994) Reflection boundary conditions for random walk models of dispersion in non-Gaussian turbulence. *Atmos. Environ.*, **28**, 1981-1987.
- Thomson, D.J., W.L. Physick, and R.H. Maryon (1997) Treatment of interfaces in random walk dispersion models. *J. Appl. Meteor.*, **36**, 1284-1295.
- van Dop, Nieuwstadt and Hunt (1985) Random walk models for particle displacements in inhomogeneous unsteady turbulent flows, *Phys. Fluids*, **28**, 1639-1653.
- van Kampen, N.G. (1992) *Stochastic processes in physics and chemistry*. North-Holland, N.Y., 465 pp.
- Weil, J.C. (1988) Dispersion in the convective boundary layer. In *Lectures on Air Pollution Modeling* (A. Venkatram and J.C. Wyngaard, eds.), pp. 167-227. Am. Met. Soc., Boston.
- Weil, J.C. (1989) Stochastic modeling of dispersion in the convective boundary layer. In *Air Pollution Modeling and Its Application VII* (H. van Dop, ed.), pp. 437-449, Plenum, New York.
- Weil, J.C. (1990) A diagnosis of the asymmetry in top-down and bottom-up diffusion using a Lagrangian stochastic model. *J. Atmos. Sci.*, **47**, 501-515.
- Willliams, A.G. and J.M. Hacker (1992) The composite shape and structure of coherent eddies in the convective boundary layer. *Bound.-Layer Meteorol.*, **61**, 213-245.
- Willliams, A.G. and J.M. Hacker (1993) Interaction between coherent eddies in the lower convective boundary layer. *Bound.-Layer Meteorol.*, **64**, 55-74.
- Willis, G.E. and J.W. Deardorff (1976a) A laboratory model of the diffusion into the convective planetary boundary layer. *Quart. J. Roy Met. Soc.*, **102**, 427-445.

- Willis, G.E. and J.W. Deardorff (1976b) On the use of Taylor's translation hypothesis for diffusion in the mixed layer. *Quart. J. Roy Met. Soc.*, **102**, 817-822.
- Willis, G.E. and J.W. Deardorff (1978) A laboratory study of dispersion from an elevated source within a modeled convective planetary boundary layer. *Atmos. Environ.*, **12**, 1305-1311.
- Willis, G.E. and J.W. Deardorff (1979) Laboratory observations of turbulent penetrative-convection planforms. *J. Geophys. Res.*, **84** (C1), 295-302.
- Willis, G.E. and J.W. Deardorff (1981) A laboratory study of dispersion from a source in the middle of the convective mixed layer. *Atmos. Environ.*, **15**, 109-117.
- Wilson, J.D. and T.K. Flesch (1993) Flow Boundaries in Random-Flight Dispersion Models: Enforcing the well-mixed condition. *J. Appl. Meteorol.*, **32**, 1695-1707.
- Wilson, J.D. and B.L. Sawford (1996) Review of Lagrangian stochastic models for trajectories in the turbulent atmosphere. *Bound.-Layer Meteorol.*, **78**, 191-210.
- Wyngaard, J.C., O.R. Coté and Y. Izumi (1971) Local free convection, similarity, and the budgets of shear stress and heat flux. *J. Atmos. Sci.*, **28**, 1171-1182.
- Wyngaard, J.C. (1985) Structure of the planetary boundary layer and implications for its modeling. *J. Climate and Applied Meteorol.*, **24**, 1131-1142.
- Wyngaard, J.C. (1988) Structure of the PBL. In *Lectures on Air Pollution Meteorology*, A. Venkatram and J.C. Wyngaard (eds.). Am. Meteorol. Soc., Boston, 390 pp.
- Young, G.S. (1988) Turbulence structure of the convective boundary layer. Part II: Phoenix 78 aircraft observations of thermals and their environment. *J. Atmos. Sci.*, **45**, 727-735.